WARWICK
THE UNIVERSITY OF WARWICK

A Thesis Submitted for the Degree of PhD at the University of Warwick

Permanent WRAP URL:
http://wrap.warwick.ac.uk/83227

Copyright and reuse:
This thesis is made available online and is protected by original copyright.
Please scroll down to view the document itself.
Please refer to the repository record for this item for information to help you to cite it.
Our policy information is available from the repository home page.

For more information, please contact the WRAP Team at: wrap@warwick.ac.uk

warwick.ac.uk/lib-publications

Thesis submitted to

The University of Warwick

for the degree of

Doctor of Philosophy

in

Mathematical Biology and Biophysical Chemistry

Kinetochore Dynamics and their Attachment to the Mitotic Spindle

Author : **Christopher Smith**

Supervisors : Andrew McAinsh, Professor of Cell Biology

Nigel Burroughs, Professor in Systems Biology

Examination panel:

External examiner : Susanne Lens

Professor of Genomic Instability, Utrecht University

Internal examiner : Till Bretschneider

Reader in Systems Biology, University of Warwick

Date of submission : 16 February 2016

Contents

List of Figures

List of Tables

Acknowledgments

One of the reasons driving my choice to pursue this PhD was my cell biology supervisor. Andrew very rarely wears a frown, but at the same time takes his lab and our work seriously. Andrew made me feel welcomed immediately, and without that I would not have enjoyed my time at MCB as much as I did. While I wasn't in immediate contact with my systems biology supervisor, Nigel, most of the time, he is easily approachable and therefore great to talk to. Importantly, he is always very honest in his scientific feedback – while on occasion cutting, it was valuable for the progress I have made as a researcher, and it is that that I truly appreciate about him. Thank you to you both for encouraging me to aim high (he says sat in a studio apartment at the prestigious Advanced Imaging Centre at Janelia Research Campus), sending our paper directly to Science (unsuccessfully might I add), and allowing me opportunities to collaborate with external groups. I would also like to thank both of you for the time you have set aside to help me with the completion of my thesis. For this I also thank Anne Straube and Jonathan Millar.

The working environment in the department and Andrew's lab was perfect. I would like to thank each and every member of Andrew's lab during my time in the department so far, as you have all helped in some aspect of the work I present here. I would also like to thank my Advisory Committee for ensuring my PhD got off the ground: thank you Jonathan Armond, Masanori Mishima, and David Rand.

Certain other members of the department have stuck out for me: those in the Coffee Gang (the legacy of the WhatsApp group lives on). In particular, I would like to thank James (the Morecambe to my Wise) for his ever-entertaining antics and ensuring I settled and felt welcomed into the lab, my Factory-neighbour Ben for enjoying "cwozunts" with coffee and being the catalyst in finding our mutual friendship group, and Sam who

kept me sane during cell-cycle dependent experiments (I purchased my cupcake-design suit because of him, so arguably not entirely sane). Additionally, I want to thank Neil, Faye, Sophie, Ella and Laura, whose company I regularly enjoyed in Coffee Gang. I want to thank the Straube lab Cake Club for allowing me to intrude, and in particular Daniel, who I can speak with about football for hours if I was allowed, and Rachel, who regularly left me silly notes and was always a breath of fresh air. Finally, I would like to thank Fred, who regularly got Jesus Christ Superstar stuck in my head, for the regular conversations while he was having to clean around me.

I've tried not to bore my parents with the actual work I do, but without them or my siblings, Andy and Sam, I wouldn't have grown into the person I am today – each one of them is incredibly caring and intelligent, and I have always loved going home to see them. Additionally, while I'm not sure how much she truly understands of my work, Charl has always made me feel like my work is the bee's knees, which is the best kind of motivation. Similarly, Mrs Lowe has always complimented me on my work, while she kept me fed and watered during more difficult times, and Roy has also helped to keep me mobile when my car thought otherwise. Amy has put up with me as a housemate the entire PhD, and was kind enough to provide me with lifts to work early on. She has also been someone with whom I have had many in-depth discussions and debates, and was the mastermind behind the Mini Cooper Birthday cake I served at work one year. There are many others, but particular thanks goes to Soph, Hev, Onur, Chris, Liv, Tom and Mr. Wink for providing me with entertainment outside of work when I really needed to relax.

Someone who deserves a great deal of appreciation is the person with whom I have spent most of my time during my PhD. She is someone I can call my best friend, someone who has kept me motivated and made me stronger, dealt with my grumpiness and stupidities, and without whom I wouldn't be where I am today. Thank you Sarah for being there during one of the most energy-depriving but exciting times of my life (so far – plenty more of those to come). Please know that I will do the same for you whenever you need me.

Declarations

This thesis is submitted to the University of Warwick in partial fulfillment of the requirements for admission to the degree of Doctor of Philosophy. The work presented here is my own, except where specifically stated otherwise, and was performed in the Division of Biomedical Cell Biology (Warwick Medical School, University of Warwick) under the supervision of Professor A. D. McAinsh during the period October 2012 to January 2016. My funding was provided by the EPSRC as part of the Molecular Organisation and Assembly in Cells (MOAC) Doctoral Training Centre (EP/F500378/1).

Christopher Smith

February 2016

Published work

As per Appendix B, I attach a copy of a paper entitled "Cdk1 Inactivation Terminates Mitotic Checkpoint Surveillance and Stabilizes Kinetochore Attachments in Anaphase" by Vázquez-Novelle *et al.* (2014) published in Current Biology. I include this paper as I generated the data for, performed the analysis for, and produced Figures 2 E and S2 F. For this contribution I am named on the paper.

Abbreviations

+TIPS	plus-tip interacting proteins
AP	away-from-the-pole (as in kinetochore state)
APC	anaphase promoting complex
C-terminus	carboxy-terminus
CCAN	constitutive centromere-associated network
CCD	charge-coupled device
CENP	centromere protein
CPC	chromosome passenger complex
EB protein	end binding protein
EM	electron microscopy
FP	fluorescent protein
FRET	Förster resonance energy transfer
FWHM	full width half maximum
JDS	joint directional switch
k-fibre	kinetochore-fibre
KMN	KNL1-MIS12-NDC80 complex
kMT	kinetochore-microtubule
LIDS	lead-initiated directional switch
MAP	microtubule-associated protein
MCC	mitotic checkpoint complex
MCMC	Monte Carlo Markov chain
MMF	mixture-model fitting
N	non-descript (as in kinetochore state)
N-terminus	amino-terminus

ND	non-degradable
NAC/CAD	nucleosome-associated complex/CENP-A distal
NEBD	nuclear envelope breakdown
P	poleward (as in kinetochore state)
PCM	pericentriolar material
PEF	polar ejection force
PSF	point spread function
RNAi	RNA interference
RWD	RING finger, WD repeat, DEAD-like helicase
RZZ	Rod-Zwilch-Zeste White 10
S	switching (as in kinetochore state)
SAC	spindle assembly checkpoint
SIM	structured illumination microscopy
TIDS	trail-initiated directional switch
WT	wild-type

Abstract

Chromosome segregation is a mechanical process that requires assembly of the mitotic spindle – a dynamic microtubule-based force-generating machine (Dumont & Mitchison, 2009). Connections between chromosomes and the spindle are mediated by kinetochores, pairs of multi-protein complexes assembled on centromeric chromatin that harness the pushing and pulling forces associated with microtubule dynamics to power chromosome movement (Rago & Cheeseman, 2013). This structure is reported to be compliant (Wan *et al.*, 2009; Maresca & Salmon, 2009; Uchida *et al.*, 2009; Dumont *et al.*, 2012; Drpic *et al.*, 2015; Etemad *et al.*, 2015; Tauchman *et al.*, 2015; Magidson *et al.*, 2016), which is the basis upon which it can transduce forces, and satisfy mitotic checkpoints. However recent studies have suggested that the kinetochore is a non-compliant linkage (Suzuki *et al.*, 2014), while others negate the requirement for intra-kinetochore stretch to allow onset of anaphase (Etemad *et al.*, 2015; Tauchman *et al.*, 2015; Magidson *et al.*, 2016). It is therefore crucial that the reasons for these differences are elucidated, and a new model developed to explain regulatory pathways sensitive to intra-kinetochore structure.

I have developed a novel semi-automated imaging assay to track kinetochore proteins tagged with two different coloured fluorescent proteins in 3D, coupled with a detailed assay for measurement of the required correction for 3D chromatic aberration directly from cells.

I reveal using three dimensional tracking that the kinetochore forms a non-compliant linkage between centromeric chromatin and kintetochore spindle fibres. Instead the outer kinetochore layer can swivel around the inner kinetochore/centromere, which results in a reduction in intra-kinetochore distance when viewed in lower dimensions, the only 3D measurement thus far being by Etemad *et al.* (2015). I show that swivel pro-

vides a mechanical flexibility that enables kinetochores at the periphery of the spindle to engage microtubules. Swivel reduces as cells approach anaphase, explaining previous suggestions that the kinetochore needs to be stretched upon bi-orientation prior to anaphase onset (Maresca & Salmon, 2009; Uchida *et al.*, 2009). Reduction in swivel suggests there is an organisational change linked to checkpoint satisfaction, and/or changes required in kinetochore mechanochemistry before sister chromatid dysjunction. I show that Cdk1 inactivation is required to suppress kinetochore-microtubule dynamics in anaphase, and therefore may mediate required changes in kinetochore state.

Finally, my work opens up the possibility to map the 3D architecture of the kinetochore, and between different domains within proteins and complexes. With such an architectural understanding, it will now be possible to investigate the mechanisms of organisational changes that occur during cycles of microtubule attachment and the regulatory processes of error-correction and SAC activation/silencing.

Chapter 1

Introduction

1.1 Mitosis

Human cells are extraordinarily complex machines being built from thousands of proteins with a wide range of functions. Perhaps the most important requirement for a cell is to replicate and duplicate itself, and to do so with high fidelity and efficiency. Indeed, errors in these processes are linked to the development of cancer, ageing and multiple human disease states. A fundamental part of this process is mitosis (nuclear division) during which the duplicated chromosomes (sister chromatids) are segregated producing two genetically identical daughter cells. Mitosis can be split into a number of different phases: during prophase the cell rounds up and the duplicated centrosomes (future spindle poles) start to separate to opposite sides of the nucleus. Following nuclear envelope breakdown (NEBD), the cell enters prometaphase and chromosomes make first contact with dynamic microtubules that are nucleated by the two centrosomes. These chromosome-microtubule interactions allow for the alignment of chromosomes to the spindle equator, forming the classic "metaphase plate". This process is termed congression and is mediated by a number of key mechanisms. Once all chromosomes have congressed to the spindle equator, the cell is in metaphase. Chromosomes in most animal cells now exhibit movement towards and away from their attached spindle poles. These movements require that the chromosomes bi-orientate – that is sister chromatids are attached to microtubules nucleated from opposite spindle poles. This is the only geometry compatible for accurate segregation, and cells have thus evolved error-correction mechanisms to drive the bi-orientation process. At the same time, cells

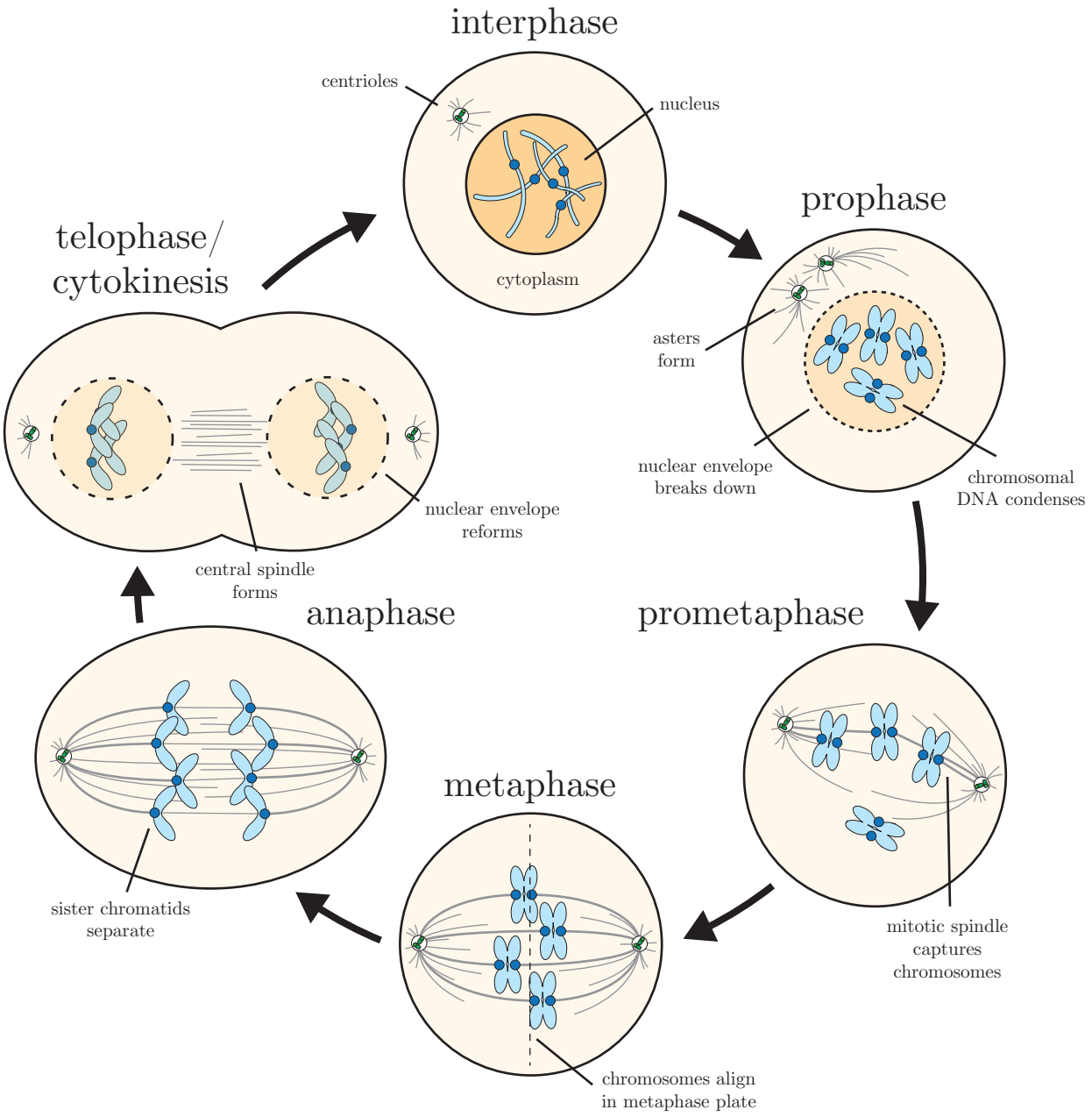

Figure 1.1 *Schematic of alignment and separation of sister chromatids in mitosis.* After DNA and centrioles have been replicated during S phase and before cells enter mitosis (interphase ⟶ prophase transition), DNA is condensed to form chromosomes. On entry into mitosis in prophase, nuclear envelope breaks down and asters begin to form from the centrioles. In prometaphase, spindle poles are at opposite ends of the cell. The mitotic spindle searches for and captures chromosomes via kinetochores, eventually aligning them at the metaphase plate. Once aligned, anaphase onset occurs as sister chromatids are separated towards opposite poles and the central spindle forms. The cellular membrane then constricts at the cell equator and a new nuclear envelope forms around the separate sets of sister chromatids.

also utilise a surveillance mechanism called the spindle assembly checkpoint (SAC) that functions to prevent anaphase onset until all chromosomes are correctly attached to microtubules in the bi-orientated state. Once this checkpoint is satisfied, the cell cycle machinery is allowed to promote anaphase onset and each set of sister chromatids move uniformly to opposite poles of the spindle. Next, the nuclear envelope re-forms around the segregated chromosomes, the cell is divided (cytokinesis) and finally daughter cells are physically separated by abscission (Figure 1.1).

1.2 The Mitotic Spindle

The complex set of chromosome movements that are required for the completion of mitosis demand that there must be force-generating mechanisms that can power the physical movements. This is achieved by the mitotic spindle (Figure 1.2), a large bipolar array of dynamic microtubules. Microtubules are built from α- and β-tubulin heterodimers that associate end-to-end forming protofilaments, which are themselves organised into a hollow tube. Microtubules are polar, so that one end starts with α-tubulin, known as the minus end, while the other end terminates with β-tubulin, known as the plus end (Figure 1.2). Tubulin heterodimers can be added and removed from either end of the microtubule giving rise to dynamic polymeric structures capable of growing (or polymerising) and shrinking (or depolymerising). The transitions between these states are termed catastrophe and rescue. Importantly, the polymerisation of microtubules allows energy to be stored in structural bonds between the tubulin subunits in the lattice. This energy source is harnessed for doing work, i.e. the growth of microtubules can generate pushing force, while the depolymerisation of microtubules has the potential to generate pulling forces (for example if attached to a chromosome). Furthermore, microtubules provide the tracks along which kinesin and dynein motors can step. Such motorised transport can therefore also generate force and further contribute to the movement of chromosomes during mitosis.

The mitotic spindle – at least in animal cells – requires the nucleation of microtubules by centrosomes, which are composed of a centriole pair and a surrounding

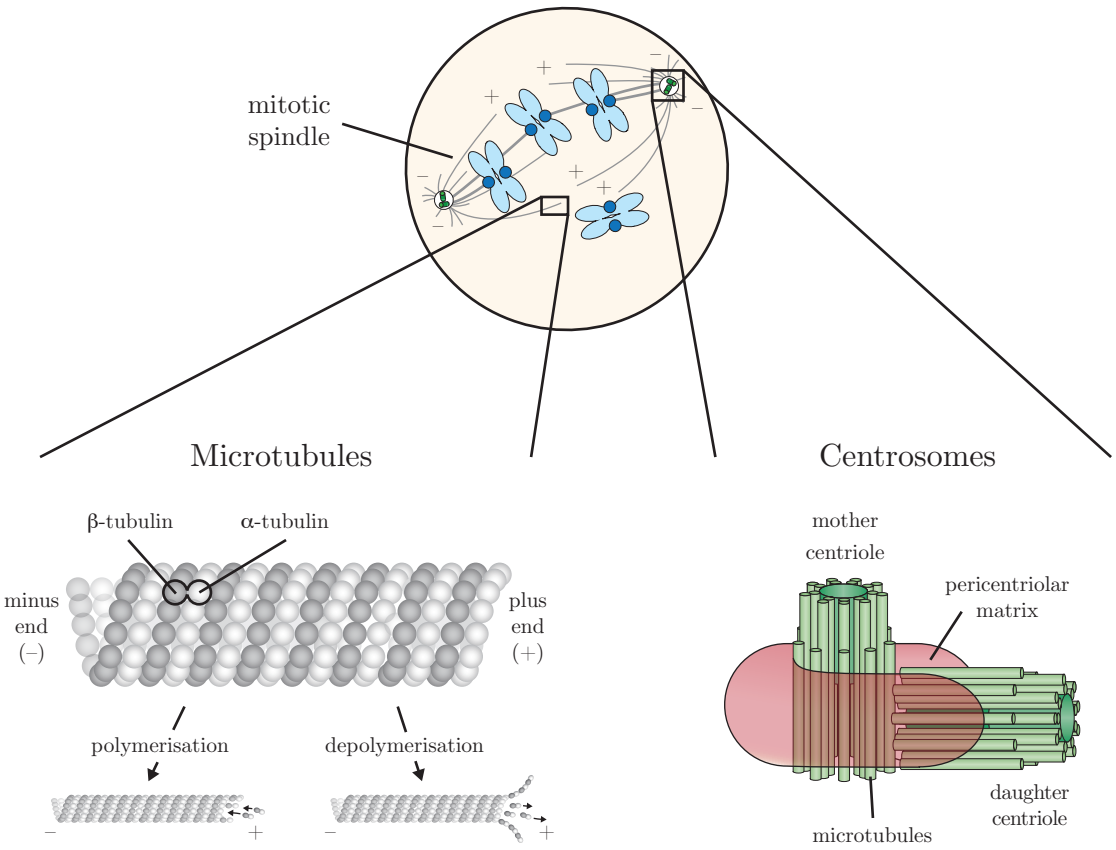

Figure 1.2 *Structure of microtubules and centrosomes.*
The mitotic spindle consists of an array of microtubules nucleating from centrioles, which themselves predominantly consist of microtubules. Microtubules are orientated so that their minus (–) ends are located at centrioles, and plus (+) ends grow outwards. Microtubules are constructed of α- and β-tubulin heterodimers, orientated so that α-tubulin is at the + end. Centrioles and the pericentriolar matrix make the centrosome. Diagram of microtubule adapted from McAinsh 2014. Diagram of centrioles adapted from Conduit *et al.* 2015.

pericentriolar material (PCM). The centriole is duplicated during S-phase and is constructed from a cylindrical array of short microtubules (Figure 1.2). The PCM contains proteins required for centriole duplication (Loncarek *et al.*, 2008; for review see Doxsey *et al.*, 2005), and crucially, γ-tubulin which nucleates spindle microtubules from their minus end (Moritz *et al.*, 1998; Schnackenberg & Khodjakov, 1998). This way, large numbers of microtubules can grow from each centrosome forming a bipolar spindle with plus ends orientated towards the opposite spindle pole (Figure 1.2). A number of these project outwards to the cell cortex (astral microtubules) where they generate forces that can re-position the spindle within the cell (reviewed in Lu & Johnston, 2013). Although there is a population of free microtubules within the spindle, a subset forms stable overlaps with microtubules nucleated from the opposite pole. These provide structural integrity to the spindle. Of critical importance are the microtubules whose plus ends connect to the chromosome – an event mediated by a large multi-protein complex called the kinetochore, which assembles at the centromere of each sister chromatid. In human cells the kinetochore binds a parallel array of microtubules called the kinetochore-fibre (k-fibre). There are between 12-24 microtubules per k-fibre (Compton, 2000; Rieder, 2005; Wendell *et al.*, 1993) and this number tends to increase as cells progress from prometaphase to metaphase (McEwen *et al.*, 1997). The k-fibre is held together along its length by a series of bridging complexes, which have been shown to form a supportive mesh (Nixon *et al.*, 2015). Loss of these factors has been shown to reduce tension in the k-fibre (Cheeseman *et al.*, 2013). In summary, the kinetochore can be thought of as a coupled-mechanical system, in which kinetochores operate as a key mechanical connector.

1.3 The Human Kinetochore

Human kinetochores are located at centromeric domains that range from ∼240 kb to more than 4,000 kb in size. Direct observations by electron microscopy using chemical fixation revealed that the kinetochore consists of a plate-like structure,that is around 300 nm wide and 150 nm deep (Jokelainen, 1967; Krishan & Buck, 1965; Comings

& Okada, 1971; Roos, 1973). However high-pressure freezing, which better preserves kinetochore structure, shows that the tri-laminar plate structure is likely to be an artefact and that the kinetochore instead appears as a fibrous network (McEwen *et al.*, 1998; discussed in O'Connell *et al.*, 2012). The first kinetochore proteins to be discovered were CENP-A, CENP-B and CENP-C and was possible because the sera of scleroderma patients recognised centromeres (Moroi *et al.*, 1980; Fritzler *et al.*, 1980; Earnshaw & Rothfield, 1985). CENP-A is a histone H3 variant that forms a specialised nucleosome that assembles into centromeric chromatin at G1 (Palmer *et al.*, 1991; Sullivan *et al.*, 1994; Jansen *et al.*, 2007). This CENP-A chromatin is interspersed with regions of histone H3 at the centromere (Blower *et al.*, 2002) with a number of models for the organisation of the domain proposed (Earnshaw, 2015).

The centromeric region contains repeated arrays of 171 base pair (bp) sequences called α-satellite DNA sequences. Within α-satellite DNA there are 17 bp sequences called the CENP-B box, which bind CENP-B (Masumoto *et al.*, 1989). CENP-B has recently been shown to bind directly the amino (N)-terminus of CENP-A (Fujita *et al.*, 2015; Fachinetti *et al.*, 2015) and CENP-T (Hellwig *et al.*, 2008), and to ensure recruitment of optimal levels of CENP-C to the centromere (Fachinetti *et al.*, 2015). There have been contrasting views on whether CENP-B is required for faithful cell division, some work observing errors in chromosome segregation (Ohzeki *et al.*, 2002; Fachinetti *et al.*, 2015), but others suggesting that inhibition of CENP-B binding causes no effect (Amor & Choo, 2002). From these founding members of the CENP family the true extent of kinetochore protein number has been elucidated using a combination of mass-spectrometry-based proteomics and genetic studies.

1.3.1 Constitutive Centromere-associated network (CCAN)

The kinetochore protein structure located proximal to the centromeric chromatin is the constitutive centromere-associated network (human CCAN; Figure 1.3 A). This consists of 16 proteins, each also named with the prefix 'CENP' (or centromere protein). The CCAN was originally discovered by affinity-purification of nucleosomes containing

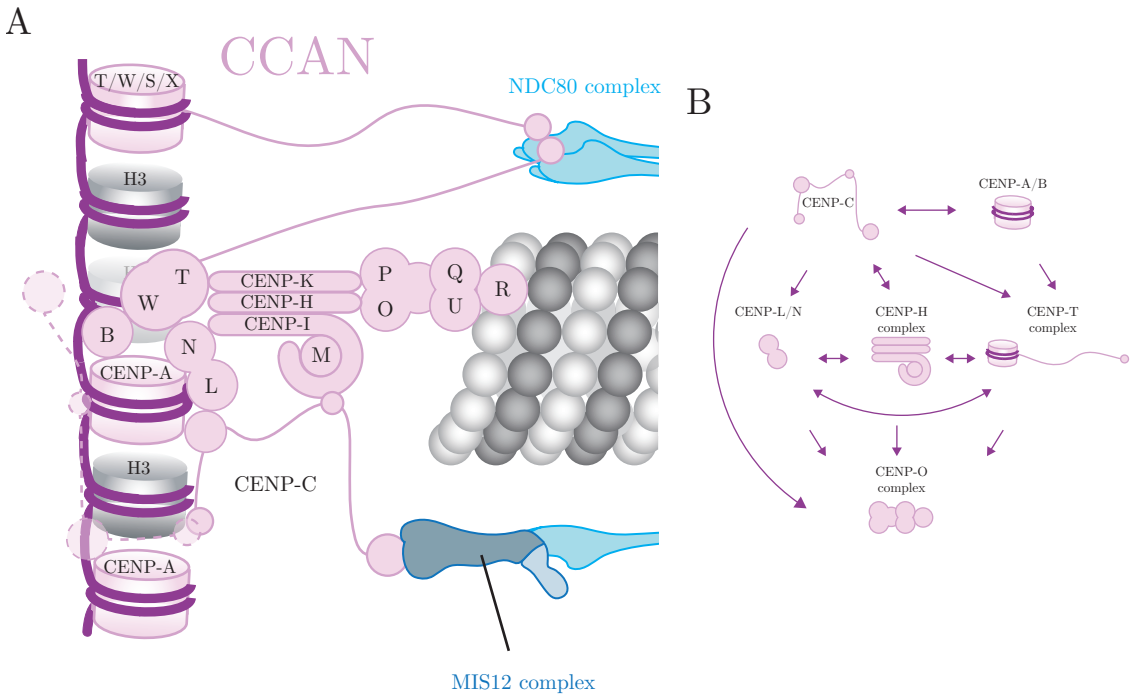

Figure 1.3 *Structure of the consititutive centromere-associated network.*
The consitutive centromere-associated network (CCAN; pink) within the kinetochore consists of an array of proteins prefixed with 'CENP-' (or centromere protein). A large number of CENPs interact with centromeric chromatin and are required for proper structure of the kinetochore, including connection to the KMN complex (blue).
(A) A structural map of the inner kinetochore, demonstrating interactions between CCAN components and sub-complexes. Direct contact between annotated proteins represents an interaction. Note that due to the complexity of the kinetochore, most, but not all, interactions are represented here.
(B) A map of dependencies of CCAN complexes on one another demonstrates the complexity in development and structure of the inner kinetochore. Dependency on localisation are represented by purple arrows, so that the purple arrow is pointing downstream in protein localisation dependency, i.e. the protein at the arrowhead depends on the presence of the protein before the arrow. Double-headed purple arrows represent a synergistic dependency of the pair of proteins/complexes.

CENP-A (Foltz *et al.*, 2006; Okada *et al.*, 2006). At this stage the CCAN was originally called the CENP-A nucleosome-associated complex/CENP-A distal (NAC/CAD) complex. Recent work has revealed that the CCAN can be separated into a series of distinct sub-complexes with specific functional roles in the kinetochore:

The amino terminal of CENP-N makes a direct physical contact with its centromere targeting domain (CATD) of CENP-A (Hellwig *et al.*, 2011; Carroll *et al.*, 2009). Recent work demonstrated a conformational change in centromeric chromatin at the G1/S transition which exposes CENP-A's RG loop to facilitate recruitment of CENP-N (Fang *et al.*, 2015). CENP-N depletion inhibits the loading of CENP-A to centromeres during G1 phase, which suggests that CENP-N is part of a feedback loop propagating centromeric chromatin in dividing cells (Carroll *et al.*, 2009). Loss of CENP-N also causes problems in chromosome congression (Foltz *et al.*, 2006), which is likely due to CENP-N's role in loading of other kinetochore proteins (Foltz *et al.*, 2006; Carroll *et al.*, 2009, 2010). Furthermore, CENP-N forms a complex with CENP-L, which is also responsible for the loading of other CCAN proteins (McKinley *et al.*, 2015). Similarly to CENP-N, depletion of CENP-L by RNA interference (RNAi) resulted in perturbed chromosome congression (Mchedlishvili *et al.*, 2012).

1.3.2 CENP-C and CENP-T

When CENP-N is bound to the N-terminus of CENP-A, its carboxy (C)-terminus is bound to CENP-C (Carroll *et al.*, 2010; Guse *et al.*, 2011; Kato *et al.*, 2013; Figure 1.3 A), which plays a central role in the recruitment of most other components of the kinetochore (Hori *et al.*, 2008; Milks *et al.*, 2009; Gascoigne *et al.*, 2011; Przewloka *et al.*, 2011; Hori *et al.*, 2013; Basilico *et al.*, 2014; Rago *et al.*, 2015; Klare *et al.*, 2015; McKinley *et al.*, 2015). Indeed, its depletion results in strong mitotic arrest (Suzuki *et al.*, 2014). CENP-C is targeted to the centromere by its disordered central region (Song *et al.*, 2002; Heeger *et al.*, 2005; Milks *et al.*, 2009; Tanaka *et al.*, 2009; Carroll *et al.*, 2010), which recognises CENP-A's hydrophobic C-terminal tail (Kato *et al.*, 2013). Its central region contains the CENP-C motif, which also recognises CENP-A

nucleosomes (Kato *et al.*, 2013). Furthermore, the C-terminus of CENP-C both binds CENP-A (Carroll *et al.*, 2010; Guse *et al.*, 2011; Logsdon *et al.*, 2015) and induces homo-dimerisation (Cohen *et al.*, 2008), while also recruiting a subunit of the CENP-A-loading Mis18 complex, M18BP1 (Moree *et al.*, 2011; Dambacher *et al.*, 2014). CENP-C has more recently been shown to be chaperoned to the centromere by the CENP-A chaperone HJURP (Tachiwana *et al.*, 2015), suggesting it has a key role in the initial assembly of the kinetochore. Furthermore, CENP-C plays a role in outer kinetochore assembly as its N-terminus binds directly to the MIS12 complex. This complex is part of the major microtubule and checkpoint regulating KNL1-MIS12-NDC80 (KMN) network within the outer kinetochore (Przewloka *et al.*, 2011; Screpanti *et al.*, 2011). Interestingly, only $\sim$ 39% of the 215 CENP-C proteins per human kinetochore are bound to the MIS12 complex and this only forms connections with $\sim$ 32% of the total number of NDC80 complexes (Suzuki *et al.*, 2014).

The remaining 68% of linkages between the inner and outer kinetochore are mediated by CENP-T. This protein binds both centromeric chromatin and directly to the Ndc80 complex (Hori *et al.*, 2008; Nishino *et al.*, 2012). More specifically, CENP-T binds the N-terminal tail of CENP-A (Logsdon *et al.*, 2015; Folco *et al.*, 2015) and forms a heterodimer with CENP-W (Prendergast *et al.*, 2011), which interacts directly with histone H3 but not CENP-A (Hori *et al.*, 2008; Figure 1.3 A). Indeed, CENP-T has been observed to be in proximity to histone H3 using super-resolution microscopy (Ribeiro *et al.*, 2010). CENP-T/W can also form a complex with a heterodimer of CENP-S and CENP-X (Amano *et al.*, 2009). Biochemical experiments suggest that the full CENP-T complex can form a nucleosome-like structure (Nishino *et al.*, 2012), which preferentially dimerises to bind $\sim$100 bp DNA linkers between nucleosomes (Takeuchi *et al.*, 2014; Figure 1.3 A). In contrast to experiments showing no preference of binding between pairs of histone H3 or CENP-A (Takeuchi *et al.*, 2014), Förster resonance energy transfer (FRET) experiments demonstrate the complex prefers to be in proximity to histone H3 (Dornblut *et al.*, 2014). The CENP-T complex also positively supercoils DNA (Nishino *et al.*, 2012), which is dependent on the CENP-T/W DNA

binding sites only (Takeuchi *et al.*, 2014). Additionally it has been suggested that not all kinetochore-associated CENP-T/W dimers are present within the CENP-T/W/S/X heterotetramer (Samejima *et al.*, 2015a). This is likely given that CENP-S- and CENP-X-deficient cells are viable (Amano *et al.*, 2009) whereas removal of CENP-T/W causes a strong mitotic delay (Hori *et al.*, 2008; Prendergast *et al.*, 2011; Suzuki *et al.*, 2014). Interestingly, removal of CENP-T from a mature kinetochore causes a much weaker phenotype (Wood *et al.*, 2016), which, along with the notion that CENP-T/W/S/X may wrap centromeric DNA around itself (Fukagawa, 2012), supports the suggestion that the CENP-T/W dimer has a role in establishing centromeric chromatin structure upstream of kinetochore assembly (Hori *et al.*, 2008). In contrast, CENP-S/X functions downstream of other CCAN proteins, but has also been shown to contribute to localisation of outer kinetochore components (Amano *et al.*, 2009). This explains why CENP-S was discovered in affinity purifications of CCAN proteins downstream of CENP-T/W in kinetochore formation (Foltz *et al.*, 2006). One such sub-complex of the CCAN that localises upstream of CENP-S/X is the CENP-H complex. Its degradation results in loss of CENP-S/X (Amano *et al.*, 2009), but maintains localisation of CENP-T/W (Hori *et al.*, 2008).

1.3.3 Other CCAN sub-complexes

The CENP-H complex consists of CENP-H, -I, -K and -M (Figure 1.3 A) and is required for efficient chromosome congression and normal regulation of kinetochore-microtubule (kMT) dynamics (Sugata *et al.*, 1999; Nishihashi *et al.*, 2002; McClelland *et al.*, 2007; Nishimura *et al.*, 2009; Amaro *et al.*, 2010; Suzuki *et al.*, 2014). The inability to faithfully align chromosomes may be due to its role in loading of newly-synthesised CENP-A (Okada *et al.*, 2006), which would result in poorly-structured centromeric chromatin in mitosis. On the other hand, it may be due to its association with CENP-T/W (Basilico *et al.*, 2014; Klare *et al.*, 2015) or, more likely it essential role in recruitment of the CENP-O complex (see below). While CENP-T/W binds DNA it also requires its interaction with CENP-H/K to stably localise to kinetochores (McKinley *et al.*, 2015).

Thus any loss of the CENP-H complex would destabilise linkages between the inner and outer kinetochore. Similarly, CENP-C also requires CENP-H for kinetochore-binding although CENP-H to some extent also requires CENP-C (Fukagawa *et al.*, 2001; Nishihashi *et al.*, 2002; Kwon *et al.*, 2007; Milks *et al.*, 2009; Carroll *et al.*, 2010; Basilico *et al.*, 2014; Klare *et al.*, 2015; McKinley *et al.*, 2015). In fact, CENP-C binds the CENP-H complex directly via a region in the N-terminus of CENP-C (Klare *et al.*, 2015). As a further interesting structural note, CENP-M doesn't directly bind CENP-H or -K, but is believed to be located within a concave region of the solenoid-shaped CENP-I, an interaction which is key to loading of CENP-I/M to kinetochores (Basilico *et al.*, 2014). Together these findings imply a synergistic role for each protein complex in the assembly of the kinetochore (Figure 1.3 B, purple arrows). This is supported by observation of compromised inner-kinetochore structure when either CENP-C, CENP-T, CENP-H or a combination of the three is depleted by RNAi in human cells (Suzuki *et al.*, 2014). Thus CENP-H/I/K/M, along with CENP-T and CENP-C are the central linkers that physically connect the inner and outer kinetochore.

Four of the remaining five CCAN proteins, CENP-P, -O, -Q, and U (also called PBIP1), form the CENP-O complex (Figure 1.3 A). The CENP-O complex contains the only set of subunits within the CCAN that, upon their depletion, do not cause the loss of any other inner kinetochore proteins (Hori *et al.*, 2008; Kagawa *et al.*, 2014; Samejima *et al.*, 2015a). Furthermore, when any other CCAN proteins or subcomplexes are depleted by RNAi, the CENP-O complex no longer localises to kinetochores (Okada *et al.*, 2006; Foltz *et al.*, 2006; McClelland *et al.*, 2007; Hori *et al.*, 2008). This result was confirmed recently in HeLa cells using deletion of the endogenous genes by CRISPR/Cas9 (McKinley *et al.*, 2015). The one exception is CENP-R, which associates with the CENP-O complex directly and is not required for CENP-O complex binding at the kinetochore (Hori *et al.*, 2008). The CENP-O complex loads to kinetochores during S phase, and is then thought to oligomerise, an idea supported by the formation of CENP-Q octomers *in vitro* (Amaro *et al.*, 2010), and an increase in FRET signal between N- and C-termini of CENP-Q and CENP-U during late S

phase (Eskat *et al.*, 2012). The CENP-O complex has been suggested to associate with a number of kinetochore proteins including CENP-L, -K (Eskat *et al.*, 2012), the C-terminus of Ndc80 in human cells (Hua *et al.*, 2011), the CENP-H complex in DT40 cells (Minoshima *et al.*, 2005), and the CENP-C and Mis12-Nnf1 homologues Mif2 and Mtw1-Nnf1 in budding yeast (Hornung *et al.*, 2014). In human cells CENP-U may also form interactions with CENP-B/CENP-I based on FRET experiments (Hellwig *et al.*, 2009) and is a key targeting subunit for polo like kinase 1 (Plk1; Kang *et al.*, 2011a; Park *et al.*, 2011; Bancroft *et al.*, 2015; Park *et al.*, 2015). The CENP-Q and -U components have also been observed to directly bind microtubules *in vitro* (Amaro *et al.*, 2010), and contribute to chromosome congression (Foltz *et al.*, 2006; Hori *et al.*, 2008; Kang *et al.*, 2011a; Bancroft *et al.*, 2015). Finally, the complex has been linked to the generation of kinetochore-based pushing forces that contribute to the pushing apart of centrosomes during prometaphase (Toso *et al.*, 2009).

Interestingly, depletion of CENP-O complex subunits varies across cell types: mouse ES cells are not viable after removal of CENP-U, whereas chicken DT40 and mouse embryonic fibroblasts experienced mitotic defects that were not detrimental to cell proliferation (Kagawa *et al.*, 2014). Indeed knockout of any of the CENP-O complex subunits from DT40 cells did not affect cell viability, all knockouts aside from CENP-R resulting only in delayed mitotic progression albeit with increased numbers of uncongressed chromosomes (Hori *et al.*, 2008). In line with this, our experiments in human cells show how CENP-O is important for chromosome congression (McAinsh *et al.*, 2006). Why conditional knock-outs of CENP-O were reported to have no phenotype is unclear (Cheeseman, 2014). Most recently it was observed that other CCAN proteins accumulate at kinetochores in CENP-O- or CENP-R-deficient DT40 cells, which suggests the CENP-O complex regulates the size of the inner kinetochore without affecting cell viability (Samejima *et al.*, 2015a). This is in line with the original reports of an increase in CENP-H/I//K/M following depletion of CENP-O in human cells (McClelland *et al.*, 2007).

Overall, the inner region of the kinetochore is home to an array of proteins with

varying loading cycles through the cell cycle (Hemmerich *et al.*, 2008). However the multitude of protein-protein interactions within the complex possibly make this one of the most difficult systems within the kinetochore to unravel (Figure 1.3 B). It is worth noting that there are other kinetochore proteins prefixed by 'CENP', including CENP-E and CENP-F, however these are not part of CCAN being localised at the fibrous corona, which is distal to the outer kinetochore. CENP-E's role in search-and-capture and congression processes is discussed below (see § 1.3.5).

1.3.4 Microtubule-binding Complexes

The inner kinetochore components build a platform upon which the outer kinetochore can be assembled (Cheeseman & Desai, 2008). The main components of the CCAN mediating this linkage between the inner and outer kinetochore are CENP-C and CENP-T, which bind components of the KNL1-MIS12-NDC80 (KMN) network (e.g. Rago *et al.*, 2015; Figure 1.4). Furthermore, the kinetochore also recruits the Ska complex as part of the outer kinetochore (Gaitanos *et al.*, 2009; Figure 1.4). While the CCAN ensures efficient assembly of the kinetochore to centromeric chromatin, the KMN and Ska complex mediate attachment to the mitotic spindle through direct interactions with microtubules. Therefore the localisation and regulation of the KMN is crucial for faithful cell division.

The NDC80 complex is the major microtubule binding sub-complex within the KMN network (DeLuca *et al.*, 2004). It consists of four subnuits: Ndc80 (also called Hec1), Nuf2, Spc24, and Spc25 (Wigge & Kilmartin, 2001; McCleland *et al.*, 2004; Cheeseman *et al.*, 2006). Each of these four proteins contain globular domains attached to extended coiled-coils that mediate the intra-complex interactions. Ndc80 and Nuf2 dimerise so that the calponin-homology domains in their N-termini are in proximity with one another, Spc24 and Spc25 doing the same so that their C-terminal heads are adjacent (Ciferri *et al.*, 2005; Wei & Sorger, 2005). The N-terminal heads of Ndc80/Nuf2 bind microtubules directly (DeLuca *et al.*, 2006; Cheeseman *et al.*, 2006), potentially forming oligomers along the microtubule lattice (Alushin *et al.*,

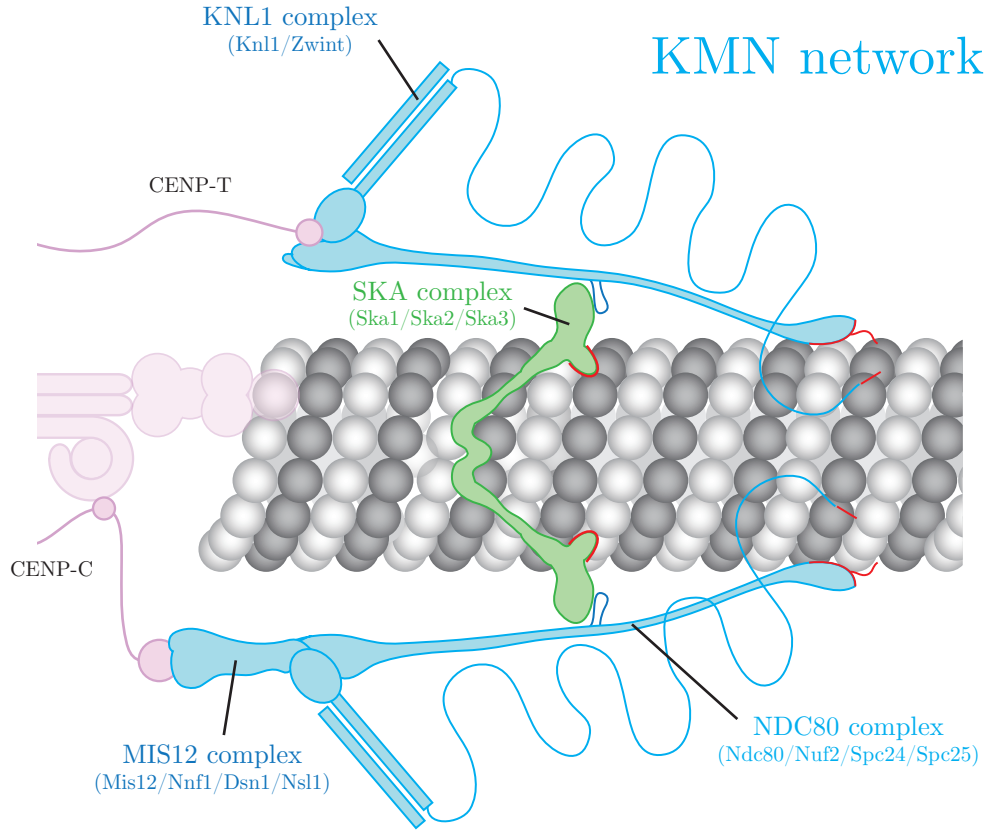

Figure 1.4 *Structure of the microtubule-binding outer kinetochore.*
The KNL1-MIS12-NDC80 (KMN; blue) is constructed upon the CCAN (pink) in the inner kinetochore. The NDC80 and KNL1 complexes bind microtobules, while the MIS12 mediates attachments between inner and outer kinetochore proteins. The SKA complex (green) also binds microtobules and associates with the KMN network. Microtubule-binding regions of each complex are shown in red.

2010). Meanwhile their C-termini associate with the amino-terminal coiled-coils of Spc24/25 to form a 50 nm length, dumb-bell shaped structure (Ciferri *et al.*, 2005; Wei & Sorger, 2005; Figure 1.5). The N-terminus of Ndc80 also contains an extension, called the Ndc80 'toe', which contains key regulatory sites that are phosphorylated by Aurora-B (DeLuca *et al.*, 2006; Nousiainen *et al.*, 2006; Ciferri *et al.*, 2008; Malik *et al.*, 2009; DeLuca *et al.*, 2011). The number of sites phosphorylated in early mitosis is high (DeLuca *et al.*, 2011), but decreases to zero or one in metaphase, presumably as PP1 is recruited to the kinetochore (Zaytsev *et al.*, 2014). The gradual dephosphorylation of the toe increases the affinity of Ndc80 for microtubules This way individual NDC80 complexes bind more tightly towards the end of metaphase leading to a stabilisation of microtubule-kinetochore attachment (Zaytsev *et al.*, 2015) (Guimaraes *et al.*, 2008; Miller *et al.*, 2008). At the centromere-facing end of the complex, each Spc24 and Spc25 have RING finger, WD repeat, DEAD-like helicase (RWD) domains at their C-terminal (Wei *et al.*, 2006; Ciferri *et al.*, 2008; Malvezzi *et al.*, 2013; Nishino *et al.*, 2013). These domains bind the Nsl1 and Dsn1 subunits of the MIS12 complex (Petrovic *et al.*, 2010; Malvezzi *et al.*, 2013; Aravamudhan *et al.*, 2014). Spc24/25 also bind the N-terminus of CENP-T in a mutually exclusive manner to MIS12, an association that is strengthened by phosphorylation of CENP-T's N-terminus (Nishino *et al.*, 2013). Truncation, or expression of a non-phosphorylatable version of CENP-T diminishes the recruitment of the KMN network (Rago *et al.*, 2015). This connection is therefore important for the linkage between the inner and outer kinetochore (Rago *et al.*, 2015). Taken together the NDC80 complex forms a rigid rod-like structure that binds microtubules and is recruited to kinetochores via two redundant pathways (Mis12 and CENP-T).

In addition to binding the NDC80 complex, the MIS12 complex is also responsible for binding additional components of the inner and outer kinetochore (Figure 1.4). It is therefore considered a major "interaction hub" within the kinetochore. It assembles from four subunits: Mis12, Dsn1, Nsl1, and Nnf1, forming a $\sim$ 22 nm-long complex (Petrovic *et al.*, 2010; Figure 1.5). The Nsl1 and Dsn1 subunits have been shown to directly bind the NDC80 complex (Petrovic *et al.*, 2010; Malvezzi *et al.*, 2013; Arava-

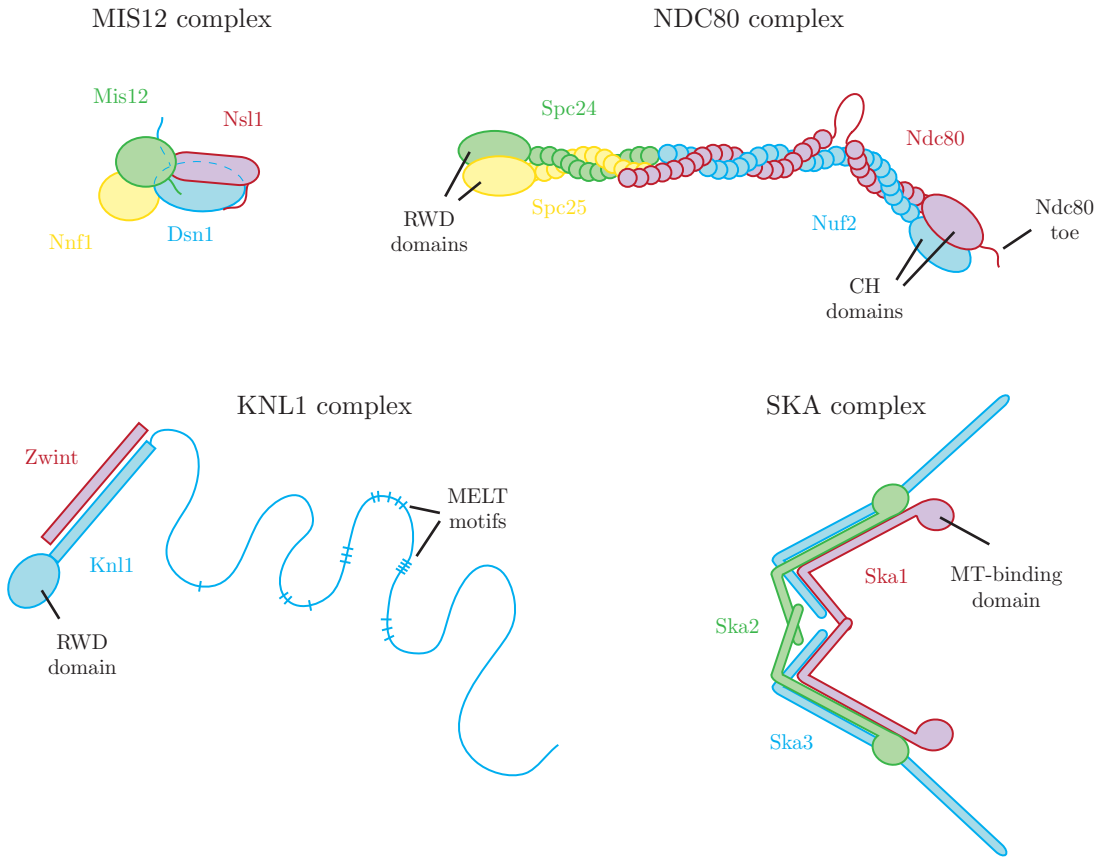

Figure 1.5 *Structure of each complex in the outer kinetochore.*
Schematics of the MIS12, NDC80, KNL1 and SKA complexes demonstrating the currently understood intra-complex structure. Calponin-homology (CH), RING finger, WD repeat, DEAD-like helicase (RWD), and microtubule- (MT-)binding domains of each complex are annotated. MELT motifs within Knl1 are also annotated.

mudhan *et al.*, 2014) while the MIS12 complex binds CENP-C's N-terminus (Screpanti *et al.*, 2011) via the Nnf1 subunit (Przewloka *et al.*, 2011). Similar to perturbation of CENP-T's linkage with outer kinetochore components, over-expression of a truncated version of CENP-C devoid of its ability to bind centromeric chromatin resulted in perturbed chromosome congression (Screpanti *et al.*, 2011). When endogenous full-length CENP-C was still present in these cells the truncated form competed for binding to outer-kinetochore proteins causing mis-localisation of both the MIS12 and NDC80 complexes. Similar regions of the Nsl1 and Dsn1 subunits also bind an RWD domain in Knl1's C-terminus (Petrovic *et al.*, 2014). This recruitment is important, as Knl1 plays a central role in spindle assembly checkpoint (SAC) signalling through recruitment of Bub3 (see section 1.4), recruitment of the PP1 phosphatase, as well as a minor role in microtubule binding (Cheeseman *et al.*, 2006; for review see Ghongane *et al.*, 2014). Moreover, Knl1 is required for the Aurora B-dependent phosphorylation of Ndc80 (Caldas *et al.*, 2013). Knl1 forms a stable complex with Zwint-1 which stabilizes the binding of the Rod-Zwilch-Zeste White 10 (RZZ) complex at kinetochores and contributes to SAC function (see section 1.3.7 below; Wang *et al.*, 2004; Kops *et al.*, 2005; Kiyomitsu *et al.*, 2011).

MIS12 may make an additional contribution to kinetochore assembly: in budding yeast Mtw1 (Mis12) and Nnf1 subunits of the MIND (Mis12) complex has been suggested to interact with the inner-kinetochore COMA complex (De Wulf *et al.*, 2003), the equivalent of the human CENP-O complex (Hornung *et al.*, 2011). This implies a potential link between the MIS12 and CENP-O complexes in humans with their RWD domains potentially mediating interaction with the MIS12 complex in a similar fashion to Spc24/25 and Knl1 (Schmitzberger & Harrison, 2012).

A complex not considered part of the KMN network whose microtubule-binding is required for faithful chromosome congression is the Spindle Kinetochore Associated (SKA) complex. This complex consists of three subunits: Ska1, Ska2, and Ska3 (Hanisch *et al.*, 2006; Daum *et al.*, 2009; Gaitanos *et al.*, 2009; Raaijmakers *et al.*, 2009; Welburn *et al.*, 2009; Ohta *et al.*, 2010) and requires the presence of the NDC80

complex for its recruitment to kinetochores (Gaitanos *et al.*, 2009). Each of the three subunits contain coiled-coil domains and form a W-shaped di-hetero-trimeric complex with two distinct microtubule binding domains (Gaitanos *et al.*, 2009; Jeyaprakash *et al.*, 2012; Figure 1.5). It is specifically thought to mediate depolymerisation-coupled pulling with the purified complex being able to track depolymerising microtubules in vitro (Welburn *et al.*, 2009; Schmidt *et al.*, 2012). As a consequence, its depletion from kinetochores results in errors in microtubule attachment and chromosome congression (Gaitanos *et al.*, 2009; Raaijmakers *et al.*, 2009; Welburn *et al.*, 2009). Loss of Ska1 or Ska2 also results in perturbation to normal timing of anaphase onset (Hanisch *et al.*, 2006; Daum *et al.*, 2009), and has been suggested to stabilise NDC80 binding (Jeyaprakash *et al.*, 2012). Furthermore, Ska1 and Ska3 contain Aurora-B dependent phosphorylation sites for regulation of binding to microtubules (Chan *et al.*, 2012).

1.3.5 MAPs and Molecular Motors

A number of microtubule-associated proteins (MAPs) and molecular motors also associate with the kinetochore. These proteins do not contribute to kinetochore structure per sé, but instead regulate microtubule dynamics, and therefore contribute to chromosome congression, the ability of kinetochores to utilise microtubule-generated forces, and spindle positioning. End binding (EB) proteins, which include EB1, EB2 and EB3, (Bu & Su, 2001) are thought to have distinct functions during mitosis. EB1 binds polymerising microtubules at kinetochores (Tirnauer *et al.*, 2002) and mediates focussing of mitotic spindle fibres (Goshima *et al.*, 2005). Furthermore, its depletion reduces kinetochore sister separation (Draviam *et al.*, 2006). Meanwhile, CLASPs ensure exclusive end-binding activity of EB1 (Grimaldi *et al.*, 2014) and stabilises overlapping microtubules in the mitotic spindle (Bratman & Chang, 2007). Plus-tip interacting proteins (+TIPS) interact with molecular motors in order to regulate microtubule dynamics (e.g. Maffini *et al.*, 2009; Montenegro Gouveia *et al.*, 2010). While not intensively studied in mitosis, +TIPS clearly play a role in faithful cell division, and therefore it will be important to elucidate their responsibilities in the future. For reviews, see

van der Vaart *et al.* (2009).

Molecular motors are capable of using the cytoskeleton to move important resources within the cell. During mitosis, molecular motors are also responsible for facilitating accurate congression of chromosomes to the spindle equator. These motors include CENP-E, dynein, Kif18a, MCAK and Kif2b. CENP-E is a plus-end directed motor, dimerising via a coiled-coil domain and binding unattached kinetochores and k-fibres through its N- and C-termini, respectively (Kim *et al.*, 2008; Gudimchuk *et al.*, 2013). Once bound to an unattached kinetochore, CENP-E utilises its motor activity to glide laterally along k-fibres to the metaphase plate (Kapoor *et al.*, 2006; Cai *et al.*, 2009), independently of whether the kinetochore is unattached or mono-orientated (Cai *et al.*, 2009). It then tracks the microtubule tip until that kinetochore becomes bi-orientated (Gudimchuk *et al.*, 2013), as it is required in the conversion of lateral to end-on attachment (Shrestha & Draviam, 2013). Its depletion or inhibition results in an increase in polar chromosomes, demonstrating that it is required for complete chromosome congression (Barisic *et al.*, 2014; Bancroft *et al.*, 2015). CENP-E's coiled-coil region is required for stable kMT attachments, demonstrating a role after bi-orientation (Vitre *et al.*, 2014). Dynein also plays a role in chromosome congression, however is instead a minus-end directed motor capable of moving chromosomes towards the spindle poles (Li *et al.*, 2007; Yang *et al.*, 2007). Once there, the kinetochore can more easily make attachments to the mitotic spindle, then may be congressed to the metaphase plate by CENP-E or by depolymerisation coupled pulling if bi-orientated. Dynein has also been proposed to have roles in spindle positioning (O'Connell & Wang, 2000; Samora *et al.*, 2011), generation of stable kMT attachments (Hoffman *et al.*, 2001; Yang *et al.*, 2007), and the stripping of various proteins from the kinetochore (Hoffman *et al.*, 2001). Kif18a and MCAK share the ability of MAPs to induce changes in microtubule dynamics, while also containing motor domains. Kif18a is a plus-end directed motor (Mayr *et al.*, 2007) capable of binding microtubules and accumulating at plus-ends near the kinetochore (Stumpff *et al.*, 2011; Weaver *et al.*, 2011). However it is also located along k-fibres, and has been suggested to regulate spindle length (Weaver *et al.*, 2011); in-

deed, its depletion results in elongated spindles (Mayr *et al.*, 2007). At the kinetochore, it inhibits microtubule activity (Bringmann *et al.*, 2004; Mayr *et al.*, 2007) in order to ensure localisation of chromosomes at the spindle equator (Stumpff *et al.*, 2008, 2012). Unlike other motors mentioned here, MCAK is in fact a non-motile kinesin, instead associating with the inner kinetochore to promote microtubule depolymerisation (Hertzer *et al.*, 2003; Hunter *et al.*, 2003). This depolymerase activity depends on an interplay between MCAK's N- and C-termini (Ems-McClung *et al.*, 2007), and its localisation depends on its C-terminus (Zong *et al.*, 2016). It is utilised both in ensuring that CENP-E-mediated lateral attachments can be removed once the kinetochore becomes partially end-on attached (Shrestha & Draviam, 2013), and as part of Aurora B-mediated error correction mechanisms during metaphase (see § 1.3.6). Kif2b, also a depolymerase, localises to the outer kinetochore and plays the same role as MCAK in correcting for erroneous kMT attachments during prometaphase.

1.3.6 Chromosome passenger complex

The chromosome passenger complex (CPC) binds centromeric chromatin and provides a mechanism to ensure that chromosomes are correctly attached to spindle microtubules at metaphase. In addition, the CPC is required for SAC function, mitotic chromosome structure, and cytokinesis (reviewed in van der Horst & Lens, 2014). The CPC is composed of Aurora B kinase, Survivin, Borealin and INCENP, and is highly conserved within eukaryotes. Its localisation to the inner centromere during mitosis depends on interaction of Survivin and Borealin with the N-terminus of the inner centromere protein (INCENP; Klein *et al.*, 2006; Vader *et al.*, 2006; Jeyaprakash *et al.*, 2007) and phosphorylation of histones H3 by Haspin kinase (Kelly *et al.*, 2010; Wang *et al.*, 2010; Yamagishi *et al.*, 2010) and H2A by the Bub1 kinase (Kawashima *et al.*, 2010). Phosphorylation of H2A has been shown to recruit Shugoshin proteins, which contribute to the localisation of not only CPC but other key proteins involved in error correction, including MCAK and PP2A (Huang *et al.*, 2007; Foley *et al.*, 2011; Eshleman & Morgan, 2014; Peplowska *et al.*, 2014; Meppelink *et al.*, 2015). INCENP then also binds

Aurora B via its C-terminus (Adams *et al.*, 2000; Kaitna *et al.*, 2000), allowing the process of Aurora B activation (Xu *et al.*, 2009). INCENP also contains binding sites for β-tubulin (Wheatley *et al.*, 2001) and heterochromatin protein 1 (HP1) (Ainsztein *et al.*, 1998; Nozawa *et al.*, 2010; Kang *et al.*, 2011b), which are required for correct localisation of the CPC to microtubules and chromatin, respectively.

During mitosis, Aurora B binding to INCENP results in phosphorylation of INCENP and auto-phosphorylation events, both of which increase its kinase activity (Bishop & Schumacher, 2002; Honda *et al.*, 2003). Full activation is thought to be caused by a positive feedback loop within local centromeric chromatin, where there is a high concentration of CPC (Kelly *et al.*, 2007). Furthermore, Aurora B phosphorylates the kinase domain of Haspin, increasing its activity and therefore promoting further incorporation of the CPC into centromeres (Wang *et al.*, 2011). Additionally, Aurora B phosphorylates Plk1 (Carmena *et al.*, 2012), which then phosphorylates sites in Survivin required for the activity of Aurora B (Chu *et al.*, 2011). Therefore initial activity of Aurora B initiates a feed-forward loop that sustains activity and localisation of the CPC during mitosis, which is necessary for efficient error correction at mitotic kinetochores.

Active CPC destabilises and corrects erroneous attachments at mitotic kinetochores and inhibition or depletion of Aurora B, or other CPC components, results in an increase in merotelic and syntelic attachments (Gassmann *et al.*, 2004; Hauf *et al.*, 2003; Lampson *et al.*, 2004; Cimini *et al.*, 2006). The mechanism by which Aurora B destabilises attachments is through phosphorylation of multiple components of the outer kinetochore. Specifically, Aurora B directly phosphorylates the N-terminus of Ndc80. Non-phosphorylatable mutants of Ndc80 display increased merotelic and syntelic attachments (DeLuca *et al.*, 2006, 2011), whereas phospho-mimetic mutants of Ndc80 fail to maintain stable attachment to microtubules (Guimaraes *et al.*, 2008). This broadly matches the phenotype of Aurora B inhibition with small molecules. Aurora B also phosphorylates sites in Knl1, to reduce binding of PP1 to Knl1, and the SKA complex (Welburn *et al.*, 2010; Chan *et al.*, 2012), which inhibits binding of SKA com-

plex to microtubules. *In vitro* microtubule binding experiments support this model as phospho-mimetic mutants of both Ska and Ndc80 complexes have lowered microtubule binding affinity (Cheeseman *et al.*, 2006; Welburn *et al.*, 2010). Interestingly, Aurora B has been shown to promote phosphorylation of MCAK at the centromere (Andrews *et al.*, 2004; Lan *et al.*, 2004; Tanenbaum *et al.*, 2011), possibly via phosphorylation of PLK1 (Shao *et al.*, 2015) and the Kif2a and Kif18b motor proteins (Knowlton *et al.*, 2009; Tanenbaum *et al.*, 2011). Aurora B has also been suggested to phosphorylate MCAK directly to spatially and temporally regulate its function (Lan *et al.*, 2004; Zhang *et al.*, 2007; Ems-McClung *et al.*, 2013). Additionally, MCAK (and PP2A) centromere recruitment is promoted by Aurora B's phosphorylation at multiple sites on shugoshin-like protein, Sgo2, in humans (Tanno *et al.*, 2010). Perturbation in MCAK's function causes problems in spindle assembly (Ems-McClung *et al.*, 2007). Along with MCAK, Kif2a and Kif18b are microtubule depolymerases, and therefore may act to destabilise microtubules erroneously attached to kinetochores. This would therefore contribute to the overall efficiency of error correction.

It is currently thought that CPC kinase activity forms a gradient from the inner centromere to spatially regulate error correction at the outer kinetochore. According to this model, bi-orientation of kinetochore pairs stretches the outer kinetochore away from the centromeric pool, thereby gradually reducing the chance that Aurora B kinase would interact with its substrates. Consistent with this, over-expression of Aurora B broadens these centromeric gradients and causes destabilisation of attachments (Muñoz-Barrera & Monje-Casas, 2014). Alternatively, another model suggests that the active pool of Aurora B is located proximal to the inner kinetochore at phosphorylated histone H3 interspersed with CENP-A, but is instead capable of targeting Aurora B by extending INCENP towards the outer kinetochore. This model requires that the outer kinetochore moves out of reach of INCENP-bound Aurora B. This has been referred to as intra-kinetochore stretch. In line with this hypothesis is that the level of outer kinetochore protein Dsn1's phosphorylation is dependent upon the length of INCENP's central α-helical domain (Samejima *et al.*, 2015b).

1.3.7 Spindle assembly checkpoint proteins

The SAC is required in all cells to ensure that every chromosome is aligned at the spindle equator and correctly attached to the mitotic spindle. Once all chromosomes are bi-orientated, the SAC becomes deactivated, allowing the cell to transition into anaphase (for review see Agarwal & Varma, 2014). When activated, SAC proteins bind to the outer kinetochore, and dissociate when the SAC is silenced. Knl1 contains a number of conserved MELT repeats in the disordered domain between its microtubule- and Zwint-binding regions, each of which are phosphorylated by Mps1 in order to promote binding of SAC signalling proteins when MELT motifs are phosphorylated by Mps1 kinase (Vleugel *et al.*, 2013). The total number of MELT repeats is crucial for a sufficient SAC signal, as non-phosphorylatable mutants fail to maintain the spindle checkpoint (Zhang *et al.*, 2014). Mps1 in fact works in conjunction with Plk1 (von Schubert *et al.*, 2015) to allow hierarchical loading of Bub3 (Primorac *et al.*, 2013) and Bub1 (Brady & Hardwick, 2000), which then promotes loading of BubR1 (Zhang *et al.*, 2015). The Mad1/Mad2 complex can then be loaded via a Mps1-dependent Bub1-binding site within Mad1 (Brady & Hardwick, 2000; London & Biggins, 2014; Moyle *et al.*, 2014). In human cells, Mad1 and Mad2 localise to kinetochores independently of Knl1 (Silió *et al.*, 2015) by a mechanism that requires the RZZ complex (Buffin *et al.*, 2005; Kops *et al.*, 2005; Silió *et al.*, 2015). It is then that, upon microtubule attachment, dynein localised to the kinetochore by Spindly (Griffis *et al.*, 2007) strips Mad1, Mad2 and the RZZ complex from kinetochores (Howell *et al.*, 2001; Wojcik *et al.*, 2001). Association of Mad1/Mad2 to the kinetochore requires Ndc80, as it provides a binding site for Mps1 kinase (Martin-Lluesma *et al.*, 2002). In unattached budding yeast kinetochores, Ndc80-bound Mps1 is located in proximity with Spc105 (Knl1 homologue), however this spatial proximity is lost upon microtubule binding (Aravamudhan *et al.*, 2014). Mps1 association with Ndc80 occurs in direct competition with microtubule binding, and therefore displaced when kinetochores engage microtubules (Ji *et al.*, 2015; Hiruma *et al.*, 2015).

Throughout mitosis, Mad2 is present in the cell in either an open or closed con-

formation (reviewed in Peters, 2006). Once located at the kinetochore, Mad2 is in its closed conformation (C-Mad2), which promotes the conversion of open Mad2 (O-Mad2) into its closed form. Any free C-Mad2 is associated as part of the mitotic checkpoint complex (MCC), which consists of C-Mad2, Cdc20, BubR1 and Bub3 (Fraschini *et al.*, 2001; Hardwick *et al.*, 2000; Sudakin *et al.*, 2001). This forces Cdc20 into an inactive form (Sudakin *et al.*, 2001). However, upon silencing of the SAC, the MCC disassembles and Cdc20 becomes active. It then targets the anaphase promoting complex (APC), which initiates the degradation of the mitotic cyclin, CyclinB1. CyclinB1 is associated with Cdk1 during mitosis to ensure its activity, however once CyclinB1 is degraded, Cdk1 becomes inactive. In parallel, active Cdc20 induces the degradation of securin, allowing the separase protein to become active. Separase then cleaves cohesin between sister chromatids, allowing for their physical separation. Cdk1 phosphorylates a large number of substrates in mitosis, including those involved in kinetochore structure, error correction, and SAC signalling (reviewed in Peters, 2006). Inactivation of Cdk1 at anaphase onset ensures that its substrates become efficiently dephosphorylated by protein phosphatases PP1 and PP2A, and therefore error correction and SAC signalling are terminated. Indeed, maintenance of Cdk1 activity after sister dysjunction results in re-localisation of Aurora B and Mad2 to kinetochores, and therefore destabilised kMT attachments (for further analysis, see § 6; Vázquez-Novelle *et al.*, 2014).

Importantly, while MAPs, molecular motors, and proteins involved in error correction mechanisms and spindle checkpoint activity do not contribute directly to kinetochore structure, their activity requires the full complement of inner and outer structural proteins, and is regulated by the interaction of the outer kinetochore with microtubules. Furthermore, CyclinB1 plays an important role in ensuring that Cdk1 activates these mechanisms during prometaphase and metaphase, but is silenced at anaphase onset. The structure and conformation of kinetochores has therefore been an important topic of interest for many groups seeking to understand the mechanisms behind force generation at kinetochores, error correction, and SAC satisfaction.

1.4 Kinetochore dynamics

A powerful way to understand kinetochore structure in relation to force generation and attachment state, is to investigate their dynamic behaviour and then define the molecular components required for specific mechanical events. Such dynamics have been studied for decades with classic studies in the late 1980s using video enhanced differential interference contrast microscopy to lay out the key sets of chromosome movements during mitosis in newt lung cells: first, kinetochores were observed to move rapidly to their attached pole, presumably driven by lateral sliding and motors. Second, sister kinetochores bi-orientate and move processively towards the spindle equator (congression). Third, once at the equator (and to some extent during congression), they exhibit deterministic back-and-forth motion about the metaphase plate (Skibbens *et al.*, 1993). This phenomenon was termed chromosome directional instability. This may provide a mechanism for kinetochores to maintain a chromosome's position ready for anaphase onset. It is the regulation of microtubule dynamics that allows the processive movement and oscillation of sister kinetochores. Imagine the most basic situation, so that a bi-orientated kinetochore pair is bound to only one individual microtubule each (as would be the case in budding yeast). Also imagine that their orientation is such that a straight line can be drawn through the kinetochore pair and both spindle poles, i.e. all four bodies are co-linear. If this pair of kinetochores moves along that line in unison, one kinetochore would move towards its spindle pole, while its sister would move away from its pole (Figure 1.6 A). This implies that the poleward (P) moving (lead) kinetochore is attached to a depolymerising microtubule, while the (trailing) away-from-the-pole (AP) moving kinetochore is attached to a polymerising microtubule.

Recent advances in our understanding of kinetochore dynamics has come form the use of fluorescent proteins (FPs) that can be fused to a marker (i.e. CENP-A), and that when exposed to light of a given wavelength, will emit light of a different wavelength. This allows direct observation of the kinetochore positions in live cells (e.g. Jaqaman *et al.*, 2010; Amaro *et al.*, 2010; Wan *et al.*, 2012; Figure 1.6 A). Importantly, the size of the kinetochore puts it below the diffraction limit of light and it will therefore appear

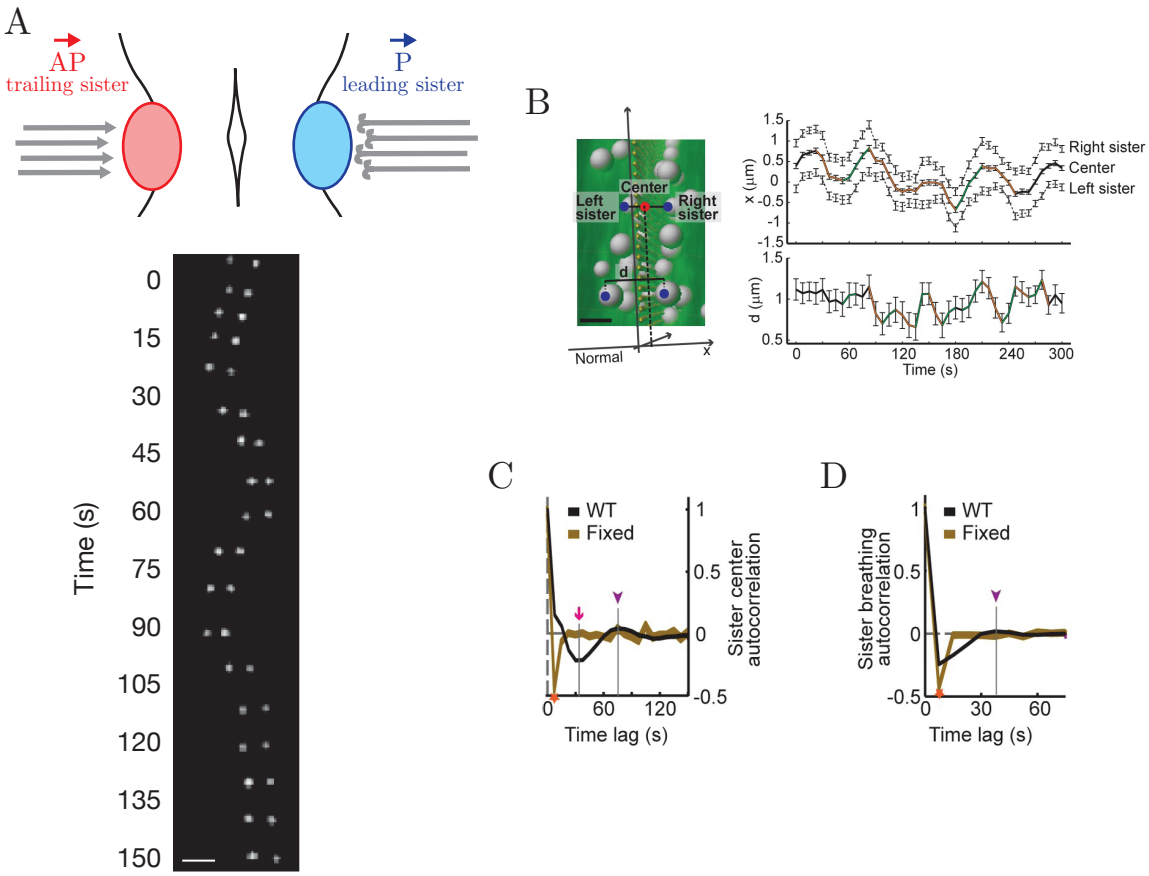

Figure 1.6 *Kinetochores exhibit quasi-periodic back-and-forth motion normal to the metaphase plate.*
(A) Schematic of a kinetochore pair exhibiting back-and-forth motion. The leading sister kinetochore moves polewards (P; blue), and is attached to a depolymerising kinetochore-fibre (k-fibre). The trailing sister kinetochore moves away-from-the-pole (AP; red), and is attached to a polymerising k-fibre. This is demonstrated in the kymograph of eGFP-CENP-A HeLa cells (from Amaro *et al.* 2010). Scale bar = 2 μm.
(B) Metaphase plate is fit to all kinetochore coordinates, forming the *yz*-plane. Kinetochores move back-and-forth in the *x*-coordinate, i.e. normal to the metaphase plate. Scale bar = 500 nm. Top trajectory is a kinetochore pair's centre *x*-coordinate (full line), and the *x*-coordinate of each sister (dashed lines). Bottom trajectory is the kinetochore pair's sister separation, *d*. Error bars are standard deviation.
(C) Autocorrelation of change in kinetochore pair's centre *x*-coordinate in live (black) and fixed cells (gold). Pink and purple arrows mark half- (approx. 35 s) and full-period (approx. 75 s) of oscillations in live cells, respectively.
(D) Autocorrelation of change in sister separation, *d*, in live (black) and fixed cells (gold). Purple arrow marks full period (approx. 35 s) of breathing in live cells.
Figures (B–D) are from Jaqaman *et al.* 2010.

as a point source in a light microscope. Kinetochores thus appear as "point objects", which has allowed them to be accurately localised using semi-automatic algorithms. This can be achieved using either the centre of mass of intensity (Jaqaman *et al.*, 2010; Amaro *et al.*, 2010; Mchedlishvili *et al.*, 2012; Vladimirou *et al.*, 2013; Armond *et al.*, 2015a) or by fitting a Gaussian distribution (Wan *et al.*, 2012; Dumont *et al.*, 2012; Burroughs *et al.*, 2015; Armond *et al.*, 2015b). The latter provides a more accurate (sub-pixel) measurement of the spot centre and therefore kinetochore position (Churchman *et al.*, 2005). These methods of spot detection are used in many MATLAB-based tracking programs, including U-track (Danuser lab, Harvard, USA) and KiT (Armond *et al.*, in press) developed during the last decade. Because the spindle is undergoing rotations and translations within the cell it is important to ensure that a rotation-free coordinates system is used to accurately track kinetochore movements. One way to do this is by fitting a sheet to the distribution of kinetochore spot centres which can provide the yz-plane. This means that any back-and-forth motion will occur in the x-axis which is normal to the metaphase plate (Figure 1.6 B; Jaqaman *et al.*, 2010). Calculating the average autocorrelation of change in a kinetochore's x-coordinate revealed quantitatively that kinetochore back-and-forth motion is quasi-periodic with a half period of around 35 s (Figure 1.6 C; Jaqaman *et al.*, 2010). Furthermore, as in the trajectory in Figure 1.6 B, the distance between kinetochores, d, changes (or 'breathes') with half the period of this back-and-forth motion, as demonstrated by autocorrelation and power analysis (Figure 1.6 D; Jaqaman *et al.*, 2010; Wan *et al.*, 2012. This inter-kinetochore linkage fluctuates between 0.7 and 1.2 μm (Jaqaman *et al.*, 2010; Wan *et al.*, 2012), consists of centromeric chromatin and is essentially stretched during metaphase. Thus the inter-kinetochore distance is a proxy for the forces exerted on the sister kinetochores.

The ability to collect large numbers of movies, semi-automatically locate spot centres, and track sister kinetochores through time has allowed thorough and unbiased analysis of these parameters. Furthermore, it has allowed high-throughput analysis of the effects of perturbations to kinetochores. In the case where microtubules are

removed or their dynamics suppressed regular oscillations are eliminated; the same is of course true when attachments are eliminated following depletion of the Ndc80 complex. Interestingly depletion of CENP-L and the CENP-H complex result in the establishment of normal inter-kinetochore tension, but an inability for kinetochores to regulate microtubule dynamics, as demonstrated by a loss of temporally-controlled back-and-forth dynamics (Amaro *et al.*, 2010; Mchedlishvili *et al.*, 2012). On the other hand, depletions of molecular motors MCAK, CENP-E and Kif18a don't affect kinetochore oscillations, although kinetochore velocities and breathing are perturbed (Jaqaman *et al.*, 2010). Furthermore, mutations in Ndc80 that prevent phosphorylation of its microtubule-binding region result in damped kinetochore mobility and a ∼30% increase in inter-kinetochore distance (DeLuca *et al.*, 2011).

To date, the most detailed analysis of inter-kinetochore dynamics has come from following the sub-pixel localisation of eGFP-CENP-A spot centres during movies of metaphase with a time resolution of 2 s (Burroughs *et al.*, 2015; Armond *et al.*, 2015b). This spatiotemporal resolution has enabled careful analysis of directional switches – an important event that allows chromosomes to be manoeuvred about the mitotic spindle. This work demonstrated that there is a bias towards directional switches being initiated by the lead (P-moving) kinetochore in human cells, as shown previously in newt lung and PtK1 cells (Skibbens *et al.*, 1993; Wan *et al.*, 2012). For a directional switch to be characterised as a lead-initiated directional switch (LIDS), the lead sister changes direction first to become AP, the second sister switching direction within an average ∼4.3 s. However, this analysis also revealed that trail-initiated directional switches (TIDS) occurred. This has led to the formulation of a new model for sister kinetochore communication and switching that did not involve a threshold tension sensor as previously suggested (Skibbens *et al.*, 1993; Rieder & Salmon, 1994; Wan *et al.*, 2012). In the new model kinetochores are said to utilise mechanical clocks (presumably related to time dependent changes in microtubule catastrophe and rescue) that are force-sensitive (Burroughs *et al.*, 2015). Analysis of such data with mathematical models is also now allowing the (relative) forces generated by kinetochores to be determined from live cell

movies (Armond *et al.*, 2015b). Furthermore, these tracking assays can be combined with a second marker to read-out events at single kinetochores. For example, EB1 has been used to quantify the levels of microtubule polymerisation at the kinetochore, revealing only a small bias between sisters (Armond *et al.*, 2015a).

1.4.1 Intra-kinetochore distance, Δ

In experiments attempting to understand dependency of kinetochore structure on kinetochore dynamics, a second kinetochore protein can be tagged with a differently coloured FP. This allows the centroids of two kinetochore subunits to be localised using the same spot tracking methods described above. The distance between them can then be derived giving intra-kinetochore distances that are termed 'delta' (or Δ). The architecture of the human kinetochore in fixed cells has been elucidated, demonstrating that measurements of Δ are typically in the range of $\sim$10's of nanometres. Given typical axial resolution of diffraction-limited spots ($\sim$200 nm) and minimum pixel sizes of $\sim$65 nm, these experiments demand considerable care and precision. Indeed, a correction for the chromatic shift between differently coloured light is required, and is typically measured using microspheres labelled with multiple fluorescent dyes (e.g. as used in Dumont *et al.*, 2012; Magidson *et al.*, 2016). However, more recent work used multiple fluorescent antibodies targeted to a common protein to calculate chromatic shift (Etemad *et al.*, 2015). Alternatively, to avoid the need for chromatic shift calculation, Δ can be measured as the average of the inter-kinetochore distance as measured between the pairs of differently-coloured fluorophores (Schittenhelm *et al.*, 2007; Maresca & Salmon, 2009; Uchida *et al.*, 2009; Wan *et al.*, 2009; Joglekar *et al.*, 2009; Varma *et al.*, 2013; Suzuki *et al.*, 2014; Tauchman *et al.*, 2015; Drpic *et al.*, 2015; Figure 1.7). However, this assumes that all four fluorescent markers of a kinetochore pair are co-linear, and therefore this measurement is effectively a 1D projection (henceforth called Δ_{1D}). The architecture of the kinetochore as measured by Wan *et al.*, 2009, and later work investigating the architecture of the RZZ and Spindly (Varma *et al.*, 2013), and CCAN (Suzuki *et al.*, 2014), used this method of Δ measurement. Of note,

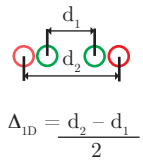

	Fixed cells	Live cells
1D	Schittenhelm *et al*, 2007 Wan *et al*, 2009* Varma *et al*, 2013* Suzuki *et al*, 2014* Tauchman *et al*, 2015 Magidson *et al*, 2016*	Joglekar *et al*, 2009 Maresca & Salmon, 2009 Uchida *et al*, 2009 Varma *et al*, 2013* Drpic *et al*, 2015
2D	Civelekoglu-Scholey *et al*, 2013 Magidson *et al*, 2016	Dumont *et al*, 2012 Drpic *et al*, 2015
3D	Etemad *et al*, 2015	

Figure 1.7 *Intra-kinetochore distance measurements can be calculated by multiple methods, and in either living or chemically fixed cells.*
Table of journal articles in which intra-kinetochore distances, Δ, have been calculated using different measurement methods: a 1D measurement which halves the difference of the inter-kinetochore measurements using each kinetochore marker (top row); a 2D measurement absent of z-directional information (middle); and a full 3D measurement (bottom). Asterisks demonstrate cases where measurement of Δ 1D has been corrected for tilt. These measurements are also divided by whether they were performed in living (left column) or chemically fixed (right) cells.

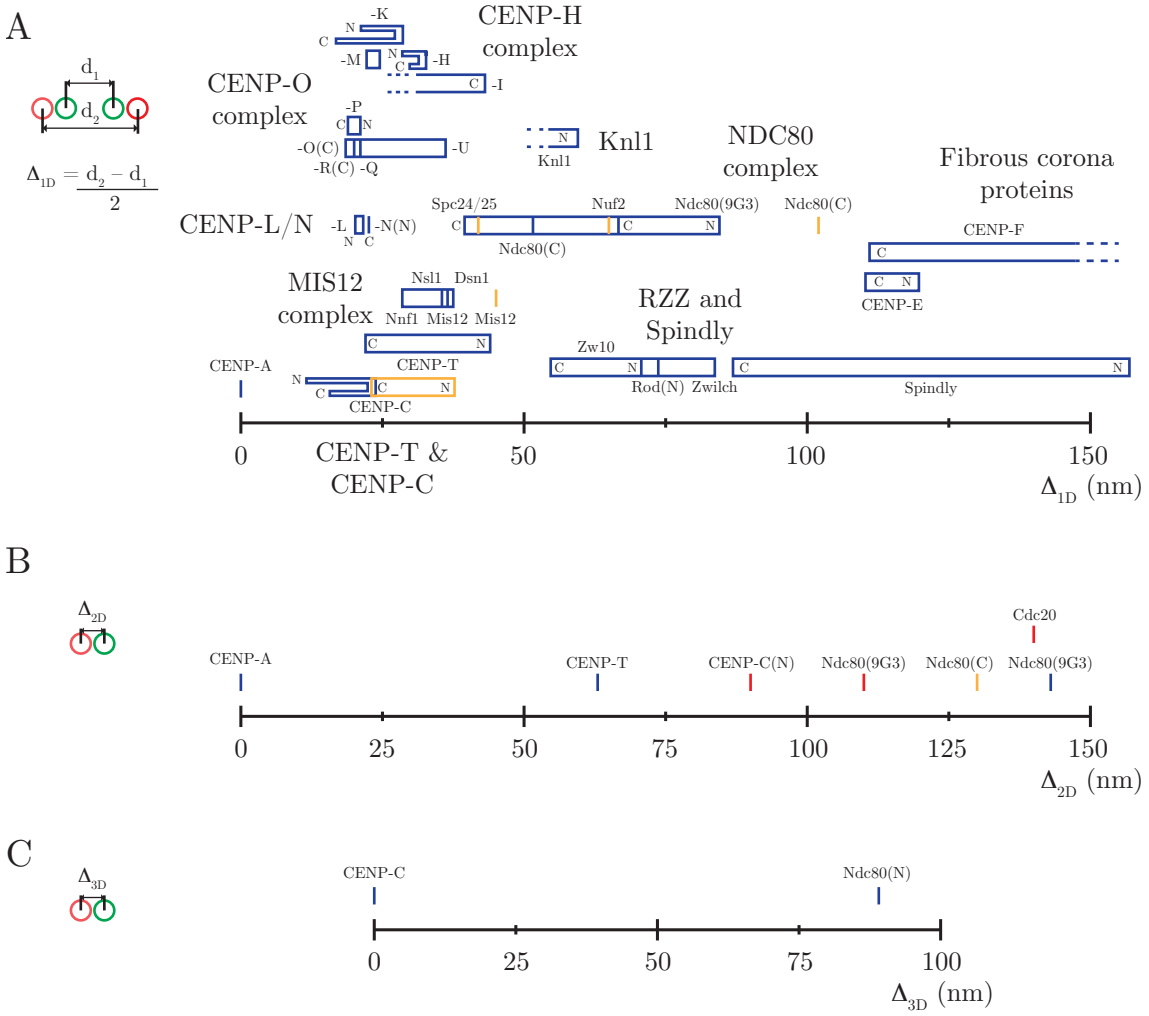

Figure 1.8 *Reported intra-kinetochore distance measurements are inconsistent.* Intra-kinetochore distances as reported: (A) using 1D projection measurement, (B) in 2D, and (C) in 3D. Schematics demonstrate each measurement method, with CENP-A (green) and Ndc80 (red) used as an example. Measurements were derived from human (HeLa and RPE1; blue), marsupial (PtK1 and PtK2; red), and *Drosophila* (S2; gold).
Distances here are reported by: Schittenhelm *et al.* 2007, Wan *et al.* 2009, Maresca and Salmon 2009, Varma *et al.* 2013, Civelekoglu-Scholey *et al.* 2013, Suzuki *et al.* 2014, Tauchman *et al.* 2015, Etemad *et al.* 2015, Drpic *et al.* 2015, Magidson *et al.* 2016.

the authors observe that the kinetochore can be tilted relative to the sister-sister axis and that this would affect the 1D measurement. This tilt effect is then corrected in order to avoid any projection issues.

Using these measurements, a large-scale decrease in Δ ($\sim$16 nm) was observed between the inner and outer kinetochore following treatment with taxol – a microtubule-stabilising drug that eliminates microtubule-dependent pulling forces (Wan *et al.*, 2009; Figure 1.9). Kinetochores were also observed to tilt more following taxol treatment (see Wan *et al.*, 2009). This has been revisited and confirmed in recent correlative light microscopy/electron microscopy experiments, where a decrease in Δ was observed in chemically-fixed RPE1 cells using multiple fixatives after taxol treatment (Magidson *et al.*, 2016). Together, this implies that tension generated by kMTs results in stretching of the kinetochore. In support of this, fixed cells treated with a range of concentrations of nocodazole, which destabilises microtubules, therefore weakening or completely destabilising kMT attachments, demonstrate a graded decrease in Δ_{1D} with increased nocodazole concentration (Maresca & Salmon, 2009; Tauchman *et al.*, 2015). Additionally, hyper-stabilising Ndc80 binding to microtubules increases inter-kinetochore tension (DeLuca *et al.*, 2011), which also results in an increase in Δ_{1D} (Tauchman *et al.*, 2015). Although these measurements suffer from the 1D projection issue, similar measurements in fixed HeLa cells were made in chromatic shift-corrected 3D imaging (Figure 1.7), deriving similar results (Etemad *et al.*, 2015). Other work in formaldehyde-fixed HeLa cells treated with 160 ng ml^{-1} nocodazole concluded that Δ decreased compared to untreated cells (Uchida *et al.*, 2009). This observation is based on a sub-population ($\sim$15%) of untreated kinetochores exhibiting significant stretch in Δ that no longer exists in nocodazole-treated cells. Furthermore, immuno-electron microscopy (EM) experiments after glutaraldehyde fixation of chicken DT40 cells demonstrated a decrease in inner kinetochore proteins, but not the outer kinetochore (Suzuki *et al.*, 2011). More specifically, CENP-T was observed to stretch within the kinetochore when under tension, and therefore has a role in changes in intra-kinetochore structure. Additionally, CENP-T, CENP-C and the CENP-H complex all have roles in

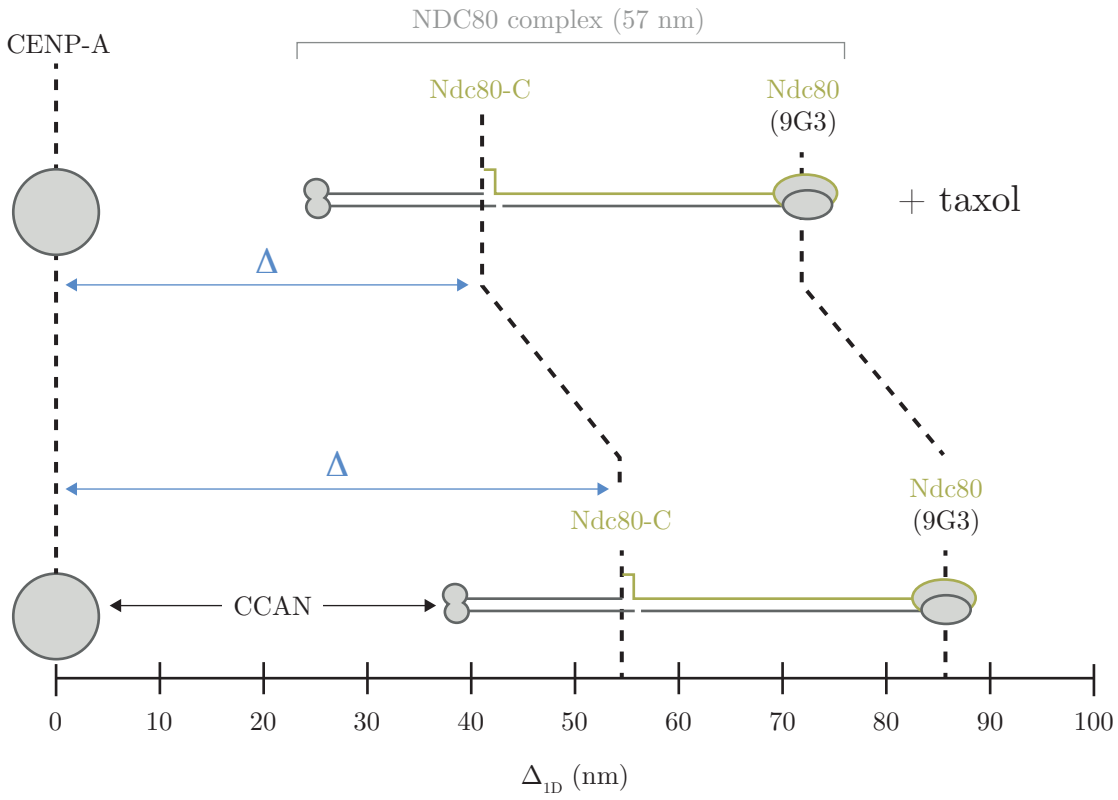

Figure 1.9 *Intra-kinetochore distances decrease under loss of tension.*
Outer kinetochore components (e.g. the NDC80 complex) move 15 nm closer to the inner kinetochore (e.g. CENP-A) under loss of intra- and inter-kinetochore tension after taxol-treatment, as demonstrated here (Wan *et al.* 2009). Decreases between kinetochore subunits have been observed in multiple other works, either induced by perturbation of the system (Maresca & Salmon, 2009; Uchida *et al.* 2009; Drpic *et al.* 2015; Tauchmann *et al.* 2015; Etemad *et al.* 2015; Magidson *et al.* 2016), or by analysis of different kinetochore states during mitosis (Joglekar *et al.* 2009; Dumont *et al.* 2012; Drpic *et al.* 2015).

maintaining the structure of the kinetochore, their depletion causing hyper-extension of the human kinetochore (Suzuki *et al.*, 2014). Δ_{1D} measured between CID (inner kinetochore marker) and Ndc80 in *Drosophila* S2 cells treated with colchicine, which destabilises microtubules, was observed to decrease relative to cells treated with MG132, which arrests cells in a bi-orientated state in metaphase (Drpic *et al.*, 2015). Δ was also measured within individual kinetochores located at single chromatids in cells with unreplicated genomes. Strikingly, despite the fact these chromatids can only form monotelic attachments, kinetochores are still stretched relative to colchicine-treated kinetochores. Interestingly, these measurements were performed in live cells, which are the only measurements of their kind using spindle poisons. However, differences in intra-kinetochore distances have been observed between P and AP kinetochores in live PtK2 cells (Dumont *et al.*, 2012). During kinetochore back-and-forth motion, P kinetochores are compressed (reduced Δ) compared to their trailing sister. This suggests that the kinetochore is pulled by components further inside the kinetochore relative to the Ndc80 binding site. However, this result contradicts multiple models of kinetochore microtubule attachment suggesting that the kinetochore would stretch under pulling force from depolymerising microtubules (reviewed in Civelekoglu-Scholey *et al.*, 2013). Moreover, it is not consistent with the experiments described above in which delta decreases on the loss of microtubule pulling forces. That the both CCAN and Ndc80 linkages in the kinetochore are non-compliant (i.e. delta does not increase as inter-sister increases) raises further questions over the exact conformational changes occurring in the kinetochore and how these relate to force.

Alternatively, changes in Δ following the destabilisation or hyper-stabilisation of kMT attachments have been suggested to represent changes in intra-kinetochore conformation. For example, budding yeast Mps1 changes localisation depending on the kinetochore's attachment status (Aravamudhan *et al.*, 2014). More specifically, Mps1 is in close proximity with Spc105 (Knl1 homologue) at unattached kinetochores, a proximity that is lost upon attachment. This requires a conformational change in the outer kinetochore in order to target the Mps1, which binds Ndc80's N-terminus, to Knl1 –

a change that may not be possible by simple loss of intra-kinetochore stretch. Additionally, outer kinetochore proteins in *Xenopus laevis* egg extracts involved in spindle checkpoint signalling and lateral attachment (Mad1, Bub1, BubR1) have been observed to expand along CENP-A-free chromatin, however this is much less pronounced in human RPE1 cells (Wynne & Funabiki, 2015). Nevertheless, this expansion was also observed in CENP-C, demonstrating potential conformational changes within the inner kinetochore. These expansions were dependent upon activity of mitotic kinases, which suggests that the kinetochore may experience conformation changes depending on its phospho-state.

Traditionally it was believed that intra-kinetochore stretch was a requirement for the satisfaction of the SAC (Maresca & Salmon, 2009; Uchida *et al.*, 2009; Drpic *et al.*, 2015; Tauchman *et al.*, 2015; Etemad *et al.*, 2015). Based on experiments in fixed HeLa cells, inter- and intra-kinetochore tension can be separated using sufficiently low doses of nocodazole, doses which result in mitotic delay in cells lacking intra-kinetochore stretch while maintaining inter-kinetochore tension (Uchida *et al.*, 2009). Meanwhile, decrease in measurement of Δ_{1D} in live *Drosophila* S2 were associated with SAC signal and increased phosphorylation of 3F3/2 (Maresca & Salmon, 2009), which is a signature of chromosomes that aren't under tension. However, recent investigations into Δ-dependent SAC signalling have revealed that stable kMT attachments are sufficient to satisfy the human SAC. Expressing a mutant of Ndc80 with increased microtubule-binding affinity (9A-Ndc80) in HeLa cells demonstrates an increase in intra-kinetochore stretch compared to kinetochores with wild-type Nd80 (Tauchman *et al.*, 2015; Etemad *et al.*, 2015). Remarkably, cells expressing 9A-Ndc80 and treated with low doses of spindle poisons (300 nM nocodazole and 20 nM taxol) exit mitosis after a delay. Meanwhile Δ decreases significantly compared to untreated cells expressing 9A-Ndc80, and therefore intra-kinetochore stretch is not a requirement for SAC silencing. As a result the model by which kinetochores sense bi-orientation needs revisiting.

1.5 Aim of this thesis

Our current understanding is that the intra-kinetochore distances (delta) within the kinetochore increase under force. That is the kinetochore is stretched. However, recent work is challenging this view with some evidence suggesting that the kinetochore is largely non-compliant (stiff). A major limitation of current investigations is that they are not performed in live cells, and of those that are, Δ has not been measured in all three dimensions. Therefore, in this thesis I will develop an assay to track live human kinetochores expressing multiple fluorescent markers tagged to different kinetochore proteins in 3D. In order to ensure accurate 3D measurements of Δ, I will develop a method of calculating sub-pixel measurements of chromatic shift in 3D. With this assay in place, I aim to investigate individual kinetochore structure and dynamics throughout mitosis.

Chapter 2

Materials and Methods

2.1 Plasmid production

In order to produce the geneticin-resistant eGFP-CENP-A plasmid (pMC385; Figure 2.1 A), a pEGFP-C1 plasmid (pMC005; Clonetech) was modified by exchanging the eGFP for eGFP-CENP-A (from pMC167; Jaqaman *et al.*, 2010) using the *NheI* and *BamHI* restriction sites. The production of the geneticin-resistant Ndc80-tagRFP (pMC389) required multiple stages. Firstly, tagRFP was amplified by PCR from a tagRFP-T-EEA1 plasmid (AddGene #42,635) using forward primer 5'-TCCGCTAGCATGGTGTCTAAGGGCGAA-3' and reverse primer 5'-GAGCTCGAGATTAAGTTTGTGCCCCAGTTT-3', and cloned into the pEGFP-N1 plasmid (pMC004; Clonetech) using *NheI* and *XhoI* sites to produce a tagRFP-N1 plasmid (pMC388). Secondly, Ndc80 was amplified by PCR from an Ndc80-mCherry plasmid (kind gift by E. Nigg) using forward primer 5'-ATCCGCTAGCATGAAGCGCAGTTCAGT-3' and reverse primer 5'-GGATCCCGGGTGGAACAGAACTTCCAG-3' (Figure 2.1 B) – this amplification was cloned into pMC388 using *NheI* and *XmaI* sites to produce the Ndc80-tagRFP plasmid (pMC389; Figure 2.1 B). Plasmids pMC385, pMC388 and pMC389 were all confirmed by sequencing (Source Bioscience). All plasmids are listed in Table 2.1.

2.2 Cell culture and cell line production

All HeLa-K cell lines were grown in DMEM media (Fisher) supplemented with 10% foetal calf serum (Fisher), 100 μg ml^{-1} penicillin and 100 μg ml^{-1} streptomycin maintained in 5% CO2 in a humidified incubator at 37°C. eGFP-CENP-A cells (MC024)

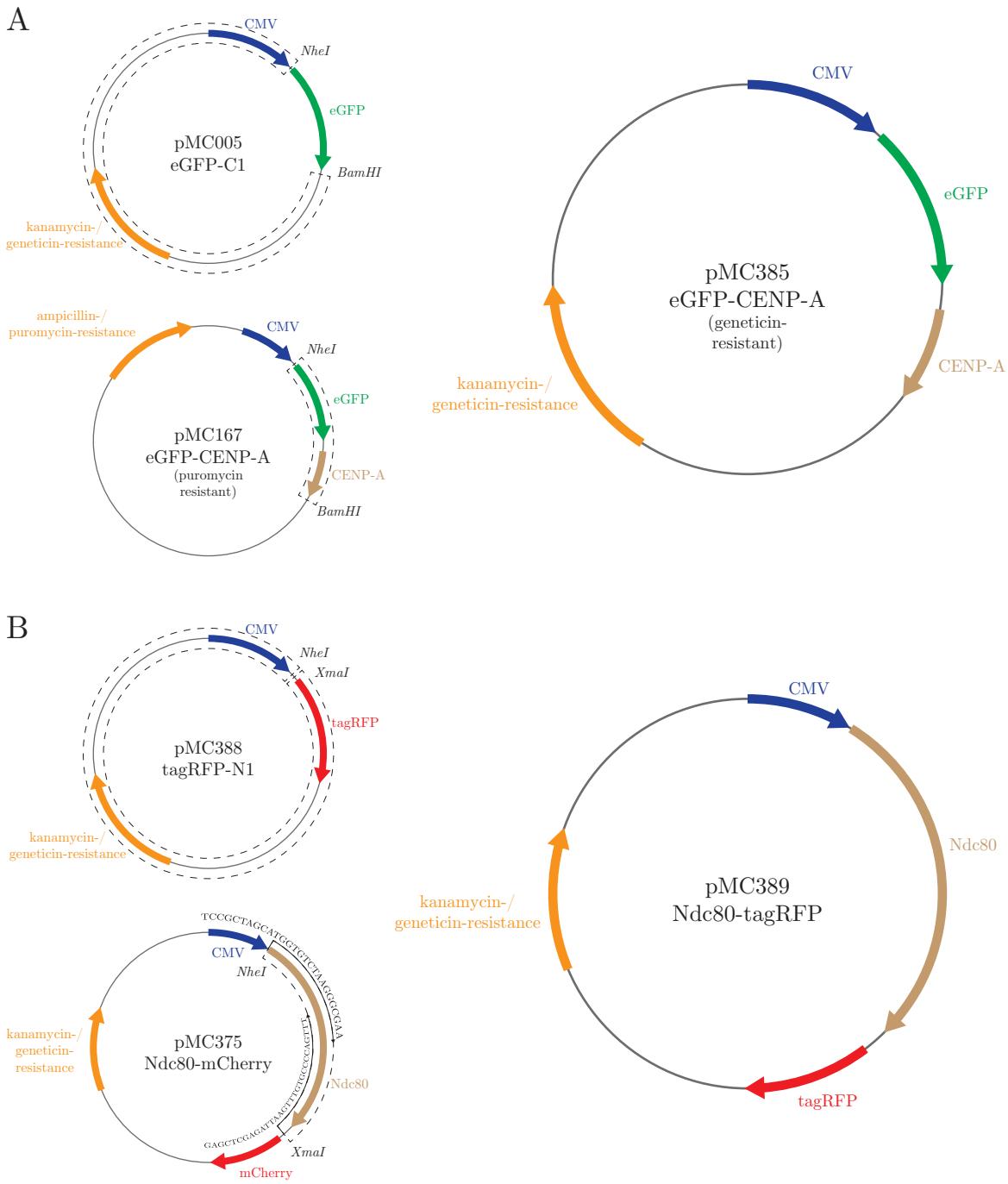

Figure 2.1 *eGFP-CENP-A and Ndc80-tagRFP plasmid production.*
(A) Geneticin-resistant plasmid containing eGFP-CENP-A (pMC385) produced by replacing eGFP in pMC005 with eGFP-CENP-A in pMC167 using *NheI* and *BamHI* sites.
(B) Geneticin-resistant plasmid containing Ndc80-tagRFP (pMC389) produced by inserting Ndc80 (PCR product from pMC375) into tagRFP-N1 (pMC388) using *NheI* and *XmaI* sites.
For both (A) and (B), labelled are promoters (blue), genetic code for proteins (brown) and fluorescent proteins (appropriately coloured), drug resistance genes (orange) and PCR primers (black). Dashed boxes represent region of plasmid used to construct final plasmid, flanked by restriction sites used.

Used in plasmid production:

Plasmid code	Encoded protein	Drug resistance	Mammalian selection by	Reference
pMC004	eGFP-N1	kanamycin	G418	Clonetech
pMC005	eGFP-C1	kanamycin	G418	Clonetech
pMC167	eGFP-CENP-A	ampicillin	puromycin	Jaqaman *et al.* 2010
pMC386	tagRFP-T-EEA1	kanamycin	G418	AddGene #42,635
pMC388	tagRFP-N1	kanamycin	G418	This work

Used for transfection in HeLa-K cells:

Plasmid code	Encoded protein	Drug resistance	Mammalian selection by	Reference
pMC360	Bub3-eGFP	kanamycin	G418	Virginia Silio
pMC385	eGFP-CENP-A	kanamycin	G418	This work
pMC389	Ndc80-tagRFP	kanamycin	G418	This work

Table 2.1 *Details of plasmids used.*

were maintained in 0.1 μg ml^{-1} puromycin (Fisher). mCherry-CENP-A cells (MC051) were maintained in 0.3 μg ml^{-1} puromycin. GFP-Dsn1 cells (a kind gift from J. Welburn; MC113) needed no specific drug for maintenance. eGFP-CENP-A/mCherry-Mis12 (MC093) and its parent cell line eGFP-CENP-A (MC092 – note that this cell line is distinct to MC024) were a kind gift from T. Hirota. They were both maintained in 500 μg ml^{-1} geneticin (Fisher), while the mCherry-Mis12 in MC093 was maintained in 0.25 μg ml^{-1} puromycin. Cells expressing eGFP-CENP-O (MC132) were kindly gifted by P. Meraldi, and were maintained in 300 μg ml^{-1}. eGFP-CENP-A/mCherry-CENP-A (MC131), eGFP-CENP-A/eGFP-Centrin1 (MC060) and mCherry-CENP-A/eGFP-CENP-P (MC072) cells were all maintained in 0.3 μg ml^{-1} puromycin and 300 μg ml^{-1} geneticin.

The eGFP-CENP-A/mCherry-CENP-A cell line was established by stable transfection of eGFP-CENP-A plasmid (pMC385) into cells stably expressing mCherry-CENP-A (Armond *et al.*, 2015a). This plasmid was transfected using FuGENE® 6 (Promega) and single clones were selected by 300 μg ml^{-1} geneticin (MC131). MC131 cells were imaged overnight to ensure that mitotic timings were unaffected by the incorporation of the eGFP-CENP-A (see § 3 for more information). All cells for live cell experiments were cultured in FluoroDish tissue culture dishes with cover glass bottoms (WPI). All cell lines are listed in Table 2.2.

2.3 Plasmid transfection

For transfections, plasmid DNA and 4.5 μl FuGENE® 6 (Promega) were allowed to separately homogenise in 50 μl OptiMEM for 5 min, then combined for 30 min before application to cells. DMEM not containing selection drugs was transferred to cells prior to addition of transfection reagent to cultured MC024, MC060 or MC051 cells. Ndc80-tagRFP (pMC389) and Bub3-eGFP (pMC360; produced by Virginia Silio) were incubated at 1,000 ng of plasmid DNA per 1.5 ml of DMEM. Wild-type (WT; pMC373) and non-degradable (ND; pMC374) forms of CyclinB1-mCherry, both kind gifts from M. Petronczki, were incubated at 500 ng DNA per 1.5 ml DMEM. Transfection was

Cell line code	Exogeneous gene(s)		Reference
	Gene	Maintenance	
MC024	eGFP-CENP-A	puromycin @ 0.1 ng ml^{-1}	Jaqaman *et al.* 2010
MC051	mCherry-CENP-A	puromycin @ 0.3 ng ml^{-1}	Armond *et al.* 2015
MC060	eGFP-CENP-A eGFP-Centrin1	puromycin @ 0.3 ng ml^{-1} G418 @ 300 ng ml^{-1}	Burroughs *et al.* 2015
MC072	mCherry-CENP-A eGFP-CENP-P	puromycin @ 0.3 ng ml^{-1} G418 @ 300 ng ml^{-1}	James Bancroft
MC092	eGFP-CENP-A	G418 @ 500 ng ml^{-1}	Gerlich et al. 2006
MC093	eGFP-CENP-A mCherry-Mis12	G418 @ 500 ng ml^{-1} puromycin @ 0.25 ng ml^{-1}	Uchida *et al.* 2009
MC113	GFP-Dsn1	-	Julie Welburn
MC131	eGFP-CENP-A mCherry-CENP-A	G418 @ 300 ng ml^{-1} puromycin @ 0.3 ng ml^{-1}	This work
MC132	eGFP-CENP-O	G418 @ 300 ng ml^{-1}	Amaro *et al.* 2010

Table 2.2 *Details of cell lines used.*

Plasmid code	Gene	DNA in 1.5 ml medium	Duration
pMC360	eGFP-Bub3	1,000 ng	24 hr
pMC373	WT CyclinB1-mCherry	500 ng	24 hr
pMC374	ND CyclinB1-mCherry	500 ng	24 hr
pMC385	eGFP-CENP-A	250 ng	24 hr
pMC389	Ndc80-tagRFP	1,000 ng	24 hr

Table 2.3 *Details of transfection concentrations used.*

performed for 24 hr prior to nocodazole or taxol treatment, or prior to imaging for untreated experiments. All information about transient transfections are located in Table 2.3.

2.4 Drug treatments

Spindle perturbation experiments were performed by addition of nocodazole or taxol. Nocodazole treatments were performed with either 100 nM or 3 μM nocodazole (Fisher) for 16 hr prior to imaging. Taxol treatment was performed with 10 μM taxol (Tocris Bioscience) for 1 hr prior to imaging. Synchronisation of cells in metaphase was started immediately after transient transfection, and 30-36 hr before imaging. Cells were incubated with 2 mM thymidine (Sigma) for 20-22 hr, before being released of drug treatment for 10-12 hr, then 10 μM MG132 (Sigma) was added to cells for 2 hr, before being releasing and imaged. For Aurora B inhibition experiments, 2 μM ZM1 was added to cells for the final 1 hr of MG132 treatment. Drug treatments for synchronisation and perturbation experiments are listed in Table 2.4.

2.5 Immunofluorescence

HeLa-K cells were prepared as above, except glass coverslips were used, and then fixed with 0.5% glutaraldehyde for 10 min in MTSB-TX (MTSB and 0.5% Triton-X100). Excess glutaraldehyde was reduced with 0.1% sodium borohydride (diluted in PBS) for 7 min, and then blocked for 10 min in AbDil (TBS, 0.1% Triton-X100 and 20 mg ml^{-1} BSA). Cells were then incubated for 30 min with mouse α-tubulin (Sigma-Aldrich; 1:1000 dilution), then for a further 30 min with goat anti-mouse 647 nm AlexaFluor (1:500 dilution) and DAPI (1:6000 dilution); all antibodies were diluted in AbDil buffer. Wash steps before and after antibody incubations were performed in TBS-TX (TBS and 0.5% Triton-X100). For imaging of immunofluorescence experiments, a single camera was used. Cells were first identified by eye for DAPI signal. Both interphase cells imaged for chromatic shift calculation and metaphase cells imaged for experiments in

Drug	Purpose	Concentration	Duration	Source
nocodazole	microtubule destabilisation (aligns at prophase)	3 μM 100 nM	16 hr 16 hr	Fisher
MG132	inhibits ubiquitinylation (aligns at metaphase)	10 μM	2 hr	Sigma
taxol	microtubule hyperstabilisation	10 μM	1 hr	Tocris Bioscience
thymidine	inhibits DNA synthesis (aligns at S phase)	2 mM	20–22 hr	Sigma

Table 2.4 *Details of drug concentrations used.*

Cell line	Transient	Antibody staining	Spatial resolution	Laser power						Drug treatment	n	
				525 nm		615 nm		615 nm				
				%	exp.	%	exp.	%	exp.		expts	cells
eGFP-CENP-A	Ndc80-tagRFP	αTubulin	69.4 x 69.4 x 200 nm	5	50 ms	5	50 ms	5	50 ms	-	1	12
										3 μM noc.	2	50
										100 nM noc.	2	32
										10 μM taxol	2	27

Table 2.5 *Details of imaging setup, and number of cells obtained for each drug treatment, for immunofluorescence experiments.*

§ 3.6 & 4.7 were imaged over 121 z-slices separated by 100 nm. Laser power in the 488, 561 and 640 nm wavelengths were set to 20%, with exposure time 50 nm per z-slice. Details about data obtained from these experiments are located in Table 2.5.

2.6 Overnight live-cell imaging

All overnight movies in § 3 were acquired using a Personal Deltavision microscope (Applied Precision, LLC) with a 40× 1.3 NA oil objective, with a Xenon light source and a CoolSNAP HQ2 camera (Roper Scientific), controlled by SoftWorx (Applied Precision, LLC). Camera pixels had an effective pixel size of 64.5 nm in the axial directions, as measured by a microscopic ruler (Pyser SGI). For each experiment, 20 regions of interphase cells were manually located and marked. Fields of view were imaged over 7 z-slices separated by 2 μm, for 12 hr every 3 min (241 time points). For overnight movies of both plain HeLa-K cells and those expressing GFP-Dsn1, cells were imaged in brightfield with power 32 % with 5 ms exposure. mCherry-CENP-A cells were imaged for 632 nm excitation wavelength, which was set at 32 % power with 25 ms exposure. For all other cell lines, cells were imaged for 525 nm excitation wavelength, which was set at 32 % power with 5 ms exposure. Details about overnight movie data obtained for each cell line are located in Table 2.6.

2.7 Live-cell imaging for tracking

All images and movies for tracking were acquired using a confocal spinning-disk microscope (VOX UltraView; Perkin and Elmer) with a 100× 1.4 NA oil objective and two Hamamatsu ORCA-R2 cameras, controlled by Volocity 6.0 (Perkin and Elmer) running on a Windows 7 64-bit (Microsoft) PC (IBM). Camera pixels had an effective pixel size of 69.4 nm in the axial direction, as measured using a microscopic ruler (Pyser SGI). The two cameras were preliminarily aligned using Volocity by aligning 500 nm TetraSpeck™ fluorescence microspheres (Thermofisher) in the 488 and 561 nm wavelengths. For live cell imaging, a common light path containing two wavelengths

Cell line	Resolution		Laser power						n	
			525 nm		615 nm		brightfield			
	time	space	%	exp.	%	exp.	%	exp.	expt.	cells
eGFP-CENP-A (MC024)	3 min	161.3 x 161.3 x 2,000 nm	32	5 ms	-	-	-	-	2	308
mCherry-CENP-A (MC051)	3 min	161.3 x 161.3 x 2,000 nm	-	-	32	25 ms	-	-	2	483
eGFP-CENP-A/ mCherry-CENP-A (MC132)	3 min	161.3 x 161.3 x 2,000 nm	32	5 ms	-	-	-	-	2	340
eGFP-CENP-A (MC092)	3 min	161.3 x 161.3 x 2,000 nm	32	5 ms	-	-	-	-	2	297
eGFP-CENP-A/ mCherry-Mis12 (MC093)	3 min	161.3 x 161.3 x 2,000 nm	32	5 ms	-	-	-	-	2	112
HeLa-K (MC009)	3 min	161.3 x 161.3 x 2,000 nm	-	-	-	-	32	5 ms	1	135
GFP-Dsn1 (MC113)	3 min	161.3 x 161.3 x 2,000 nm	-	-	-	-	32	5 ms	1	103

Table 2.6 *Details of imaging setup, and number of cells obtained, for overnight live cell experiments.*

Cell line	Transient	Resolution		Laser power				Drug treatment	n		
				525 nm		615 nm					
		time	space	%	exp.	%	exp.		expt.	cells	traj.
eGFP-CENP-A (MC024)	Ndc80-mCherry	2 s	138.1 x 138.1 x 500 nm	5	50 ms	-	-	-	4	73	6,547
								3.3 μM noc.	1	15	286
eGFP-CENP-A (MC024)	Ndc80-tagRFP	7.5 s	69.4 x 69.4 x 200 nm	5	50 ms	20	50 ms	-	7	71	333
								3 μM noc.	3	47	372
								100 nM noc.	3	43	240
								10 μM taxol	5	55	162
mCherry-CENP-A (MC051)	Bub3-eGFP	-	69.4 x 69.4 x 100 nm	15	50 ms	25	50 ms	-	2	47	N/A
mCherry-CENP-A/ eGFP-CENP-P (MC072)	-	-	69.4 x 69.4 x 100 nm	50	50 ms	25	50 ms	-	2	39	N/A
eGFP-CENP-O (MC132)	Ndc80-tagRFP	-	69.4 x 69.4 x 100 nm	50	50 ms	20	50 ms	-	2	52	N/A
eGFP-CENP-A (MC092)	-	2 s	138.1 x 138.1 x 500 nm	5	50 ms	-	-	-	3	15	516
								3.3 μM noc.	1	28	1222
eGFP-CENP-A/ mCherry-Mis12 (MC093)	-	2 s	138.1 x 138.1 x 500 nm	5	50 ms	-	-	-	4	47	870
								3.3 μM noc.	1	24	802
eGFP-CENP-A/ eGFP-Centrin1 (MC060)	WT CyclinB1-mCherry	7.5 s	138.1 x 138.1 x 500 nm	5	50 ms	25	500 ms	-	6	70	14,690
eGFP-CENP-A/ eGFP-Centrin1 (MC060)	ND CyclinB1-mCherry	7.5 s	138.1 x 138.1 x 500 nm	5	50 ms	25	500 ms	-	8	69	12,390
								2 μM ZM1	1	25	4,158

Table 2.7 *Details of imaging setup, and number of cells obtained for each drug treatment, for live cell imaging experiments.*

was split by a dichroic to each of the two cameras to allow simultaneous imaging of two wavelengths. Cells were first identified using bright-field illumination to minimise phototoxicity. Interphase cells imaged for chromatic shift calculation were imaged over 121 z-slices separated by 100 nm for a single image stack. Laser power in the 488 and 561 nm wavelengths were both set to 15% with exposure time 50 ms per z-slice. Metaphase cells imaged for dual colour tracking were imaged over 61 z-slices separated by 200 nm, for 5 min every 7.5 s (41 time points). Laser power in the 488 nm wavelength was set to 5%. Laser power in the 561 nm wavelength was set to 20% over z-slices 26-41 (from the bottom of the cell, amounting to a 3 μm z-stack), and set to 0% for all other z-slices to minimise phototoxicity. Exposure time was 50 ms per z-slice. Details about data obtained from these experiments are located in Table 2.7.

2.8 Image processing and analysis

All confocal spinning-disk microscope images and movies were exported from Volocity 6.0 in .OME.TIFF format (The Open Microscopy Environment). All images and movies were then deconvolved within Huygens 4.1 (SVI). eGFP-only movies were deconvolved in the 488 nm wavelength using a point spread function (PSF) calculated using the Huygens 4.1 PSF distiller (same as that used in Burroughs *et al.*, 2015; Figure 2.2 A). Multiple-colour movies and images were deconvolved in the 488 and 561 nm wavelengths using PSFs calculated from 100 nm TetraSpeck™ fluorescent microspheres (Invitrogen) also calculated using the Huygens 4.1 PSF distiller (Figure 2.2 B). z-directional resolution of the PSF is defined by the z-resolution of the images of fluorescent microspheres used to distil the PSFs – the PSF in Figure 2.2 A has z-resolution of 500 nm, while those in Figure 2.2 B have z-resolution of 100 nm. Images were deconvolved in the 640 nm wavelength using a theoretical PSF within Huygens 4.1. Deconvolved images were exported from Huygens 4.1 in .r3d format (Applied Precision), and read into MATLAB (R2012a, Mathworks) using the loci-tools java library (The Open Microscopy Environment). Chromatic shift was calculated as described below. For tracking experiments, sister kinetochores in movies were detected for eGFP

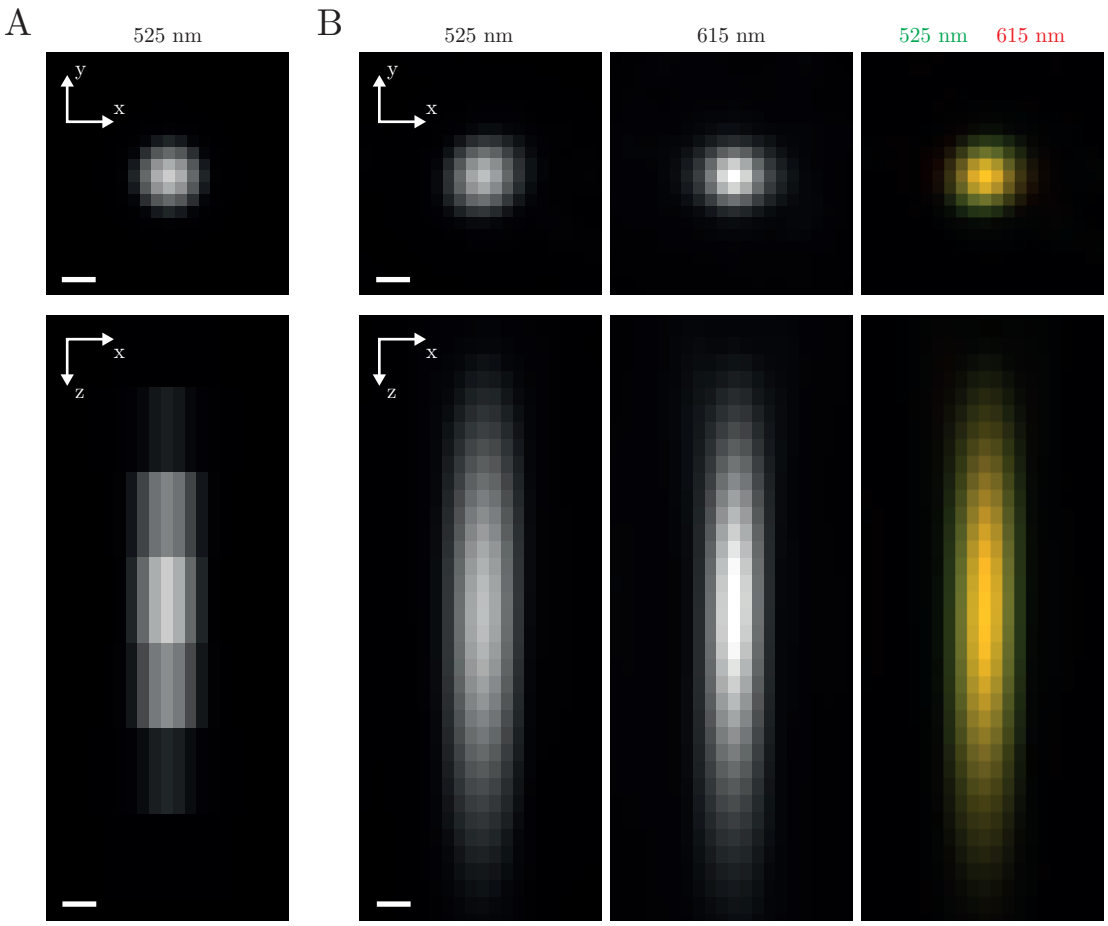

Figure 2.2 *Point spread functions calculated using Huygens.*
All point spread functions (PSFs) were calculated for the confocal spinning disk microscope, using Huygens Professional X11's PSF distiller, using images of 100 nm diameter tetraSpeck™ fluorescent microspheres.
(A) Image of PSF calculated by Ed Harry in 525 nm emission wavelength for deconvolution of single-channel movies with eGFP fluorescence, in the *xy* (top) and *xz* (bottom) planes. Scale bar = 200 nm.
(B) Image of PSFs in 525 and 615 nm emission wavelengths for deconvolution of dual-channel movies with eGFP and tagRFP/mCherry fluorescence, in the *xy* (top row) and *xz* (bottom row) planes. Scale bar = 200 nm.

signal, aligned, tracked and paired in MATLAB as previously described (Burroughs *et al.*, 2015). tagRFP fluorescence signal was originally detected within a hemispherical mask with 300 nm radius directed normal to the metaphase plate and away from the sister pair centre; the hemisphere was centred at the eGFP coordinate, plus chromatic shift from the 488 to 561 nm wavelength. 3D Gaussians were then fit to tagRFP spots to find sub-pixel spot centre coordinates (in the same way as is done for eGFP signal), and corrected for chromatic shift. For more information, see § 5.3.

2.9 Delta (Δ) measurements

Δ_{3D} was measured as the 3D Euclidean distance between eGFP and tagRFP spot centres:

$$\begin{aligned}\Delta_{3D} &= \sqrt{\Delta_x^2 + \Delta_y^2 + \Delta_z^2} \\ &= \sqrt{(x_{\text{eGFP}} - x_{\text{tagRFP}})^2 + (y_{\text{eGFP}} - y_{\text{tagRFP}})^2 + (z_{\text{eGFP}} - z_{\text{tagRFP}})^2}\end{aligned} \tag{2.1}$$

where Δ_i are differences in eGFP and tagRFP coordinates in the ith-coordinate, for $i = (x, y, z)$, and x_c, y_c and z_c are the individual coordinates in the cth-channel. Data was filtered so that the z-component of Δ_{3D} (distance between eGFP and tagRFP signal from the same kinetochore) was no larger than 100 nm (half the z-pixel resolution). Δ_{1D} measurements were calculated as before (Maresca & Salmon, 2009; Drpic *et al.*, 2015; Tauchman *et al.*, 2015),

$$\Delta_{1D} = \frac{d_{\text{tagRFP}} - d_{\text{eGFP}}}{2}, \tag{2.2}$$

where d_c is the Euclidean interkinetochore distance in the cth-coordinate. All statistical tests were Mann-Whitney U tests.

Location of the centre of a spot is derived by fitting a 3D Gaussian to the deconvolved spot. The uncertainty in this location, $\sigma_{i,c}$, can be approximated using (Waters

& Wittmann, 2014),

$$\sigma_{i,c} = \frac{1}{2}\sqrt{\left(\frac{s_{i,c}^2}{N_c} + \frac{a_i^2}{12N_c} + \frac{8\pi s_{i,c}^4 b_c^2}{a_i^2 N_c^2}\right)} \tag{2.3}$$

for $i = (x, y, z)$ and $c = (\text{eGFP}, \text{tagRFP})$. In each coordinate c, $s_{i,c}$ is the standard deviation of the spot in the i-coordinate, N_c is the total number of photons within the spot, a_i is the pixel size in the i-coordinate, and b_c is the average background pixel intensity (Figure 2.3 A). The expression is halved in order to find the uncertainty in a single direction from the fitted spot centre, i.e. to allow measurements to be written in the form $p \pm \sigma_p$ for some measurement p. Analysis of coordinate-directed line profiles through eGFP and tagRFP spots allowed derivation of the spot full width half maximum (FWHM; Figure 2.3 B), which gave an approximation of the spot standard deviations, $s_{i,c}$. b_c values were derived by averaging a region of the image not containing spots, and N_c was calculated by encasing spots within a region and multiplying the total pixels by the average signal (Figure 2.3 A). Values derived from images of eGFP-CENP-A and Ndc80-tagRFP yielded the values in Figure 2.3 C. This uncertainty is ∼3 % and ∼6 % of the pixel size for eGFP and tagRFP, respectively (demonstrated in Figure 2.3 D).

The uncertainties in individual components of Δ_{3D}, σ_{Δ_i}, were calculated using,

$$\sigma_{\Delta_i}^2 = \sigma_{i,eGFP}^2 + \sigma_{i,tagRFP}^2.$$

Non-linear propagation of coordinate uncertainties required the general formula for error propagation,

$$\sigma_f^2 = \left(\frac{df}{dx}\right)^2 \sigma_x^2 + \left(\frac{df}{dy}\right)^2 \sigma_y^2 + \left(\frac{df}{dz}\right)^2 \sigma_z^2. \tag{2.4}$$

Using the assumption that $\Delta_x = \Delta_y = \Delta_z$, and therefore $\Delta = \sqrt{3}\Delta_x$, the uncertainty in measurement of Δ_{3D} could be written,

$$\sigma_{\Delta_{3D}}^2 = \frac{4}{3}\left(\sigma_{\Delta_x}^2 + \sigma_{\Delta_y}^2 + \sigma_{\Delta_z}^2\right). \tag{2.5}$$

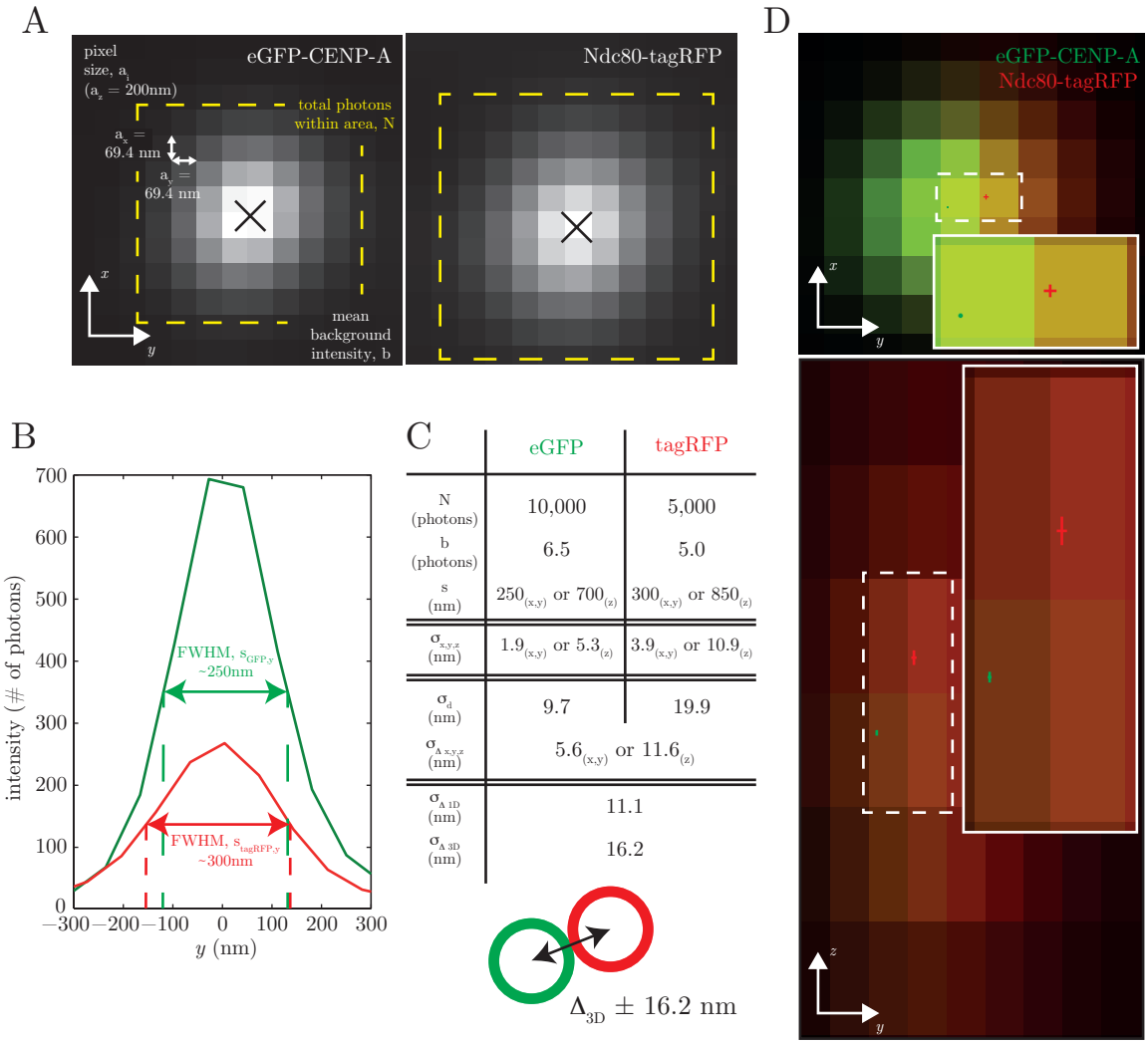

Figure 2.3 *Sub-pixel accuracy of eGFP and tagRFP 3D Gaussian spot fitting.* (A) Example image of a kinetochore expressing eGFP-CENP-A (left) and Ndc80-tagRFP (right) in the *xy*-plane, demonstrating source of measurements: pixel size, $a = [a_x, a_y, a_z] = [69.4, 69.4, 200]$ nm; total photons, N; and background intensity, b. N is measured within the yellow dashed boxes.
(B) Intensity measured along a line profile in the *y*-direction through the centre of the eGFP (green) and tagRFP (red) spot in (A). The full width half maximum (FWHM) of the fluorescent spot in each coordinate yields the spread of the spot, $s = [s_x, s_y, s_z]$.
(C) Table of typical values obtained for N, b and s, and the values for uncertainty, σ, in localisation of Gaussian-fitted eGFP and tagRFP spot centres, and subsequent measurements of d, Δ_x, Δ_y, Δ_z, Δ_{1D} and Δ_{3D}.
(D) Images of a kinetochore expressing eGFP-CENP-A and Ndc80-tagRFP in the xy- (top) and zy-planes (bottom), demonstrating uncertainty in localisation of the spot centres. Green and red pluses are centred at the Gaussian-fitted spot centre, and each of the plus' lines has length equal to the uncertainty in the measurement in that coordinate. White dashed boxes represent location of the insets.

Using the values given in Figure 2.3 C, $\sigma_{\Delta_{3D}} = 16.2$ nm.

Similarly, to calculate uncertainty in the measurement of Δ_{1D}, the steps above were done in reverse. Using Equation 2.4, the equation for sister separation, $d = \sqrt{d_x^2 + d_y^2 + d_z^2}$, and the assumption that $d_x = d_y = d_z$, uncertainty in measurement of d was calculated, $\sigma_{d_c}^2 = \frac{8}{3}(\sigma_{x,c}^2 + \sigma_{y,c}^2 + \sigma_{z,c}^2)$, for $c = (\text{eGFP}, \text{tagRFP})$. Linearly propagating these values resulted in an uncertainty in Δ_{1D}, $\sigma_{\Delta_{1D}}$, with value 11.1 nm.

All of the above calculated uncertainties are given in Figure 2.3 C.

2.10 Swivel (ϑ) measurement

$\vartheta_{\text{swivel}}$ was calculated using the dot product of the sister-sister and the intra-kinetochore axes. y- and z-directional $\vartheta_{\text{swivel}}$ of a given kinetochore was calculated using the cosine rule with the coordinates of the kinetochore's tagRFP centre and the eGFP centres of the kinetochore pair, in either the xy- or xz-plane. All statistical tests were Mann-Whitney U tests, except for in Figure 5.13, where the F-test was used to compare distribution variances of y- and z-directional $\vartheta_{\text{swivel}}$.

Chapter 3

Cell Line Development

3.1 Background

To understand how the structure of the kinetochore correlates with its state, a method typically used is to measure distances between different kinetochore components, the intra-kinetochore distance, Δ. This distance has been measured in a number of organisms, between different pairs of kinetochore proteins, and during different kinetochore processes (Figure 1.8). This is typically performed by fluorescence imaging of cells expressing a pair of kinetochore proteins tagged with different fluorophores. The fluorescent spots are then localised, and the distance between the different coloured fluorescent proteins calculated. Δ has previously been measured between inner kinetochore protein CENP-C's amino (N)-terminus and outer kinetochore-localised protein Cdc20 in PtK2 cells, which revealed a difference in intra-kinetochore structure between poleward (P) and away-from-the-pole (AP) moving kinetochores (Dumont *et al.*, 2012). This was also observed in Δ between Ndc80's carboxy (C)-terminus and Cdc20 in the same work. Intra-kinetochore distance has also been measured in live HeLa-K cells expressing both eGFP-CENP-A at the inner kinetochore, and mCherry-Mis12 at the outer kinetochore, which also yielded structural changes in the form of large stretches in Δ. These stretches were correlated with a directional movement of CENP-A towards its spindle pole (Uchida *et al.*, 2009). In the same work, and similar experiments in *Drosophila melanogaster* S2 cells (Maresca & Salmon, 2009), changes in Δ were suggested to be crucial for progression into anaphase, the idea being that stretch is a requirement to silence the spindle assembly checkpoint (SAC). A common feature of

these assays is a cell line expressing pairs of kinetochore proteins tagged with different fluorophores. I describe here my efforts to develop a human cell line that would allow live tracking of intra-kinetochore measurements. In particular, we have sought to ensure that such cell lines do not perturb kinetochore function as previously reported (Mattiuzzo *et al.*, 2011).

3.2 Ndc80's C-terminus

Initially, I obtained the stable cell line used by the Hirota group to measure Δ in live HeLa cells (Uchida *et al.*, 2009). This cell line has eGFP fused to CENP-A's N-terminus and Mis12's N-terminus tagged with mCherry. My analysis of this cell line showed that chromosome congression was delayed and force generation at the lead kinetochore is perturbed (for detail, see Appendix A). This cell line was therefore not used for live measurements of Δ. My attention turned to other members of the microtubule-binding KMN network within the kinetochore, which include Knl1 and the NDC80 complex. The former is likely to be problematic, as Knl1 is a large ($> 2,300$ amino acids) and disordered protein, where its C-terminus is the only region with an ordered structure (Caldas & DeLuca, 2014). As such, proteins associated with Knl1, or indeed Knl1 itself, as an outer-kinetochore marker is likely to lead to more noise in measurements of intra-kinetochore distances. In contrast, the NDC80 complex has been shown to be a stiff element in the kinetochore (Suzuki *et al.*, 2014). However, fluorescent labelling of the N-terminus of Ndc80 produces errors in force generation and microtubule-binding affinity (Mattiuzzo *et al.*, 2011). Therefore any region of the NDC80 complex required for binding to kinetochore-microtubules (kMTs) or other kinetochore proteins was avoided for fusing fluorescent protein. The C-terminus of Ndc80 (Ndc80-C), which is located at the end of a coiled-coil region that binds the Spc24 subunit of the complex, was originally chosen as a target for localisation of an mCherry fluorescent marker. In order to maximise brightness and localisation of Ndc80 throughout movies, we also used another red fluorescent protein, tagRFP. This has been shown to have better quantum yield, resistance to photobleaching, and greater than 3$\times$ the brightness of

mCherry (Merzlyak *et al.*, 2007). Plasmids containing these fusions were produced as described in § 2. In these constructs, Ndc80 and its fluorescent marker were separated by a 42-amino acid linker, which under full extension would have length ∼18 nm (Berg *et al.*, 2002, Figure 3.24); it was made to this length to reduce interference by the fluorescent marker on the full NDC80 complex, which is essential as it has been suggested that transient transfection of C-terminally tagged Ndc80 can be inefficient (Mattiuzzo *et al.*, 2011). This construct could now be used as a marker for the outer-kinetochore in cells that already express eGFP-CENP-A, allowing measurements of intra-kinetochore distance in the direct linkage between the centromeric DNA (CENP-A) and microtubule binding (Ndc80). Due to repeated failure to obtain a double stable cell line, all Ndc80-tagRFP experiments were performed using transient transfection.

To ensure fusion of a fluorescent marker to Ndc80-C does not alter kinetochore function, I next determined the dynamics of CENP-A using our established kinetochore tracking and analysis pipeline (Jaqaman *et al.*, 2010; Burroughs *et al.*, 2015; Armond *et al.*, 2015b). These experiments were performed prior to the production of the Ndc80-tagRFP construct, and therefore were performed using transient transfection of the Ndc80-mCherry plasmid. Given the similarity in size of both fluorescent protein and linker, it is assumed that Ndc80's fusion to tagRFP produces no difference in effect when compared to mCherry. Transfection of the mCherry plasmid in cells expressing eGFP-CENP-A resulted in a range of expression of Ndc80-mCherry (Figure 3.1 A). Metaphase cells were imaged for eGFP-CENP-A signal every 2 s for 5 min, and imaged for mCherry signal at the first time point. Cells in these cultures that failed to express Ndc80-mCherry were used as a control, as they had undergone the same incubation with the transfection reagent but did not express the mCherry. Cells were divided into one of three groups: no (Figure 3.1 A), low (Figure 3.1 B) and high expression (Figure 3.1 C) of Ndc80-mCherry. eGFP-CENP-A signals were tracked in each movie and sister kinetochores found. Next, the distance between eGFP-CENP-A signals at each kinetochore pair, d, was calculated within cells expressing no Ndc80-mCherry, low levels, and high levels of Ndc80-mCherry. The median (± standard error) distance

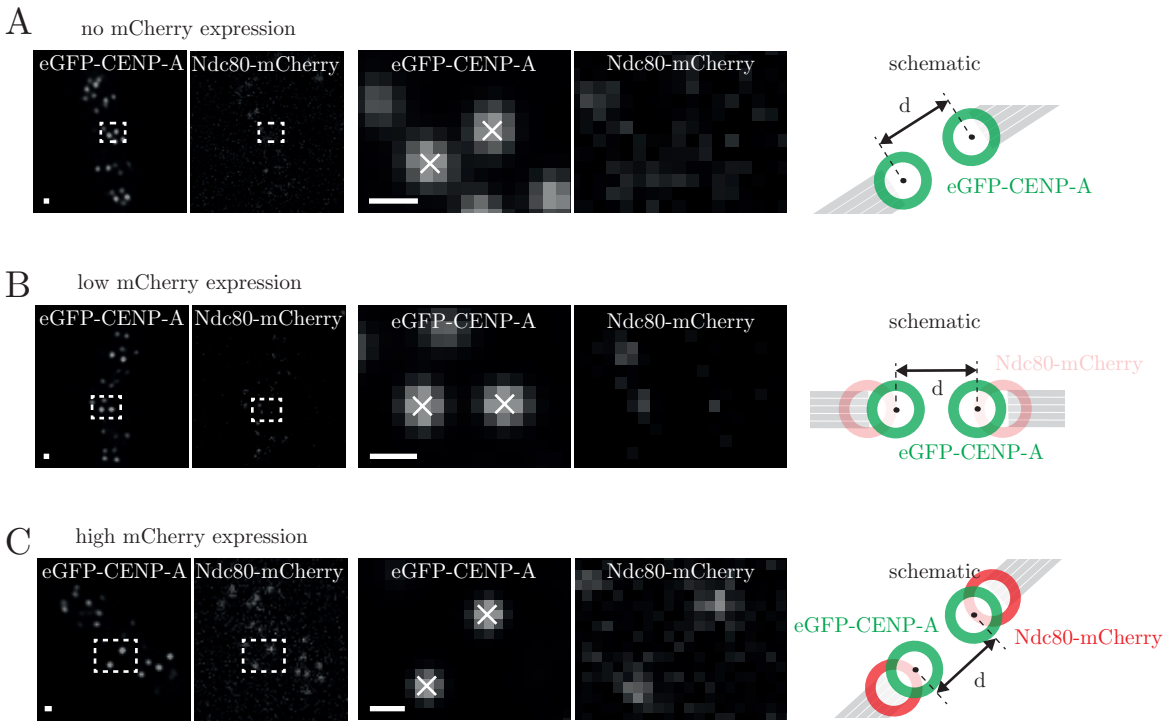

Figure 3.1 *Ndc80-mCherry can be transfected with a range of expression levels at kinetochores.*
Example fluorescence images of eGFP and mCherry signal in eGFP-CENP-A cells after transient transfection of Ndc80-mCherry, with (A) no, (B) low, or (C) high expression of Ndc80-mCherry. Dashed white boxes represent location of kinetochore pairs within insets; white crosses are the Gaussian-fitted centres of eGFP signals. Schematics demonstrate the level of Ndc80-mCherry signal and the measurement of interkinetochore distance, *d*. Scale bars = 500 nm.

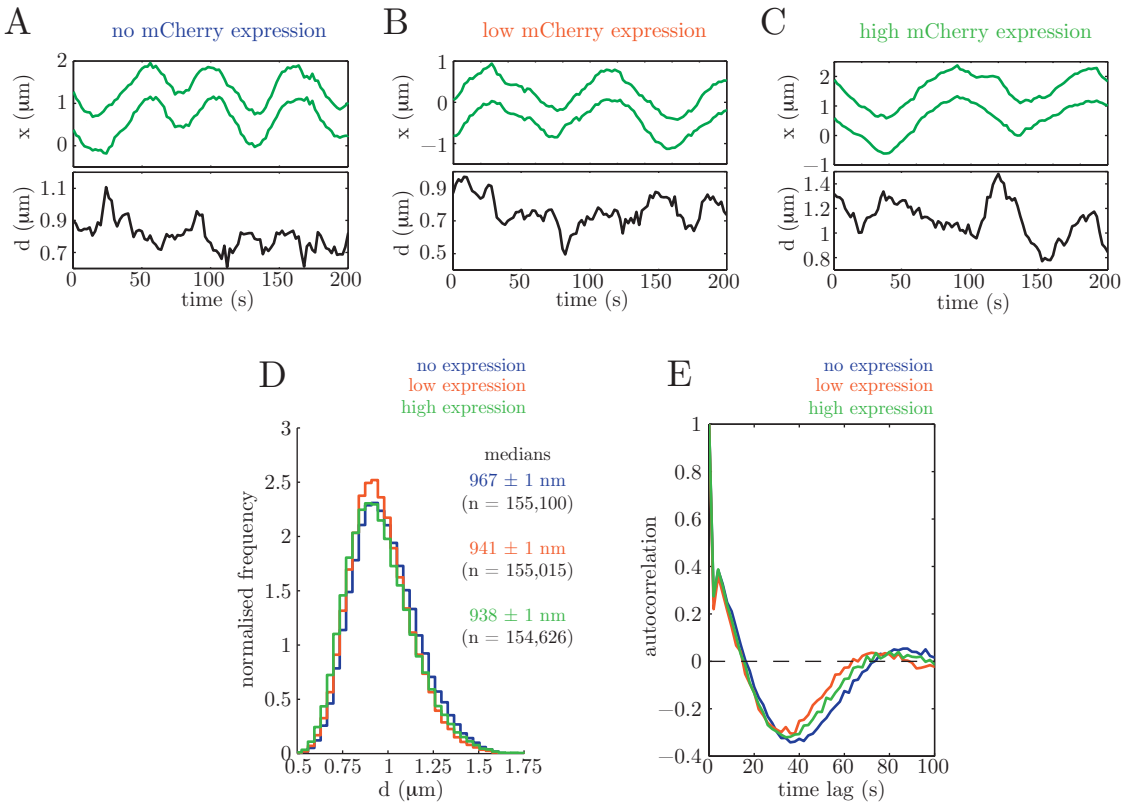

Figure 3.2 *Ndc80-mCherry incorporation does not affect overall kinetochore dynamics.*
Example eGFP-CENP-A trajectories in cells transfected with Ndc80-mCherry, with: (A) no, (B) low, or (C) high expression of Ndc80-mCherry. Green lines represents each kinetochore's position in the metaphase plate's x-coordinate. Black lines represent 3D interkinetochore distance, d, for each kinetochore pair. (D) Histogram of interkinetochore distance, d, for eGFP-CENP-A cells with no (blue; n = 155,100), low (gold; n = 155,015) and high expression (green; n = 154,626) of Ndc80-mCherry. Values given are medians ± standard error.
(E) Autocorrelation of a kinetochore's eGFP-CENP-A location in the metaphase plate's x-coordinate for cells with no (blue), low (gold) and high expression (green) of Ndc80-mCherry. Each curve demonstrates periodic behaviour of a kinetochore's location about the metaphase plate with half-period of approximately 35 s.

between sister kinetochores in cells expressing eGFP-CENP-A alone was 967 (± 1) nm (n=155,100), while those also expressing low or high Ndc80-mCherry had median sister separations 941 (± 1) nm (n=155,015) and 938 (± 1) nm (n=154,626), respectively (Figure 3.2 D). Thus, only a small decrease in the distance between kinetochore pairs was apparent when high Ndc80-mCherry expression was present. As a further test for ability for kinetochore pairs to generate force efficiently, the back-and-forth motion of sister kinetochores about the metaphase plate was investigated. This was measured by calculating the autocorrelation of change in a kinetochore's metaphase plate x-coordinate. Cells expressing no, low, and high levels of Ndc80-mCherry had the same characteristic periodicity of kinetochores' back-and-forth motion. All cells exhibited an average half-period of 35-40 s, and the strength (or depth) of autocorrelation at the half-period did not change (Figure 3.2 E).

There is a slight alteration in half-period in high Ndc80-mCherry expressing cells, so this prompted me to investigate directional switches during kinetochore back-and-forth motion in more detail. My lab has previously used a mathematical model of kinetochore dynamics to investigate directional switches in detail Armond *et al.* (2015b). By fitting the model to kinetochore coordinate data using Monte Carlo Markov chain (MCMC) methods, distributions of values for each of the model's parameters are produced. These distributions give a best approximation of the model given the data. However, there is an identifiability issue between the inter-kinetochore spring's natural length, L, and kMT polymerisation (+) and depolymerisation (−) speeds, $v_{\pm}$. To overcome this, a measured distribution for L is required before running the model-fitting. A hidden variable derived by the model-fitting is the state of each kinetochore-fibre (k-fibre). This variable derives the probability that a directional switch was initiated by the lead (or poleward, P) or trail (or away-from-the-pole, AP) kinetochore. Each directional switch can then be classed as a lead-initiated directional switch (LIDS), trail-initiated directional switch (TIDS) or joint directional switch (JDS). Once directional switch times are found, average profiles of other variables, e.g. inter-kinetochore distance, can be observed during each type of switch. HeLa-K cells exhibit a bias towards LIDS

and exhibit signature profiles in their inter-kinetochore distance during both LIDS and TIDS (Burroughs *et al.*, 2015; Armond *et al.*, 2015b). These detailed analyses revealed that the LIDS bias was lost in cells expressing mCherry-Mis12, and inter-kinetochore profiles during LIDS and TIDS were perturbed (see Appendix A).

In order to calculate natural length of inter-kinetochore chromatin required before running the modelling in cells expressing Ndc80-mCherry, cells were incubated with 3.3 μM nocodazole to deconstruct the mitotic spindle. This removed any inter-kinetochore tension, and therefore provided the natural length. Kinetochores were tracked using their eGFP-CENP-A signal (Figure 3.3 A), giving a distribution of inter-kinetochore distances, d, in cells devoid of inter-kinetochore stretch. The median ($\pm$ standard deviation) value of d measured in these cells was 749 ($\pm$ 131) nm (n = 106, 722); these values were used as enforced priors for the MCMC model-fitting. After fitting the model to the kinetochore coordinate data, a variable for k-fibre state for the pair of kinetochores can be extracted, so that this state changes at a directional switch. With this, probabilities that either the leading or trailing kinetochore initiated a directional switch can be calculated. A calculation of normalised probability that a directional switch was lead-initiated (LIDS) was made, so that the more likely a directional switch is a LIDS the closer the normalised probability is to 1. This way, a LIDS could be defined as any normalised probability above 0.67 (i.e. is twice as likely to be a LIDS than a trail-initiated directional switch (TIDS)), and a TIDS defined as normalised probability below 0.33 (i.e. is twice as likely to be a TIDS than a LIDS). Of all directional switches within cells not expressing Ndc80-mCherry (n = 968), 62.0% were calculated as LIDS, while 17.3% were TIDS (Figure 3.3 C), yielding an expected bias of 3.6:1 LIDS:TIDS (c.f. 3.8 for J-CENP-A in Figure A.3). Meanwhile, cells expressing both eGFP-CENP-A and low or high levels of Ndc80-mCherry also yielded biases of 5.1:1 LIDS:TIDS (n = 391) and 4.3:1 LIDS:TIDS (n = 797), respectively (Figure 3.3 C). While the bias for low expression appears larger than that of no and high expression of Ndc80-mCherry, there is only a difference of $\sim$4% between the probabilities of LIDS and TIDS between no and low expression levels. Furthermore, the

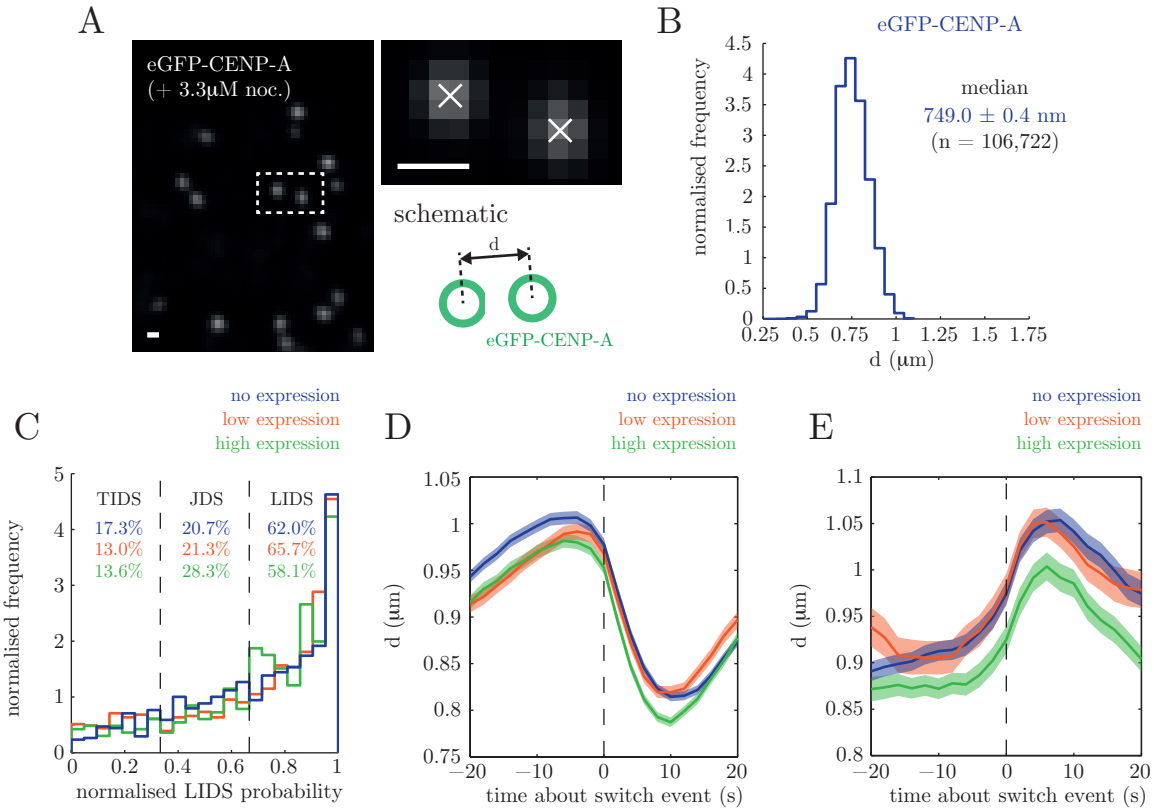

Figure 3.3 *Ndc80-mCherry incorporation does not affect kinetochore directional switching behaviour.*
(A) Example image of eGFP-CENP-A cells after addition of 3.3 μM nocodazole. Dashed white box represents location of the kinetochore pair within inset; white crosses are the Gaussian-fitted spot centres. Schematic demonstrates the measurement of interkinetochore distance, *d*. Scale bar = 500 nm.
(B) Histogram of interkinetochore distance, *d*, for eGFP-CENP-A cells after addition of 3.3 μM nocodazole (n = 106,722), providing a prior distribution for modelling natural length, *L*, of the interkinetochore 'spring'. Values given are median ± standard error.
(C) Histogram of normalised probabilty a directional switch is lead-initiated for eGFP-CENP-A cells with no (blue; n = 968), low (gold; n = 391) and high expression (green; n = 797) of Ndc80-mCherry.
(D) Interkinetochore distance, *d*, about a LIDS for eGFP-CENP-A cells with no (blue; n = 584), low (gold; n = 245) and high expression (green; n = 447) of Ndc80-mCherry. Areas either side of each line represent the standard error of the mean.
(E) Interkinetochore distance, *d*, about a TIDS for eGFP-CENP-A cells with no (blue; n = 157), low (gold; n = 49) and high expression (green; n = 97) of Ndc80-mCherry. Areas either side of each line represent the standard error of the mean.

histograms of normalised LIDS probability in each case overlap considerably. To check whether this increase in bias towards LIDS in low and high Ndc80-mCherry expressing cells is not a significant effect, it was important to ensure that force generation on the approach to directional switches was not perturbed.

In order to investigate force generation about directional switches, inter-kinetochore distance, d, was calculated at the 10 time points both prior to and after a LIDS and a TIDS, which would provide a proxy for the tension generated between the kinetochore pair. Importantly, the rate of generation of inter-kinetochore tension on approach to a LIDS was unaffected in cells expressing low and high levels of Ndc80-mCherry (Figure 3.3 D). Furthermore, the profiles in d about a TIDS in low and high levels of Ndc80-mCherry were unaffected (Figure 3.3 E), the only difference being a decrease in inter-kinetochore distance ∼15 s prior to the TIDS. This is likely a consequence of the low number of kinetochore pairs in low expressing cells exhibiting this type of directional switch (n = 49), compared to both no expressing (n = 157) and high expressing (n = 97) cells. Overall, the mCherry, and therefore presumably the tagRFP, produces very little difference in coordination of directional switch behaviour in sister kinetochore. Coupled with the observation that cells expressing both eGFP-CENP-A and Ndc80-mCherry, and therefore Ndc80-tagRFP, exhibit the behaviour demonstrated by cells expressing eGFP-CENP-A alone, eGFP-CENP-A cells transiently transfected with Ndc80-tagRFP can be faithfully investigated for intra-kinetochore dynamics.

3.3 dual-tagged (dt)CENP-A

Previously published measurements of intra-kinetochore distances, Δ, have been on the scale of 10's of nanometres. Given that image pixel size will be a minimum of $69.4 \times 69.4 \times 100$ nm, it is crucial that all potential sources of error are carefully controlled for. Given that measurements of Δ will be made in cells expressing both eGFP-CENP-A and Ndc80-tagRFP, one such source of error is chromatic shift of light with different wavelengths. The filters within the optical path of the spinning-disk confocal microscope being used allow measurement of emission wavelengths of 525 nm

and 615 nm, allowing imaging of the eGFP and tagRFP fluorophores, respectively. In order to accurately measure the chromatic shift between these two wavelengths from the same source, we developed a HeLa-K cell line stably expressing both eGFP-CENP-A and mCherry-CENP-A (dtCENP-A), as described in § 2. The use of mCherry as the red fluorescent protein didn't produce any differences, as the emission wavelength being measured by the filter wheel was independent of the fluorophore. In order to faithfully calculate chromatic shift using this cell line, we needed to ensure that the cell line expressing both eGFP and mCherry in the centromeric chromatin would not cause errors in mitosis. This could be directly observed by imaging cells every 3 min for 12 hr, which would allow observation of timing of mitotic events. dtCENP-A cells and cells expressing eGFP-CENP-A alone were imaged for eGFP signal, while cells expressing mCherry-CENP-A alone were imaged for mCherry signal as a further control. Example images of cells progressing through nuclear envelope breakdown (NEBD), metaphase plate formation and anaphase onset show very little difference in mitotic timings in the three cell lines (Figure 3.4 A). Times of these events were manually collated for two experiments for each cell line, and time differences calculated therein, showing that indeed the population of cells in all three cell lines progress through mitosis with very similar timings (Figure 3.4 B,C,D). More specifically: the mean (± standard error) time taken for eGFP-CENP-A, mCherry-CENP-A and dtCENP-A cells to progress from NEBD to metaphase plate formation were 17.5 (± 0.4) min, 17.9 (± 0.4) min, and 19.8 (± 0.4) min, respectively (Figure 3.4 B); the mean (± standard error) time taken for eGFP-CENP-A, mCherry-CENP-A and dtCENP-A cells to progress from metaphase plate formation to anaphase onset were 13.5 (± 0.5) min, 15.2 (± 0.5) min, and 12.4 (± 0.4) min, respectively (Figure 3.4 C); and the mean (± standard error) time taken for eGFP-CENP-A, mCherry-CENP-A and dtCENP-A cells to progress from NEBD to anaphase onset were 31.0 (± 0.6) min, 33.1 (± 0.6) min, and 32.8 (± 0.6) min, respectively (Figure 3.4 D). This demonstrates that the dtCENP-A cell line produces fluorescent signal at kinetochores without perturbation to a kinetochore's normal function in mitosis, and therefore chromatic shift could be faithfully

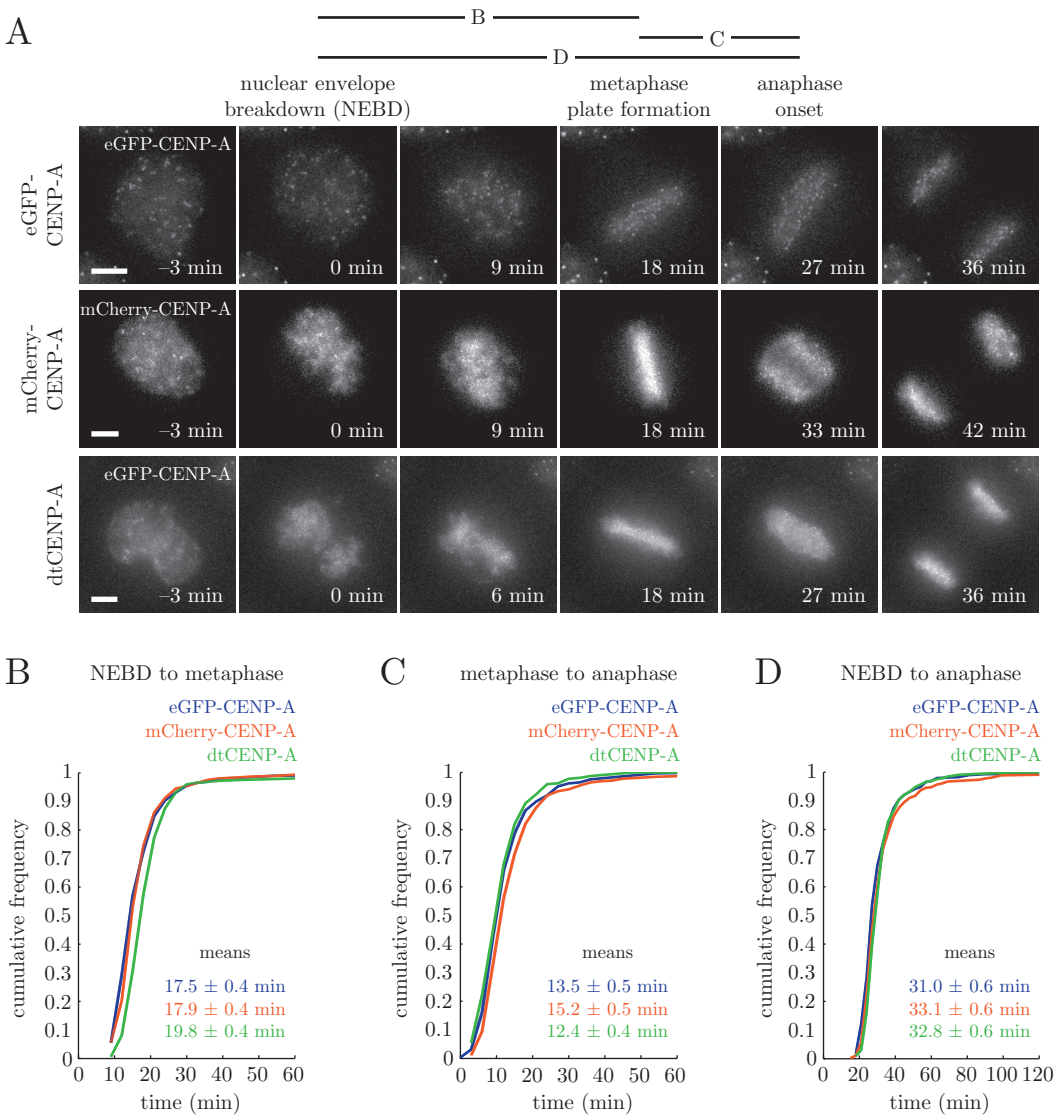

Figure 3.4 *Incorporation of mCherry tag to CENP-A N-terminus produces no effect on mitotic timing.*
(A) Example images of eGFP-CENP-A (top), mCherry-CENP-A (middle) and dtCENP-A (bottom) cells in mitosis, with NEBD (column 2), metaphase plate formation (column 4) and anaphase onset (column 5). Lines above plots denote which times are calculated for (B), (C) and (D). Scale bars = 5 μm.
(B) Cumulative frequency of time between NEBD and metaphase plate formation in eGFP-CENP-A (blue; n = 290), mCherry-CENP-A (gold; n = 454) and dtCENP-A (green; n = 322) cells. Values given are means ± standard error.
(C) Cumulative frequency of time between metaphase plate formation and anaphase onset in eGFP-CENP-A (blue; n = 286), mCherry-CENP-A (gold; n = 460) and dtCENP-A (green; n = 315) cells. Values given are means ± standard error.
(D) Cumulative frequency of time between NEBD and anaphase onset in eGFP-CENP-A (blue; n = 293), mCherry-CENP-A (gold; n = 456) and dtCENP-A (green; n = 327) cells. Values given are means ± standard error.

calculated using this cell line for experiments measuring intra-kinetochore distances.

3.4 Summary

In order to measure intra-kinetochore distances in human cells during mitosis, a pair of kinetochore proteins fused to different fluorescent markers can be imaged by fluorescence microscopy. To ensure that calculations of intra-kinetochore distance are representative of typical HeLa-K cells, kinetochore dynamics and/or mitotic progression were investigated in all cells expressing multiple fluorophores to multiple kinetochore proteins. This revealed that the incorporation of mCherry to the N-terminus of Mis12 results in perturbation in force generation at the lead kinetochore when a kinetochore pair move in unison (see Appendix A). In fact, incorporation of any fluorophore to the MIS12 complex may result in this perturbation, as delayed chromosome congression is also observed in cells expressing Dsn1-GFP (see Appendix A). Nevertheless, I have developed an assay in which cells expressing both eGFP-CENP-A and Ndc80-tagRFP can be faithfully used for intra-kinetochore distance measurements. Expression of Ndc80-mCherry in these cells has been carefully investigated with in-depth analysis of directional switches, ensuring that the incorporation of the fluorophore yielded no significant perturbations to kinetochore dynamics. With this in mind, I also developed a HeLa-K cell line expressing both eGFP- and mCherry-CENP-A (dtCENP-A) in order to accurately calculate chromatic shift between the measured eGFP and mCherry emission wavelengths within a cellular environment. To this end, I developed an assay to calculate accurate chromatic shift, ζ, using dtCENP-A cells required to accurately measure 3D intra-kinetochore distances.

Chapter 4

Calculating Chromatic Shift in 3D

4.1 Background

The physical separation of kinetochore components has previously been measured in multiple organisms, and in all cases intra-kinetochore distances are typically 10s of nano-metres (see Figure 1.8). Given such small differences being measured between fluorescent spots of different wavelengths, a careful appreciation of chromatic aberration is first required. With a view to doing fluorescence imaging of pairs of kinetochore proteins fused to different fluorescent proteins (FPs), I will use a spinning disk confocal microscope equipped with two charge-coupled device (CCD) cameras and a dichroic beam splitter, allowing two wavelengths of light to be imaged simultaneously. This would eliminate artefacts associated with "time effects". However, through a 100× objective lens these CCD cameras have apparent pixel size of ~ 69.4 nm, while profiles through diffraction-limited fluorescent spots have standard deviations of 200-300 nm – the combination of these two effects makes it crucial that all potential inaccuracies in measurement of intra-kinetochore distances are considered. One source of inaccuracy in the measurement of the distance between two different-wavelength fluorescent spots is the chromatic shift.

Chromatic shift is the observed difference in position of a fluorescent signal in two different wavelengths originating from the same source. This shift is caused by a wavelength dependence of the refractive index of materials as electromagnetic waves travel along the optical path, resulting in different diffraction angles (basic principle demonstrated in Figure 4.1). In the case where a point source emits both green and

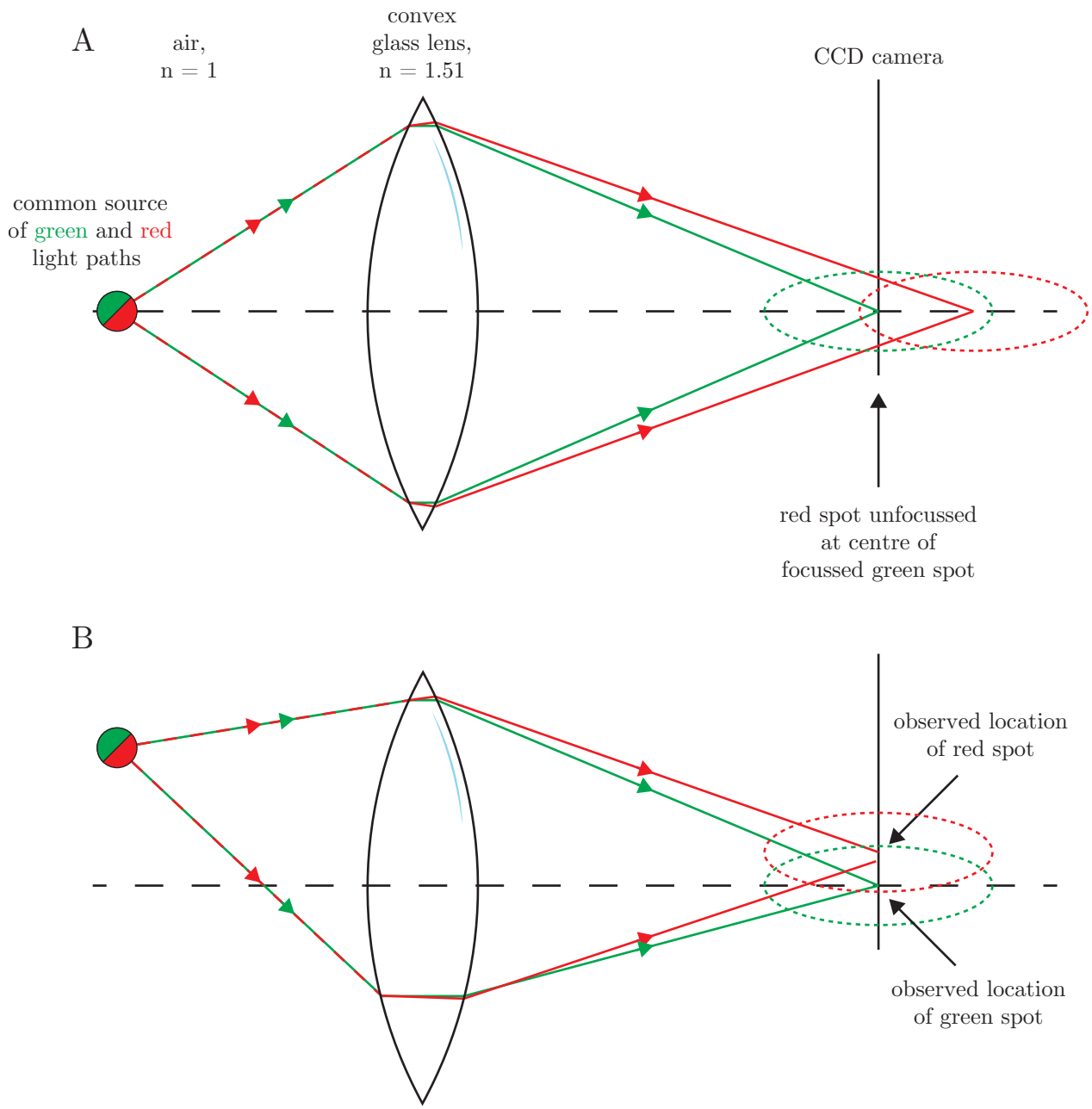

Figure 4.1 *Schematic of axial and transversal chromatic shift between green and red light.*
Light paths in 525 nm (green line) and 615 nm (red line) wavelengths travelling through a focussing lens onto a CCD camera, demonstrating both axial (A) and transversal (B) chromatic shift. Longer wavelength light has a larger refraction angle as it enters the lens, due to a decrease in refractive index, n, in glass relative to shorter wavelength light. This results in the red spot being unfocussed when the green spot is in focus (A), and/or green spots appear in a different location that red spots on the CCD. Dashed spots represent location of observed spots.

red light, the difference in position can occur either axially, where red signal would appear unfocussed when green signal is in focus (Figure 4.1 A), or transversally, where red signal would appear to be located in a different position to green signal in a single focal plane (Figure 4.1 B).

Designed to combat chromatic aberration, objective lenses are available in a number of forms (for review see Pawley, 2006, Chapter 7). Achromat lenses are designed to remove chromatic aberration between two wavelengths, while removing spherical aberration in a single wavelength. Fluorite (or neoflar) lenses can correct for up to three wavelengths in both chromatic and spherical aberrations, while apochromat lenses improve spherical aberrations in an additional wavelength again. Additionally, these lenses produce curved image projections rather than a flat field, which can be reduced significantly using either plan achromat, plan fluorite, or plan apochromat lenses. As such, all experiments measuring sub-pixel distances in this thesis were performed on a spinning disk confocal microscope installed with a 100× plan apochromat objective, which is superior to all other objective lens designs. However, despite correction of multiple sources of chromatic shift, objectives are designed to correct for specific wavelengths, meaning there remains a small, but significant, shift between any two of the wavelengths being measured here. This chromatic shift needs to be quantified in all three dimensions.

Given that no two microscopes and their optics can be constructed identically to within nano-metre accuracy, the chromatic shift must be determined specifically for each microscope. In order to measure the intra-kinetochore distance I use a two camera setup, one to measure each of eGFP fluorescence (525 nm emission wavelength) and tagRFP fluorescence (615 nm emission wavelength), imaging a sample where fluorescent signals of both 525 nm and 615 nm emission wavelengths originate from the same location. In order to measure the chromatic shift sub-pixel with maximum precision, I tested the measurement of chromatic shift correction using fluorescent microspheres, a traditional method of deriving chromatic shift, to ensure accurate correction of FPs located at kinetochores in live cells.

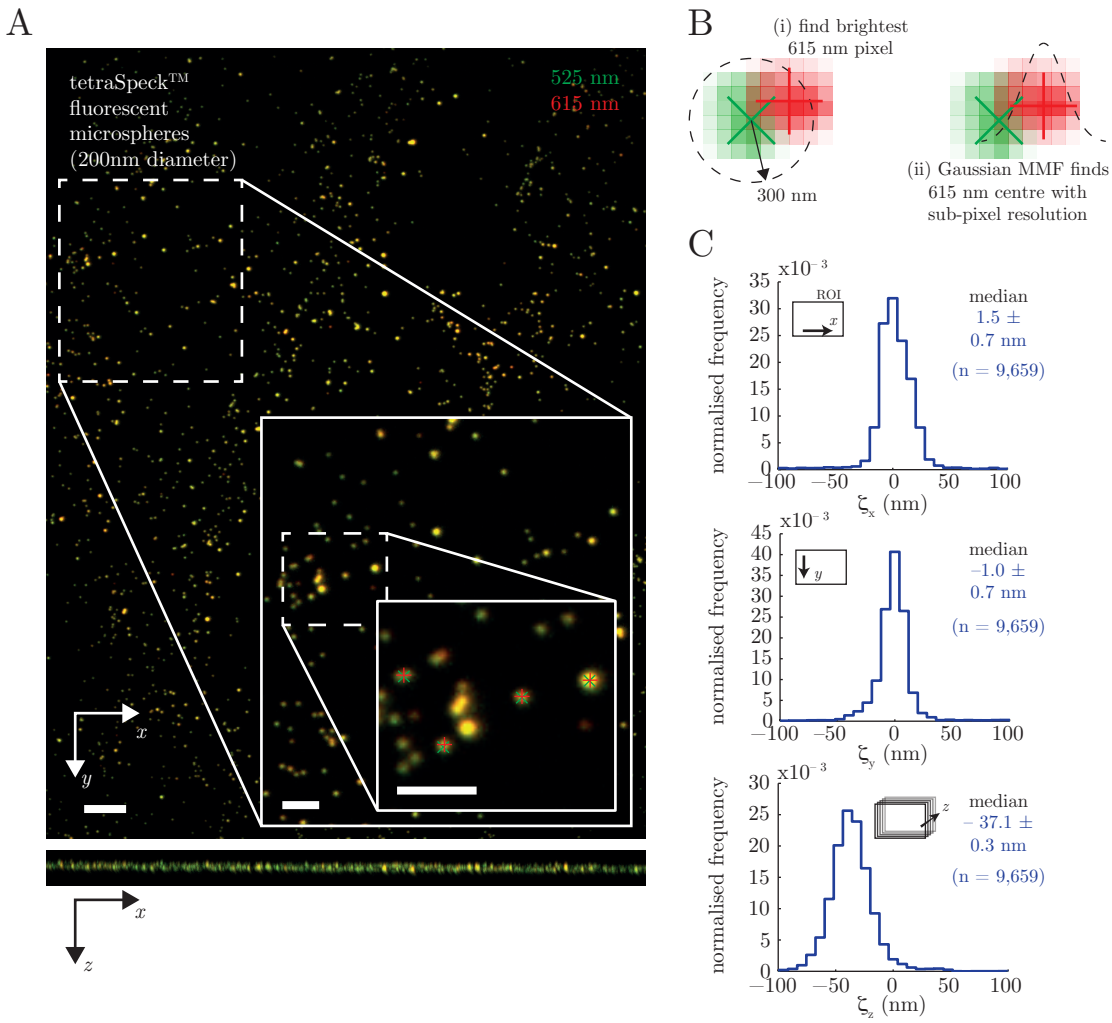

Figure 4.2 *Fluorescent microspheres as used to calculate 3D chromatic shift.*
(A) Example of 200 nm-diameter tetraSpeck™ fluorescent microspheres imaged in emission wavelengths of 525 nm and 615 nm. Top panel shows microscope *xy* plane, bottom panel shows microscope *xz* plane. Insets show regions denoted by white dashed boxes. Green crosses and red pluses show the Gaussian-fitted centres of 525 nm and 615 nm fluorescence signal, respectively. Scale bars = 5 μm for full image, 2 μm for both insets.
(B) Schematic demonstrating method of locating a 615 nm (red) spot based on location of 525 nm (green) spot. Dashed circle represents region of radius 300 nm, centred at green spot centre, within which to find brightest red spot. Green crosses represent Gaussian-fitted centre of green spot, red cross represents location of brightest red pixel, and red plus represents Gaussian-fitted centre of red spot.
(C) Histograms of chromatic shift, $\zeta = [\zeta_x, \zeta_y, \zeta_z]$, as measured from 525 nm to 615 nm fluorescence. Distributions of ζ_x, ζ_y and ζ_z are shown in the top, middle and bottom panels, respectively. Values given are medians ± standard error.

4.2 Fluorescent microspheres

Traditionally chromatic shift is calculated using fluorescent microspheres (e.g. Dumont *et al.*, 2012; Magidson *et al.*, 2016), spheres of uniform diameter on the scale of the point spread functions (PSFs) of fluorescent spots. They are stained with a number of fluorescent dyes spanning the wavelengths typically used for cell biology-related imaging assays. This allows imaging in multiple wavelengths of these point sources; thus the relative shift can be determined of an object's position as measured by each wavelength. One such example are tetraSpeck™ fluorescent microspheres with a range of diameters (100 nm up to 4 μm), which will be used for the experiments in this study. They are labelled with four different fluorescent dyes, but most importantly will allow imaging of 525 nm and 615 nm emission wavelengths. As fluorescent microspheres were relatively evenly distributed across the glass cover slip, and therefore gave a wide spread of spots when observed in an image stack, they were used to calibrate the two cameras during simultaneous imaging. Volocity® 6.1.3 (Perkin Elmer) has a dual camera calibration method which utilises images of either 500 nm or 1 μm diameter tetraSpeck™ fluorescent microspheres to align the two cameras in the 525 nm and 615 nm emission wavelengths in the xy-plane (z-directional alignment isn't a feature of this in-built calibration). Given that the previously reported distances between kinetochore subunits are sub-pixel measurements, I sought to further correct for chromatic shift after calibration in order to utilise our sub-pixel spot finding assay (Burroughs *et al.*, 2015).

In order to calculate sub-pixel chromatic shift between the 525 nm (green) and 615 nm (red) emission wavelengths on the dual camera setup, fluorescent microspheres were imaged under the same setup for green and red signals with 100 nm z-resolution (Figure 4.2 A). It is worth noting that the fluorescent beads are located in a common focal plane, as all beads are located on the glass surface (Figure 4.2 A). Chromatic shift, $\zeta = [\zeta_x, \zeta_y, \zeta_z]$, was calculated as the 3D vector separating the measured green and red spot centres, with direction towards the red signal (Figure 4.2 B,C). Spot centres were localised by Gaussian mixture-model fitting (MMF), resulting in sub-pixel measurements; green spot centres were first localised, and then red signal located within a

spherical mask of radius 300 nm centred at the green spot (Figure 4.2 B). Compiling measurements of ζ_x, ζ_y and ζ_z across 10 image stacks of fluorescent microspheres yielded median ($\pm$ standard error) distances of 1.5 ($\pm$ 0.7) nm, -1.0 ($\pm$ 0.7) nm and -37.1 ($\pm$ 0.3) nm, respectively (n = $9,659$; Figure 4.2 C). The population standard deviation of measurements of ζ_x, ζ_y and ζ_z were $\sigma_x = 68.6$ nm, $\sigma_y = 66.5$ nm and $\sigma_z = 32.0$ nm, respectively. The standard deviation of measurements of ζ_z, σ_z, was much smaller than the standard deviation of measurements of ζ_x and ζ_y. This difference may represent variation in the measurements of ζ depending on its position in the image stack. As the fluorescent microspheres are all glued onto the glass cover slip surface, and therefore only cover a narrow range in the microscope's z axis (Figure 4.2 A), smaller variation would be observed, and therefore a narrower population standard deviation. Nevertheless, axial (xy-plane) chromatic shift is precise to within the size of one pixel, while lateral (z-directional) chromatic shift is precise to within a third of a pixel. One limitation of this approach however is that I propose to correct for chromatic shift of fluorescently-labelled objects in live cells, whose refractive index (n $\sim$ 1.33, like water) differs from that of optical glue (n = 1.52) in which the fluorescent microspheres in this experiment are embedded. Additionally, different constituents within the cell have different microenvironments, and therefore may have different effective refractive indices, causing non-linear changes in diffraction of light through the cell. This could result in a difference in chromatic shift as a result of sample thickness, as light needs to travel through more cellular matter. Thus, fluorescent microspheres, which lack this cellular environment, may not sufficiently correct for the chromatic shift from labelled kinetochore proteins in live cells.

4.3 Using dtCENP-A to test fluorescent beads

In order to test whether the chromatic shift calculation calibration as determined from fluorescent microspheres is sufficiently accurate for correcting the location of FPs in live cells, I produced a cell line containing both eGFP- and mCherry-tagged trans-genes of CENP-A (see § 4.3), a protein previously localised and tracked in time (Jaqaman

et al., 2010; Amaro *et al.*, 2010; Wan *et al.*, 2012; Mchedlishvili *et al.*, 2012; Vladimirou *et al.*, 2013). Henceforth I shall refer to this cell line as dual-tagged (dt)CENP-A. In this cell line, both the eGFP and mCherry fluorescence signals will be localised to the centromere. If the chromatic shift correction is accurate, a kinetochore's mCherry signal should map onto its eGFP signal.

dtCENP-A cells were imaged in both 525 nm (green) and 615 nm (red) wavelengths with data collected from 10 metaphase cells and 10 fields containing interphase cells (Figure 4.3 A). Cells are in interphase for the majority of the cell cycle, and therefore could be found in groups that filled the field of view. In contrast, mitosis is a rarer event (even more so is metaphase), and therefore only individual cells could be imaged. eGFP and mCherry spot centres were localised by Gaussian MMF, and the vector from green to red fluorescence, $\eta = [\eta_x, \eta_y, \eta_z]$, was calculated, similarly to ζ (Figure 4.3 B,C). If the chromatic shift correction, $\overline{\zeta} = [\overline{\zeta_x}, \overline{\zeta_y}, \overline{\zeta_z}]$, calculated using fluorescent microspheres in Figure 4.2 B is sufficiently accurate, the median values of $\eta_i - \overline{\zeta_i}$, for $i \in [x, y, z]$, should be consistent with being zero, any deviation from zero should be consistent with experimental error in the measurement (see § 2.9 for theoretical measurement error). Indeed, the median values ($\pm$ standard deviation) calculated for metaphase dtCENP-A cells were -10.1 ($\pm$ 126.3) nm, -7.3 ($\pm$ 112.2) nm and 15.7 ($\pm$ 200.1) nm for the x, y and z components, respectively (n = 530; Figure 4.3 B). However, a concern is that the standard deviation in the population of η_z measurements ($\sigma_z = 200.1$ nm) for metaphase is $\sim 2\times$ the z-directional imaging resolution, demonstrating a wide range of measurements. Furthermore, the median values of $\eta_i - \overline{\zeta_i}$ for interphase dtCENP-A cells were 3.9 ($\pm$ 82.2) nm, -3.8 ($\pm$ 85.0) nm and -42.1 ($\pm$ 112.0) nm for $i = x$, y and z, respectively (n = $3,571$; Figure 4.3 C). Given that the population standard deviations for ζ_x and ζ_y are similar to those for fluorescent beads, and the population standard deviation for ζ_z is approximately that of one pixel, the chromatic shift measurement is much more precise than in metaphase dtCENP-A cells. The correction in the x- and y-coordinates is sufficient, as they each have an inaccuracy (3.9 and -3.8 nm) less than the theoretical accuracy of measurements between green and red fluorescent

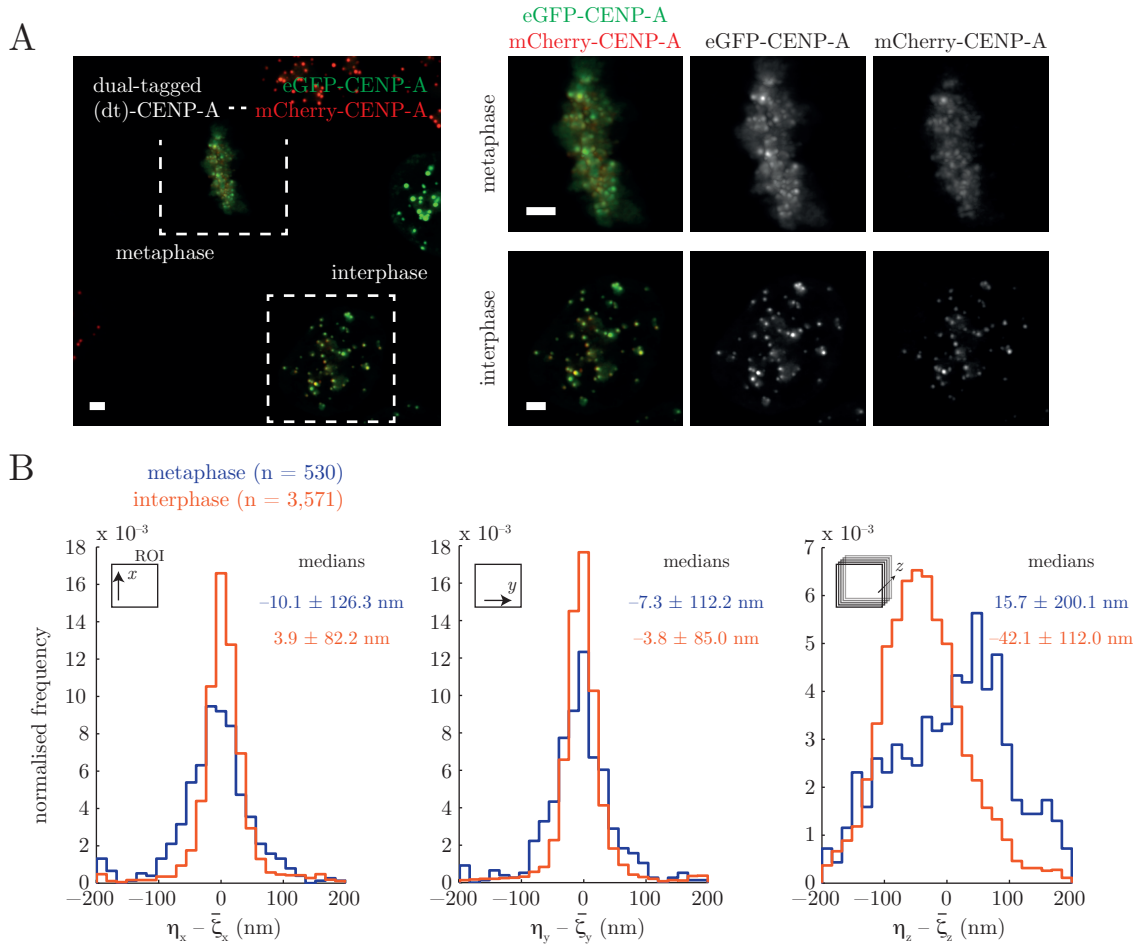

Figure 4.3 *Fluorescent microspheres are unable to accurately correct z-directional chromatic shift in interphase dtCENP-A cells.*
(A) Example image of dual tagged (dt)CENP-A cells in metaphase and interphase. White dashed boxes locate images of metaphase (top row) and interphase (bottom row) cells, showing eGFP-CENP-A (centre), mCherry-CENP-A signal (right), and their merge (left). Scale bars = 2 μm.
(B) Histograms of distributions in measured η_x, η_y and η_z, calculated using metaphase (blue; n = 530) and interphase (gold; n = 3,571) dtCENP-A cells. Images were corrected for chromatic shift using the average of measurements calculated using fluorescent microspheres, $\bar{\xi}_i$. Values given are median ± distribution standard deviation.

spots (5.6 nm; Figure 2.3). However, there is a clear underestimate in the z-component of $\overline{\zeta}$. The underestimate in η_z exposes an inability of the fluorescent microspheres to correct 3D chromatic shift in live interphase HeLa-K cells, and therefore raises doubts that they can correct chromatic shift in metaphase HeLa-K cells. Therefore, given that the dtCENP-A cells contain multiple fluorophores localised to the same protein, the dtCENP-A cell line was examined as a candidate for quantifying the chromatic shift in the cellular environment; the issue is whether the broader distributions of the distance between the two fluorophores in dtCENP-A (Figure 4.3 B, right) as compared to fluorescent microspheres is a problem. Therefore I sought to develop my chromatic shift assay by imaging dtCENP-A cells at 525 nm and 615 nm emission wavelengths.

4.4 Quantifying chromatic shift using dtCENP-A

Given that the eGFP and mCherry signals in dtCENP-A cells were not co-localised in the z-direction based on the chromatic shift calculated from fluorescent microspheres, dtCENP-A cells were investigated for calculating the chromatic shift between 525 nm and 615 nm emission wavelengths themselves. However, η_z as measured in metaphase dtCENP-A cells yielded a broad distribution. To ensure that this wasn't specific to one experiment and therefore one batch of cells, image stacks of $\geq$5 metaphase cells were captured as before over a number of experiments on different days. Similarly, $\geq$5 fields of interphase dtCENP-A cells were also imaged on each occasion. As discussed previously, eGFP was located using Gaussian MMF and the mCherry signal found within a spherical mask of radius 300 nm centred at the GFP spot. The vector, η, was calculated for each kinetochore, again pointing from the eGFP to the mCherry signal. Given that the microscope setup may be subject to drift, the measurements of η were experiment-specific. In order to compare all experiments, each experiment's distributions in η_x, η_y and η_z were normalised to zero by subtracting their median measurement, $\overline{\eta_i}$ for $i \in [x, y, z]$, for that experiment – these distributions will be referred to as centralised distributions. Each of the centralised distributions of η_i, for $i \in [x, y, z]$, as derived from metaphase dtCENP-A cells were very broad when

compared to those derived from interphase dtCENP-A cells, particularly in the z-direction (Figure 4.4). This is confirmed by the population standard deviation, σ_i, for $i \in [x, y, z]$, for each distribution, where interphase cells (blue; n = 36,727) yielded smaller σ_i than those derived from metaphase cells (gold; n = 6,664) (Figure 4.4). Most significantly, σ_z took values 59.1 nm and 120.0 nm for interphase and metaphase cells, respectively, demonstrating that the broad distribution observed previously was not specific to the experiment, and is indeed a consistent issue with metaphase dtCENP-A cells. However, visual inspection of calculated measurements of η highlighted a potential quality issue, as some eGFP and mCherry spots appeared to be incorrectly located in both interphase and metaphase dtCENP-A cells (e.g. Figure 4.5 A). It was therefore crucial that measures for quality control were enforced in order to minimise the occurrences of these events – these events could even be the cause for the broader distribution in measurements of η_z in metaphase cells.

In order to investigate events where η has visibly been incorrectly calculated, vectors for η in the xy-plane were plotted onto images of interphase cells (Figure 4.5 A, yellow vectors). It became apparent that there were two possible reasons for these incorrect measurements: firstly, some eGFP signals were located nearby another eGFP signal of similar signal, however they were accompanied by mCherry signals with very different intensity signals. Sometimes the result of this was that the same mCherry signal was localised for both eGFP spots and the lower-intensity spot ignored (Figure 4.5 A, yellow vector labelled †). This resulted in erroneous measurement of η for both pairs of eGFP-mCherry markers, as the Gaussian MMF assumed that there were two Gaussians contributing to the brighter signal. To reduce the number of these instances, any eGFP spots located within 750 nm in 3D from another eGFP spot were removed from the calculation of chromatic shift (Figure 4.5 B). A second apparent source of erroneous η measurement were extremely low eGFP signals (Figure 4.5 A, yellow vector labelled $*$). These instances were removed by removal of all eGFP spots below a certain intensity threshold, so that all eGFP spots with intensity below 25% of that of the image's maximum eGFP spot intensity were removed from the chromatic

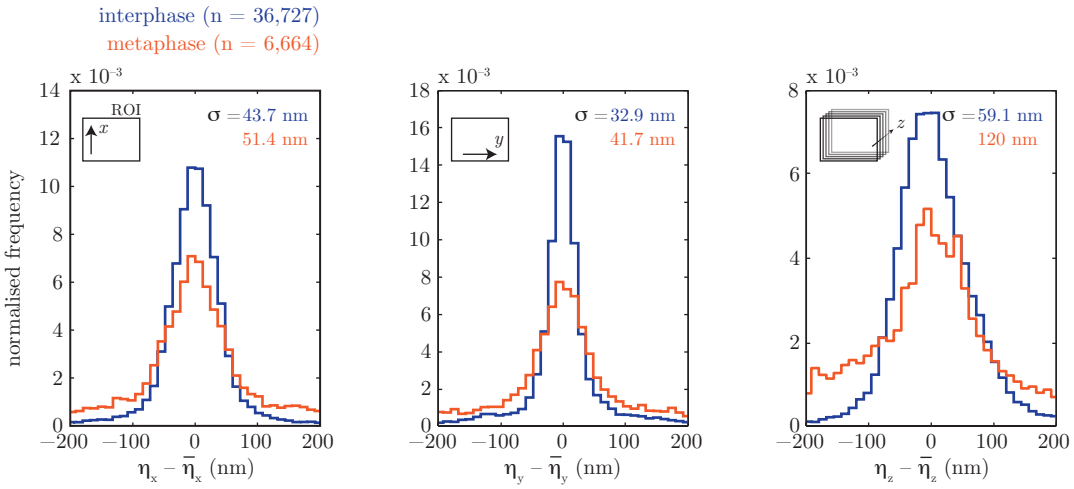

Figure 4.4 *Calculation of inter-marker separation using interphase dtCENP-A cells gives better resolution than metaphase cells.*
Histograms of residuals in measured η_x, η_y and η_z, calculated using interphase (blue; n = 36,727) and metaphase (gold; n = 6,664) dtCENP-A cells. Residuals are calculated relative to the median in each coordinate, i, for each experiment, $\bar{\eta}_i$, resulting in distributions centred at 0. Values given are distribution standard deviations, σ.

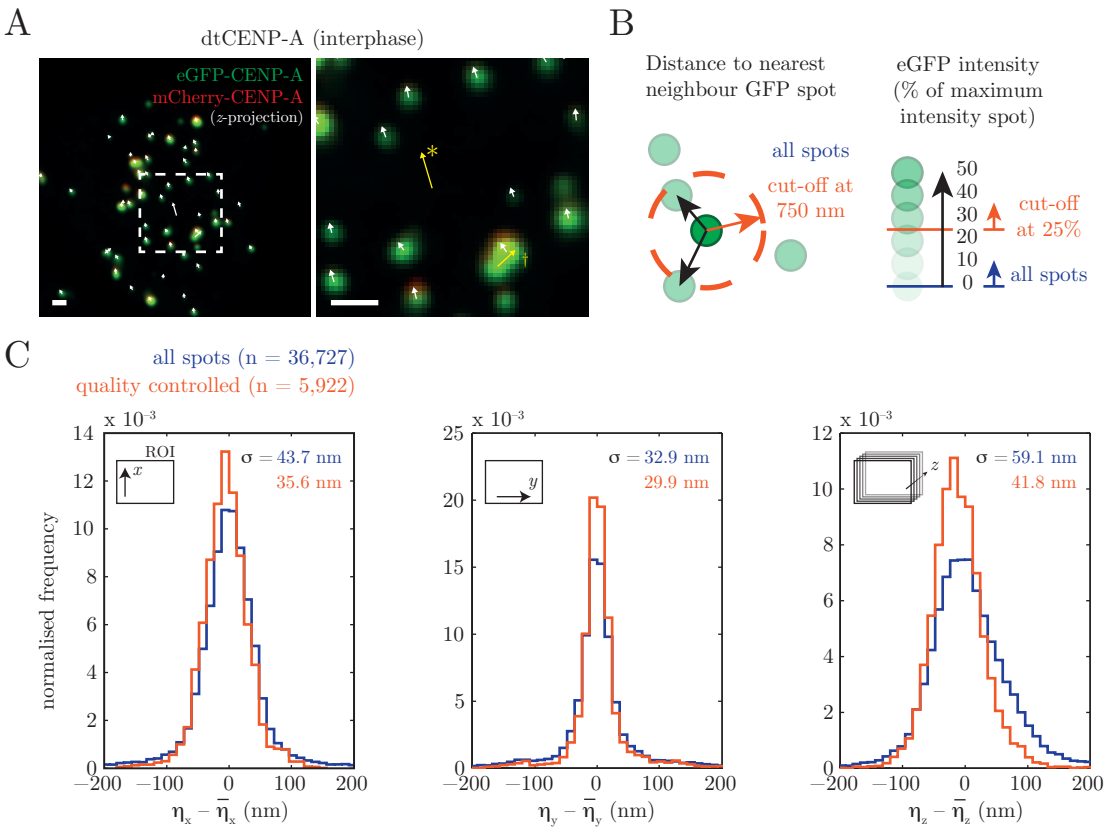

Figure 4.5 *Chromatic shift calculation in interphase cells can be improved by removal of interfering and low-brightness spots.*
(A) Image of interphase dtCENP-A showing the chromatic shift between eGFP and mCherry signal. White arrows point from eGFP to mCherry signal. Yellow arrows demonstrate false positive measurements: (*) vector originating from a GFP spot of low intensity; (†) vector originating from GFP signal not distinct from a neighbouring GFP spot. Scale bars = 750 nm.
(B) Quality control imposed on GFP signal, so that: (left) GFP spots must be separated by at least 750 nm; and (right) GFP signal intensity must be higher than 25% of the maximum intensity spot in the image.
(C) Histograms of residuals in measured η_x, η_y and η_z, calculated using all raw data (blue; n = 36,727) and quality-controlled data (gold; n = 5,922) from interphase dtCENP-A cells. Residuals are calculated relative to the median in each coordinate, i, for each experiment, η_i, resulting in distributions centred at 0. Values given are standard deviation, σ, of the distribution.

shift calculation (Figure 4.5 B). Indeed, centralised distributions of η_i in interphase cells, for $i \in [x, y, z]$, were improved after quality control, where standard deviations of the centralised distributions, σ_i, decreased by 14.9%, 9.1% and 29.3% for $i \in [x, y, z]$, respectively (Figure 4.5 C). Quality control therefore proved incredibly important in ensuring accurate determination of the chromatic shift using dtCENP-A cells, yielding its biggest improvement in the z-direction. I hypothesised then that this method of quality control could also help improve the standard deviations of centralised distributions of η in metaphase dtCENP-A cells, and therefore the accuracy of the median measurement of η.

In order to check initially whether restricting nearest-neighbour distance and eGFP intensity in η measurements from metaphase dtCENP-A cells would improve the accuracy of their measurement, vectors of η in the xy-plane were plotted on images of metaphase dtCENP-A cells (Figure 4.6 A, yellow vectors). Like interphase cells, erroneous measurements appeared to occur as a consequence of both the localisation of a neighbouring mCherry signal rather than its own counterpart (Figure 4.6 A, yellow vector labelled †), and also vectors originating from eGFP spots with low intensity (Figure 4.6 A, yellow vector labelled $*$). To check whether removal of these erroneous measurements could also decrease the η_i ($i \in [x, y, z]$) distribution's variance, and perhaps rectify the large uncertainty in z-directional η measurements, quality control was imposed on metaphase dtCENP-A cell data. The criteria were slightly loosened as the amount of metaphase cell data was much smaller than for interphase cells (n = 6,664 vs. 36,727, respectively): eGFP spots had to be at least separated by 750 nm and eGFP spots with an intensity smaller than 33% of the maximum eGFP spot intensity were removed (Figure 4.6 B). Comparing centralised distributions in η_i between metaphase cells before and after these measures of quality control yielded smaller standard deviations in η in x, y and z, where σ_i decreased by 30.7%, 13.7% and 29.2% for $i \in [x, y, z]$, respectively (Figure 4.6 C). However, despite the decrease in population standard deviation measured for η_z, the distribution was still broad whilst appearing to contain multiple peaks. Therefore, even after quality control, z-directional mea-

surements of chromatic shift, η_z, from metaphase dtCENP-A cells had a clear large standard deviation (Figure 4.6 C, right). In contrast, population standard deviations of chromatic shift, η_i ($i = [x, y, z]$), from interphase dtCENP-A cells were improved after quality control to within almost half a pixel in each coordinate (Figure 4.5 C).

This difference may be a result of the difference between cellular environment within interphase and metaphase cells – metaphase cells contain a well-organised spindle and condensed DNA in chromosomes, whereas interphase cells contain a nuclear envelope, outside which is the main population of microtubules. Therefore, light may experience chromatic shift to a different extent in metaphase as compared to interphase cells. On the other hand, the average axial chromatic shift (η_x and η_y) calculated in both interphase and metaphase cells for a single experiment were consistent to within measurement accuracy (Figure 4.3). The only difference measured between each cell type was in η_z. I therefore wanted to utilise the superior precision in measurement of chromatic shift in interphase cells to apply to each experiment in § 5. Firstly, I sought to optimise the precision of measurements of chromatic shift in interphase dtCENP-A cells.

4.5 Spatial chromatic shift: The xy-plane

Another anomaly was observed in interphase dtCENP-A cells that was potentially contributing to the η variance; for example there is a suggestion of bi-modality in the ζ_y distribution (Figure 4.7 B, blue). This bi-modality was also observed in images of fluorescent microspheres imaged on the same day (Figure 4.7 B, gold). This observation hints that there are regions of the xy image plane that have different y-directional chromatic shift. In order to investigate this, images of interphase dtCENP-A cells were divided in the xy image plane into 5×5 equally-sized regions, and the average axial chromatic shift, ζ_{xy}, measured within each region. Arrows representing the vector for the average $\zeta_{xy} = [\zeta_x, \zeta_y]$ were plotted at the centre of each region and scaled in length dependent on the vector's magnitude. It is clear that chromatic shift is non-constant across the image plane (Figure 4.7 D). The change in chromatic shift across the image

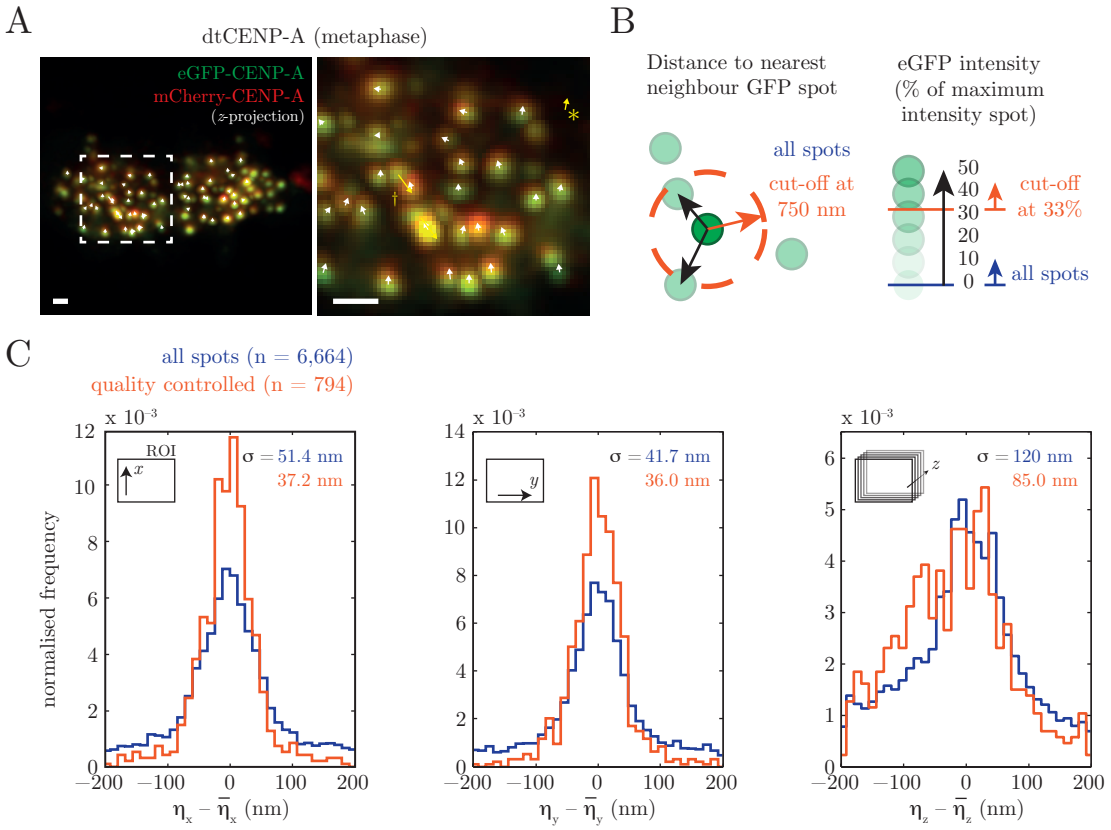

Figure 4.6 *Only axial chromatic shift calculation in metaphase cells can be improved by removal of interfering and low-brightness spots.*
(A) Image of metaphase dtCENP-A showing the chromatic shift between eGFP and mCherry signal. White arrows point from eGFP to mCherry signal. Yellow arrows demonstrate false positive measurements: (*) vector originating from a GFP spot of low intensity; (†) vector originating from GFP signal not distinct from a neighbouring GFP spot. Scale bars = 750 nm.
(B) Quality control imposed on GFP signal, so that: (left) GFP spots must be separated by at least 750 nm; and (right) GFP signal intensity must be higher than 33% of the maximum intensity spot in the image.
(C) Histograms of residuals in measured η_x, η_y and $\eta_{z,}$ calculated using all raw data (blue; n = 6,664) and quality-controlled data (gold; n = 794) from metaphase dtCENP-A cells. Residuals are calculated relative to the median in each coordinate, i, for each experiment, $\bar{\eta}_i$, resulting in distributions centred at 0. Values given are standard deviation, σ, of the distribution.

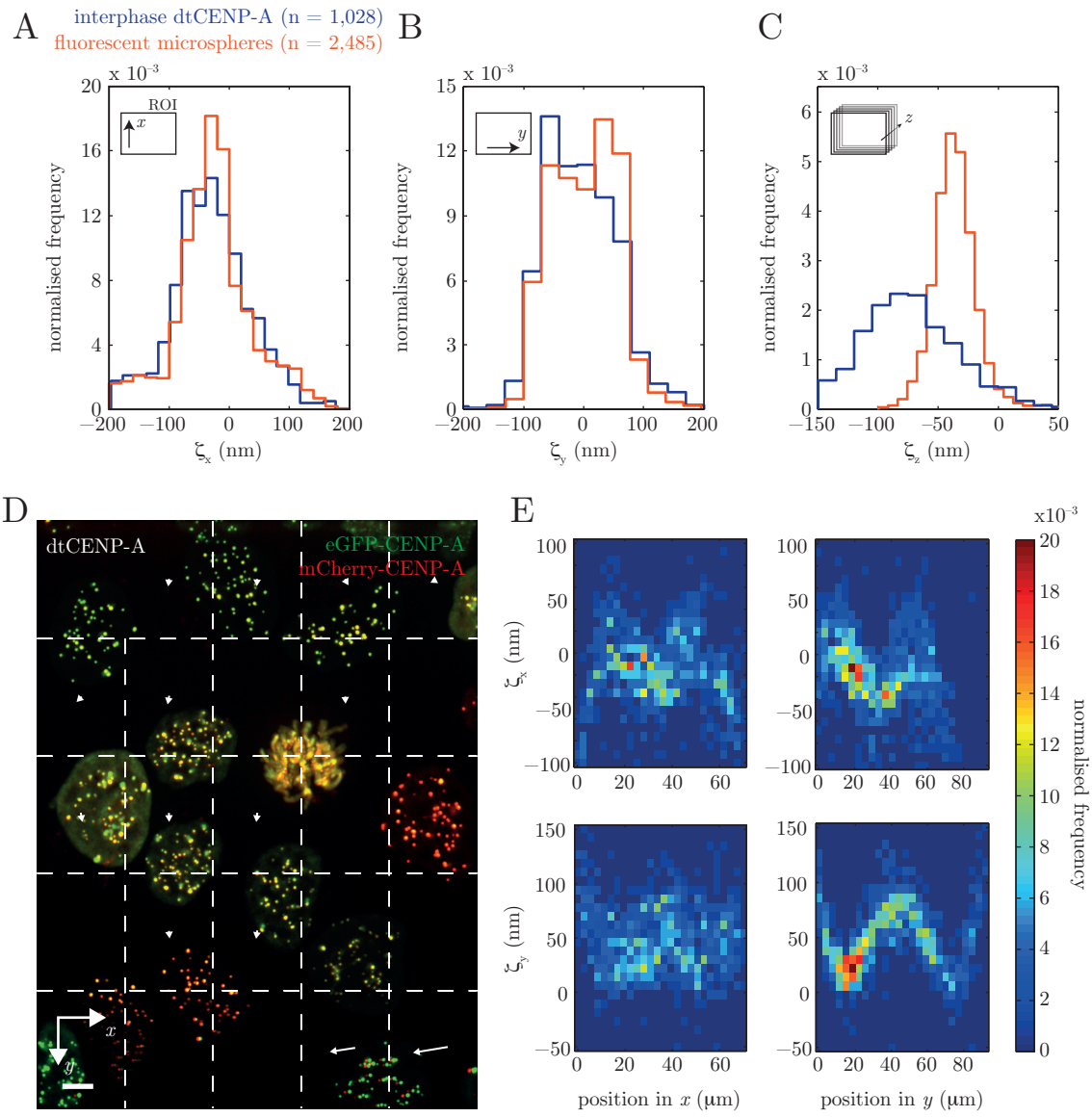

Figure 4.7 *Bimodal distributions in* ζ *are produced by non-linearity of* ζ *across the* xy *plane.*
(A,B,C) Histograms of: (A) ζ_x; (B) ζ_y; and (C) ζ_y demonstrating potential bimodal distributions in chromatic shift calculation, observed in distributions of ζ measured in both interphase dtCENP-A cells (blue; n = 1,028) and fluorescent microspheres (gold; n = 2,485).
(D) Regional chromatic shift between eGFP and mCherry across *xy* imaging plane of dtCENP-A cells. White arrows are averaged vectors pointing from eGFP to mCherry signals for each region. Scale bar = 5 μm.
(E) 2D histograms of ζ_i, i ∈ [*x*,*y*], against position in the j'th coordinate, j ∈ [*x*,*y*], from images of dtCENP-A (n = 1,028). Red denotes higher frequency, blue denotes lower frequency.

plane could also be visualised by plotting 2D histograms of chromatic shift in the x- or y-direction against position in each coordinate (Figure 4.7 E). The 2D histograms of ζ_y against position reveal the source of the bi-modal distribution: ζ_y exhibits a sinusoidal-like distribution with y-direction, so that ζ_y takes values ranging 100 nm depending on whether the fluorescent microsphere is at the top, centre or bottom of the image plane. A sinusoidal pattern could be a result of the two-camera alignment method built into Volocity®, where the patterns observed may be the residual signal after minimisation of misalignment using sinusoidal mathematical formulae. Nevertheless, it is important to identify these variations and adjust imaging protocols accordingly. This analysis suggests that chromatic shift correction requires a non-linear spatial map for the chromatic shift. However if images are within a small region of the full image plane, it may be possible to assume that the chromatic shift is constant within that region. This may be possible for correction of single cells which can be localised within a smaller region of the full image plane. Therefore I sought to investigate whether chromatic shift appears constant within a region of the image plane large enough to image all eGFP-CENP-A spots once in a metaphase plate during mitosis.

Metaphase cells can be imaged within a region a ninth of the area of the full image plane (Figure 4.8 A, shown for example in the centre when the image plane is divided into 3×3 regions). This means that, should chromatic shift be constant within a region, metaphase cells can be placed within that region and potentially more precisely corrected for chromatic shift. In order to minimise variation in ζ in each the x- and y-coordinates, the profiles observed in the 2D histograms in Figure 4.7 E must be horizontal. For example, in the bottom right panel of Figure 4.7 E, the profile in ζ_y against y-position is steepest at the extremes of the y-coordinate. However, it reaches a stationary point in the centre of the image plane. Therefore mitotic cells are best located at the centre of the image y-axis. Furthermore, observation of ζ_x in the x-direction (Figure 4.7 E, top left panel) suggests that there is a relatively constant chromatic shift across all values of x-coordinate (except for the extreme left and right of the image plane). However, ζ_x has a smaller spread of values within the central

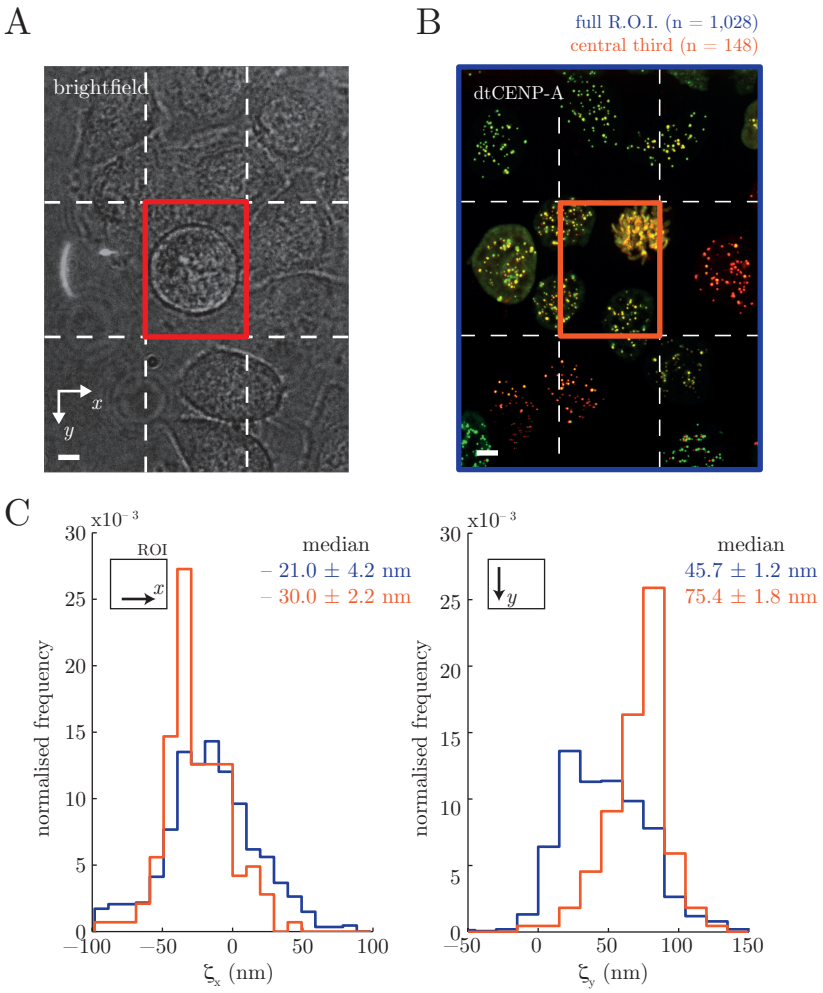

Figure 4.8 *Chromatic shift correction at centre of ROI.*
(A) Brightfield image of metaphase cell manually positioned at the centre of the imaging plane. White dashed lines divide each of the x and y coordinates into three regions, and the red box surrounds the central region. Scale bar = 5 μm.
(B) Image of dtCENP-A cells annotated as in (A).
(C) Histograms of ζ_x (left) and ζ_y (right) comparing all spots in the imaging plane (blue; n = 1,028) and spots in the central region (gold; n = 148). Values given are median ± standard error.

third, and therefore a mitotic cell located within this region of the image x-axis may incur relatively constant chromatic shift. Based on this hypothesis, I wanted to check that the bi-modality in the distribution of measurements of y-directional chromatic shift decrease, ideally to a uni-modal distribution when restricted, within the central region.

Distributions of ζ_x and ζ_y in the central third were compared to measurements made across the entire image plane (Figure 4.8 C). After restricting chromatic shift measurements to the central region, the distribution in ζ_y appeared to contain a single peak, which resulted in a large change in the measured median for ζ_y. The bimodal distribution in ζ_y measured across the image plane has a median ($\pm$ standard error) measurement of 45.7 ($\pm$ 1.2) nm (n = $1,028$), however median y-directional ζ in the central region of the image plane is 75.4 ($\pm$ 1.8) nm (n = 148; Figure 4.8 C) – nearly a 30 nm difference, corresponding to nearly half a pixel. Additionally, the distribution standard deviation of ζ_y decreased from 38.5 nm for measurements across the image plane, to 21.9 nm in the central third, demonstrating that the measurement of ζ_y in the central third of the image plane does indeed provide a more precise measurement of ζ. A final note is that the precision in the measurement of of ζ_x was also greatly improved – the distribution standard deviation of ζ_x across the entire image plane was 134.7 nm, which decreased dramatically to 26.8 nm when measured within only the central region. This was accompanied by a change in median ($\pm$ standard error) measurement of ζ_x from -21.0 ($\pm$ 4.2) nm when measured across the entire image plane (n = $1,028$), to -30.0 ($\pm$ 2.2) nm when restricted to the central region (n = 148), again demonstrating the heterogeneity in the chromatic shift across the image. Therefore, limiting chromatic shift measurements to a region sufficient to accommodate a mitotic HeLa-K cell provides a sufficient approximation of chromatic shift measured in both x- and y-coordinates microscope coordinates. Given that chromatic shift can vary dependent on its localisation in the xy image plane, it seems natural to also ask if chromatic shift is dependent on focal depth, i.e. dependent on the microscope's z-coordinate. It is especially important here as the interphase dtCENP-A cells being used for deter-

mination of chromatic shift are located in a different focal plane to the centre of the metaphase cells requiring correction of chromatic shift. Interphase cells are relatively flat to the glass cover slip surface, whilst cells become round at the start of mitosis and therefore their centre of mass moves upwards away from the surface. I therefore decided to investigate the possibility that chromatic shift may change dependent on position in the z-direction.

4.6 Spatial chromatic shift: z-depth

I wanted to examine whether chromatic shift, ζ, in each the microscope x-, y- and z coordinates was dependent on focal depth. An extrapolation of ζ, specific to each coordinate, might be required if ζ changes with z-coordinate. Furthermore, this could possibly explain why fluorescent microspheres, which are located on the glass cover slip (Figure 4.9 A), cannot correct for z-directional chromatic shift, ζ_z, in interphase dtCENP-A cells (Figure 4.3 B). In order to determine whether ζ changes with microscope z-coordinate, the distance of the eGFP spot centre relative to the glass cover slip on which cells are grown is needed. This was approximated by using the lowest spot detected (smallest value of z) in each image as $z = 0$, i.e. the location of the glass cover slip. This means that eGFP spots located within a metaphase cell would have a larger value of z-coordinate on average than an eGFP spot located within an interphase cell.

To visualise any changes in ζ with focal depth, 2D histograms were plotted of ζ in each the microscope x-, y- and z-coordinate against position in z. Measurement of correlation coefficients, r, for each coordinate yielded little correlation between x- and y-directional chromatic shift and position in the focal plane; the correlation coefficients measured were $r = 0.070$ for ζ_x, and $r = 0.076$ for ζ_y, with probabilities of significance $p = 0.025$ and $p = 0.014$, respectively. However, there was a much stronger correlation between ζ_z and z position, where the correlation coefficient was $r = 0.332$, which was highly significant, $p < 10^{-4}$. The low correlation of the x- and y-directional chromatic shift with z-position demonstrates that ζ_x and ζ_y do not vary much with focal depth. However the observed correlation between ζ_z and z-position demonstrates that

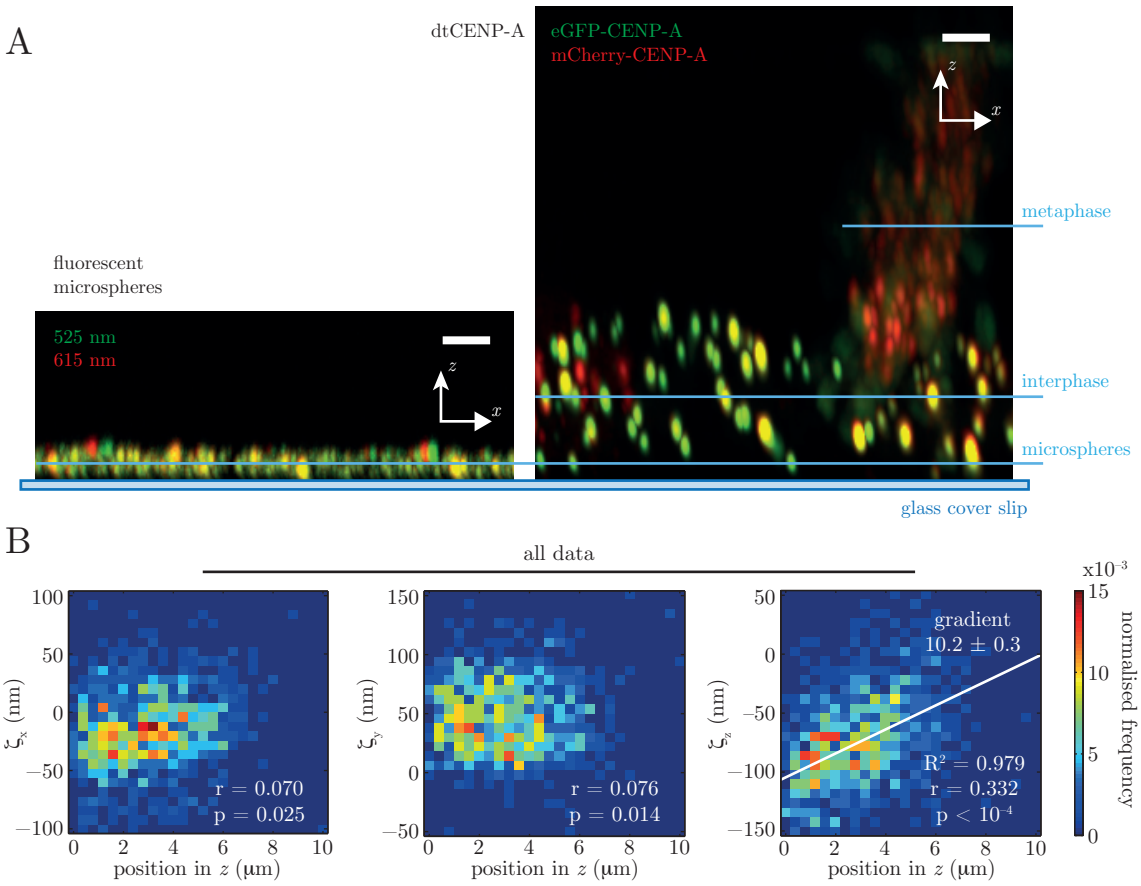

Figure 4.9 *z-directional chromatic shift correction varies with depth.*
(A) Dual colour fluorescence images of 200 nm-diameter fluorescent microspheres (left) and dtCENP-A cells (right) in the *xz* plane. Horizontal blue lines are located in the focal plane at the centre of metaphase cells, interphase cells, and microspheres. Location of glass cover slip has been approximated manually. Scale bar = 2 μm.
(B) 2D histograms of ζ_x (left), ζ_y (centre), and ζ_z (right) against position in microscope *z*-coordinate, measured upwards from the glass cover slip, for all spots in the imaging plane (n = 1,028). Red indicates high frequency, blue indicates low frequency. White lines are best fit lines by minimising absolute residuals, and values given are gradients ± 95% confidence interval, coefficients of determination, R^2, correlation coefficients, r, and probability of significance, p.

ζ_z changes with focal depth – this means that there may be a required adjustment in ζ_z, but not ζ_x or ζ_y, to properly correct for the chromatic shift in metaphase cells located further away from the glass cover slip. The dependence of ζ_z with z is consistent with a linear increase with sample depth, and therefore a straight line can be fit through the 2D histogram in order to calculate a projected value for chromatic shift at larger values of ζ. Fitting a straight line through the data, by minimising absolute residuals, for ζ_z against z-position yielded a gradient ($\pm$ 95% confidence interval) of 10.2 $\pm$ 0.3 nm μm^{-1}. This reveals that the value for ζ_z measured in interphase dtCENP-A cells needs to be increased in order to correct for chromatic shift observed in metaphase dtCENP-A cells at larger z-coordinates. Additionally, setting the z-coordinate of the lowest GFP spot detected to zero yielded a ζ_z-intercept, $\zeta_0 = -104.5$ (i.e. the value for ζ_z at the cover slip). The correction can be calculated using the average distance between interphase and metaphase cells in the z-direction – therefore I determined the average distance of interphase and metaphase dtCENP-A cells away from the glass cover slip.

In order to calculate a correction for ζ_z between the z-coordinates of interphase and metaphase cells, the distance between these focal planes needs to be multiplied by the gradient of the straight line through the 2D histogram of ζ_z against z-position (Figure 4.9 B). The median value of ζ_z calculated for dtCENP-A interphase cells, using only points within the central third of the xy image plane, was -79.8 ± 5.2 nm (Figure 4.10 A). This value for ζ_z corresponds to the centre of all interphase cells. Using the linear relationship calculated in Figure 4.9 B between ζ_z and position in z,

$$\zeta_z = 10.2 \times (z\text{-position}) - 104.5,$$

the centre of interphase cells can be calculated as 2.42 μm above the cover slip. An interesting observation is that the z-directional chromatic shift calculation made using fluorescent microspheres had a median of -38.8 nm, which, using the same equation in reverse, would imply the microspheres are located 6.44 μm above the cover slip. Given that this is highly unlikely, there must be additional factors (such as refractive index) other than ζ dependence on z that results in an inaccurate calculation of ζ using the fluorescent microspheres.

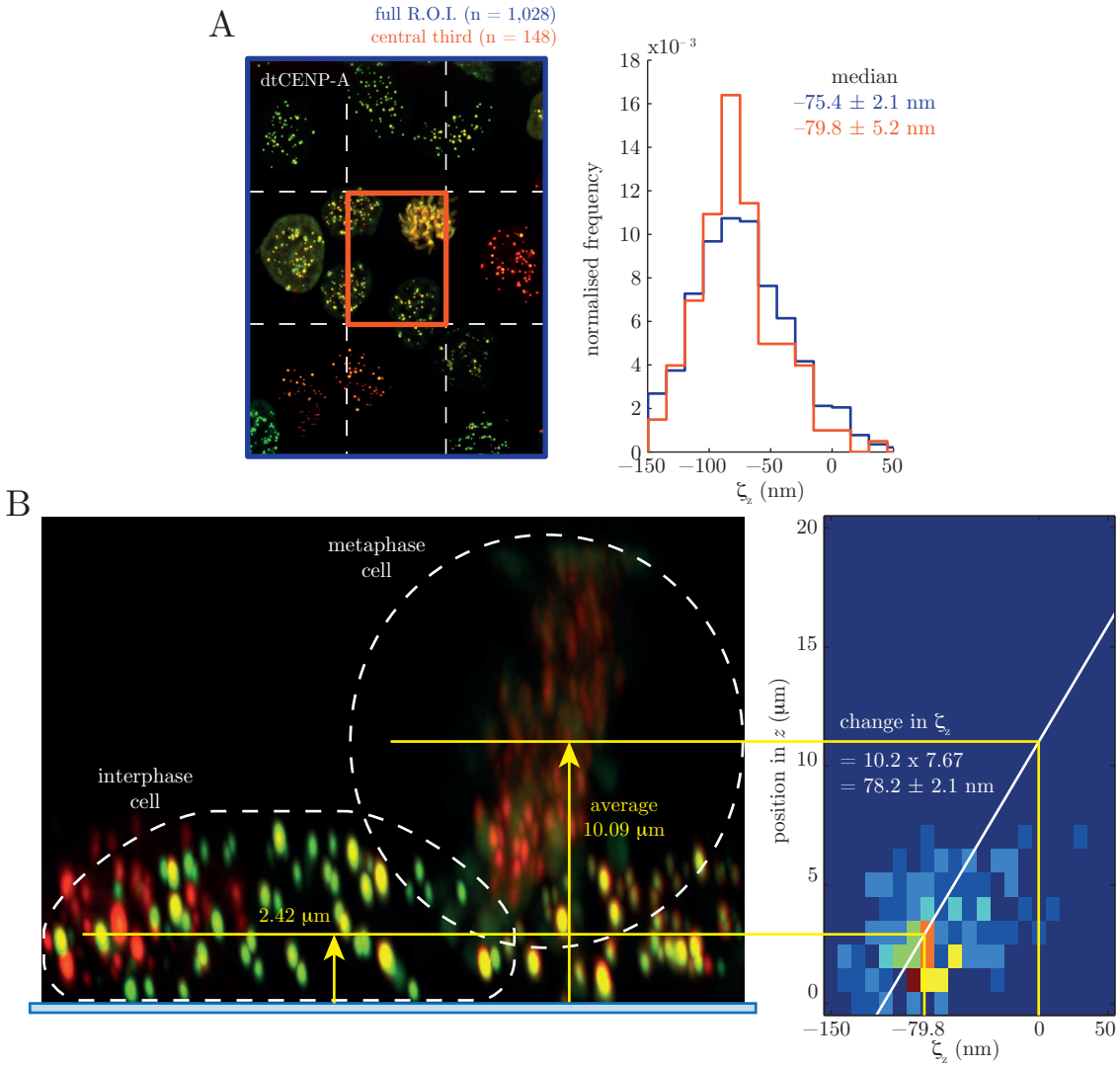

Figure 4.10 *Adjustment of* z*-directional chromatic shift correction from interphase to metaphase cells' focal plane.*
(A) Fluorescence image of dtCENP-A cells in *xy* plane with central region annotated, and histogram of ζ_z for all spots in the imaging plane (blue; n = 1,028) and spots in the central *xy* region (gold; n = 148). White dashed lines divide each of the *x* and *y* coordinates into three regions, and the red box surrounds the central region. Values given are medians ± standard error. Scale bar = 5 µm.
(B) Fluorescence image of dtCENP-A cells in the *xz* plane, and 2D histogram of position in the *z*-direction, measured upwards from the glass cover slip, against ζ_z. Closed white dashed lines show the approximate outline of an interphase and a metaphase cell. Full white line is the best fit line by minimising absolute residuals, as calculated in Figure 4.9 B. The bottom yellow line is located at the average centre of all interphase cells, the top yellow line at the average centre of metaphase cells. Yellow values given are average distance of interphase cells above the glass slide, and average distance between these two lines (n = 12). White values given are (gradient of white line x average distance between interphase and metaphase cell centres) ± 95% confidence interval.

In order to calculate the cell-specific distance of metaphase cells from the glass cover slip for each chromatic shift measurement, the z-depth as determined by the focus drive itself would instead be correlated with ζ_z. However, this information was not included in image metadata or Volocity® raw data. Therefore, I manually measured the distance between metaphase cells and the glass cover slip using fluorescence imaging. Image stacks of metaphase dtCENP-A cells were imaged over 24 μm in z. This gives a sufficient enough range in z-direction to ensure that both the glass cover slip and metaphase cells were incorporated within image stacks. Images were then produced in the xz- or yz-plane, and the glass cover slip located at the eGFP spot closest to the bottom of the image (Figure 4.10 B). Circles manually centred at metaphase cells were drawn to give the central point of the metaphase plate. The distance between the lowest GFP spot and the circle's centre gives the distance between metaphase cells and the cover slip. Distance measurements were calculated over 12 images (Figure 4.11), giving an average distance of metaphase cell centres above the cover slip as 10.09 μm (n = 12; Figure 4.10 B). Given the calculated distance of interphase cells above the cover slip, 2.42 μm, the average distance measured between interphase dtCENP-A cells and metaphase dtCENP-A cells was 7.67 μm (Figure 4.10 B). On the assumption that metaphase cells are located on average this distance from the glass cover slip across all experiments, the adjustment to interphase cell-derived ζ_z required for use in metaphase cells is:

$$\begin{aligned}&(\text{gradient of } \zeta_z \text{ vs. } z \text{ position}) \times (\text{distance from interphase to metaphase})\\ &\qquad = 10.2 \times 7.67\\ &\qquad = 78.2 \pm 2.1 \text{ nm.}\end{aligned}$$

Therefore, given that the median measurement of ζ_z from interphase cells was $\zeta_z = -79.8$ nm, the corrected value for ζ_z for use in metaphase cells was $-79.8 + 78.2 = -1.7$ nm. This was demonstrated in graphical form by plotting a 2D histogram of each eGFP spot's position in z against the z-directional chromatic shift, ζ_z, for all eGFP spots within the central region of the xy image plane (Figure 4.10 A). By plotting the calculated line of best fit through the data, and extrapolating up to the average centre

of metaphase cells, the value for ζ is as expected.

This adjustment gives a final median ($\pm$ standard error) measurement of chromatic shift, $\zeta = [-30.0, 75.4, -1.7] \pm [2.2, 1.8, 5.6]$ nm, where the z-directional standard error was calculated as the propagation of the standard error in median measurement (5.2 nm) and the error in adjustment of ζ_z (2.1 nm). A final check will be required to ensure that this does indeed correct for chromatic shift observed in metaphase HeLa-K cells expressing both green (e.g. eGFP) and red (e.g. mCherry, tagRFP) FPs. However, given that the distribution standard deviation of ζ_z measured using metaphase dtCENP-A cells was on the scale of z-directional image sampling, metaphase cells could not be used to mediate the final check for chromatic shift accuracy using this assay. Instead, average kinetochore pair conformation within a mitotic spindle will be used to determine accuracy of chromatic shift (see § 5.4).

4.7 Summary

I have developed an assay to use interphase cells expressing both eGFP and mCherry fluorophores attached to CENP-A to calculate the 3D chromatic shift correction appropriate for live cell imaging. This assay utilises specific regions of the image plane in order to minimise error in the chromatic shift correction. It also corrects for a dependence of the z-directional chromatic shift on the height above the glass cover slip, important here in extrapolating the correction to metaphase cells. All calculations of chromatic shift are given in Table 4.1. I have also demonstrated that pre-prepared fluorescent microspheres, such as the example used in this study, may be unsatisfactory for measurement of 3D chromatic shift correction of live cells – in fact they were unable to correct either interphase or metaphase HeLa-K cells. Not only do the microspheres suffer due to a dependence of z-directional chromatic shift on focal plane, but they exhibit a different value for ζ_z than that expected based on their location on the glass cover slip surface. This means that other methods used for 3D chromatic shift measurement, such as fluorescent microspheres suspended in agarose should be checked for their ability to correction chromatic aberration in live cells.

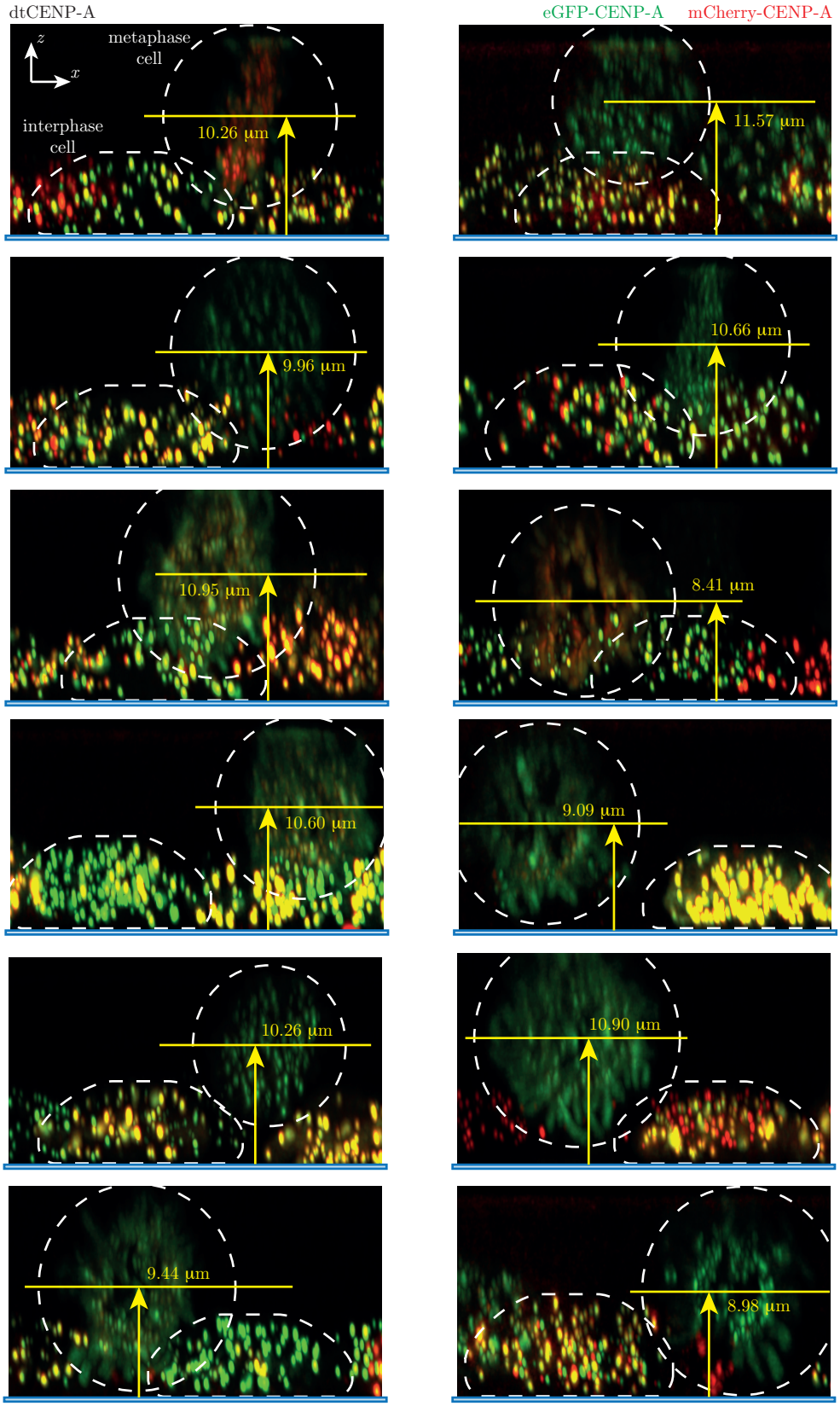

Figure 4.11 *Gallery of separation of metaphase and interphase focal planes.* Fluorescence images of dtCENP-A cells in *xz* plane. Closed white lines show approximate outline of interphase and metaphase cells. Yellow lines denote average centre of denoted metaphase cells. Values given are distance measured between the two yellow lines: average = 10.09 µm.

However, the assay developed here is not perfect. Ideally the chromatic aberration correction should be determined in cells with a similar shape to the cells under study, e.g. using metaphase dtCENP-A cells to calibrate the chromatic aberration would be preferable to using interphase cells, which are closer to the cover slip. This would remove the requirement for an adjustment in ζ_z between the interphase and metaphase cell focal planes. However, interphase cells provided a more accurate and precise system for calibration due to higher intensity of eGFP and mCherry signals, as z-directional chromatic shift measured in metaphase cells yielded a relatively broad distribution (Figure 4.3 A). This difference in intensity is likely due to the subset of interphase cells in G1 phase which contain twice the levels of CENP-A as those just prior to G2, so that each G2 and mitotic kinetochore contains half the CENP-A present at the centromere of the original chromosome during its preceding G1 phase (Jansen *et al.*, 2007; Schuh *et al.*, 2007). Additionally, unlike the eGFP-CENP-A cell line used in § 5 to measure intra-kinetochore distances, a large number of metaphase cells within the dtCENP-A cell line had chromosomes with eGFP signal visible along chromosome arms (Figure 4.3 A), which is a consequence of over-expression of exogenous eGFP-CENP-A beyond that which can be localised at kinetochores. A benefit of both G1 and G2 interphase cells is that their chromosomal DNA is not yet condensed, and any over-expressed eGFP-CENP-A signal is therefore dispersed throughout the cell. The increased intensity of eGFP-CENP-A at G1 kinetochores and the dispersion of over-expressed eGFP-CENP-A in interphase cells increase the signal-to-noise ratio of kinetochore signals during interphase compared to metaphase.

In order to develop a system whereby metaphase cells can be used for calibration of the chromatic shift, cells within the dtCENP-A cell line can be selected for lower eGFP-CENP-A expression levels. With eGFP- and mCherry-CENP-A signals located at only the kinetochore, spot finding would be improved and distance measurements made more accurate. Another option is to utilise fluorescent dyes that target specific constructs, e.g. SNAPtag or HaloTag. Production of a HeLa-K cell line expressing HaloTag-CENP-A, so that it is only located at kinetochores, would allow targeting of fluorescent dyes

to CENP-A. The simultaneous addition of both green and red fluorescent dyes would allow imaging of both colours at the same locus. This approach would require the cells to express only one exogenous protein, unlike the double-stable dtCENP-A cell line which expresses two. Furthermore, different combinations of fluorescent dyes could be used simultaneously to correct for the chromatic shift between, say, red and far red wavelengths. Nevertheless, with an accurate and precise cell-based chromatic shift correction assay using dtCENP-A cells, it was now possible to accurately measure intra-kinetochore distances in metaphase HeLa-K cells expressing both eGFP-CENP-A and Ndc80-tagRFP.

Drug Treatment	Date	Chromatic Shift, ζ (nm)			n
		ζ_x	ζ_y	ζ_z	
Untreated	29/10/2014	1.2 ± 13.0	5.2 ± 10.8	–18.7 ± 39.4	114
	30/10/2014	12.6 ± 15.4	41.3 ± 11.7	17.4 ± 36.1	139
	12/11/2014	3.5 ± 30.6	10.7 ± 23.0	7.6 ± 55.8	164
	23/01/2015	–54.5 ± 26.1	10.3 ± 18.4	–12.1 ± 32.8	157
	06/03/2015	12.6 ± 20.7	–0.5 ± 14.5	7.2 ± 43.0	91
	13/03/2015	–1.8 ± 19.5	0.7 ± 25.8	9.1 ± 36.9	108
	02/04/2015	1.7 ± 21.6	–7.7 ± 25.9	–8.4 ± 43.3	191
3µM nocodazole	19/03/2015	4.6 ± 21.0	–37.0 ± 16.1	–11.8 ± 42.3	143
	26/03/2015	10.1 ± 11.8	–27.0 ± 10.7	11.8 ± 32.3	48
	22/04/2015	4.4 ± 23.4	–4.3 ± 27.2	5.1 ± 40.9	62
100nM nocodazole	10/03/2015	–1.1 ± 20.7	–28.8 ± 15.6	–2.9 ± 36.7	76
	14/03/2015	–1.8 ± 19.5	0.7 ± 25.8	9.1 ± 36.9	108
	24/04/2015	–6.0 ± 33.3	12.7 ± 33.5	–0.6 ± 37.6	210
10µM taxol	12/01/2015	–29.5 ± 21.5	18.9 ± 15.4	4.7 ± 41.1	72
	06/02/2015	–49.0 ± 18.0	–12.5 ± 16.0	–0.2 ± 32.6	97
	10/02/2015	–41.7 ± 23.6	–9.3 ± 18.2	–2.5 ± 33.5	137
	11/02/2015	–30.8 ± 21.6	12.0 ± 16.1	–6.1 ± 40.4	75
	13/02/2015	–44.7 ± 21.9	40.2 ± 13.1	24.0 ± 31.3	86

Table 4.1 *Calculated chromatic shift, ζ, for each experiment in § 5.*

Chapter 5

Kinetochores Are Swivel Joints That Mediate Microtubule Attachments

5.1 Background

In an attempt to understand how kinetochores read their environment in order to regulate dynamics during mitosis, recent studies have measured intra-kinetochore structure with dynamics. This is typically achieved by tagging multiple kinetochore proteins with different coloured fluorescent markers. The kinetochore is smaller than the diffraction limit of light, and therefore each kinetochore protein appears as a point source within the kinetochore structure. The two fluorescent markers then allow measurement of intra-kinetochore distance, Δ.

However, one problem with this approach is the variety in experimental setup. Furthermore, there are a number of different analysis methods used, and therefore multiple different results are derived for the same distance measurement (Figure 1.8). For example, due to the difficulty in producing stable cell lines over-expressing two exogenous genes encoding different kinetochore proteins, most analyses of this kind are performed in chemically-fixed cells. This means that the dynamics of intra-kinetochore distances have not been investigated in detail. Furthermore, of the few studies investigating intra-kinetochore distances in live cells, Δ has either been measured in 2D, or measured under the pretence of a co-linear approximation. The measurement us-

ing co-linear approximation, called Δ_{1D}, requires that, for a kinetochore pair, all four fluorescent markers (that is one of each fluorescent protein (FP) on each kinetochore) are located along a common axis. However, this measurement is useful as it eliminates the need for correcting images of two different wavelengths for chromatic shift. Nevertheless, regardless of measurement method, upon bi-orientation, kinetochores are stretched, so that intra-kinetochore distance decreases when inter-kinetochore tension is lost (Maresca & Salmon, 2009; Uchida *et al.*, 2009; Wan *et al.*, 2009; Tauchman *et al.*, 2015; Etemad *et al.*, 2015; Drpic *et al.*, 2015; Magidson *et al.*, 2016). However, this has been challenged both by the observation that the kinetochore is non-compliant under force (Suzuki *et al.*, 2014), and that PtK2 kinetochores moving poleward are counter-intuitively compressed compared to away-from-the-pole (AP) kinetochores (Dumont *et al.*, 2012).

However, one limitation to all of these measurements is they are not measured in 3D in live cells. To this end, I sought to develop a novel 3D assay to perform live cell imaging of two different fluorescent markers bound to different proteins within the kinetochore, both fluorophores imaged simultaneously using a dual camera setup. To enable this, in § 4 I developed an assay to accurately calculate chromatic shift in 3D.

5.2 Establishing the assay

In order to measure intra-kinetochore distances, Ndc80, a subunit of the NDC80 complex, was chosen as an outer kinetochore marker for tracking outer kinetochore dynamics relative to eGFP-CENP-A (an inner kinetochore marker) 4D tracking assay. These kinetochore markers allow measurement of a direct linkage between the centromeric chromatin (CENP-A) and the microtubule-binding apparatus (Ndc80-C). A plasmid containing Ndc80 with tagRFP attached to its carboxy (C)-terminus was transiently transfected into HeLa-Kyoto (HeLa-K) cells expressing eGFP-CENP-A. The incorporation of a fluorophore to the carboxy-terminus of Ndc80 could perturb its function; thus I determined using detailed analyses of kinetochore dynamics that it did not cause any perturbations (see § 3.1). Upon 24 hr transient transfection of Ndc80-tagRFP, visual

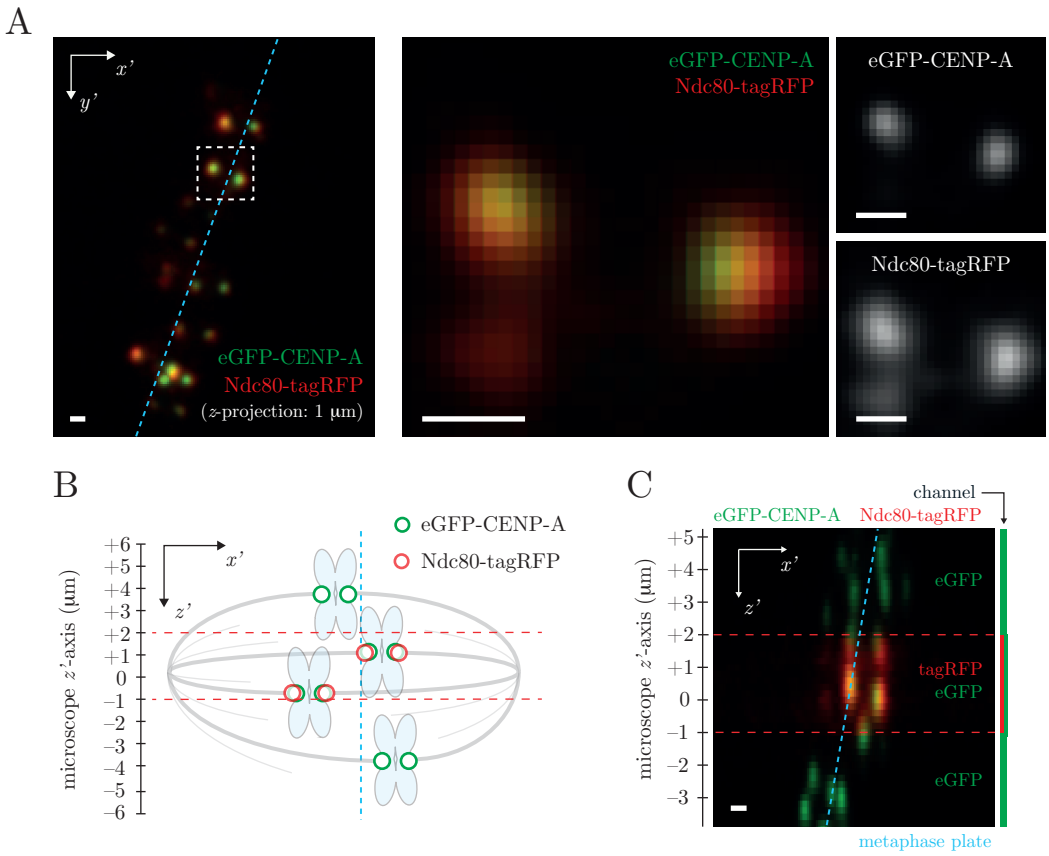

Figure 5.1 *Imaging of successful localisation of Ndc80-tagRFP to kinetochores.*
(A) Image of HeLa-Kyoto cell in metaphase expressing both eGFP-CENP-A and Ndc80-tagRFP in the *x'y'*-plane. The blue dashed line represents the metaphase plate, the white dashed box represents the kinetochore pair shown in images on the right. The whole-cell image is a 1 µm projection in *z*, while images of the kinetochore pair are single *z*-slices. Scale bars = 500 nm.
(B) Schematic diagram of a cell in metaphase in the *x'z'*-plane, with green and red circles representing eGFP-CENP-A and Ndc80-tagRFP kinetochore-localisation, respectively. Thick and thin grey lines are kinetochore- and non-kinetochore-microtubules, respectively.
(C) An example of a cell imaged by the same method as represented in (B). The bar to the right demonstrates in which *z*-slices fluorescent signals have been imaged (green = eGFP, red = tagRFP). Scale bar = 500 nm.
In both (B) and (C), red dashed lines respresent the *z*-slices between which the tagRFP is excited, while eGFP is excited across the full *z*-stack. The blue dashed line represents the metaphase plate.

inspection of the kinetochores showed that tagRFP signal was localised “outside" of the eGFP signal for the majority of kinetochores, meaning that the Ndc80-tagRFP was localised as expected (Figure 5.1 A). All images were deconvolved using measured point spread functions (PSFs; Figure 2.1), and corrected for chromatic shift as described in § 4.

In order to ascertain the dynamics of the intra-kinetochore distance during metaphase oscillations, both eGFP and tagRFP signals need to be tracked for a suitable duration at high enough temporal resolution. Previous work tracking eGFP-CENP-A have been able to image cells as often as every 2 s for 5 min, over a 12 μm imaging stack with resolution 500 nm, without the eGFP signal significantly photobleaching (Burroughs *et al.*, 2015; Armond *et al.*, 2015b). However, intra-kinetochore distances are of the order 10's of nanometres, so that 3D measurements of these distances require optimal resolution in all three dimensions. Images would therefore need to be taken every 200 nm in the microscope's focal axis (z'-axis). In order to ensure minimal photobleaching of each fluorophore, and to minimise phototoxicity to cells, time resolution was balanced with laser power used for fluorophore excitation. Cells expressing both eGFP-CENP-A and Ndc80-tagRFP were imaged for 5 min every 7.5 s for the eGFP signal, over a 12 μm imaging stack with resolution 200 nm in the z'-axis. This z range for the stack was required to obtain accurate fitting of the metaphase plate at each time point. However, tagRFP signal could only be imaged in the central 3 μm of the spindle in the z'-direction (Figure 5.1 B), as imaging for tagRFP over the entire stack resulted in both phototoxicity to cells and photobleaching of the tagRFP signal. However, enough of the z'-direction was imaged to ensure sufficient coverage of kinetochore near the mid-plane for localisation of the tagRFP spots (Figure 5.1 C). By imaging both eGFP and tagRFP signals, with signal intensity maintained over 5 min movies, eGFP and tagRFP spot centres could now be located using our established Gaussian mixture-model fitting (MMF) spot finding and tracking algorithms (Burroughs *et al.*, 2015).

5.3 Tracking the tagRFP signal

To develop a dual marker tracking assay, I wanted to make the most of the already-established assay for locating eGFP spots in live cell imaging (Burroughs *et al.*, 2015). Due to a lower signal-to-noise ratio and a broader point spread function in tagRFP's emission wavelength compared to that of eGFP (Figure 2.2 B), attempting to independently search for tagRFP spots yielded a smaller number of spots than that for eGFP spot detection. Therefore, I developed an algorithm that uses the location of eGFP spots in tracked kinetochore sister pairs to restrict the search for the tagRFP signal. Specifically, the eGFP spots were found by Gaussian MMF for every time point throughout each movie (Figure 5.2 A (i)), then tracked through time and tracks paired to allow allocation of sister kinetochores, as described previously (Jaqaman *et al.*, 2010; Armond *et al.*, 2015b). The metaphase plate, and associated coordinate system is defined at each time point.

In order to locate the tagRFP signal accurately, a mask was constructed in the expected vicinity of the outer kinetochore. The tagRFP signal is located outside the eGFP signal (Figure 5.1), and so a semi-circular mask with radius 300 nm was placed in the direction of the spindle pole to which the kinetochore is anticipated to be bound (Figure 5.2 A (i)). The mask was then shifted by the chromatic shift, $\zeta_{\mathrm{GFP}\rightarrow\mathrm{tagRFP}}$, calculated using HeLa cells expressing both eGFP- and mCherry-CENP-A. This ensured that the centre of the tagRFP spot was more likely located within the mask (Figure 5.2 A (ii)). The brightest pixel in the tagRFP signal within each of these masks were recorded per time point, and used as first approximations of spot centres for 3D Gaussian MMF across entire stacks. The number of tagRFP spots was fixed so that a maximum one tagRFP spot could be located per eGFP (Figure 5.2 A (iii)). The sub-pixel coordinates of tagRFP spot centres were then corrected back for chromatic shift (Figure 5.2 A (iv)). For eGFP spots for which there is little or no neighbouring tagRFP signal, a spot was not allocated. For eGFP spots with good neighbouring tagRFP signal, both GFP and tagRFP spot centres are accurately located, as confirmed by visual inspection (Figure 5.2 B). With an array of eGFP and tagRFP coordinates,

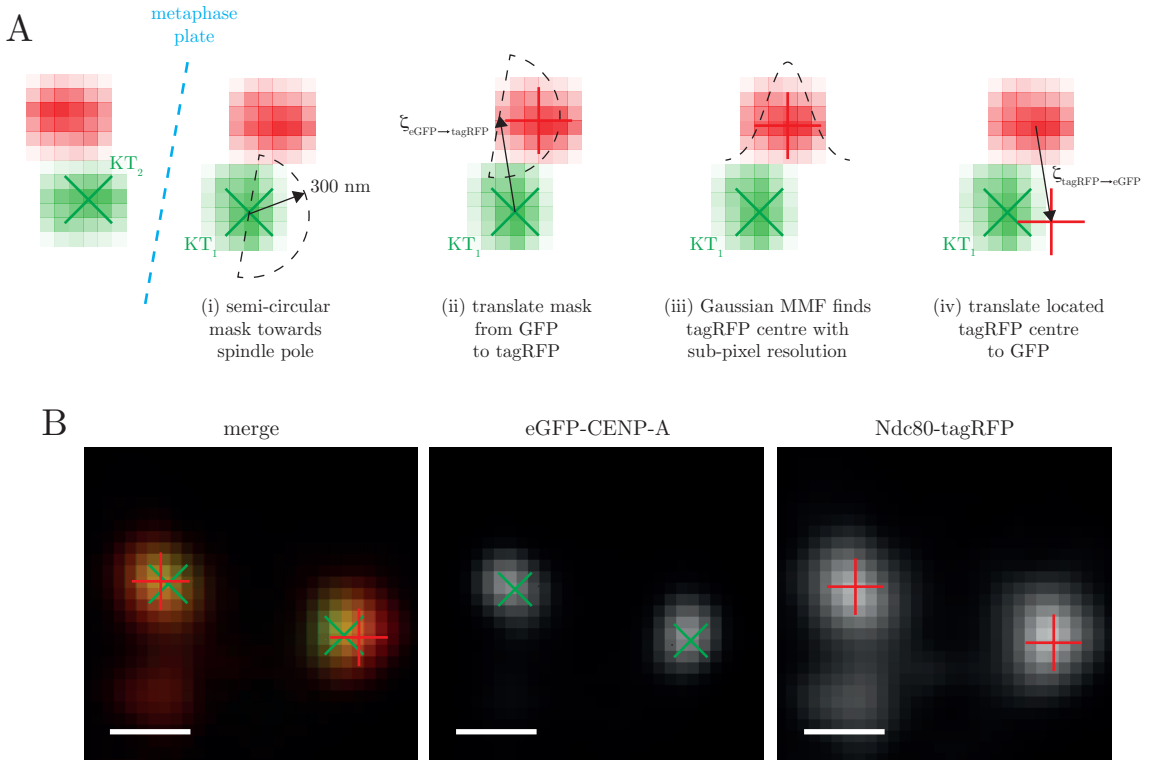

Figure 5.2 *TagRFP spot successfully localised within mask located at eGFP spot centre.*
(A) Schematic demonstrating the localisation of given kinetochore's (KT_1) tagRFP signal within a mask after eGFP spot centre location (green crosses) and sister allocation:
(i) A semi-circular mask (black dashed semi-circle) of radius 300 nm is created pointing perpendicular to the metaphase plate (blue dashed line) and away from the kinetochore's sister (KT_2).
(ii) The mask is translated by the chromatic shift (black arrow) from eGFP to tagRFP wavelengths ($\xi_{eGFP \rightarrow tagRFP}$) calculated in § 4, and maximum intensity tagRFP signal found (red plus).
(iii) The centre of the tagRFP signal (red plus) is located by Gaussian MMF (dashed Gaussian profile).
(iv) The coordinates translated by the chromatic shift (black arrow) from tagRFP to eGFP wavelengths ($\xi_{tagRFP \rightarrow eGFP}$).
(B) Example image of a kinetochore pair with eGFP spot centres (green crosses) and tagRFP spots' localisation (red pluses) using the method described in (A). Scale bars = 500 nm.

intra-kinetochore distance could now be calculated per kinetochore. In order to ensure minimal error in Δ measurement, I sought to control for the quality of the obtained spot centre coordinates before analysing the derived intra-kinetochore measurements.

5.4 Quality control of Δ measurements

The intra-kinetochore distance, $\Delta = [\Delta_x, \Delta_y, \Delta_z]$, between eGFP-CENP-A and Ndc80-tagRFP was calculated as the magnitude of the 3D vector directed from the eGFP spot centre to the tagRFP spot centre for a given kinetochore pair (Figure 5.3 A). These are given in the coordinate system defined by the metaphase plate and the microscope z-direction; the metaphase plate forms the yz-plane, and the x-coordinate points in the direction of the normal of the metaphase plate towards the rightmost spindle pole (Figure 5.3 A). To ensure maximum accuracy of measurements of Δ in the microscope z-direction, the tagRFP centres were required to be located within the same z-plane of the corresponding eGFP centre. More specifically for these experiments, the tagRFP centre needed to be within half the z-resolution of the eGFP centre, i.e. Δ can take a maximum magnitude of 100 nm in the microscope z'-axis (Figure 5.3 B). Any spot pairs that failed this criterion were not used in the analysis. For all experimental data from here on, Δ will have been filtered in this way.

In order to check that the tagRFP spot was being faithfully localised by the localised search around eGFP spot centres, and that quality control measures were only including correctly localised tagRFP spots for analysis, trajectories of eGFP and tagRFP spot centres in the x-coordinate were examined. The example trajectory in Figure 5.3 C demonstrates that a kinetochore pair's tagRFP signals were localised outside of their eGFP signals, as expected for the inner-outer kinetochore orientation. Furthermore, the estimates of Δ throughout these trajectories, for pairs that passed quality control, (Figure 5.3 C, full blue lines) were $\sim$ 100 nm, while those time points removed by quality control were typically considerably larger than this value (Figure 5.3 C, dashed blue lines). This suggested that the quality control measures were successfully filtering out poor quality data.

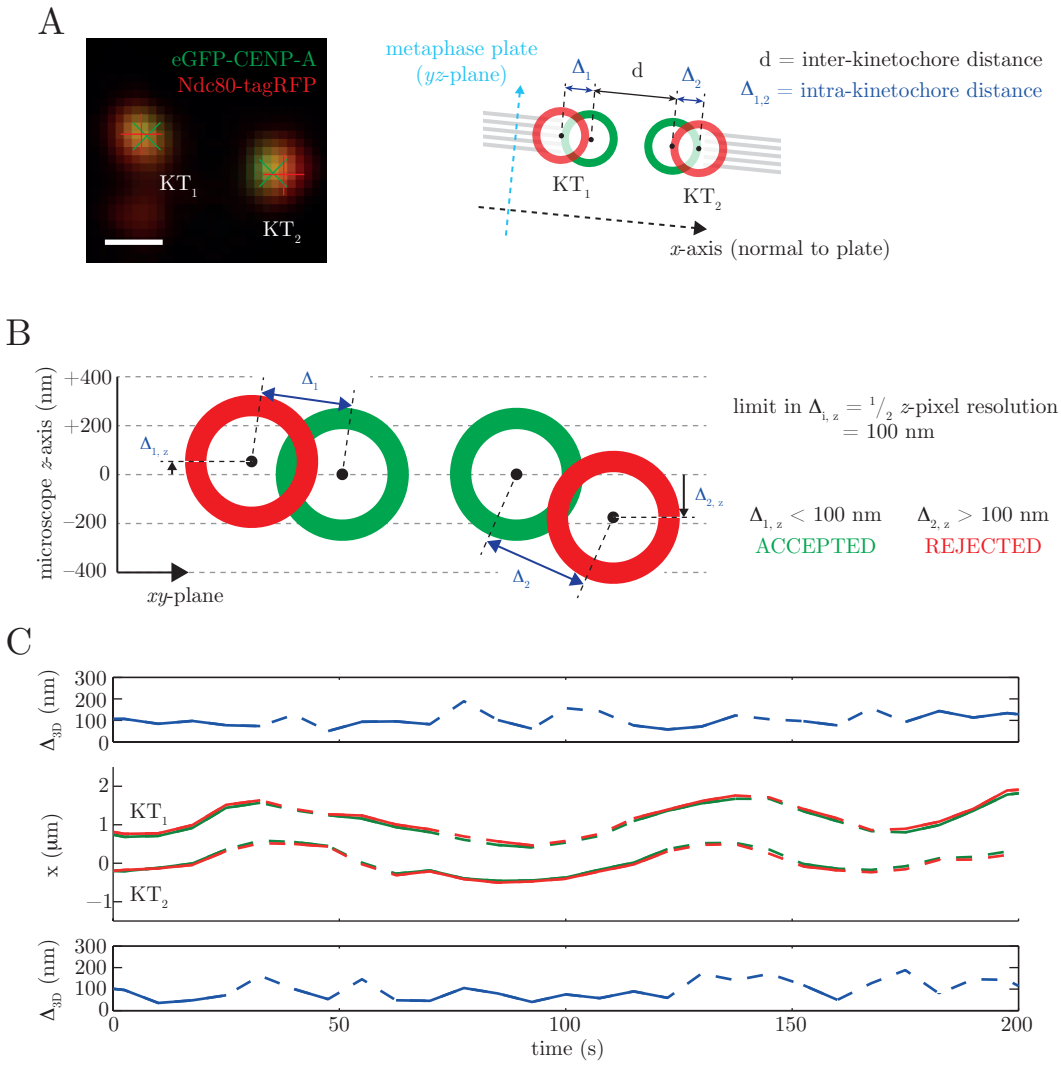

Figure 5.3 *Inter- and intra-kinetochore distance measurements.*
(A) Example kinetochore pair (KT_1 and KT_2) with eGFP (green crosses) and tagRFP (red pluses) spot centres, and a schematic of the coordinate system and distances measured between the eGFP (green circles) and tagRFP (red circles) spot centres therein. Blue dashed arrow represents the metaphase plate (and yz-plane), black dashed arrow represents the x-axis. Black full arrows represent distances Δ_1, Δ_2 and d measured in 3D. Grey lines represent kinetochore microtubules. Scale bar = 500 nm.
(B) Schematic demonstrating quality control of measurements of Δ in the z-direction, where the distance between eGFP (green circles) and tagRFP (red circles) must be less than half the z-pixel resolution (100 nm). The kinetochores on the left and right would pass and fail quality control, respectively.
(C) An example trajectory of a kinetochore pair's eGFP (green line) and tagRFP (red line) signals throughout a movie. 3D measurements of Δ for kinetochores KT_1 (top) and KT_2 (bottom) are made for each time point (blue lines). Full and dashed lines represent time points that passed and failed quality control, respectively.

The absence of bias in the cell orientation within the microscope focal plane provides a quality control check on the chromatic aberration correction. In fact it implies that the inner-outer kinetochore orientations should be symmetric within the x, y, z coordinate system. Specifically, kinetochores pairs are expected to be aligned on average along the x-axis, i.e. one kinetochore points towards one spindle pole, and the other kinetochore points towards the other. Additionally, it would be expected that their k-fibres would be, on average, aligned along the x-axis; therefore, the vector between the inner and outer kinetochore would be, on average, aligned along the x-axis (Figure 5.4 A). This implies that the distribution of Δ_y across all kinetochores should be centred at zero, up to measurement error. The same argument can be made in the z-direction, so that the distribution of Δ_z should also be centred at zero (Figure 5.4 A). This was indeed the case, with median ($\pm$ standard error) values for Δ_y and Δ_z being 8.8 ($\pm$ 1.0) nm and 2.9 ($\pm$ 0.9) nm, respectively ($n = 4,291$ each; Figure 5.4 B). Although these are significantly different from zero ($p < 10^{-4}$ in each case), primarily because of the high sample sizes, the medians are within acceptable tolerance indicating that chromatic aberration has been corrected to within 9 nm. Furthermore, sister kinetochores' outer regions are pointing in opposite directions relative to the centromere, so that the inner-to-outer kinetochore vectors should be, on average, anti-parallel for a kinetochore pair. Measuring direction-dependent values for Δ_x should yield a distribution that is symmetrical about zero with two modes with approximate means $\pm$100 nm. Indeed, a bimodal distribution was observed, and Δ_x had a median of 5.4 ($\pm$ 1.2) nm over all experiments ($n = 4,291$; Figure 5.4 B). Given that my intra-kinetochore measurements satisfy the three kinetochore-pair orientation symmetry criteria, I conclude that the chromatic shift correction is sufficiently accurate for measurements of intra-kinetochore distance in mitotic cells expressing eGFP-CENP-A and Ndc80-tagRFP. Crucially this confirms that z-directional chromatic shift is accurately calculated using the interphase to metaphase cell extrapolation as described in § 4. Given this assay, I sought to investigate intra-kinetochore distances between CENP-A and Ndc80, obtaining the first live 3D measurements between these kinetochore subunits.

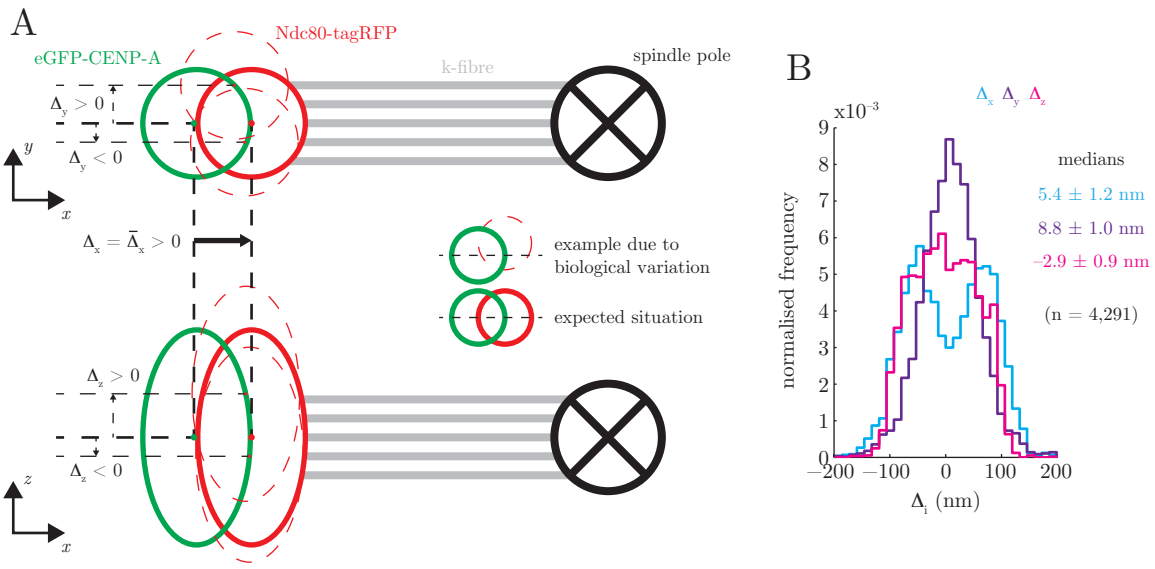

Figure 5.4 *Chromatic shift correction results in symmetrical distribution of* Δ *in each coordinate.*
(A) Schematic of the average expected orientation of a kinetochore's eGFP-CENP-A (thick green circles) and Ndc80-tagRFP (thick red circles) distribution in both the *xy*- (top) and *xz*-planes (bottom). Dashed red circles represent examples of Ndc80-tagRFP orientation relative to eGFP-CENP-A by biological and experimental variation, and dashed arrows represent their distance from the expected average. Full arrow represents average expected distance in the *x*-direction for a kinetochore attached to the right-most spindle pole. Grey lines represent kinetochore-microtubules, black crossed circles represent spindle poles. (B) Histograms of measurements of Δ_x (light blue), Δ_y (purple) and Δ_z (magenta; n = 4,291 each). Values given are medians ± standard error.

5.5 Analysis of Δ in metaphase

Intra-kinetochore distances, Δ, have only previously been measured in 3D by Etemad *et al.* (2015), however these experiments were performed in chemically-fixed cells treated with the proteasome inhibitor MG132. There is thus a gap in our understanding of the intra-kinetochore distance in live (dynamic) cells, which I am in a position to tackle with my novel dual-fluorophore assay. Firstly, I addressed the issue of the intra-kinetochore distance between CENP-A and Ndc80 in live cells during metaphase. On HeLa-K cells expressing eGFP-CENP-A and Ndc80-tagRFP, the distribution of the 3D intra-kinetochore distance had a median Δ ($\pm$ standard error) of 98.0 ($\pm$ 0.9) nm (Figure 5.5 A). This is at least 60% larger than predicted from previously published measurements (Wan *et al.*, 2009; Maresca & Salmon, 2009; Varma *et al.*, 2013; Suzuki *et al.*, 2014; Tauchman *et al.*, 2015; Magidson *et al.*, 2016). However, as mentioned, previously published measurements have been projected into two dimensions, or at best only one. Those measurements projected into 1D were used as a measure of 2D Δ whilst avoiding a requirement for chromatic shift correction. However this measurement can only produce a 2D measurement of Δ on both kinetochores if all four signals lie on a common vector in the xy-plane, and each kinetochore has the same measurement of Δ. Therefore, this measurement is ultimately 1D, as the distance is effectively projected onto the sister-sister axis. This is the reason for calling this measurement Δ_{1D}. The lower dimensionality of Δ_{1D} and Δ_{2D} will provide a source of increase in my distance measurements, however, to ensure that my data complement previously reported measurements, I measured Δ_{1D}. The 1D projection of intra-kinetochore distance onto the sister-sister axis was calculated using the 2D distance between a kinetochore pair's eGFP spots, d_{GFP}, and its tagRFP spots, d_{tagRFP}, specifically $\Delta_{1D} = \frac{d_{\mathrm{tagRFP}} - d_{\mathrm{GFP}}}{2}$ (Figure 5.5 A). It is also worth noting that Δ_{1D} could take a negative value if $d_{\mathrm{tagRFP}} < d_{\mathrm{GFP}}$. The distribution of measurements for Δ_{1D} gives a median ($\pm$ standard error) value of 57.9 ($\pm$ 1.1) nm (n = 1,002; Figure 5.5 A), which is consistent with measurements reported by Wan *et al.* (2009), demonstrating that this assay can recapitulate previous results. This gave confidence that my assay can

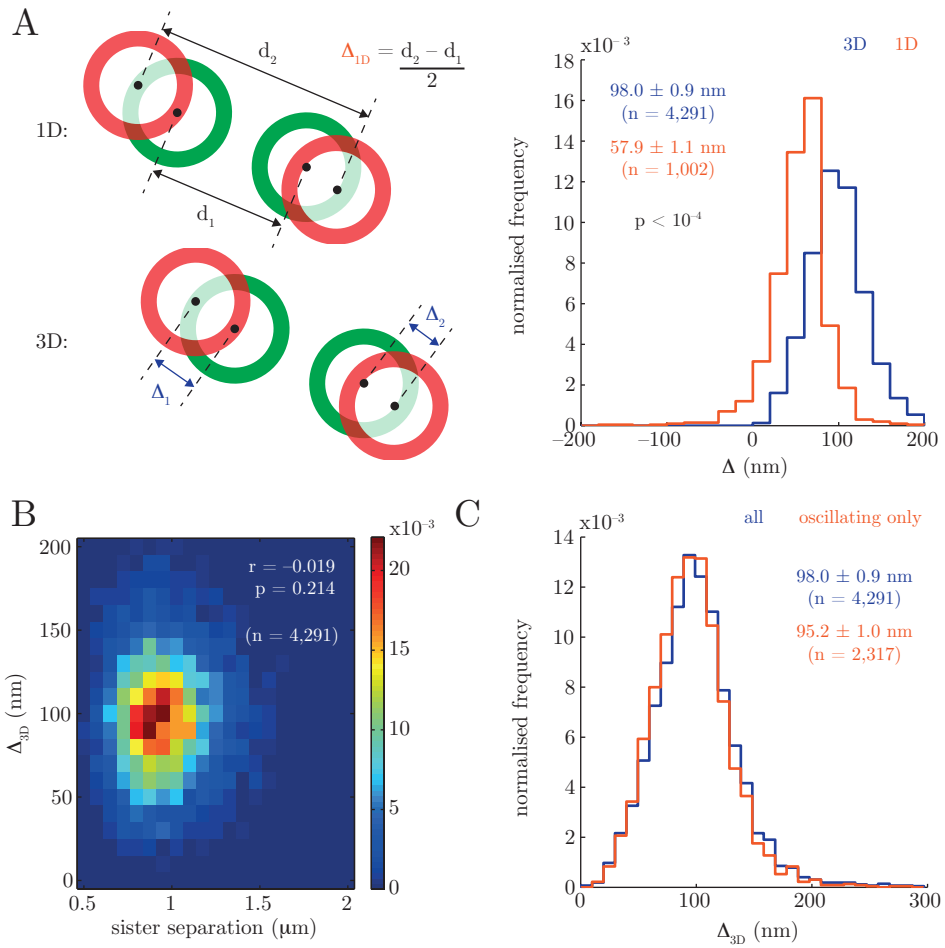

Figure 5.5 Δ_{3D} *demonstrates a previously underestimated measurement of intra-kinetochore distance, which is invariant under tension.*
(A) Schematics of measurements of Δ for a given kinetochore pair using traditional (1D; top) and full 3D (bottom) methods of measurement, and a histogram of measurements for both the 1D (gold; n = 1,002) and 3D (blue; n = 4,291) methods. Green and red circles represent eGFP and tagRFP signals, respectively. Black arrows represent the distances measured between fluorescent markers for each method. Values given are medians ± standard error.
(B) A 2D histogram of 3D intra-kinetochore distance, Δ, against sister separation, d (n = 4,291). Values given are correlation coefficient, r, and probability of significance, p.
(C) Histogram of 3D measurements of Δ for all kinetochores (blue; n = 4,921) and only kinetochores that exhibit oscillating trajectories (gold; n = 2,317). Values given are mediands ± standard error.

accurately measure 3D intra-kinetochore distances in live cells, and therefore I sought to investigate whether there was any correlation between Δ_{3D} and dynamic kinetochore behaviour.

Firstly, I wanted to understand the degree of compliancy in the linkage between CENP-A and Ndc80. It has recently been observed in fixed cells that the human kinetochore's binding apparatus is a rigid structure (Suzuki *et al.*, 2014). If the kinetochore were not rigid, i.e. it formed a compliant linkage between chromatin and kinetochore-microtubules (kMTs), there would be a correlation between force applied by kMTs on the kinetochore, and Δ. Inter-kinetochore distance is observed to stretch when bi-orientated, interpreted to mean the kinetochore pair is under tension. Therefore, when under tension, a compliant kinetochore would yield a positive correlation between Δ and sister separation. However, no correlation is observed when all time points in this time series are pooled, with correlation coefficient, $r = -0.019$ ($n = 4,291, p = 0.214$; Figure 5.5 B). This implies that the linkage between CENP-A and Ndc80 is rigid, and therefore supports the observations of Suzuki *et al.* (2014). It is important to recognise, though, that these values of Δ represent all kinetochore states across all observed kinetochore dynamics. Indeed, much of the published work seeking to understand kinetochore dynamics focus on kinetochore pairs exhibiting oscillatory motion, and therefore coordinated force generation between the sister kinetochores. In order to check whether kinetochores exhibiting pseudo-periodic oscillatory behaviour have a different conformation, all trajectories without clear oscillatory motion were manually removed from analysis. This resulted in a median ($\pm$ standard error) intra-kinetochore distance, $\Delta = 95.2$ ($\pm$ 1.0) nm ($n = 2,317$), which interestingly is significantly smaller than the 98.0 nm measured in all trajectories (Figure 5.5 C; $p < 10^{-4}$). Despite this difference, the correlation coefficient between Δ and inter-kinetochore distance was $r = -0.055$, ($p = 0.008$, $n = 2,317$) suggesting a lack of correlation, and therefore the CENP-A-to-Ndc80 linkage in kinetochores involved in directed motion is also rigid. The primary chromatin-microtubule binding structure within kinetochores is non-compliant, however there is a difference in Δ measurement when observing only

kinetochores exhibiting directed chromosome motion.

The failure to detect a correlation between conformation and force may be due to the fact that I have averaged over different states of the kinetochore during the oscillation. Changes in Δ between poleward (P) and away-from-the-pole (AP) moving kinetochores has been previously investigated in PtK2 cells (Dumont *et al.*, 2012), where P kinetochores were observed to be compressed compared to AP. In order to investigate the difference in Δ between all kinetochores and only those oscillating, kinetochores at each time point were subdivided into 4 classes: kinetochores that experienced prolonged movement towards the spindle pole to which they are bound, i.e. poleward moving or P; those that experienced prolonged movement away from their spindle pole, i.e. away-from-the-pole moving or AP; any time points between adjacent P and AP runs, known as switch points or S; and those that could not be characterised as P, AP or S, known as nondescript or N (Figure 5.6 A). In order to classify a kinetochore as P or AP at a given time point, it was required that it should be one of at least three consecutive time points moving in the same direction. Furthermore, directional switches are special events during a kinetochore's back-and-forth motion, as it is during this time that it needs to enforce a change in microtubule dynamics. Therefore it is possible that conformational changes may occur at directional switches. To ensure that these are not incorporated in datasets with P or AP movement, two time points at P/AP transitions were classified as a switch event, or S. All other time points were considered nondescript, or N. Dividing kinetochores into these classes, I sought to investigate whether P and AP kinetochores had different intra-kinetochore distances in their eGFP-CENP-A to Ndc80-tagRFP linkage in HeLa cells. In contrast to PtK2 cells, P and AP kinetochores were not observed to exhibit any difference in Δ; the median for Δ in P kinetochores was 95.0 ($\pm$ 1.7) nm, and the median for Δ in AP kinetochores was 93.3 ($\pm$ 2.1) nm (Figure 5.6 B, top left). As would be expected, the values for Δ in P and AP kinetochores were similar to that measured for oscillating kinetochore pairs ($\Delta_{\text{oscillating}} = 95.2$ nm). Indeed, those time points for which kinetochores were classified as nondescript (N), and therefore would not have contributed to

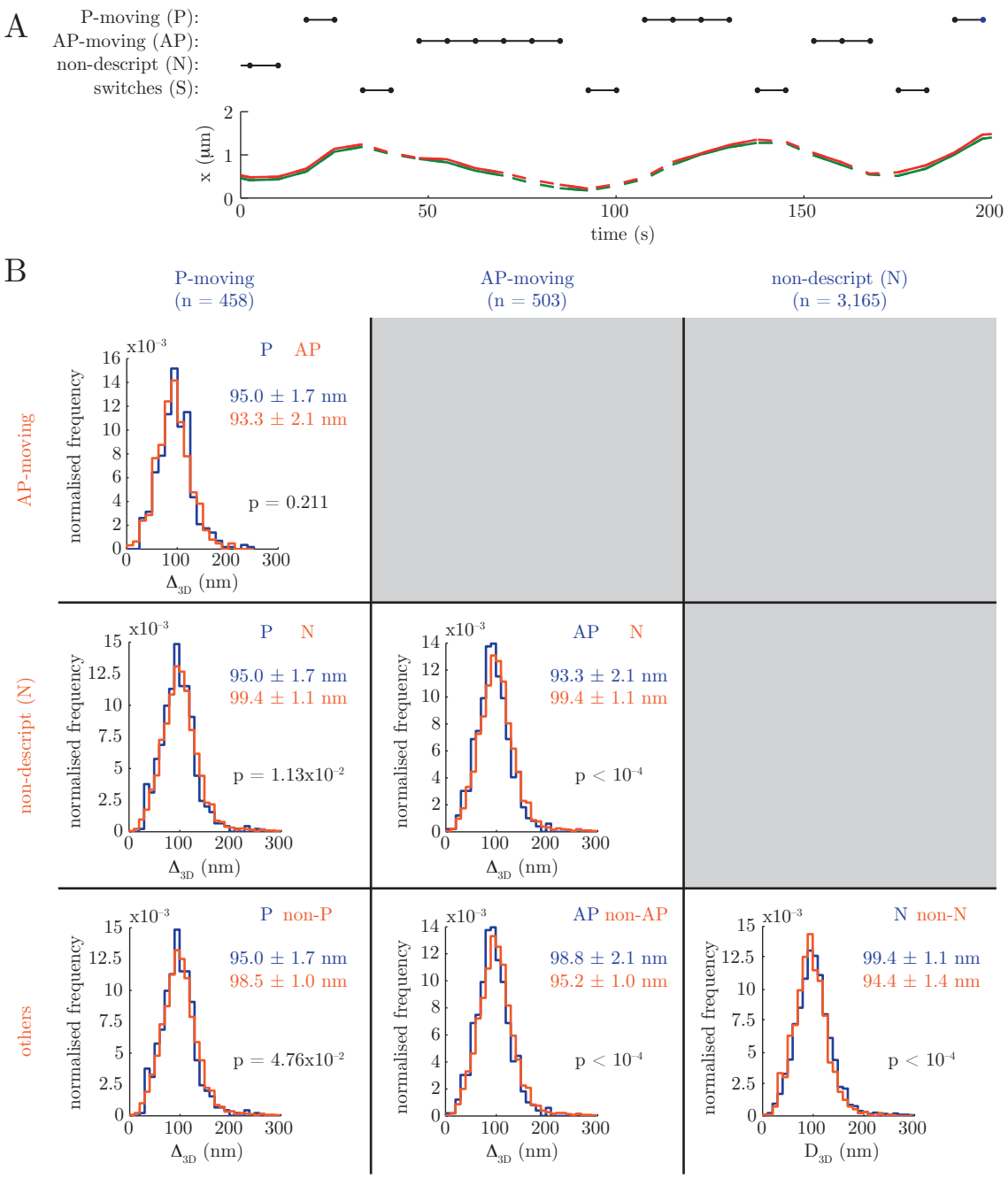

Figure 5.6 Δ *smaller on directionally-biased kinetochores.*
(A) An example trajectory for a single kinetochore's eGFP (green) and tagRFP (red) signal, with labelled direction or behavioural state. Kinetochores can be labelled as poleward (P) moving, away-from-the-pole (AP) moving, experiencing a directional switch (S) or as non-descript (N) if none of the above. Black dots are linked together for each time point that the kinetochore is in the state along the line on which it is located.
(B) Histograms of Δ for kinetochores that are P (left column; n = 458), AP (middle column, top row; n = 503) or N (right column, middle row; n = 3,165). The bottom row compares each column to all kinetochores that do not share its status. Column and row data are shown in blue and gold, respectively. Values are medians ± standard error. All statistical tests are Mann-Whitney U tests.

oscillatory trajectory measurements, had a median for $\Delta_N = 99.4$ ($\pm$ 1.1) nm, which was significantly different to Δ for P kinetochores ($p = 1.13 \times 10^{-2}$; Figure 5.6 B, middle left), AP kinetochores ($p < 10^{-4}$; Figure 5.6 B, middle centre), and all kinetochores not classed as N ($p < 10^{-4}$; Figure 5.6 B, bottom right). Furthermore, Δ measured in P kinetochores is significantly different to all non-P kinetochores ($p = 4.76 \times 10^{-2}$; Figure 5.4 B, bottom left), and Δ measured in AP kinetochores is significantly different to all non-AP kinetochores ($p < 10^{-4}$; Figure 5.6 B, bottom centre). However, in both of these cases, it would be expected that the number of data points contributing to the subset of N kinetochores is large enough compared to both P and AP kinetochores that combining P or AP with N kinetochores would mask the distributions of P and AP anyway. An additional note, the number of time points counted as directional switches was significantly lower than those measured in each of the other cases, and therefore no analyses were derived from this class. Nonetheless, these analyses do raise an important question: why do PtK2 kinetochores exhibit a difference in Δ between P and AP movement, but HeLa-K cells exhibit no significance?

Measurements in PtK2 cells have shown that P kinetochores are compressed relative to AP kinetochores ($\Delta_p = 38$ nm vs. $\Delta_{AP} = 43$ nm; Dumont *et al.*, 2012); this result was significant with $p = 10^{-5}$, but is in contrast to the measurements described above (Figure 5.6 B, top left). There are a number of potential reasons for these differences. Firstly, the method of classification for P and AP trajectories used in their work included all time points for which a kinetochore was moving in one direction, i.e. not accounting for switch events. Furthermore, their measurements were obtained by a 2D measurement assay rather than in 3D. In order to test whether their method of measurement could be the cause of the P, AP differences, I tested each of the methodological differences in turn, and then their combination. Firstly, P and AP trajectories were instead defined to include time points at each end of the P or AP run, previously classified as either S or N (Figure 5.7 A, solid lines). Measurements of Δ in P, AP and N kinetochores by this method produced very little difference in median measurements, and did not result in a significant difference between P and AP kinetochores

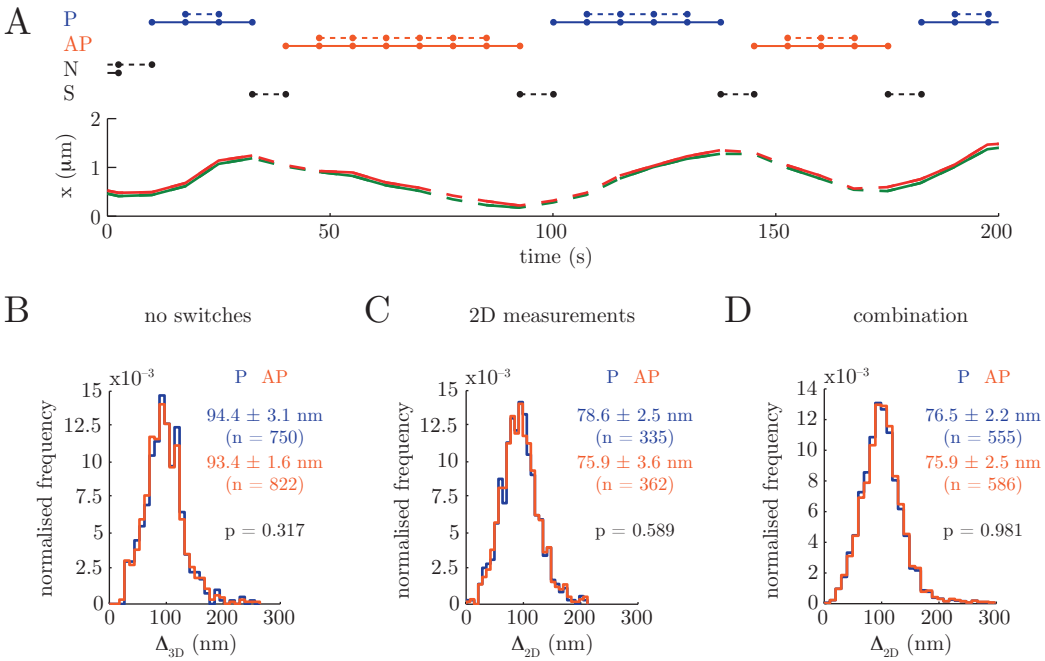

Figure 5.7 *Method of* Δ *measurement as in Dumont* et al. *gives the same results.* (A) A trajectory for a single kinetochore's eGFP (green) and tagRFP (red) signal, with labelled direction or behavioural state. Kinetochores can be labelled as poleward (P) moving (blue), away-from-the-pole (AP) moving (gold), experiencing a directional switch (S), or as non-descript (N) if none of the above. Dots represent time points in each kinetochore state, and are linked together during trajectories in each state. Dashed and full lines represent state allocation satisfying this work's and the work of Dumont *et al.*'s (2012) criteria, respectively.
(B) Histogram of Δ_{3D} in P (blue; n = 750) and AP (gold; n = 822) kinetochores using the state-allocation method used in Dumont *et al.* (2012), where time points about switch events are not omitted from directional data.
(C) Histogram of Δ_{2D} in P (blue; n = 335) and AP (gold; n = 362) kinetochores.
(D) Histogram of Δ_{2D} in P (blue; n = 555) and AP (gold; n = 586) kinetochores using the state-allocation method used in Dumont *et al.* (2012).
All values given are medians ± standard error. All statistical tests are Mann-Whitney U tests.

(p = 0.317; Figure 5.7 B). Furthermore, significant differences between N and P or AP kinetochores are retained ($p_{\text{P vs. N}} < 10^{-4}$; $p_{\text{AP vs. N}} < 10^{-4}$), and therefore the P/AP-classification cannot explain the differences in the P vs. AP analyses between these two assays. In order to test whether 2D measurements would produce a significant difference between P and AP kinetochores, I measured all kinetochores in 2D. Dumont *et al.* (2012) required that both fluorescent markers on a pair of kinetochores were within the same z-plane. All Δ measurements analysed in this thesis have been filtered so that a tagRFP signal is required to be within 100 nm (half the resolution in the z-direction) from the matching eGFP signal. Therefore all fluorescent markers are effectively within the same z-plane. This allows comparison between my measurements and those in Dumont *et al.* (2012) by projecting all Δ measurements onto the xy-plane (henceforth called Δ_{xy}). However, this yielded no significant difference between P and AP kinetochores, with median ($\pm$ standard error) $\Delta_{xy,\text{P}} = 78.6$ ($\pm$ 2.5) nm (n = 335) and $\Delta_{xy,\text{AP}} = 75.9$ ($\pm$ 3.6) nm (n = 362), with p = 0.589 so there is no evidence of a difference (Figure 5.7 C). This means that dimensionality (projected measurements) is also not the cause for the difference in P vs. AP intra-kinetochore measurements between this work and the work of Dumont *et al.* (2012). As a final precaution, I checked whether the difference was in fact a consequence of both the P/AP-classification and 2D measurement methods. In order to do this, measurements of Δ_{xy} in P and AP kinetochores as derived using the Dumont *et al.* (2012) classification method were compared to one another. Sure enough, there was no significant difference between Δ_{xy} in P and AP kinetochores, with median values $\Delta_{xy,\text{P}} = 76.5$ ($\pm$ 2.2) nm (n = 555) and $\Delta_{xy,\text{AP}} = 75.9$ ($\pm$ 2.5) nm (n = 586; p = 0.981; Figure 5.7 D).

Analysis of the intra-kinetochore distance, Δ, in this case defined as the Euclidean distance between chromatin-embedded CENP-A and microtubule-binding Ndc80, exhibits no correlation with inter-kinetochore tension or kinetochore state. This suggests that the direct kinetochore-mediated linkage between centromeric DNA and kMTs is stiff, which supports recent observations in HeLa cells. However, this also contradicts previous observations in PtK2, HeLa and *Drosophila* S2 cells (Dumont *et al.*, 2012;

Wan *et al.*, 2009; Maresca & Salmon, 2009). This raises the possibility that other observations using intra-kinetochore distance measurements, for example dependence of Δ on attachment status, may also be different, and need checking within the context of this intra-kinetochore 3D measurement assay.

5.6 Δ dependence on attachment status

Intra-kinetochore distance has been investigated with and without microtubule attachment in a number of chemically-fixed cell types (*Drosophila* S2: Maresca & Salmon, 2009; HeLa: Uchida *et al.*, 2009; Tauchman *et al.*, 2015; Etemad *et al.*, 2015; RPE1: Magidson *et al.*, 2016). In each of these publications, cells were treated with nocodazole in order to destabilise the mitotic spindle – this results is a loss of the intra-kinetochore stretch. Each study describes a decrease in kinetochore stretch once tension across the kinetochore is perturbed. However, I observed that kinetochores are non-compliant under force (Figure 5.5 B), which contests the idea that kinetochores relax after detachment of kMTs. I therefore wanted to understand if Δ varied when the mitotic spindle architecture is perturbed. In order to investigate Δ measurements between CENP-A and Ndc80 with attachment state, either nocodazole or taxol were added to cells prior to imaging. As mentioned, high doses of nocodazole (> 1 μM) completely destabilises microtubules structure, resulting in the loss of the mitotic spindle. Alternatively, low doses of nocodazole (< 300 nM) maintains the mitotic spindle, however tension cannot be generated between kinetochores as microtubule dynamics are suppressed. Meanwhile, 10 μM taxol treatment hyper-stabilises bonds between α- and β-tubulin, and therefore kinetochores maintain attachment to k-fibres. However dynamics of kMTs after taxol-treatment are also perturbed. Therefore higher doses of nocodazole will assess intra-kinetochore distances under complete loss of attachment and loss of inter-kinetochore tension, while low nocodazole doses will allow investigation into Δ measurement under weakened kMT attachment and loss of inter-kinetochore tension. Finally, taxol will be able to yield information on the intra-kinetochore distances upon stabilised binding.

Firstly, I confirmed using immunofluorescence that my nocodazole and taxol treatments produced the expected effect on spindle architecture. HeLa-K cells stably expressing eGFP-CENP-A and transiently expressing Ndc80-tagRFP were subject to 3 μM nocodazole or 100 nM nocodazole for 16 hr, or 10 μM taxol for 1 hr prior to imaging. Cells were fixed with glutaraldehyde at the time at which they would be imaged for measurements of Δ, and stained with anti-α-tubulin primary antibody and an anti-mouse AlexaFluor-647 secondary antibody (Figure 5.8 A). Glutaraldehyde fixation has been shown to better preserve structures when compared to formaldehyde fixation, and therefore will give a better impression of kinetochores and their microtubules (Magidson *et al.*, 2016). Mitotic spindle intensity in cells treated with 3 μM nocodazole was decreased to 3.8% that of untreated cells ($p < 10^{-4}$), demonstrating that this dose would provide an appropriate treatment for the measurement of Δ when there is no microtubule attachment. Furthermore, 100 nM nocodazole and 10 μM taxol treatments resulted in a decrease in mitotic spindle intensity to 72.8% and 67.6% of that of untreated metaphase cells, respectively (Figure 5.8 B). This provided me with assays to measure intra-kinetochore distance within kinetochores bound to perturbed spindles.

Now that I had a treatment to either remove, slightly destabilise or hyper-stabilise the mitotic spindle, I sought to ensure that kinetochore dynamics were altered as a consequence of the loss of force generation in perturbed spindles. Live mitotic cells expressing both eGFP-CENP-A and Ndc80-tagRFP were imaged over 3D stacks for eGFP and tagRFP signal as before to allow measurement of Δ after the addition of either 3 μM nocodazole, 100 nM nocodazole, or 10 μM taxol (treatment and imaging times as above). eGFP and tagRFP spots were localised as before, and kinetochores filtered so that the z-component of Δ is no larger than 100 nm, or half the z-resolution. To quantify kinetochore dynamics, and thus indirectly the microtubule dynamics within k-fibres, I calculated the autocorrelation of the change in displacement normal to the metaphase plate, x (see Figure 5.3 A). Kinetochores are observed to exhibit quasi-periodic back-and-forth motion about the metaphase plate (e.g. Jaqaman *et al.*, 2010;

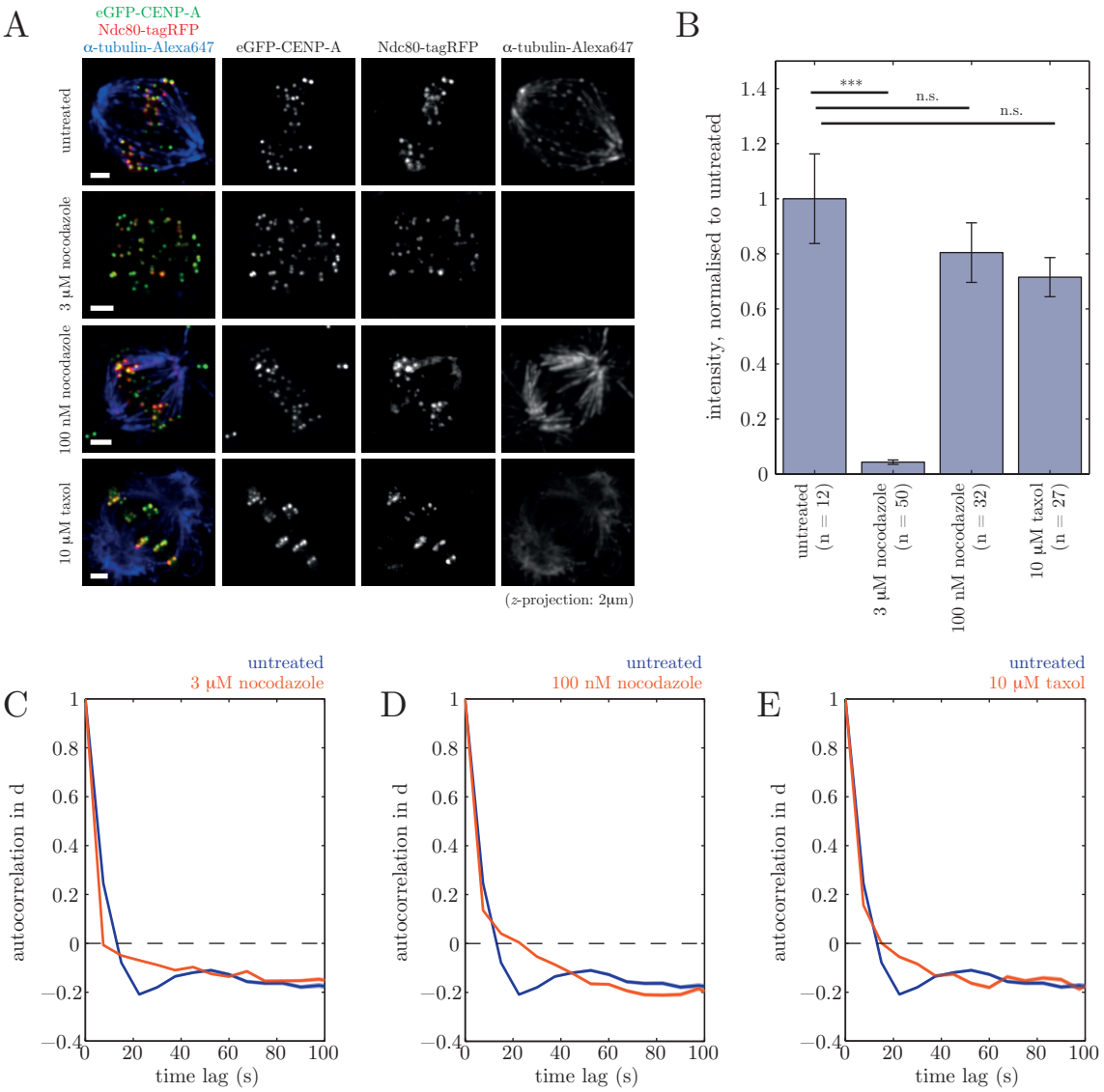

Figure 5.8 *Nocodazole and taxol treatments result in a loss of kinetochore dynamics and a loss of centromeric tension.*
(A) Images of cells expressing eGFP-CENP-A and Ndc80-tagRFP after different drug treatments and labelling α-tubulin with AlexaFluor-647. Drug treatments are: untreated metaphase (top row); 3 μM nocodazole (second row); 100 nM nocodazole (third row); and 10 μM taxol (bottom row). All images of α-tubulin-Alexa647 have common contrast to allow direct visual comparison. Each image is a 2 μm projection in *z*. Scale bars = 2 μm.
(B) Quantification of α-tubulin-Alexa647 intensity in raw images of cells as imaged in (A) for untreated metaphase (n = 12), 3 μM nocodazole (n = 50), 100 nM nocodazole (n = 32) and 10 μM taxol (n = 27). Distributions have been normalised to intensity measured in untreated cells. Error bars represent standard error. Horizontal lines demonstrate statistical significance by Mann-Whitney U tests between the spanned drug treatments (*** is $p < 10^{-4}$; n.s. = no significance).
(C,D,E) Autocorrelation in the inter-kinetochore distance, d, for untreated metaphase cells (blue) compared against (gold): (C) 3 μM nocodazole; (D) 100 nM nocodazole; and (E) 10 μM taxol.

see Figure 1.7). Furthermore, autocorrelation of change in the inter-kinetochore distance, d, shows that there are oscillations with quasi-periodicity with twice the periodicity to that of the back-and-forth motion. This is called breathing, and is due to the difference in polymerisation and depolymerisation speeds at each kinetochore (Wan *et al.*, 2012). In the drug treatments used above, microtubules should no longer be dynamic. Because x is a metaphase plate coordinate, which is absent in 3 μM nocodazole, autocorrelation of change in d was instead calculated in each drug treatment and compared to untreated cells. Untreated metaphase cells had a breathing period of $\sim$ 25 s, however periodic behaviour in d measurements was lost under each the 3 μM nocodazole (Figure 5.8 C), 100 nM nocodazole (Figure 5.8 D), and 10 μM taxol (Figure 5.8 E) treatments. This demonstrates that each perturbation resulted in loss of microtubule dynamics, and therefore loss of force generation by kMTs. I next sought to measure 3D distances between kinetochore markers in each of these treatments in order to assess kinetochore structure in different microtubule attachment states.

Incubating cells with 3 μM nocodazole for 16 hr completely destabilises the mitotic spindle, and therefore kinetochores are completely unattached. Unattached kinetochores can no longer generate inter-kinetochore tension, and therefore a decrease in sister separation is observed. Cells treated with 3 μM nocodazole had median value of inter-kinetochore distance, $d = 698$ ($\pm$ 2) nm ($\mathrm{n} = 3,669; \mathrm{p} < 10^{-4}$), which decreased from 930 ($\pm$ 3) nm in untreated metaphase cells ($\mathrm{n} = 4,291$; Figure 5.9 A).

It has been previously observed that nocodazole causes a decrease in intra-kinetochore distance, Δ (Maresca & Salmon, 2009; Uchida *et al.*, 2009; Tauchman *et al.*, 2015; Etemad *et al.*, 2015; Magidson *et al.*, 2016). However, the kinetochore has also been shown to be a non-compliant structure (Suzuki *et al.*, 2014), confirmed here (Figure 5.5 B). In order to investigate this discrepancy, I measured live 3D intra-kinetochore distances with complete loss of microtubule attachments, for the first time. Measuring the 3D Euclidean distance between eGFP-CENP-A and Ndc80-tagRFP in cells treated with 3 μM nocodazole produced a median measurement of Δ of 103.1 ($\pm$ 1.4) nm ($\mathrm{n} = 3,669$). Crucially, this value is significantly larger than that in untreated metaphase

cells (98.0 nm; $p < 10^{-4}$; Figure 5.9 B, left). This measurement contradicts all previous reports measuring intra-kinetochore distances under loss of attachment. This includes that of Etemad *et al.* (2015), which is the only other assay that has provided measurements of Δ in 3D, albeit in fixed cells. All other measurements, however, were made by projecting the intra-kinetochore distance into 2D, or onto the sister-sister axis to give Δ_{1D}. Measurement of Δ_{1D} in untreated cells provided an underestimate of the 3D measurement of intra-kinetochore distance (Figure 5.5 A). Therefore measurement of Δ_{1D} in 3 μM nocodazole-treated cells will also be underestimated compared to that measured in 3D. Interestingly, there was a substantial decrease in Δ_{1D}, median 28.4 ($\pm$ 2.0) nm in 3 μM nocodazole compared to 57.9 ($\pm$ 1.1) nm in untreated (Figure 5.9 B, right), which reproduces previous observations that the (projected) intra-kinetochore distance decreases in nocodazole treatment. This suggests that the projection of kinetochores into 1D not only underestimates the intra-kinetochore distance, but the degree of underestimate is condition-dependent. As mentioned earlier, the 1D projection requires that all four kinetochore markers are aligned along the sister-sister axis in order that the 1D projection method provides an accurate 2D measurement of the intra-kinetochore distance. Visual inspection of kinetochore pairs in nocodazole-treated cells revealed that there are a number of cases where the outer kinetochore spots are not on the same axis as the eGFP spots (Figure 5.9 C). In fact, in these cells, a large number of kinetochore markers were not lying perfectly co-linear, i.e. the Ndc80-tagRFP signal can be located by as much as 90° to the sister-sister axis (eGFP-CENP-A axis). This is a degree of freedom that has not been investigated in kinetochores. Most previous reports of intra-kinetochore distance have ignored this degree of freedom, and have therefore incurred an underestimate since the outer kinetochore can rotate about the inner kinetochore in 3D (Figure 5.9 C). The authors of Wan *et al.* (2009) describe a similar rotation, which they call "tilt". This is measured as the angle tended between the sister-sister axis and the short axis of elliptical signals. An elliptical signal is interpreted as a plate-like structure of the kinetochore, and therefore defines its orientation. While they attempted to correct their measurements of Δ_{1D} for tilt, it was not suffi-

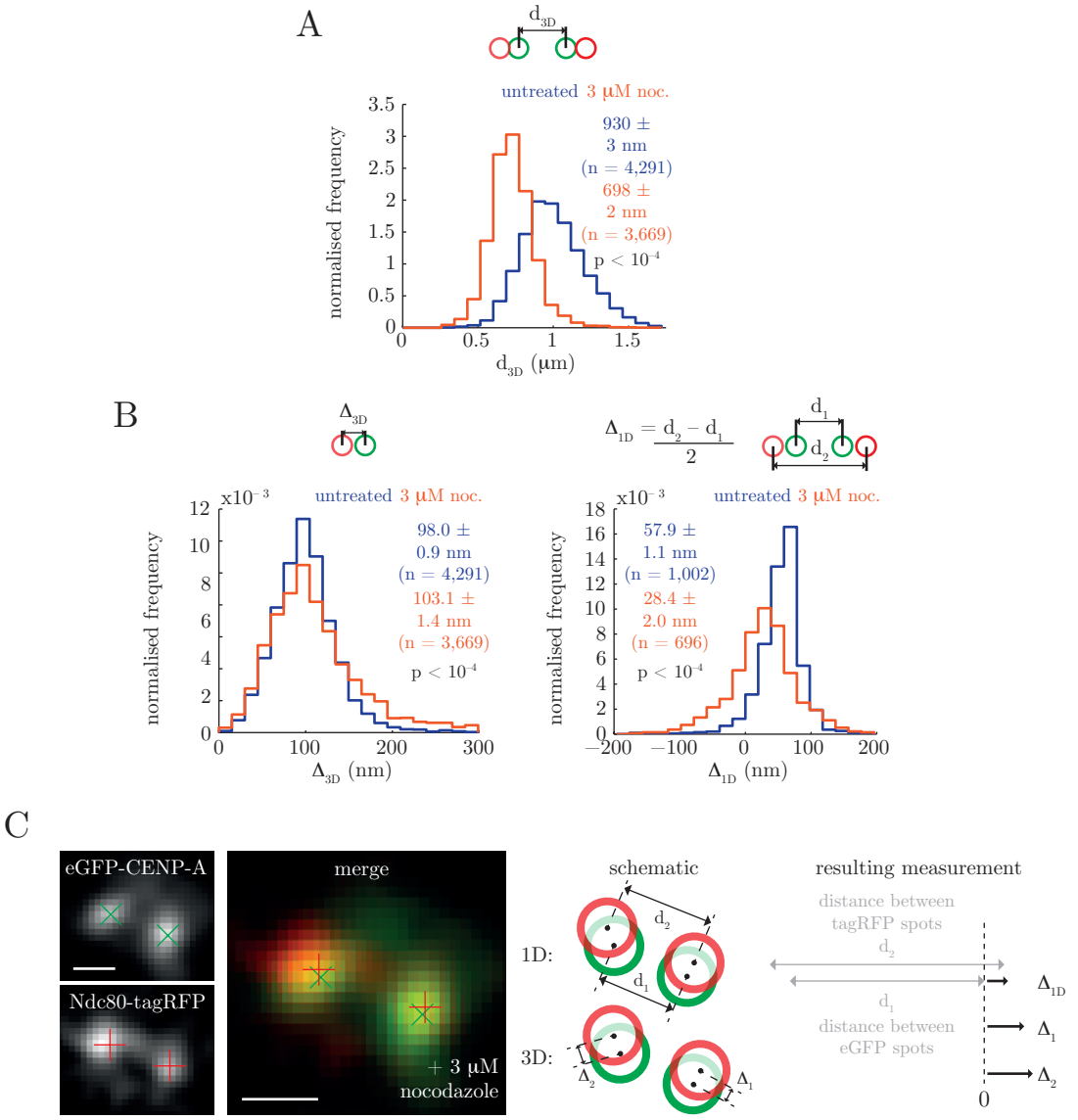

Figure 5.9 *Complete loss of microtubule attachment does not decrease* Δ_{3D}.
(A) Histograms of d_{3D} for untreated metaphase (blue; n = 4,291) and 3 µM nocodazole-treated (gold; n = 3,669) cells. Schematics demonstrate the measurement of d. Statistical tests are Mann-Whitney U. Values given are medians ± standard error.
(B) Histograms of Δ_{3D} (left) and Δ_{1D} (right) for untreated metaphase (blue; n_{3D} = 4,291, n_{1D} = 1,002) and 3 µM nocodazole-treated (gold; n_{3D} = 3,669, n_{1D} = 696) cells. Schematics demonstrate the measurements of Δ. Statistical tests are Mann-Whitney U. Values given are medians ± standard error.
(C) A kinetochore pair in mitosis after 3 µM nocodazole treatment, demonstrating an example of non-co-linearity of green and red pairs of kinetochore markers (eGFP = green crosses; tagRFP = red pluses). Schematics represent the measurements of Δ_{1D} (top) and Δ_{3D} (bottom) for this kinetochore pair. eGFP-CENP-A and Ndc80-tagRFP are represented by green and red circles, respectively. The resulting 1D and 3D intra-kinetochore measurements are compared, demonstrating the possibility for an underestimate in Δ_{1D} for kinetochore pairs in this orientation. Scale bars = 500 nm.

cient to rescue the result I have here. Therefore, Δ_{3D} does not decrease upon 3 μM nocodazole treatment, but in fact may increase (Figure 5.9 B, left).

I next sought to measure Δ_{3D} after 100 nM nocodazole-treatement. Measurements of d first demonstrated the loss of inter-kinetochore tension, decreasing to 865 ($\pm$ 4) nm (n = 3, 128) from 930 nm in untreated cells. This is a smaller decrease compared to the higher dose of 3 μM nocodazole, possibly due to a small subset of microtubules that can generate pulling forces on kinetochores (Figure 5.10 A). Interestingly, as with the 3 μM nocodazole dose, 3D Δ increased to 106.7 ($\pm$ 1.1) nm (n = 3, 128; Figure 5.10 B, left) in cells treated with 100 nM nocodazole. This was significantly different to Δ_{3D} measured in untreated cells ($p < 10^{-4}$). Once again, previous work has described a decrease in intra-kinetochore distance in nocodazole doses as low as 100 nM (Uchida *et al.*, 2009; Tauchman *et al.*, 2015; Etemad *et al.*, 2015). However a couple of these results were based upon the 1D measurement of Δ, Δ_{1D}, which I have already shown results in an underestimate of the intra-kinetochore distance when kinetochores are completely unattached to microtubules. Calculating Δ_{1D} in cells treated with 100 nM nocodazole resulted in a significant decrease from 57.9 nm down to 44.6 ($\pm$ 2.0) nm (n = 648; Figure 5.10 B, right), $p < 10^{-4}$. The increase observed in Δ_{3D} implies that a weakening of microtubule attachments can produce a similar increase in intra-kinetochore length to that observed under complete loss of microtubule attachment. This suggests that loss of inter-kinetochore tension alone is responsible for the observed increase.

In order to confirm this, an acute dose of 10 μM taxol was used to hyper-stabilise microtubules in the mitotic spindle. As mentioned, this acts to stabilise kMT attachments, however it results in a loss of kinetochore dynamics and inter-kinetochore tension (Jaqaman *et al.*, 2010). Indeed, after addition of 10 μM taxol, 3D measurement of inter-kinetochore distance d decreased to 757 ($\pm$ 3) nm (n = 2, 324; Figure 5.11 A). Taxol has previously been shown to decrease intra-kinetochore distances by $\sim$ 16 nm, including the distance between CENP-A and the NDC80 complex (Wan *et al.*, 2009). This suggests that there is a large conformational change within the

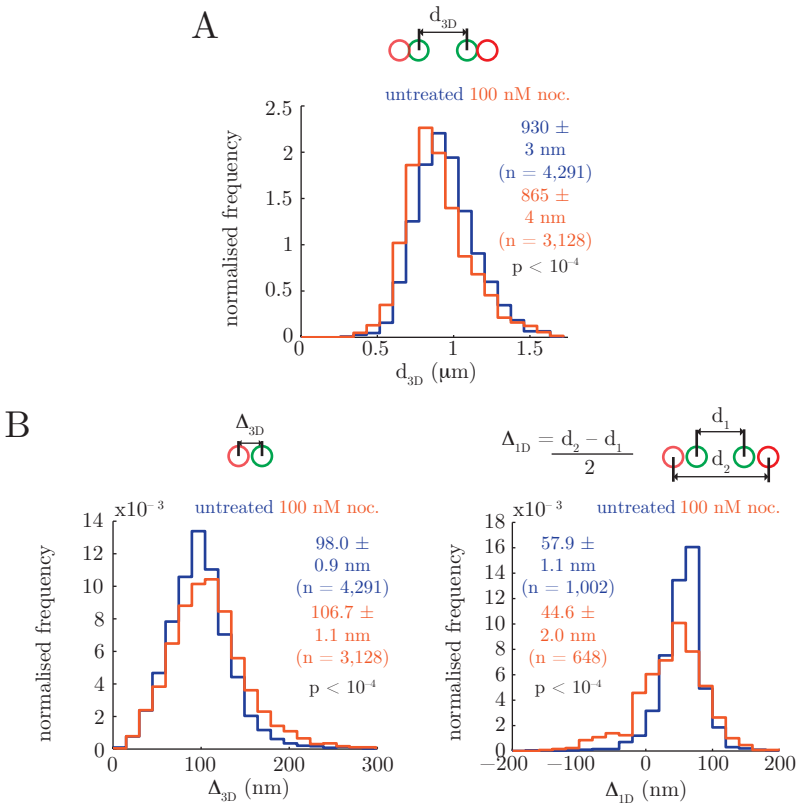

Figure 5.10 *A destabilised spindle also results in an underestimate in* **Δ**.
(A) Histogram of d_{3D} for untreated (blue; n = 4,291) and 100 nM nocodazole-treated (gold; n = 3,128) cells in metaphase. Schematic demonstrates the measurement of d. Statistical tests are Mann-Whitney U. Values given are medians ± standard error.
(B) Histograms of Δ_{3D} (left) and Δ_{1D} (right) for untreated (blue; n_{3D} = 4,291, n_{1D} = 1,002) and 100 nM nocodazole-treated (gold; n_{3D} = 3,128, n_{1D} = 648) cells in metaphase. Schematics demonstrate the measurements of **Δ**. Statistical tests are Mann-Whitney U. Values given are medians ± standard error.

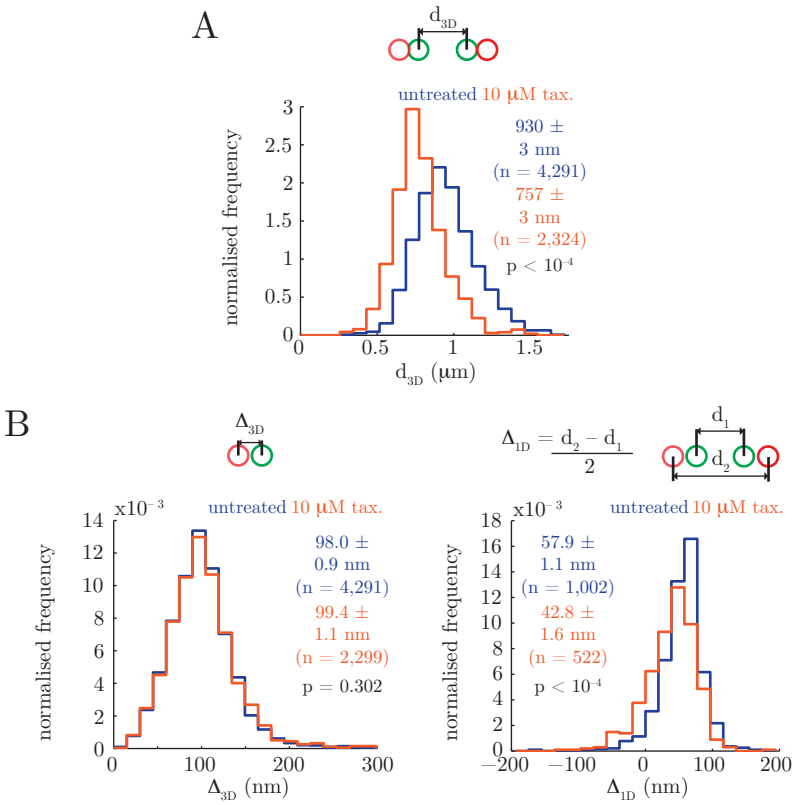

Figure 5.11 *Stabilised kinetochore-microtubule attachment under loss of inter-kinetochore tension does not reduce* Δ_{3D}.
(A) Histogram of d_{3D} for untreated (blue; n = 4,291) and 10 μM taxol-treated (gold; n = 2,324) cells. Schematic demonstrates the measurement of d. Statistical tests are Mann-Whitney U. Values given are medians ± standard error.
(B) Histograms of Δ_{3D} (left) and Δ_{1D} (right) for untreated (blue; n_{3D} = 4,291, n_{1D} = 1,002) and 10 μM nocodazole-treated (gold; n_{3D} = 2,299, n_{1D} = 522) cells. Schematics demonstrate the measurements of Δ. Statistical tests are Mann-Whitney U. Values given are medians ± standard error.

kinetochore upon loss of inter-kinetochore tension. However, this report was based on measuring Δ_{1D}, and therefore likely suffers an underestimate similar to that demonstrated under other treatments. However, measuring Δ_{3D} in taxol-treated cells gave a median of 99.4 ($\pm$ 1.1) nm (n = 2,299), not significantly different to untreated cells (p = 0.302; Figure 5.11 B, left). Furthermore, measuring Δ_{1D} gave a significant decrease ($p < 10^{-4}$) compared to untreated cells, 42.8 ($\pm$ 1.6) nm (n = 522; Figure 5.11 B, right) – reproducing the decrease reported by Wan *et al.* (2009). This indicates that kinetochores do not exhibit any difference in Δ_{3D} under loss of inter-kinetochore tension and therefore the increase in Δ_{3D} after nocodazole treatment is a consequence of either loss, or weakening, of kinetochore attachment to the k-fibre. Previous reports that used a projected distance to analyse the intra-kinetochore distance failed to discriminate these effects because the projection introduced artefacts that result in a reduction of Δ_{1D} in all drug treatments (Figure 5.9 B, 5.10 B, 5.11 B, all left). As was demonstrated for kinetochores in 3 μM nocodazole-treated cells, not all kinetochores are aligned so that their inner and outer kinetochore markers are located along a single axis. Therefore any measurement of Δ_{1D} suffers a projection onto the sister-sister axis. Based on the observed decreases of Δ_{1D} in all three drug treatments, I hypothesised that the kinetochore marker axis is undergoing varying levels of rotation depending on the treatment.

5.7 Intra-kinetochore swivel

In order to quantify kinetochore rotations, I defined kinetochore swivel as the rotation of the kinetochore marker axis relative to the sister axis. A kinetochore's swivel, $\vartheta_{\text{swivel}}$, was defined as the absolute angle tended by the line through the eGFP and tagRFP marker signals, the marker-marker axis, and the vector connecting the paired sister kinetochore's eGFP-CENP-A signals, the sister-sister axis (Figure 5.12 A). Measuring swivel across all kinetochores in untreated metaphase cells gave a median ($\pm$ standard error) of 51.6° ($\pm$ 0.5°). This reveals that human kinetochores are capable of outer-kinetochore rotation during metaphase. Projecting Δ_{3D} onto the sister-sister axis using

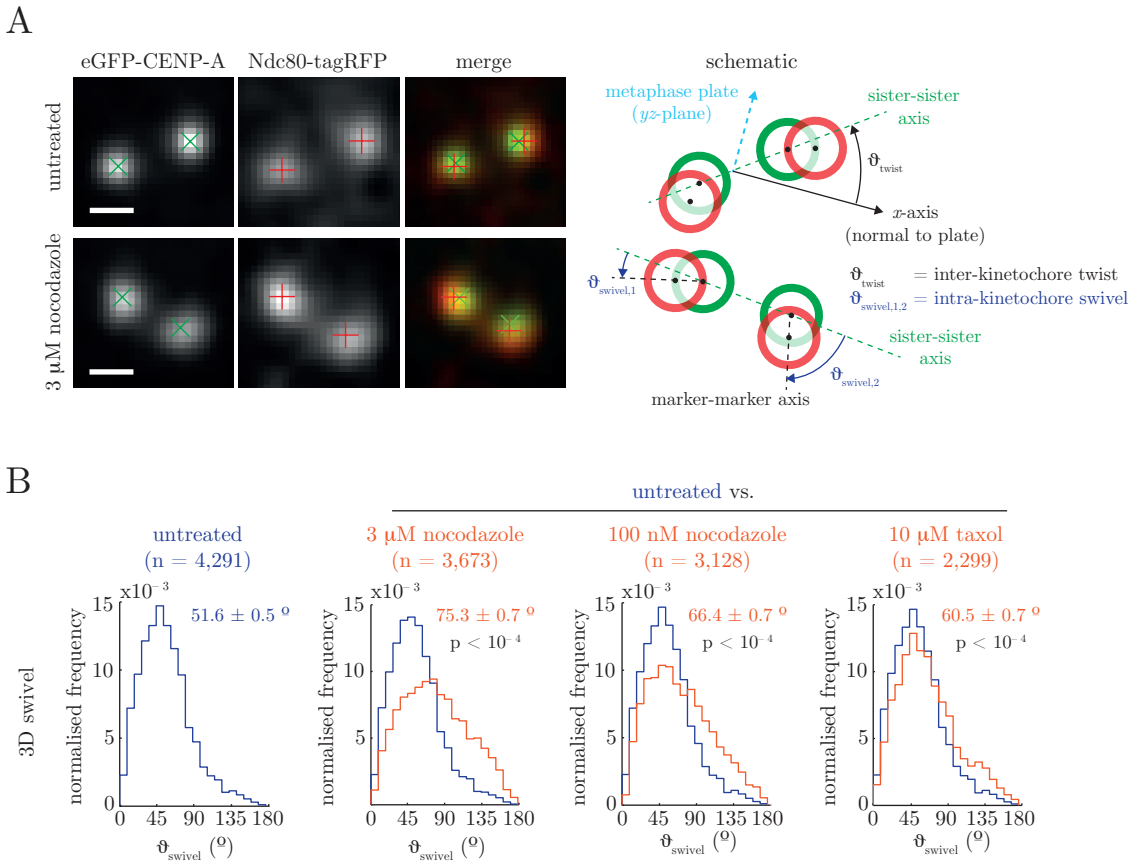

Figure 5.12 *The outer-kinetochore is capable of swivel, a phenomenon more apparent under loss of microtubule pulling forces.*
(A) Example images of kinetochores in untreated metaphase (top) and 3 μM nocodazole-treated (bottom) cells expressing eGFP-CENP-A and Ndc80-tagRFP. Green and red crosses represent eGFP and tagRFP spot centres, respectively. Schematics demonstrate the images to their left, and the angular measurements that can be calculated, with green and red circles representing eGFP and tagRFP signals, respectively. Measurements of swivel, ϑ_{swivel}, are shown in blue and demonstrated by blue curved arrows; twist, ϑ_{twist}, are shown in black and demonstrated by black curved arrows; dashed green lines are sister-sister axes; dashed black lines are marker-marker axes; dashed blue arrow represents the metaphase plate (or *yz*-plane); black arrow represents the *x*-axis. Scale bars = 500 nm.
(B) Histograms of ϑ_{swivel} for untreated (blue; n = 4,291), compared with: 3 μM nocodazole- (middle left; n = 3,669); 100 nM nocodazole- (middle right; n = 3,128); and 10 μM taxol- (right; n = 2,299) treated cells in metaphase. Values given are medians ± standard error. Statistical tests are Mann-Whitney U.

this angle gives an approximation of the 1D intra-kinetochore distance Δ_{1D}, giving an estimate of 60.9 nm in untreated cells similar to Δ_{1D}. This measurement is only equal to Δ_{1D} when the vectors between the two eGFP signals and the two tagRFP signals are parallel. As can be seen in the example for 3 μM nocodazole, this isn't necessarily the case. There are also events where $\vartheta_{\text{swivel}} > 90°$. It remains to be determined whether these extreme events are due to erroneous microtubule attachments, for example merotelic or syntelic attachments, that may physically pull the outer kinetochore around the inner kinetochore towards the opposite pole.

I next quantified the swivel under the different treatments to determine whether swivel can explain the observed changes in Δ_{1D}. In all drug treatments, median swivel significantly increased relative to untreated metaphase cells ($p < 10^{-4}$ in each case). Cells exposed to the highest dose of nocodazole had the largest increase in swivel with a median ($\pm$ standard error) of 75.3 ($\pm$ 0.7) ° (n = 3,669; Figure 5.12 B). The 100 nM nocodazole treatment resulted in a median of 66.4 ($\pm$ 0.7) ° (n = 3,128; Figure 5.12 B). Furthermore, after 10 μM taxol treatment, kinetochores increased the median swivel to 60.5 ($\pm$ 0.7) ° (n = 2,299; Figure 5.12 B). These swivel measurements are in 3D, and therefore swivel measurement is affected by the lower resolution in the z-direction, i.e. subject to higher error for kinetochores swivelling into the z-axis. This would be especially important in nocodazole-treated cells, where kinetochore pairs exhibit a larger range of orientations. In order to investigate this quantitatively, swivel was deconstructed into y and z components. Measurements of $\vartheta_{y\text{-swivel}}$ or $\vartheta_{z\text{-swivel}}$ were calculated within the relevant 2D plane using polar coordinates and thus a sign (and therefore a direction relative to the x-axis) could be assigned. Untreated cells had median values of 8.6 ° and -2.8 ° for y- and z-directional swivel, respectively. This demonstrates that the Ndc80-tagRFP are located on average pointing away from the centromeric chromatin, and towards their spindle pole (Figure 5.4 A), within a small error of swivel measurement. This provides further confirmation that chromatic shift correction was sufficiently accurate.

In order to check whether nocodazole and taxol treatment also caused an increase

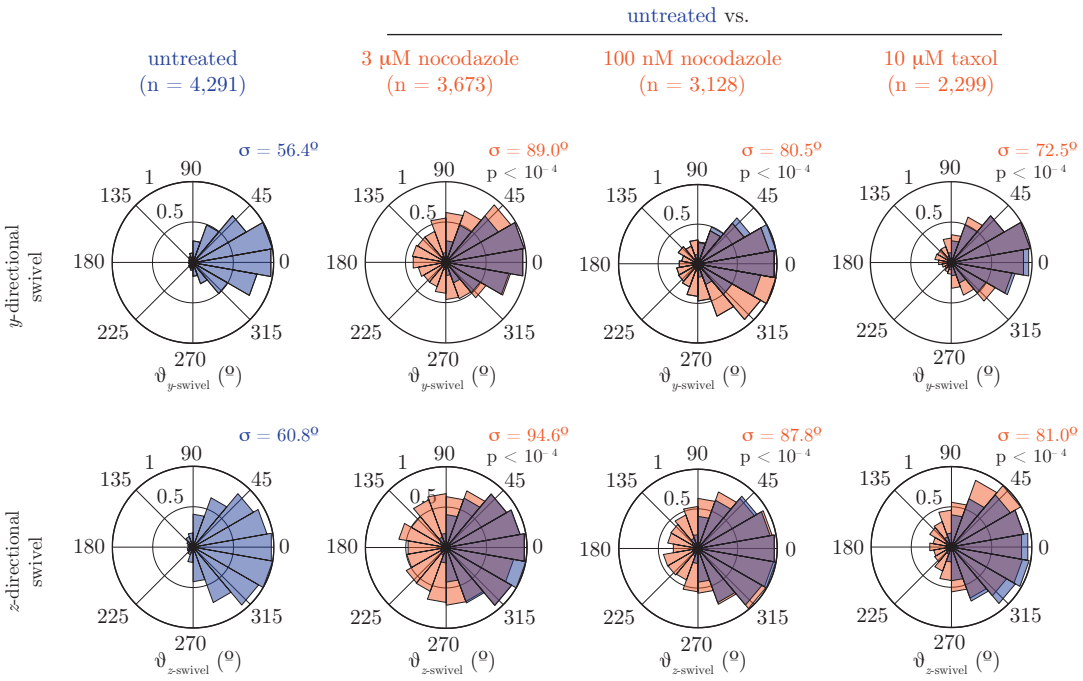

Figure 5.13 *Broadening of the projected swivel distributions under drug treatment.* Rose diagrams of $\vartheta_{y\text{-swivel}}$ (top row) and $\vartheta_{z\text{-swivel}}$ (bottom row) for untreated metaphase cells (blue; n = 4,291), compared with cells treated with (gold): 3 μM nocodazole (middle left; n = 3,669); 100 nM nocodazole (middle right; n = 3,128); and 10 μM taxol (right; n = 2,299). Values given are standard deviations. Standard deviations are statistically compared using F-tests.

in y-directional swivel independent of z-swivel, standard deviations, σ, of the y- and z-swivel distributions were calculated. Kinetochores exhibited a significant increase in σ for $\vartheta_{y\text{-swivel}}$ in cells treated with 3 μM nocodazole ($p < 10^{-4}$, F-test), increasing from 56.4 ° (n = 4,291) to 89.0 ° (n = 3,673; Figure 5.13). Therefore, kinetochores have more pronounced swivel after drug treatment, an increase that is also observed in the xy-plane. Further to this, the 100 nM nocodazole treatment yielded a distribution of $\vartheta_{y\text{-swivel}}$ with σ = 80.5 ° (n = 3,128), while 10 μM taxol treatment resulted in a smaller increase with a σ of 72.5 ° (n = 2,299). Similarly, in the z-direction, untreated metaphase cells had a spread in measurements of $\vartheta_{z\text{-swivel}}$ with a standard deviation of 60.8 °. As expected, $\vartheta_{z\text{-swivel}}$ distributions for the 3 μM and 100 nM nocodazole treatments had increased standard deviations of 94.6 ° and 87.8 °, respectively, and an increase in σ to 81.0 ° in 10 μM taxol. Recall in all this analysis that the kinetochores are filtered so that the eGFP-CENP-A and Ndc80-tagRFP signals are within 100 nm in z, thus $\vartheta_{y\text{-swivel}}$ and $\vartheta_{z\text{-swivel}}$ will not have identical distributions.

The outer kinetochore layer can rotate about the centromeric chromatin. This is observed to be most pronounced when a kinetochore is no longer bound to a microtubule. This gives implications for a role of swivel during prophase and prometaphase, i.e. at a time when kinetochores are establishing attachments to spindle poles. However I now wanted to understand the role of kinetochore swivel during metaphase.

5.8 Swivel dynamics across the metaphase plate

I first chose to investigate the spatial distribution of the kinetochore swivel. Given that Δ could only be measured across a range of 3 μm in the z-axis, I chose to investigate swivel in the xy plane relative to position in the mitotic spindle. Therefore y-directional swivel was investigated with respect to the kinetochore's position in the metaphase plate's y-axis. The metaphase plate was divided into three regions to allow comparison of kinetochores at the centre and the periphery. Any kinetochores further than 4 μm either side of the centre of the metaphase plate in the y-direction were defined as peripheral kinetochores, while those less than 4 μm from the centre were defined as

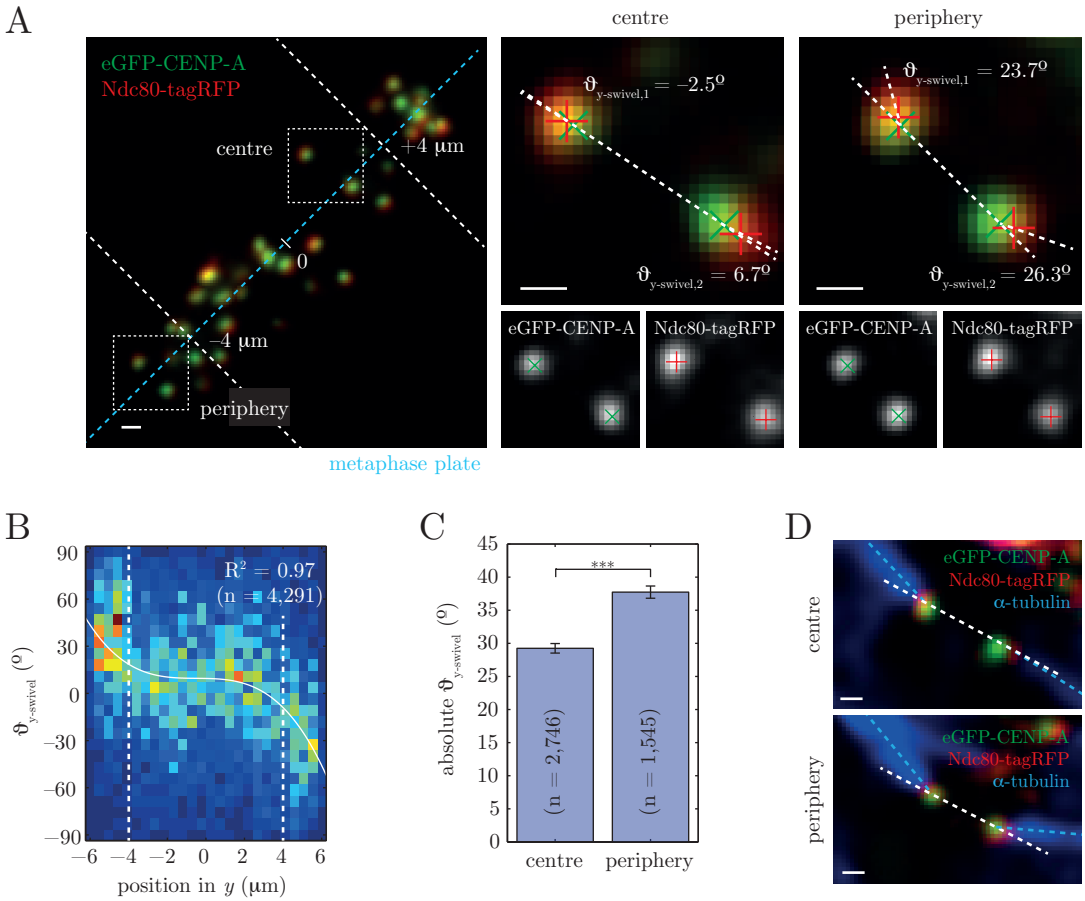

Figure 5.14 *Swivel may allow kinetochores to maintain attachment at the periphery of the mitotic spindle.*
(A) Example image of a cell divided into its metaphase plate's centre and periphery. The blue dashed line represents the metaphase plate, and the white line marks its central point. The perpendicular white dashed lines spaced 4 µm either side of the central point separate the central third (centre) and the outside two thirds (periphery). Each of the images of kinetochore pairs are shown inside white dashed boxes, with appropriate labels. Green crosses and red pluses represent the centre of eGFP and tagRFP spots, respectively. Thick white lines through the kinetochore pairs represent both sister-sister and marker-marker axes. Values given are . Scale bars = 500 nm.
(B) 2D histogram of $\vartheta_{y\text{-swivel}}$ against position in the y-axis (n = 4,291). Dashed white lines represent the divisions between plate centre and periphery. White line represents the best fit 3-fold polynomial, with coefficient of determination, R^2.
(C) Bar plots of median values for $|\vartheta_{y\text{-swivel}}|$ comparing kinetochores in the centre (n = 2,746) and the periphery (n = 1,545). Range bars are standard error. Statistical test is Mann-Whitney U test.
(D) Example images of kinetochore pairs at the metaphase plate centre (top) and periphery (bottom) in cells expressing eGFP-CENP-A and Ndc80-tagRFP after labelling α-tubulin with AlexaFluor-647. White dashed lines are sister-sister axes, blue dashed lines are kinetochore-microtubule axes for each kinetochore. Scale bars = 500 nm.

central (Figure 5.14 A).

By visual inspection, central kinetochores exhibited less pronounced swivel as compared to those at the periphery (Figure 5.14 A). Most significantly, both sister kinetochores at the periphery almost always exhibited y-directional swivel in the same direction, towards the spindle poles (Figure 5.14 A, right panel). To quantify this, a 2D histogram of $\vartheta_{y\text{-swivel}}$ against position in the y-axis was plotted, and the periphery and centre regions annotated (n = 4,291; Figure 5.14 B). On approach towards the periphery of the metaphase plate, kinetochores exhibited a clear change in $\vartheta_{y\text{-swivel}}$. The increase in $\vartheta_{y\text{-swivel}}$ with decreasing y, and the decrease in $\vartheta_{y\text{-swivel}}$ with increasing y, shows that peripheral kinetochores begin to rotate their outer components towards their associated spindle pole. This is more clearly represented by a degree-3 polynomial of best fit (minimising absolute residuals of the equation $ay^3 + by^2 + cy + d = 0$ with the data), where $R^2 = 0.97$ demonstrates that this distribution fits well to the data. To provide a statistical comparison of swivel at kinetochore in the centrals and the peripheral regions, absolute values of $\vartheta_{y\text{-swivel}}$ were measured for each region. Central kinetochores had a median (± standard error) y-directional swivel of 29.3 (± 0.7) ° (n = 2,746), while those in the periphery had a median (± standard error) of 37.7 (± 0.9) ° (n = 1,545). These were significantly different with $p < 10^{-4}$ (Figure 5.14 C). The most likely explanation for the outer kinetochore to point towards the spindle poles is in order to engage microtubules emanating from that direction. In order to test this hypothesis, cells expressing eGFP-CENP-A and Ndc80-tagRFP were fixed with glutaraldehyde. AlexaFluor-647 was then targeted to α-tubulin by antibody staining, allowing direct observation of kMTs. This revealed that microtubules approaching peripheral kinetochores do not approach perpendicular to the metaphase plate, in contrast to those in the centre (Figure 5.14 D). In each of the cases shown in Figure 5.14 D, the microtubule and intra-kinetochore (marker-marker) axes are co-linear. This was observed to be true in almost all kMT attachments not only in untreated cells, but also in 100 nM nocodazole and 10 μM taxol treatments (Figure 5.15). This result implies that a kinetochore's angle of swivel is constrained by its k-fibre, and

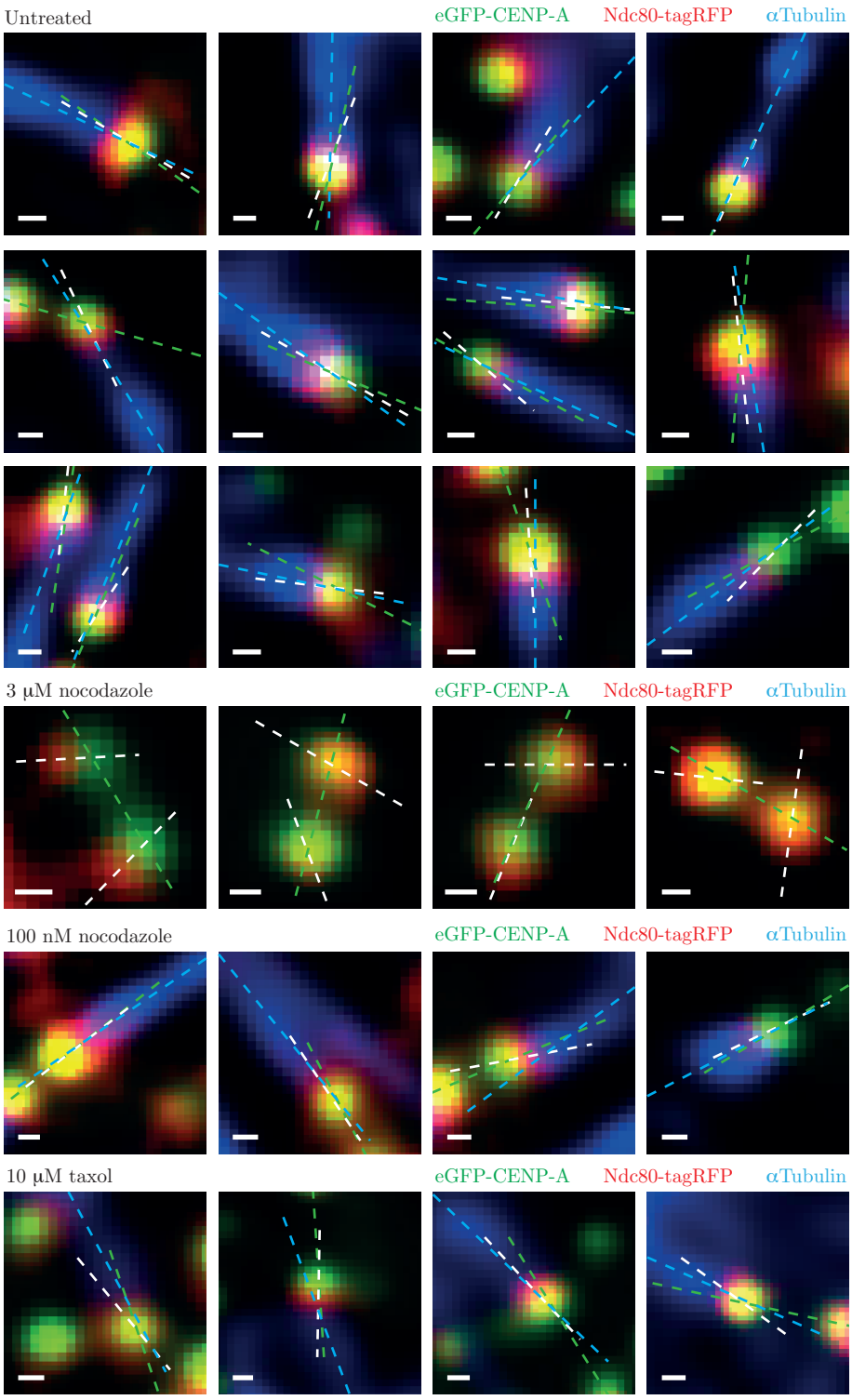

Figure 5.15 *Marker-marker axes appear to correlate with kinetochore-microtubule axes.*
Example images of kinetochores in cells expressing eGFP-CENP-A and Ndc80-tagRFP after targetting AlexaFluor-647 to αTubulin for untreated cells (top three rows), and cells treated with 3 μM nocodazole (fourth row), 100 nM nocodazole (fifth row), and 10 μM taxol (sixth row). Green, white and blue dashed lines represent sister-sister, marker-marker and kinetochore-microtubule axes, respectively. Scale bars = 200 nm.

therefore suggests a kinetochore may experience swivel passively once bi-orientated.

Intra-kinetochore distance, Δ, correlates with spindle assembly checkpoint (SAC) activity (Maresca & Salmon, 2009; Uchida *et al.*, 2009). Various drug and RNA interference (RNAi) conditions revealed a decrease in intra-kinetochore distance results in an active SAC, and therefore kinetochores require a stretch in Δ in order to allow anaphase onset. However, more recent work has demonstrated that, despite a loss of intra-kinetochore stretch, stable kinetochore attachments can satisfy the spindle checkpoint (Tauchman *et al.*, 2015; Etemad *et al.*, 2015; Magidson *et al.*, 2016). Some of these results depended on the 1D measurement of Δ, and therefore suffers the issue of projection onto the sister-sister axis as discussed above. I hypothesised then that swivel may instead play a role in the approach to anaphase onset. As all measurements of Δ in untreated cells used in this work were measured during metaphase, there is no specific reference point for time until anaphase onset. However, it has previously been observed that the metaphase plate thins as a cell progresses through metaphase (Jaqaman *et al.*, 2010). Therefore metaphase plate thickness provides a proxy for time until anaphase onset. Metaphase plate thickness was defined as the standard deviation of all sister kinetochore pair centres for a given time point. After calculating plate thicknesses for all time points, they were divided into three groups: plate thicknesses greater than 0.65 μm were defined to represent early metaphase, those smaller than 0.45 μm were considered to be late metaphase, and those between the two values were considered to be in middle metaphase. Firstly, 2D histograms of Δ_{1D} and Δ_{3D} against plate thickness were plotted (n = 3,056 for 1D, n = 4,291 for 3D; Figure 5.16 A). Correlation analysis of Δ_{1D} yielded a negative correlation coefficient, $r = -0.166$, which was significant ($p < 10^{-4}$). The negative correlation suggests that (projected) intra-kinetochore distance decreases with increasing plate thickness. Indeed, kinetochores in early metaphase had a median ($\pm$ standard error) Δ_{1D} of 51.8 ($\pm$ 1.6) nm (n = 974), which increased significantly to 61.2 ($\pm$ 1.5) nm in late metaphase (n = 860, $p < 10^{-4}$; Figure 5.16 B). Importantly, this matches the suggestion of Maresca & Salmon (2009) that intra-kinetochore distance stretches prior to anaphase onset, which was consid-

ered a necessary step in silencing the SAC. However, the same analysis on 3D intra-kinetochore distance, Δ_{3D}, derived no significant correlation between the Δ_{3D} and plate thickness ($r = 0.023$, $p = 0.137$). Furthermore, there was no significant difference in median Δ_{3D} throughout metaphase ($p = 0.693$), where early and late metaphase kinetochores had median ($\pm$ standard error) Δ_{3D} of 99.9 ($\pm$ 1.9) nm ($n = 1,361$) and 98.9 ($\pm$ 1.3) nm ($n = 1,208$; Figure 5.16 B), respectively. Therefore 3D measurements of intra-kinetochore distance reveal that kinetochores do not stretch prior to anaphase onset, and once again the 1D projection measurement of Δ has yielded misleading results.

Kinetochore swivel causes a decrease in measurements of Δ_{1D} due to projection onto the sister-sister axis, while 3D measurements show that kinetochores are in fact non-compliant. Therefore the decrease in Δ_{1D} between early and late metaphase could be a result of decreased swivel in late metaphase. 2D histograms of 3D kinetochore swivel, and its projections in the xy- and xz-planes, were plotted against plate thickness. The relationship between 3D swivel and plate thickness had a positive correlation coefficient, $r = 0.088$, which was significant ($p < 10^{-4}$; Figure 5.16 C). This suggests that kinetochore swivel increases with plate thickness, or more importantly it decreases with progression through metaphase. This supports the hypothesis that an increase in Δ_{1D} observed as cells progress through metaphase is in fact caused by a decrease in $\vartheta_{\text{3D-swivel}}$. As expected, 3D swivel significantly decreased between kinetochores in early and late metaphase ($p < 10^{-4}$; Figure 5.16 D). Despite the correlation between plate thickness and 3D swivel, the correlation coefficients between plate thickness and either $\vartheta_{\text{y-swivel}}$ or $\vartheta_{\text{z-swivel}}$ were both $r = 0.005$, demonstrating no significant correlation ($p > 0.70$ in both cases; Figure 5.16 C). However, calculating median $\vartheta_{\text{y-swivel}}$ and $\vartheta_{\text{z-swivel}}$ on kinetochores in early and late metaphase yielded a significant difference between the two populations ($p < 10^{-4}$; Figure 5.16 D), supporting the observation that 3D swivel decreases on approach to anaphase. Therefore intra-kinetochore stretch does not increase on approach to anaphase onset, but instead the degree of swivel decreases as the cell progresses through metaphase. I now wanted to investigate whether this

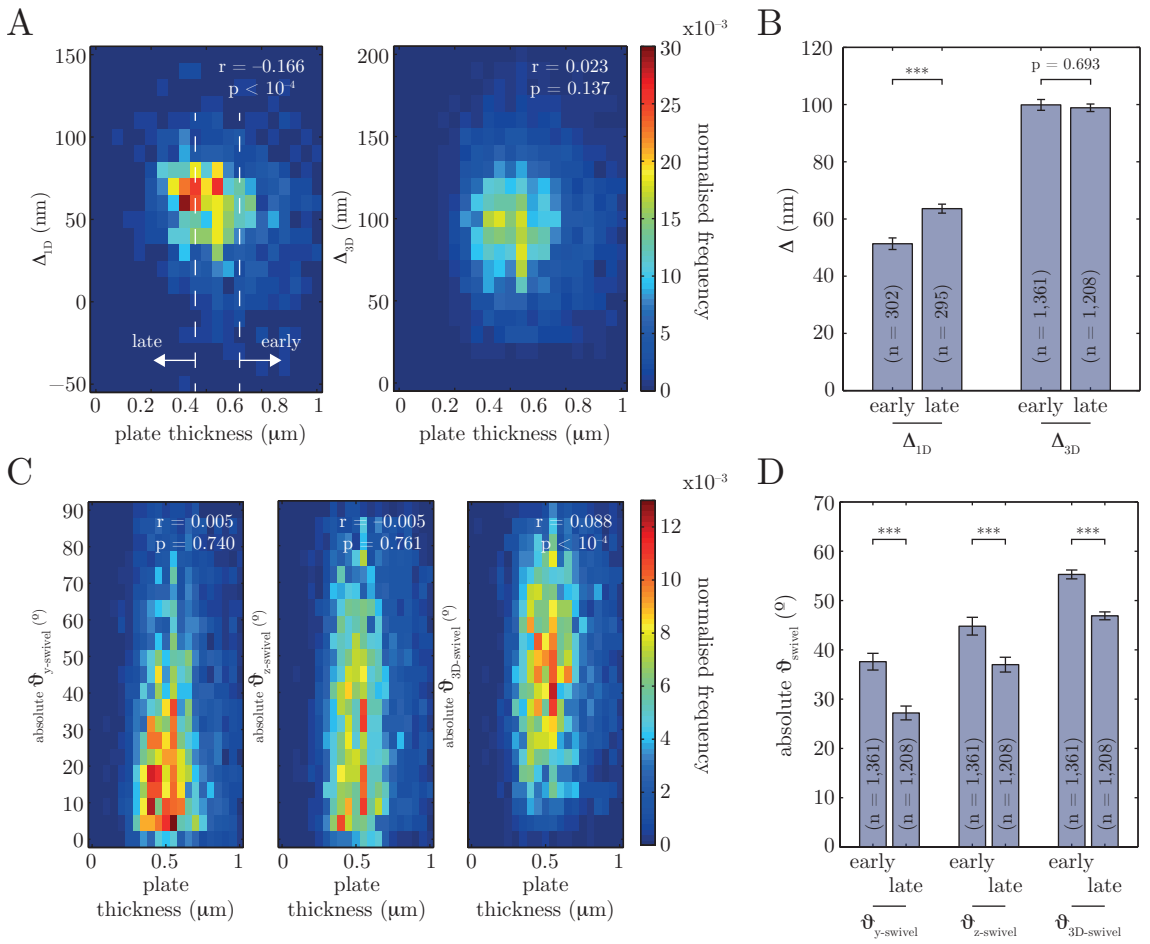

Figure 5.16 Δ *does not correlate with metaphase timing, however* ϑ_{swivel} *does.*
(A) 2D histograms of Δ_{1D} (left; n = 1,002) and Δ_{3D} (right; n = 4,291) against metaphase plate thickness, which serves as a proxy for progression through metaphase. Dashed white lines represent the divisions of early (plate thickness = 0.65 mm) and late metaphase (plate thickness = 0.45 mm). Values given are correlation coefficients, r, and probability of correlation, p.
(B) Bar plots of median Δ_{1D} and Δ_{3D} in early (n_{1D} = 302, n_{3D} = 1,361) and late (n_{1D} = 295, n_{3D} = 1,208) metaphase. Range bars represent standard error. Horizontal lines represent Mann-Whitney U tests (*** represents $p < 10^{-4}$).
(C) 2D histograms of $|\vartheta_{y\text{-swivel}}|$ (left), $|\vartheta_{z\text{-swivel}}|$ (centre) and $\vartheta_{3D\text{-swivel}}$ (right) against metaphase plate thickness (each n = 4,291). Values given are correlation coefficients, r, and probability of correlation, p.
(D) Bar plots of median $|\vartheta_{y\text{-swivel}}|$, $|\vartheta_{z\text{-swivel}}|$ and $\vartheta_{3D\text{-swivel}}$ in early (n = 1,361) and late (n = 1,208) metaphase. Range bars represent standard error. Horizontal lines represent Mann-Whitney U tests (*** represents $p < 10^{-4}$).

decrease in degree of swivel is a relaxation of peripheral kinetochores.

Given that kinetochore swivel measured at the cell periphery is larger than in central kinetochores, it was possible that the observed decrease in swivel through metaphase was due to a smaller swivel at peripheral kinetochores in late metaphase. Temporal and spatial behaviour of kinetochore swivel was investigated by dividing kinetochores firstly into central and peripheral kinetochores, and then by plate thickness to derive whether they are in early, middle or late metaphase. As in the spatial swivel analysis, $\vartheta_{y\text{-swivel}}$ was used in order to allow comparison of peripheral and central kinetochores. A 3D histogram was plotted for $\vartheta_{y\text{-swivel}}$ against position in y and plate thickness (Figure 5.17 A). A sheet was fit through the data, which fit a degree-3 polynomial for correlation between y-directional swivel and position in y, and a linear correlation between swivel and plate thickness ($R^2 = 0.95, n = 2,987$). Interestingly, the correlation between y-directional swivel and position in y observed in Figure 5.14 B was maintained across the spectrum of plate thicknesses, showing that peripheral kinetochores exhibit larger swivel angles throughout metaphase. However, as plate thickness decreased, the range of swivel also decreased. Kinetochores at the periphery of the metaphase plate exhibited a decrease in median values of absolute $\vartheta_{y\text{-swivel}}$ from 45.6 ($\pm$ 1.9) $^\circ$ in early metaphase (n = 455), to 33.5 ($\pm$ 1.4) $^\circ$ in late metaphase (n = 460; Figure 5.17 B). Meanwhile, kinetochores at the centre of the plate also exhibited a decrease in median absolute $\vartheta_{y\text{-swivel}}$ from 33.5 ($\pm$ 1.3) $^\circ$ in early metaphase (n = 906), to 23.1 ($\pm$ 1.2) $^\circ$ in late metaphase (n = 748; Figure 5.17 B). Both central and peripheral kinetochores exhibited statistically different swivel measurements between early and late metaphase, with $p < 10^{-4}$ in each case. This decrease was observed directly in metaphase plates with both high and low plate thicknesses. The examples in Figure 5.17 C are the most peripheral pair of kinetochores in the plate, and therefore those most strongly affected by peripheral swivel. The kinetochore pair located at the periphery of a late metaphase plate had swivel angles much smaller than those at the periphery of an early metaphase plate. Interestingly, the decrease in swivel at peripheral kinetochores primarily occurred between early and middle metaphase, whereas central kinetochores exhibited decrease

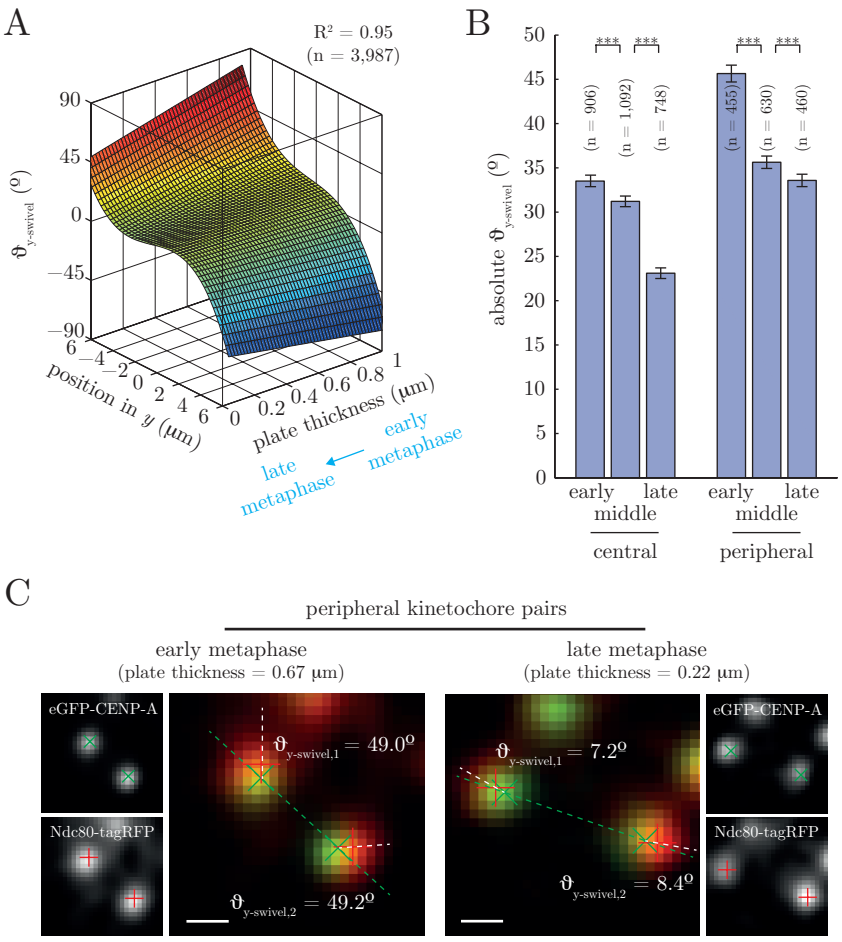

Figure 5.17 *Spatial distribution of swivel is maintained as it decreases through metaphase.*
(A) Best fit sheet through data with axes x'' = plate thickness, y'' = position in y and $z'' = \vartheta_{y\text{-swivel}}$ (n = 4,291). Sheet is fit with a degree-1 polynomial in $x''z''$, and a degree-3 polynomial in $y''z''$, with coefficient of determination, R^2.
(B) Bar plots of median $|\vartheta_{y\text{-swivel}}|$ for central and peripheral kinetochores in early ($n_{central}$ = 906, $n_{peripheral}$ = 455), middle ($n_{central}$ = 1,092, $n_{peripheral}$ = 630) and late metaphase ($n_{central}$ = 748, $n_{peripheral}$ = 450). Range bars represent standard error. Horizontal lines represent Mann-Whitney U tests (*** represents $p < 10^{-4}$).
(C) Example images of kinetochore pairs at the metaphase plate periphery during early metaphase (left; plate thickness = 0.67 μm) and late metaphase (right; plate thickness = 0.22 μm). Green crosses and red pluses represent centre of eGFP and tagRFP spots, respectively. Green and white dashed lines represent sister-sister and marker-marker axes, respecively. Values given are $\vartheta_{y\text{-swivel}}$. Scale bars = 500 nm.

in swivel primarily between middle and late metaphase. This suggests that kinetochores in the peripheral regions of the metaphase plate may prime themselves for anaphase onset more quickly than in the centre, however further investigation is required to better understand SAC activity with respect to spindle architecture and time remaining in metaphase.

5.9 Other Intra-kinetochore Linkages

The kinetochore's linkage between eGFP-CENP-A and Ndc80-tagRFP is rigid under changing levels of tension and attachment status. However it is capable of rotation about the sister-sister axis, which results in a misleading interpretation of intra-kinetochore distances using 1D projection methods. Kinetochore swivel, while not explicitly mentioned, can be observed in previous work with different marked kinetochore proteins in different kinetochore sub-complexes (e.g. Uchida *et al.*, 2009; Tauchman *et al.*, 2015). This gives support that the entire kinetochore is capable of this rotation. However, to investigate this in 3D with accurate chromatic shift correction, cells expressing other pairs of kinetochore proteins tagged with FPs were imaged and processed in the same way as the assay developed here. Firstly, CENP-A was paired with Bub3, which localises to MELT motifs along the length of Knl1 in the outer kinetochore. Bub3 therefore should be localised a similar distance from CENP-A as Ndc80. A Bub3-eGFP plasmid was transiently transfected into mCherry-CENP-A cells and imaged for a single image stack. Bub3-eGFP was observed to swivel about mCherry-CENP-A, suggesting that the entire outer kinetochore region can rotate (Figure 5.18 A). Next, in order to investigate whether kinetochore swivel is restricted only to outer kinetochore proteins, a cell line expressing mCherry-CENP-A and eGFP-CENP-P was imaged over a single z-stack. CENP-P is a subunit of the constitutive centromere-associated network (CCAN), which is part of the inner region of the kinetochore, i.e. it is localised closer to CENP-A than Ndc80. Swivel events were also observed between the centromeric chromatin and inner region of the kinetochore (Figure 5.18 B). This implies that the kinetochore may swivel as a complete entity. As a further measure, CENP-O, which

is part of the same subcomplex of the kinetochore as CENP-P, was observed relative to Ndc80-tagRFP. This was achieved by transient transfection of Ndc80-tagRFP into CENP-O-eGFP cells and imaged over a single image stack. Once again, swivel was observed between CENP-O and Ndc80 (Figure 5.18 C), which demonstrates that kinetochore swivel is a degree of freedom important for the entire kinetochore structure. These measurements however cannot distinguish whether or not the kinetochore can deform, so that the outer kinetochore would exhibit different swivel angles with the centromeric chromatin and CCAN sub-complex. In order to investigate differences in swivel angles between the kinetochore sub-complexes, kinetochores would have to be imaged with three (or more) kinetochore proteins tagged with three (or more) different FPs.

Given the presence of a number of image stacks of cells expressing different pairs of kinetochore proteins tagged with different FPs, preliminary measurements of 3D intra-kinetochore measurements could be obtained as for eGFP-CENP-A and Ndc80-tagRFP. The centre of green and red fluorescent spots were located using Gaussian MMF in all experiments shown in Figure 5.18. Δ_{3D} was then measured between each pair of fluorescent markers and filtered so that Δ_z was no larger than 100 nm as before. The median ($\pm$ standard error) Δ_{3D} between mCherry-CENP-A and Bub3-eGFP was 143.5 ($\pm$ 5.7) nm (n = 337; Figure 5.19 A), suggesting that Bub3 is on average located outside of Ndc80. Furthermore, eGFP-CENP-P was localised a median distance of 125.5 ($\pm$ 4.9) nm outside mCherry-CENP-A (n = 877; Figure 5.19 B). Finally, median Δ between CENP-O-eGFP and Ndc80-tagRFP was 90.9 ($\pm$ 2.1) nm (n = $2,050$), which implies that the C-terminus of CENP-O is localised relatively closely to CENP-A. However, the measurements locating Bub3 and CENP-P are based on a relatively small number of data points when compared to those measured here between CENP-A and Ndc80. Additionally, the presence of positive tails in their distributions may be skewing median measurements. Visual inspection of the distribution suggests that peak values in each distribution derive measurements closer to 120 nm in Bub3-C to CENP-A-N distance, and 80 nm in both CENP-P-N to CENP-A-N and CENP-O-

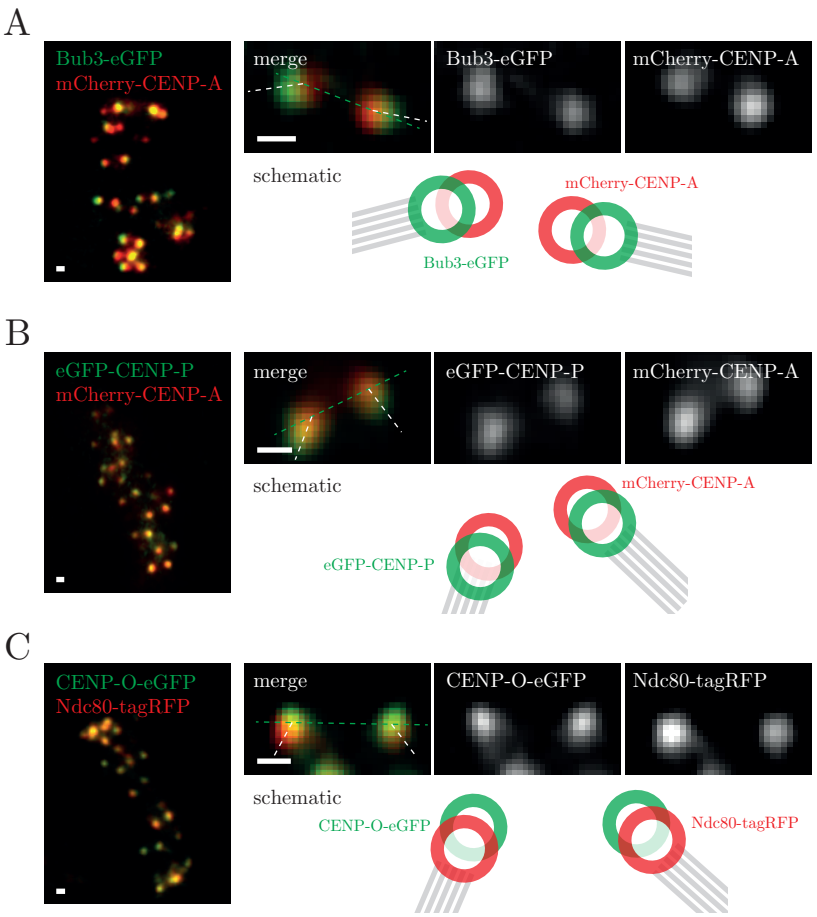

Figure 5.18 *Swivel occurs between the centromeric chromatin, the CCAN, and the outer kinetochore.*
(A–C) Example images of cells expressing: (A) eGFP-Bub3 and mCherry-CENP-A; (B) eGFP-CENP-P and mCherry-CENP-A; and (C) CENP-O-eGFP and Ndc80-tagRFP. Kinetochore pair shown to the right demonstrate presence of swivel between other kinetochore regions. Green and white dashed lines represent sister-sister and intra-kinetochore axes, respectively. Schematics show the orientation of the fluorescent markers, and therefore the kinetochore proteins. Scale bars = 500 nm.

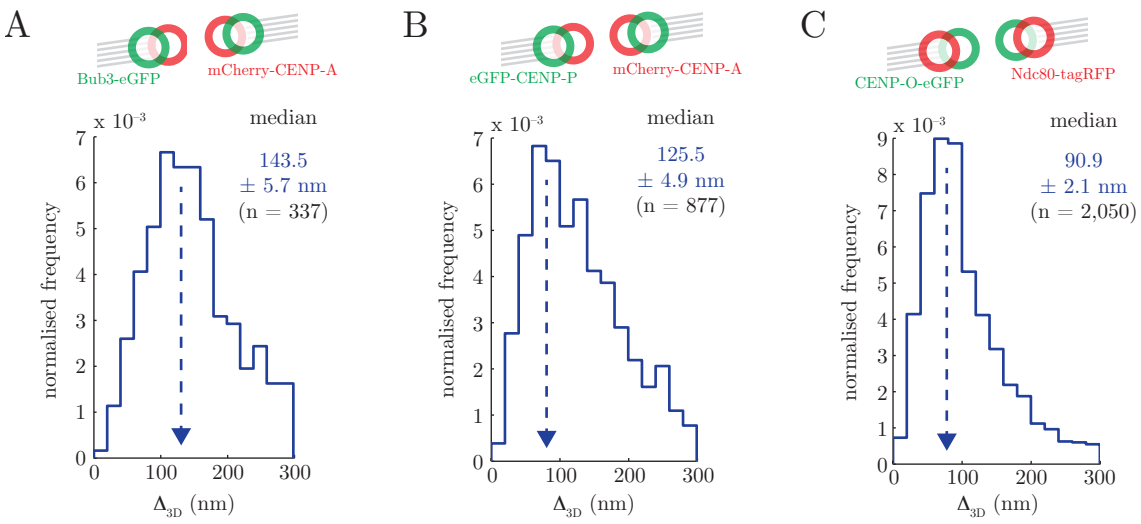

Figure 5.19 *Measurements of* Δ *between other kinetochore proteins.*
(A–C) Measurements of Δ_{3D} in cells expressing: (A) eGFP-Bub3 and mCherry-CENP-A (n = 337); (B) eGFP-CENP-P and mCherry-CENP-A (n = 877); and (C) CENP-O-eGFP and Ndc80-tagRFP (n = 2,050). Dashed blue arrows annotate approximate distribution peak values. Values given are medians ± standard error.

C to Ndc80-C measurements (Figure 5.19; blue dashed arrows). Nevertheless, these preliminary measurements demonstrate that the assay developed in this chapter is capable of allowing us to finally begin to understand the 3D architecture of the human kinetochore in live cells.

5.10 Summary

Here I have shown that the kinetochore scaffold binding chromosomes to microtubules is capable of deformations in 3D during mitosis. However, these deformations occur in a novel degree of freedom not previously investigated in kinetochore structure or dynamics. Once bound to microtubules, kinetochores do not undergo changes in intra-kinetochore distance, Δ, only exhibiting ($\sim$ 8 nm) increase in length once their kMTs are destabilised and detachment can occur. Instead, kinetochores are capable of rotations, called swivel, between multiple inner and outer kinetochore proteins. Upon drug additions, which seek to inhibit kMT force generation capabilities, kinetochore swivel is increased. Increased swivel can explain the previously observed decrease in 1D measurements of Δ after both nocodazole (Maresca & Salmon, 2009; Tauchman *et al.*, 2015) and taxol treatment (Wan *et al.*, 2009). As their measurements of Δ are in fact a pseudo-projection of the kinetochore pair onto the sister-sister axis, an event of large kinetochore swivel results in an underestimate of intra-kinetochore measurement. Further to this, kinetochore pairs at the periphery of untreated mitotic spindles exhibit swivel in the direction of their spindle pole, demonstrating a requirement of swivel for metaphase kinetochores. This swivel both in the centre and at the periphery of the spindle decrease as a cell progresses through metaphase, representing either a requirement of reduced swivel in order to deactivate the SAC, or a maturation step upon SAC satisfaction and reduction in Cdk1-CyclinB1 activity.

Chapter 6

Control of Directional Switching by Kinetochore Phosphorylation

6.1 Background

Sister kinetochores exhibit coordinated dynamics during metaphase and congression (Skibbens *et al.*, 1993), however after the onset of anaphase, sister chromatids are now independent bodies that exhibit directed motion only towards their spindle pole. During interphase, CyclinB1 is associated with Cdk1, however Cdk1's activity is inhibited by PP2A and Wee1 (Mueller *et al.*, 1995). In order to drive the cell into mitosis PP2A activity is inhibited in a kinase-dependent manner (for review see Krasinska *et al.*, 2011). This inhibits Wee1's phosphorylation of its sites on Cdk1 (McGowan & Russell, 1993), these sites instead becoming dephosphorylated by Cdc25 (Dunphy & Kumagai, 1991; Gautier *et al.*, 1991). Complete anaphase onset relies on the degradation of CyclinB1, as their dissociation inhibits Cdk1's activity. In parallel with CyclinB1 degradation, securin is also degraded in order to allow activation of the protein separase (Clute & Pines, 1999). This initiates cleavage of cohesin rings between sister chromatids, and therefore allowing sister chromatids to be segregated (Wheatley *et al.*, 1997; Hagting *et al.*, 2002). Interestingly, it has been shown that if CyclinB1 degredation is slowed, cells are still able to enter anaphase (i.e. sisters separate). However, this is not a normal anaphase because sister chromatids remain at the spindle equator in a metaphase-like plate (Wolf *et al.*, 2006). More recently, work in the Petronczki and other labs has shown that proteins responsible for spindle assembly checkpoint (SAC)

signalling and error correction relocalise to kinetochores during this pseudo-anaphase (Vázquez-Novelle *et al.*, 2014; Rattani *et al.*, 2014; Kamenz & Hauf, 2014; Clijsters *et al.*, 2014). They suggest that continued error correction destabilises kinetochore-microtubule (kMT) binding, resulting in enhanced movement of chromosomes during pseudo-anaphase. Alternatively, their data could suggest that kinetochores remain in a phosphorylated, metaphase-like state while the cell is in an anaphase state. In this chapter I investigated this using kinetochore tracking in collaboration with the Petronczki group.

6.2 A common coordinate system for mitosis

To follow kinetochore dynamics in anaphase, we required a marker for spindle poles. In the absence of a metaphase plate or sister-sister linkage in anaphase, spindle poles provide a reference frame for individual kinetochores. We first sought to confirm the reported pseudo-anaphase phenotype (Vázquez-Novelle *et al.*, 2014; Rattani *et al.*, 2014; Kamenz & Hauf, 2014; Clijsters *et al.*, 2014) in cells expressing kinetochore and spindle pole markers. Cells expressing eGFP-CENP-A (kinetochore) and eGFP-Centrin1 (spindle pole) were transiently transfected with either wild-type (WT) or non-degradable (ND) CyclinB1-mCherry (Figure 6.1 A; both provided by Mark Petronczki). Cells were treated with thymidine in order to align cells in G2 phase of the cell cycle, and then MG132 in order for cells to be aligned just prior to anaphase onset. As expected, during metaphase in both cells expressing WT or ND CyclinB1, kinetochores were aligned at the metaphase plate and CyclinB1-mCherry was present throughout the cell (Figure 6.1 A; left column). Cells expressing WT CyclinB1 showed depleted levels of CyclinB1-mCherry during late anaphase and kinetochores were segregated into two organised plates of sister chromatids (Figure 6.1 A; right column). As previously reported, presence of ND CyclinB1-mCherry throughout the cell during anaphase at levels similar to metaphase meant that kinetochores were no longer capable of moving uniformly towards each spindle pole (Figure 6.1 A; right column). Visual inspection of cells in late or pseudo-anaphase imaged every 7.5 s confirms that kinetochores exhibit

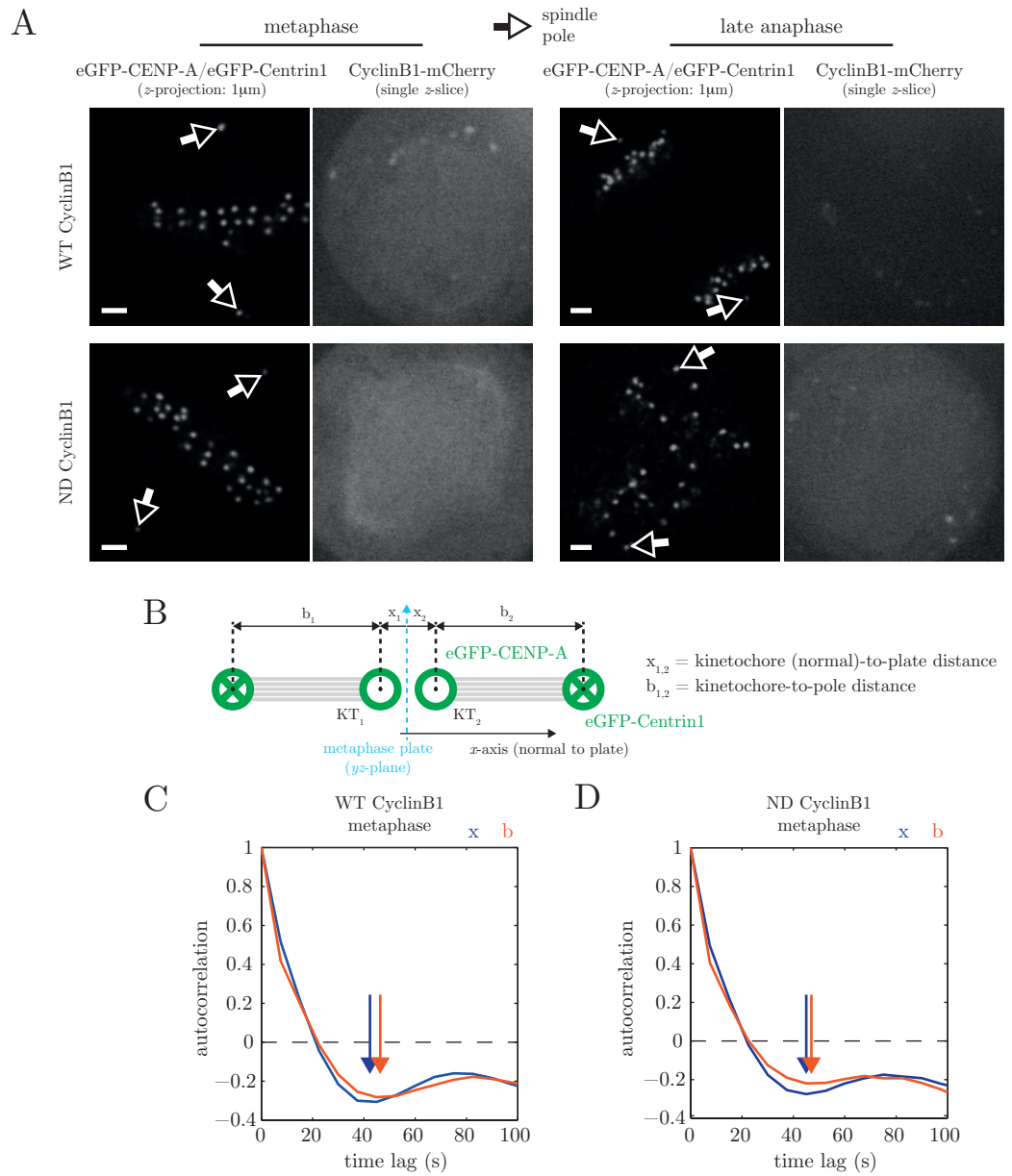

Figure 6.1 *Overexpression of non-degradable CyclinB1 results in no changes to periodic behaviour observed in kinetochore position.*
(A) Example images of cells co-expressing eGFP-CENP-A and eGFP-Centrin1 after transient transfection with wild-type (WT) CyclinB1-mCherry (top row) or non-degradable (ND) CyclinB1-mCherry. Levels of mCherry signal are shown in both metaphase (left column) and late anaphase (right column) for each form of CyclinB1. eGFP signal is shown over a 1 μm z-projection, mCherry signal is shown for a single z-slice. Hollow-headed arrows point towards manually-selected spindle poles. Scale bars = 2 μm.
(B) Schematic demonstrating measurement of x and b using eGFP-CENP-A (hollow green circles) and eGFP-Centrin1 (crossed green circles) location. Blue dashed arrow represents the metaphase plate.
Autocorrelation curves of x (blue) and b (gold) for cells expressing: (C) WT CyclinB1 and (D) ND CyclinB1, demonstrating no difference in periodic behaviour in metaphase between WT and ND CyclinB1. Arrows represent half-period.

more movement during pseudo-anaphase as compared to late anaphase.

To quantify this alteration in kinetochore movement, I tracked kinetochores during metaphase. The metaphase plate typically provides a coordinate system for observation of kinetochore dynamics during metaphase. In this coordinate system, the metaphase plate is the yz-plane, and its normal is therefore the x-coordinate (Figure 6.1 B). However, during late and pseudo-anaphase, the metaphase plate is absent. By measuring the distance between each sister kinetochore and its spindle pole, the kinetochore (k)-fibre length, b, can be determined (Figure 6.1 B). This measurement allows comparison of kinetochore movement dynamics between metaphase and anaphase. Kinetochores have been observed to exhibit quasi-periodic back-and-forth motion about the metaphase plate (e.g. Jaqaman *et al.*, 2010). This motion can be quantified by measuring the autocorrelation of change in a kinetochore's position in metaphase plate x-coordinate. If the spindle poles remained relatively fixed during metaphase, it would therefore be expected that the kinetochore-pole distance, b, would also exhibit quasi-periodic behaviour for a given kinetochore in metaphase. In order to investigate this hypothesis, kinetochores and spindle poles were tracked for their eGFP-CENP-A and eGFP-Centrin1 signals, respectively, in movies of cells expressing WT CyclinB1-mCherry; both x-coordinates and distance b were calculated for each kinetochore during metaphase. The autocorrelation of change in x-coordinate for all kinetochores was plotted (Figure 6.1 C, blue), demonstrating that kinetochores in eGFP-CENP-A/eGFP-Centrin1 cells exhibit back-and-forth motion with half period of $\sim$ 40 s. In order to compare this with potential periodicity in b, the autocorrelation of change in b was calculated for the same kinetochores during metaphase (Figure 6.1 C, gold), which yielded quasi-periodic changes in kinetochore-pole distance with half period very similar to that observed in the x-coordinate. This demonstrates that b distance can be used to represent the temporally regulated dynamics of kMTs, which will allow characterisation of kMT dynamics during late and pseudo-anaphase. In order to ensure that the expression of ND CyclinB1-mCherry does not perturb a kinetochore's ability to regulate kMT dynamics, autocorrelation of changes in both metaphase plate

normal position, x (Figure 6.1 D, blue), and kinetochore-pole distance, b (Figure 6.1 D, gold), were plotted. There is very little difference in the quasi-periodic behaviour of each distance or coordinate measurement, and the expression of ND CyclinB1 during metaphase does not change quasi-periodicity of kinetochore position and kMT dynamics. Thus I have a distance measurement, b, that will be independent of metaphase plate presence, which allows investigation of the observed motion of kinetochores during pseudo-anaphase.

6.3 Dynamic kinetochores in pseudo-anaphase

I next investigated how expression of ND CyclinB1-mCherry would affect kinetochore (k-fibre) dynamics after anaphase onset. Spindle pole (eGFP-Centrin1) and kinetochore markers (eGFP-CENP-A) were tracked in anaphase cells expressing either WT or ND CyclinB1-mCherry. Given the disordered distribution of kinetochores in pseudo-anaphase cells, spindle poles were carefully located by thorough inspection of eGFP signal in both space and time, spindle pole trajectories only being allocated when completely sure. Visual inspection of spindle pole and kinetochore trajectories in cells in late anaphase (Figure 6.2 A, top) demonstrated very little movement relative to their spindle pole over a 2 min trajectory, as expected. Green and red trajectories in Figure 6.2 A represent the position of each kinetochore during the 1 min before (green) and after (red) the time point of the image shown. However, kinetochores in pseudo-anaphase exhibited movement both towards and away from its spindle pole over the 2 min (Figure 6.2 A, bottom). To quantify this movement, the kinetochore-pole distance, b, was measured in late and pseudo-anaphase cells. Calculation of autocorrelation in change in b during late anaphase showed that kinetochores exhibited a slowly decreasing negative autocorrelation (Figure 6.2 B, blue), which is representative of a gradual decrease in b over time. This represents the slow movement of the kinetochores towards their spindle pole expected in late anaphase. Performing the same autocorrelation of change in b for kinetochores in pseudo-anaphase revealed quasi-periodic behaviour in kinetochore-pole distance. Moreover, this behaviour retained the half-period of $\sim$ 40 s exhibited

by kinetochores in their b-distance during metaphase (Figure 6.2 B, gold). Both the observation of trajectories away from the spindle pole and the temporal regulation of a kinetochore's position make it difficult to suggest that kinetochores are losing attachment to k-fibres. Kinetochore speeds during trajectories towards and away from the spindle pole were calculated to investigate further. If a kinetochore detaches from its k-fibre, it would be expected that its velocity away from its spindle pole would be different, if not much smaller, than the motion generated by microtubule pulling forces (at kinetochores moving towards their spindle pole). Velocity measurements were only measured at kinetochores moving towards or away from its spindle pole over at least two consecutive time steps (spanning 15 s). Taking velocity between consecutive 7.5 s time points produced a distribution of velocities for either poleward (P; a decrease in b) or away-from-the-pole (AP; an increase in b) movement. Kinetochores in pseudo-anaphase exhibited median ($\pm$ standard error) velocity measurements of 1.93 ($\pm$ 0.03) μm min^{-1} for AP kinetochores, and -2.01 ($\pm$ 0.03) μm min^{-1} for P kinetochores. Therefore any movement towards the pole exhibits the same dynamics as any movement away from the pole, demonstrating that AP movement is likely caused by a polymerising k-fibre. Interestingly, metaphase cells expressing ND CyclinB1-mCherry had median velocity for AP and P kinetochores of 1.09 ($\pm$ 0.01) μm min^{-1} and -1.14 ($\pm$ 0.01) μm min^{-1}, respectively, which are significantly smaller than those in pseudo-anaphase (Figure 6.2 C, comparing pairs of gold bars). Kinetochores during pseudo-anaphase also exhibit faster velocities than kinetochores in both metaphase and late anaphase in cells expressing WT CyclinB1 (Figure 6.2 C, comparing blue bars to the right-most gold bars). Given pseudo-anaphase kinetochores retain the quasi-periodic behaviour of metaphase kinetochores, this increase in kinetochore velocity may simply be a result of a change in force balance. Kinetochores in metaphase are linked to another kinetochore through centromeric chromatin, so therefore experience more opposing forces through tension within centromeric chromatin, friction caused by the physical bonds between kinetochore proteins and k-fibres, and drag of chromosome arms. After anaphase onset, drag forces on a chromosome may be halved upon separation of the two sister chro-

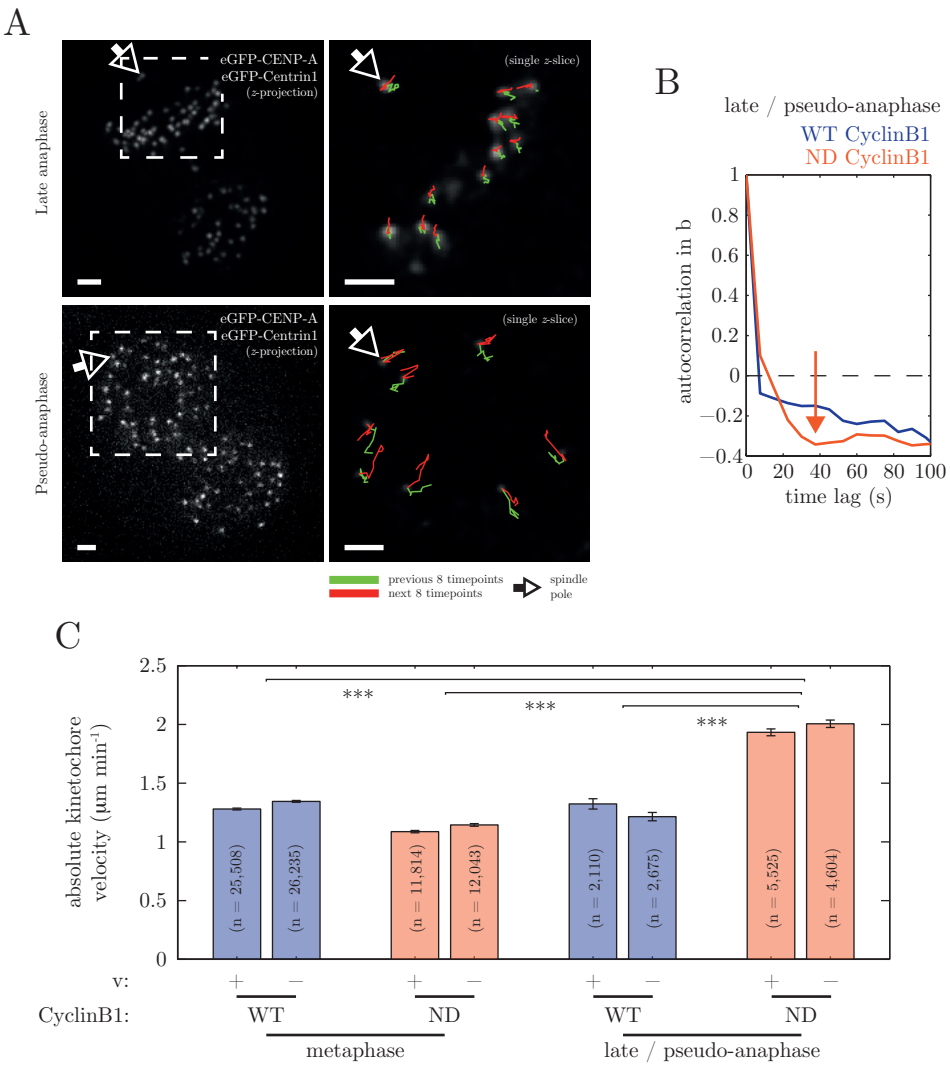

Figure 6.2 *Cdk1 activity in anaphase sustains kinetochore back-and-forth motion.* (A) Example images of kinetochore motion relative to its spindle pole, in late anaphase (top) and pseudo-anaphase (middle). White dashed boxes represent regions shown in the right column. Left column shows full cell z-projections, right column shows single z-slices. Hollow-headed arrows locate manually-selected spindle poles. Green and red lines represent the previous and next 8 time points, respectively. Scale bars = 2 μm.
(B) Autocorrelation in b during late anaphase (or pseudo-anaphase) for cells expressing WT CyclinB1 (blue) and ND CyclinB1 (gold). Gold arrow represents timing of half-period.
(C) Comparison of median kinetochore speed at either kinetochores moving towards (–) or away from (+) their spindle pole. Measurements were made in both metaphase (left) and late anaphase (or pseudo-anaphase; right), comparing cells expressing WT CyclinB1 (left) and ND CyclinB1 (right). Kinetochore speeds in pseudo-anaphase were significantly different ($p < 10^{-4}$; Mann-Whitney U tests) to all other conditions.

matids. Additionally, there is no longer a linkage between kinetochores in anaphase, and therefore inter-kinetochore tension acting against kinetochore movement will be lost. Therefore it may be that kinetochores in pseudo-anaphase may now be able to cause faster polymerisation and depolymerisation of their k-fibres, and therefore can travel faster about the cell. I therefore investigated how stabilising kMT attachment might affect this growth speed.

6.4 Stabilising kMT binding

To investigate whether kinetochores are experiencing less drag in pseudo-anaphase due to loss of its linkage with its sister, an Aurora B inhibitor, ZM1, was added to cells in order to increase drag during microtubule polymerisation and depolymerisation. Aurora B typically destabilises binding of Ndc80 to microtubules by phosphorylating its binding region, however Aurora B inhibition will act to ensure this region is dephosphorylated. eGFP-CENP-A/eGFP-Centrin1 cells expressing ND CyclinB1-mCherry and treated with ZM1 were imaged in metaphase and anaphase. Metaphase kinetochore dynamics were observed after ZM1 treatment in order to ensure it caused the expected effect. Kinetochores expressing a mutant form of Ndc80, acting to stabilise attachment to microtubules (9A-Ndc80), exhibit dampened oscillations during metaphase (DeLuca *et al.*, 2011). Therefore it would be expected that Aurora B inhibition would produce the same phenotype. The autocorrelation of a kinetochore's change in metaphase plate normal position, x, was calculated to observe kinetochore back-and-forth motion. As previously reported, the quasi-periodicity of kinetochores in metaphase were retained after stabilisation of Ndc80-microtubule binding, with half-period $\sim$40 s. Furthermore a shallower first trough demonstrates an expected dampening of these oscillations (Figure 6.3 A). Therefore Aurora B was being successfully inhibited using 2 μM ZM1.

After anaphase onset, Aurora B activity inhibited in parallel with maintained Cdk1 activity also resulted in a pseudo-anaphase state, so that kinetochores were unable to uniformly move towards their attached spindle pole (Figure 6.3 B). Furthermore, like untreated pseudo-anaphase kinetochores, they exhibited back-and-forth motion

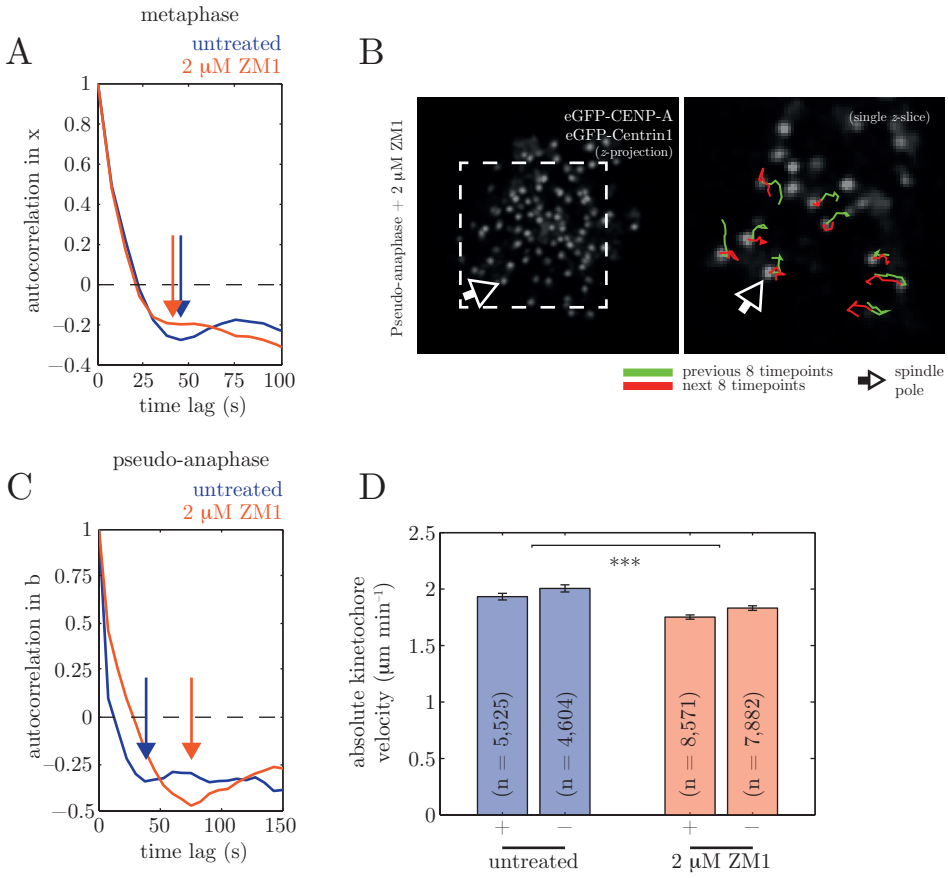

Figure 6.3 *Kinetochore speed during periodic movement increases in psuedo-anaphase.*
(A) Autocorrelation in x during metaphase for cells without (blue) and with (gold) treatment with 2 μM ZM1. Blue and gold arrows represent half-periods.
(B) Example images of kinetochore motion relative to its spindle pole in pseudo-anaphase with Aurora B inhibition (2 μM ZM1). White dashed boxes represent regions shown in the right column. Left column shows full cell *z*-projections, right column shows single *z*-slices. Hollow-headed arrows locate manually-selected spindle poles. Green and red lines represent the previous and next 8 time points, respectively. Scale bars = 2 μm.
(C) Autocorrelation in b during pseudo-anaphase for cells without (blue) and with (gold) treatment with 2 μM ZM1. Blue and gold arrows represent half-periods.
(D) Comparison of median kinetochore speed at either kinetochores moving towards (−) or away from (+) their spindle pole. Measurements were made in pseudo-anaphase, comparing cells not treated (left) or treated with 2 μM ZM1 (right). Significance test was a Mann-Whitney U test (*** represent $p < 10^{-4}$).

towards and away from their spindle pole (Figure 6.2 B), supporting the idea that kinetochores maintain attachment to their k-fibre during pseudo-anaphase. However, calculating the autocorrelation of change in kinetochore-pole distance, b, in Aurora B-inhibited pseudo-anaphase revealed a significant increase in half-period of kinetochore back-and-forth motion, from ∼40 s in untreated pseudo-anaphase to ∼75 s after Aurora B inhibition (Figure 6.3 C). This suggests that Aurora B can affect an individual kinetochore's ability to regulate microtubule dynamics, yet is somewhat suppressed when coupled to its sister during metaphase. In order to understand whether increased drag causes a difference in kinetochore speeds, kinetochores were measured for speed towards and away from the spindle pole in pseudo-anaphase after Aurora B inhibition. The speed of kinetochores decreased to -1.83 ($\pm$ 0.02) μm min^{-1} on P kinetochores, and 1.75 ($\pm$ 0.02) μm min^{-1} for AP (Figure 6.3 D). This is a significant decrease compared to untreated pseudo-anaphase kinetochores ($p < 10^{-4}$), which implies that a kinetochore's speed upon loss of linkage with its sister is dependent upon drag forces from its microtubule-binding scaffold. Notably, the speed of pseudo-anaphase kinetochores after Aurora B inhibition is still significantly larger than those in metaphase.

6.5 Summary

Prior to a normal anaphase in HeLa cells, CyclinB1 is degraded, meaning that Cdk1 can no longer phosphorylate its targets which are dephosphorylated at anaphase onset by mitotic protein phosphatases (Bollen *et al.*, 2009; Wurzenberger *et al.*, 2012). However, when CyclinB1 is no longer degraded and Cdk1 remains active, cells enter an anaphase-like state, called pseudo-anaphase. Sister chromatids are separated in pseudo-anaphase, however can no longer be uniformly moved towards opposite spindle poles. Instead kinetochores move towards and away from their spindle pole. I have discovered here that kinetochores in pseudo-anaphase exhibit quasi-periodic behaviour in their kinetochore-to-spindle pole distance, b, which is not observed in normal late anaphase. Furthermore, I have shown that the half-period of this behaviour is similar to that found in metaphase, suggesting that kinetochores are in a metaphase-like state,

even after the cell has progressed into anaphase. However, kinetochores are capable of faster movement towards and away from spindle poles during pseudo-anaphase when compared to metaphase. This increase could be due to a decrease in drag on the kinetochores as they move about the cell, as Aurora B inhibition, which stabilises kinetochore binding to microtubules, reduces the speed of kinetochores, albeit not down to metaphase speeds. Furthermore, I discovered that Aurora B inhibition maintains quasi-periodic back-and-forth motion of kinetochores in pseudo-anaphase, however with an almost doubled half-period compared to those observed in both an untreated and Aurora B-inhibited metaphase. How a kinetochore is capable of directional switching in the absence of inter- or intra-kinetochore tension will be interesting to solve. Furthermore, it is important to understand the mechanism behind Aurora B's effect on the directional switching frequency, whether directly or through phosphorylation of kinetochore proteins.

Chapter 7

Discussion

7.1 Δ_{3D} measurement in live cells

In this thesis, I have developed a 3D semi-automated live cell imaging assay to track kinetochore proteins tagged with two different coloured fluorophores. Using this assay I have discovered that kinetochores form a non-compliant linkage between centromeric chromatin and the microtubule via the NDC80 complex. This challenges a long-standing model that kinetochores stretch upon attachment to microtubules which exert pulling forces. Crucially, this work differs from previous studies as it measures intra-kinetochore distances in 3D from living cells. Live intra-kinetochores distances have either been measured in 2D (Dumont *et al.*, 2012; Drpic *et al.*, 2015), or after a 1D projection of Δ on the sister-sister axis (Maresca & Salmon, 2009; Uchida *et al.*, 2009). These methods suffer from projection into either the 2D plane or the sister-sister axis (as in the 1D projection). As the work in this thesis demonstrates, kinetochores experience dynamic rotation in all three dimensions, which would therefore result in an underestimate of Δ when projected into either one or two dimensions (Figure 7.1). This is already apparent when comparing published work that uses the same cell line (*Drosophila* S2 cell line expressing fluorescently-tagged CID and Ndc80), but different analysis methods (Maresca & Salmon, 2009; Drpic *et al.*, 2015). Using the 1D projection method (62 nm; Maresca & Salmon, 2009), Δ was 40% shorter than 2D measurements (103 nm; Drpic *et al.*, 2015). This demonstrates the extent of the potential underestimate derived from projecting Δ by even just one dimension.

There is also emerging evidence that the fixation used may have a significant effect

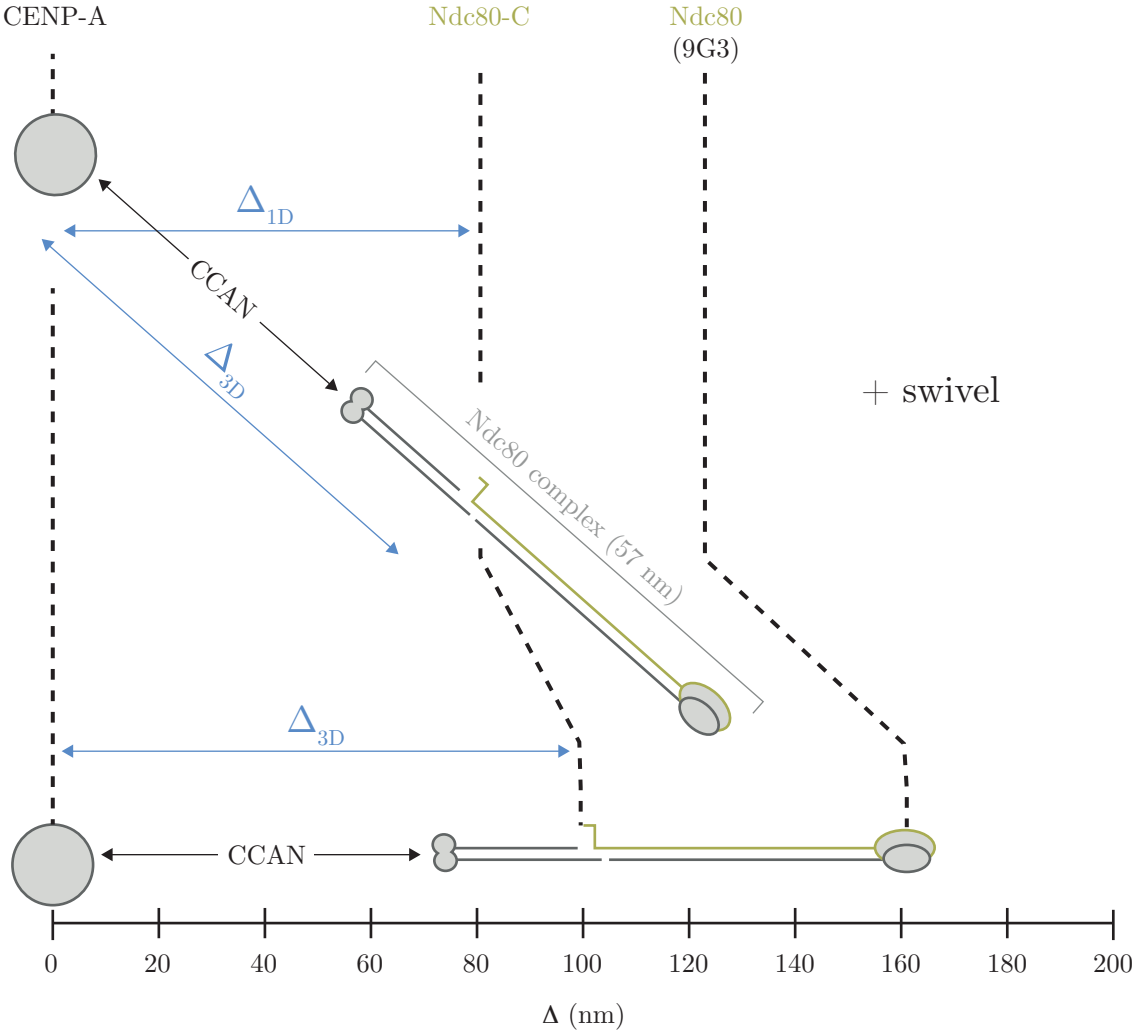

Figure 7.1 *Intra-kinetochore distance is underestimated by measurements in lower dimensions due to intra-kinetochore swivel.*
Swivel events in 3D allow for the outer kinetochore to rotate about the inner kinetochore, meaning that the intra-kinetochore axis is no longer co-linear with the sister-sister axis. Measurements of Δ in 1D or 2D result in an underestimate of intra-kinetochore distances due to these swivel events, as demonstrated above in the distance between CENP-A and the NDC80 complex.

on Δ measurements. Recent work in RPE1 cells showed that Δ measurements differ between chemical fixatives (Magidson *et al.*, 2016). Δ measured in 2D between CENP-T and Ndc80 in cells after formaldehyde-fixation (60 nm) were 25% smaller than those in cells after glutaraldehyde-fixation (80 nm). However, effects on Δ measurements are not consistent within a given fixation method. Experiments in paraformaldehyde-fixed human cells using different Δ measurement methods gave rise to similar distances (Wan *et al.*, 2009; Etemad *et al.*, 2015). Both the 3D- and 1D projection-based measurements of Δ between CENP-C and Ndc80's amino (N)-terminus was $\sim$80 nm for metaphase kinetochores, and $\sim$60 nm when inter-kinetochore tension was perturbed. On the other hand, Δ measured in fixed human cells between CENP-A and the N-terminus of Ndc80 using the 1D projection method (105 nm; Wan *et al.*, 2009) was 25% shorter than that measured in 2D (143 nm; Magidson *et al.*, 2016). One possibility is that chemical fixation may have stronger effects on different sub-structures of the kinetochore. Indeed, electron microscopy of chemically-fixed cells suggests that the outer kinetochore is compacted following protein cross-linking (O'Connell *et al.*, 2012). Despite this, measurements of Δ_{1D} between CENP-C's amino terminus and Ndc80-C are no different between live cells and cells after paraformaldehyde fixation (Varma *et al.*, 2013). It is also apparent that the distance between CENP-A (sister kinetochores) differs in live and fixed cells. The median distance is $\sim$1 μm in live cells, and increases by 60% following fixation (e.g. Magidson *et al.*, 2016). This is an overlooked issue in mitosis research. Therefore, Δ measurements may suffer – or simply be incorrect – depending on which linkages are being studied and the fixation used.

Chemical fixation and reduced dimensionality therefore call into question the measurements of intra-kinetochore distances in fixed cells treated with mitotic spindle poisons. The assay developed in this thesis reveals that kinetochores do not stretch following microtubule attachment, or even when under tension when bi-orientated. Whilst this appears to contradict many studies it is in fact consistent with the data reported by Uchida *et al.* (2009). Although they report that Δ decreases in nocodazole, closer inspection of the distribution of Δ measurements between CENP-A and

Mis12 in HeLa cells reveals a different story, appearing to remain relatively unchanged before and after 160 ng ml^{-1} nocodazole treatment (Uchida *et al.*, 2009, Figure 1 B). The authors avoid quoting average Δ measurements, instead suggesting that there was an increased incidence of stretched kinetochores when attached to the mitotic spindle. However, here kinetochores were considered stretched when its Δ measurement was larger than 95% of measurements calculated after nocodazole-treatment. Crucially, they observed only 15% of untreated kinetochores being stretched relative to this limit, meaning 85% of all untreated kinetochores have nocodazole-like Δ measurements. This therefore supports the result derived in this thesis that kinetochores do not stretch under establishment of kinetochore-microtubule (kMT) attachment and inter-kinetochore tension.

Additionally, the observation of an decrease in intra-kinetochore distance when a kinetochore pair is under tension is consistent with the observation by Dumont *et al.* (2012) that poleward (P) kinetochores are compressed relative to away-from-the-pole (AP) kinetochores in 2D. P kinetochores experience pulling force from the kinetochore-fibre (k-fibre), and therefore would be expected to stretch under the model that kinetochores are compliant. However, the compression on the P kinetochore observed in PtK2 cells could not be reproduced in Δ measurement between CENP-A and Ndc80 in HeLa cells. The reason for this may be that the compression was instead observed using CENP-C as an inner kinetochore marker. CENP-C has more recently been shown to contribute to 32% of linkages with the NDC80 complex, while 61% of its constituents potentially have a structural role in the inner kinetochore (Suzuki *et al.*, 2014). Therefore the observed compression could instead represent a conformational change in inner-kinetochore structure of the P kinetochore, perhaps required to counteract the pulling forces from the depolymerising k-fibre. Alternatively, the difference could originate in experimental methods, as cells were compressed under 2% agarose gel pads to increase the number of kinetochores in one imaging plane. Cells were characterised as viable based on the presence of metaphase oscillations, a microtubule-dense mitotic spindle, and the ability to enter anaphase – criteria also satisfied by J-CENP-

A/Mis12 cells that experience perturbed chromosome congression (see Appendix A). Another source of error could be the projection of Δ into the xy-plane, ignoring effects of z-directional swivel, however this is less likely as my 2D measurements also cannot reproduce their result. A final difference is that my coordinates for eGFP-CENP-A and Ndc80-tagRFP are corrected for chromatic shift in the z-direction, including an appreciation for chromatic shift's dependence on focal depth. Nevertheless, it will be interesting to investigate the dynamic CENP-C to Ndc80 linkage in more detail to better understand its importance in human cells during kinetochore oscillations.

My data reveals that Δ increases at nocodazole-treated kinetochores. Meanwhile measurements of Δ in Uchida *et al.* (2009) still represents a decrease in intra-kinetochore distance under loss of kinetochore attachment, albeit very small. However, their Δ measurements were calculated using the 1D projection, and therefore suffer the underestimate due to projection. Given our observation that nocodazole-treated kinetochores suffer more from this projection issue than untreated kinetochores, their data might in fact represent a slight increase in Δ after nocodazole-treatment. Furthermore, recent electron microscopy of human kinetochores before and after taxol-treatment suggests a compaction of the outer kinetochore upon application of force (Magidson *et al.*, 2016). Crucially, this would explain our observation of an increase in Δ in nocodazole-treated cells. The physical mechanism behind this compaction is not yet understood, however it may represent a conformational change upon establishment of kMT attachment. Mps1 kinase, which directly competes with microtubules for binding to Ndc80's N-terminus (Ji *et al.*, 2015; Hiruma *et al.*, 2015), is re-localised upon microtubule attachment in budding yeast kinetochores (Aravamudhan *et al.*, 2014). The intra-kinetochore mechanism mediating this re-localisation of Mps1 may represent such a change in conformation. Indeed, many different combinations of kinetochore proteins have been used to measure intra-kinetochore distances, some of which may reveal conformational changes within the kinetochore. The assay developed here now provides the tools to be able to faithfully deconstruct live 3D structural changes of the kinetochore, if any, throughout mitosis.

7.2 The mechanism and purpose of swivel

A key finding from this work is kinetochores are able to swivel, that is rotate relative to the sister-sister axis. However, the mechanism behind this rotation is unclear. On one hand, it could represent a full rotation of the entire kinetochore – which was reported previously by Wan *et al.* (2009) and called "tilting". In this situation the distribution of CENP-A and Ndc80 rotate in unison (Figure 7.2 A). Alternatively, outer kinetochore subunits may move around the distribution of CENP-A nucleosomes at the centromere. We call this event outer layer remodelling (Figure 7.2 B).

Kinetochore tilt, parameterised as Θ, was previously discussed as a possible cause for underestimate of Δ measurements using the 1D projection method (Wan *et al.*, 2009, Supplementary Figure S3; shown for swivel in Figure 7.1). They observed correlated rotation of the inner and outer kinetochore, based on measurement of the long and short axes of elliptical fluorescent signal. Crucially, kinetochores after taxol-treatment are more tilted relative to the sister-sister axis than untreated kinetochores, consistent with my observation of increased swivel. This was also confirmed recently in RPE1 cells (Magidson *et al.*, 2016), where tilt was instead parameterised as $kTilt$. However, tilt was not sufficient to completely correct for rotation of the intra-kinetochore axis away from the sister-sister axis, and therefore their "corrected" measurements of Δ in taxol remained smaller than those in untreated kinetochores. Their correction method relies on fitting a line through the distribution of Δ_{1D} against average tilt on both kinetochores in each pair, so that measurement of zero tilt would provide the corrected measurement of Δ. However, if tilt was the only factor causing any underestimate in Δ after 1D projection, the measurement of Δ at 90° tilt should be zero, as the two kinetochore proteins would be projected on top of one another. However, this is not the case in their analyses. For example measurement of Δ between CENP-A and Ndc80 at 90° tilt yields $\Delta = 77$ nm. This implies that, while tilting of the kinetochore exists, it cannot completely explain the underestimate in Δ measurement after 1D projection. Therefore, it is likely that the outer kinetochore can remodel itself around inner kinetochore subunits. In fact, preliminary observation of untreated

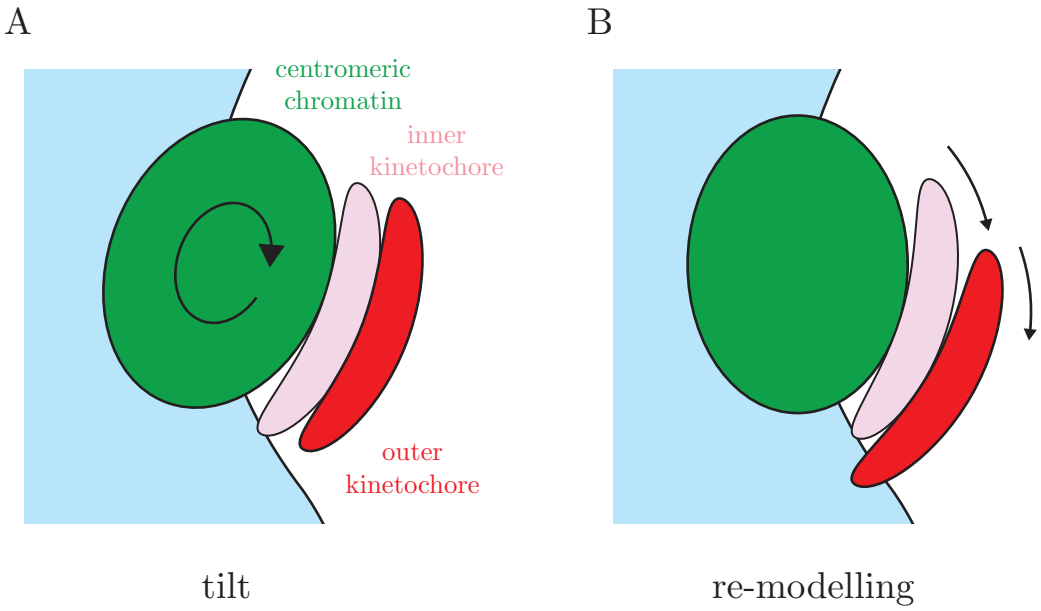

Figure 7.2 *Swivel can be manifested by either tilt or re-modelling.*
In the case of a swivel event, a kinetochore may have rotated in one of two ways. (A) As has been previously observed (Wan *et al.* 2009; Magidson *et al.* 2016), the entire kinetochore can rotate in unison. This is known as 'tilt', and has been previously parameterised as both Θ (Wan *et al.* 2009) and ktilt (Magidson *et al.* 2016). (B) Additional proposed form of observed rotation, where outer kinetochore rotates about the inner kinetochore, which rotates about the centromeric chromatin, known as 're-modelling'.

HeLa kinetochores expressing eGFP-CENP-A and Ndc80-tagRFP using 3D structured illumination microscopy (SIM) demonstrates that tilt and swivel do not necessarily correlate (Smith and McAinsh, unpublished observations). However, more 3D-SIM experiments observing the distribution of each kinetochore component in live cells is required to determine the correct mechanism, if not a combination of the two.

The intra-kinetochore axis corresponds with the k-fibre axis suggesting that swivel occurs as a consequence of external forces applied by microtubule dynamics. This is supported by the observation that swivel was more pronounced in taxol-treated cells where microtubule dynamics are suppressed (Figure 5.11). This swivel was significantly smaller than that in either high or low doses of nocodazole. This demonstrates that microtubule-attachment is sufficient to limit the amount of swivel from the kinetochore. Furthermore, mitotic spindle architecture is perturbed after taxol-treatment, decreasing in length (Snyder & Mullins, 1993). With spindle poles closer to the kinetochores, the angle at which k-fibres approach metaphase kinetochores (and therefore angle of swivel) may be larger (Figure 7.3), and may therefore explain the increase compared to untreated metaphase cells. Remodelling of the outer kinetochore layer would require dissociation and re-association of inner-to-outer kinetochore linkages. One idea is that mitotic kinase activity may be required to destabilise the binding of CENP-C and -T with outer kinetochore proteins. This implies that tilting may be the most favourable mechanism for the observed swivel. However, given that previous observations of tilt cannot fully account for underestimates in Δ measured in taxol-treated cells (given Δ is fixed), swivel may require an active process. A recently observed redistribution of outer kinetochore proteins on chromosome arms would allow remodelling of the outer kinetochore. In *Xenopus* egg extracts and RPE-1 cells, CENP-C was distributed within chromatin neighbouring the centromere when treated with nocodazole (Wynne & Funabiki, 2015). This CENP-C signal is therefore located in regions where Ndc80-tagRFP was observed to swivel. This may provide a mechanism by which subunits of the KNL1-MIS12-NDC80 (KMN) complex can rotate around centromeric chromatin, and more importantly be localised inside of the CENP-A, manifesting as swivel (Figure 7.4). Fur-

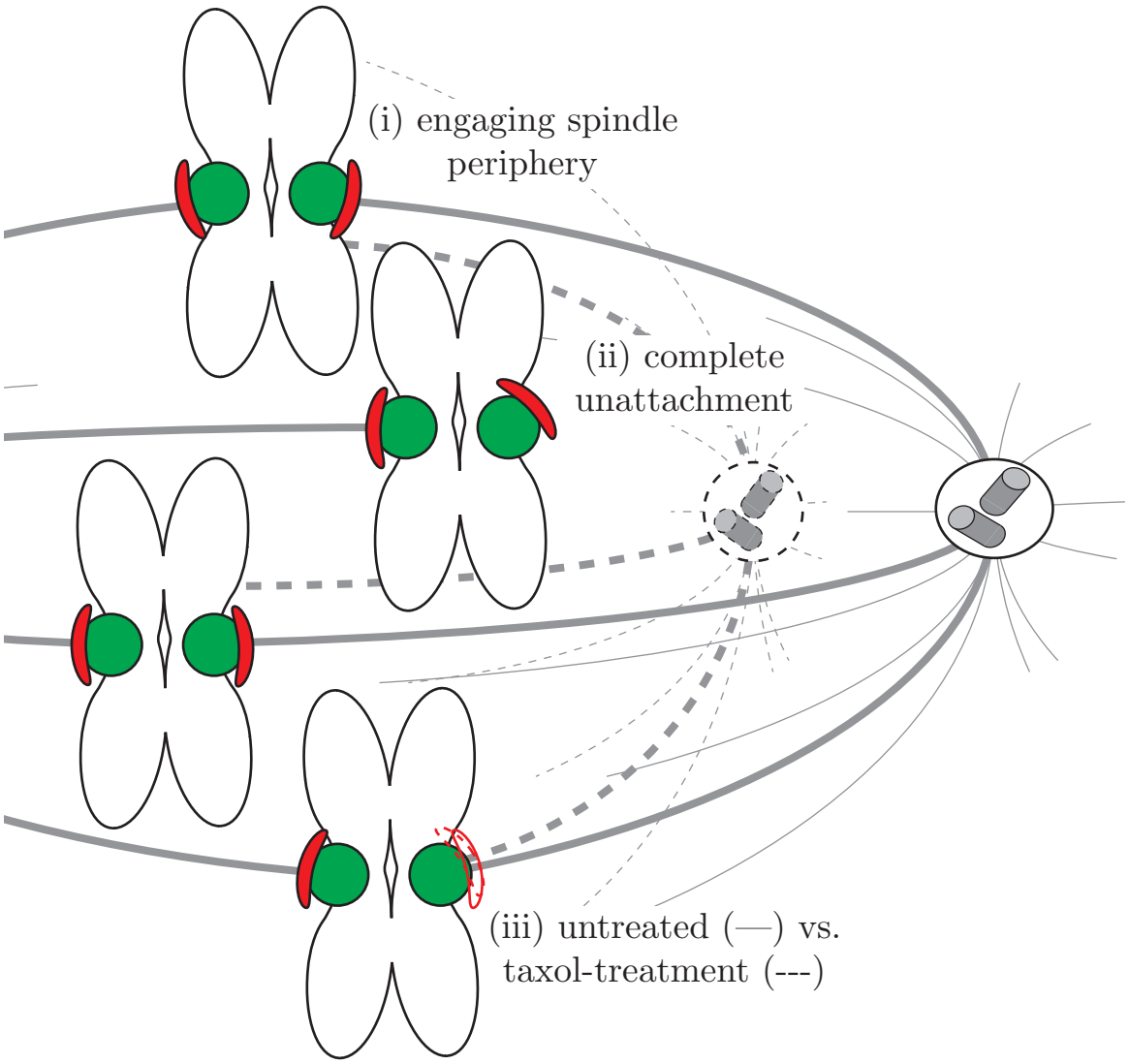

Figure 7.3 *Occurrences of swivel within the spindle.*
Swivel events occur throughout the mitotic spindle, but are more pronounced (i) at kinetochores at the spindle periphery, (ii) when not bound to a kinetochore-fibre, and (iii) potentially after taxol-treatment (dashed spindle, spindle poles and outer kinetochore) as a consequence of shorter spindle length, and therefore spindle architecture.

thermore, given that the spreading of CENP-C either side of the centromere decreases in the absence of multiple mitotic kinases (Mps1, Aurora B, Plk1), and is deregulated by PP1 phosphatase, swivel could be actively regulated and/or deregulated. This would also explain the gradual decrease in swivel during metaphase, at a time when kinetochores become gradually dephosphorylated by protein phosphatases. This could be tested by, for example, inhibition of Aurora B. However, to avoid consequential intra-kinetochore "stretch" due to hyper-stabilisation of Ndc80 microtubule-binding, its inhibition would need to be investigated either in nocodazole-treated cells or cells expressing an Ndc80 mutant with lower microtubule-binding affinity.

Importantly, allowing kinetochores the ability to swivel increases the likelihood of encountering microtubules during search-and-capture in prometaphase. CENP-E in the fibrous corona has been observed to form crescent-shaped collars in the absence of microtubules (Thrower *et al.*, 1996; Yao *et al.*, 1997; Hoffman *et al.*, 2001). The formation of crescent-shapes have been investigated in balancing speed and accuracy of search-and-capture at the start of mitosis (Magidson *et al.*, 2015), however outer kinetochore swivel with a constant plate size has not yet been investigated. Modelling of search-and-capture with this in mind, and comparing to knowledge of typical time in this process in live cells, may allow predictions for certain parameters in the mechanism, such as friction of rotation. Additionally, investigation of swivel in unattached kinetochores with improved temporal resolution would allow characterisation of the kinetics of swivel. This would give an indication whether swivel is a passive or active process, where rotation may be more deterministic if active, or free if passive.

The absence of intra-kinetochore stretch challenges current models of error correction by the CPC, each of which rely on the physical movement of Aurora B's outer-kinetochore substrates away from the pool of CPC at the inner centromere (Lampson & Cheeseman, 2011). However, swivel provides a perfect alternative, which if anything allows a more clear-cut model. Instead of merotelic attachment manifesting itself as a, say, $\sim$ 15 nm decrease in distance between the inner centromere and outer kinetochore, this model would allow erroneously attached kinetochores to swivel into direct

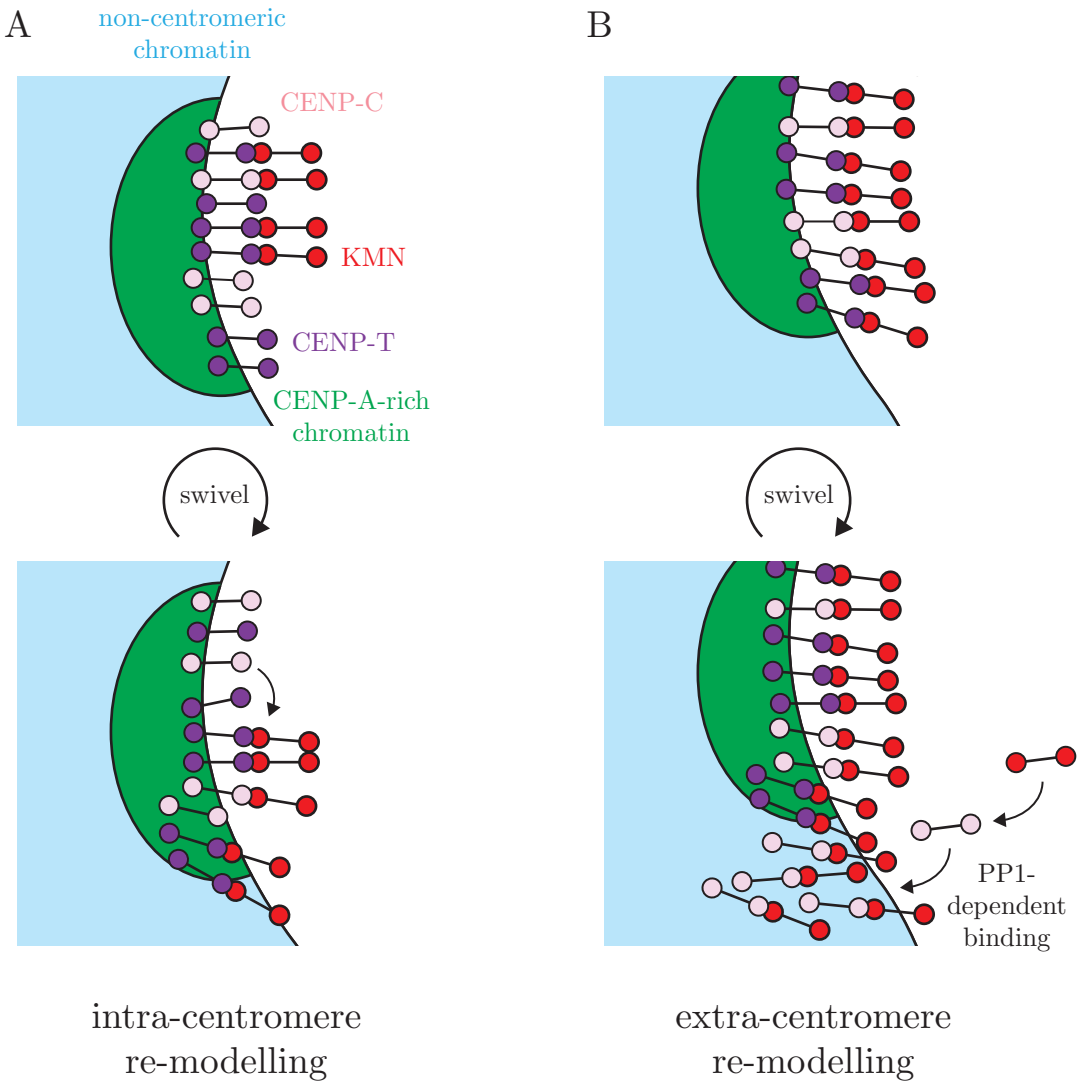

Figure 7.4 *Re-modelling may occur within centromeric, or neighbouring, chromatin.* Kinetochore re-modelling may occur as a consequence of (A) movement of outer kinetochore subunits within the already-established inner centromere, and/or (B) due to previously reported PP1-deregulated recruitment of CENP-C to extra-centromeric chromatin, forming binding sites for the KMN.

contact with the concentrated pool of Aurora B (Figure 7.5). This model would enforce a bias in kinetochore orientation so that the outer kinetochore would favour distal positioning from the inner centromere. This supports the current model for efficient error correction: the concentration gradient model, in which microtubule-binding components of the outer kinetochore making erroneous kMT attachments are more more likely to be localised closer to the concentrated CPC pool at the inner centromere. However, the only difference is that erroneous attachment leads to $> 90°$ swivel, which would be would more easily move these outer kinetochore components in the vicinity of the CPC pool than a decrease in delta. Another model for CPC's mechanism of error correction, the "dog leash" model, suggests that the INCENP/Survivin/Borealin complex, which binds H3 and H2B nucleosomes immediately proximal to the kinetochore, can extend to the outer kinetochore in order to target Aurora B to its substrates. However, another reason for this extension may be to target Aurora B to substrates in the inner kinetochore. For example, Aurora B phosphorylates MCAK in order to promote its depolymerase activity (Shao *et al.*, 2015). MCAK is located at the inner centromere during metaphase, and therefore the "dog leash" model would promote MCAK's activity, increasing frequency of catastrophe within the k-fibre. Therefore the "dog leash" model may play a role in destabilising attachments when the kinetochore swivels, but instead has a primary role in regulating microtubule dynamics via inner kinetochore-localised mitotic motors.

7.3 Cdk1-dependent kinetochore state

Overall, the favoured mechanism for actively distributing inner kinetochore linkers to outer components requires activity from mitotic kinases, and deregulation by protein phosphatases. These phosphatases become most important at anaphase onset when the Cdk1 kinase becomes inactive, at which time PP1 and PP2A dephosphorylate the kinetochore. Inefficient degradation of CyclinB1 allows sister chromatid dysjunction, however sisters are no longer uniformly segregated (Wolf *et al.*, 2006). Cells become arrested in what is called pseudo-anaphase. As has been published (Vázquez-Novelle

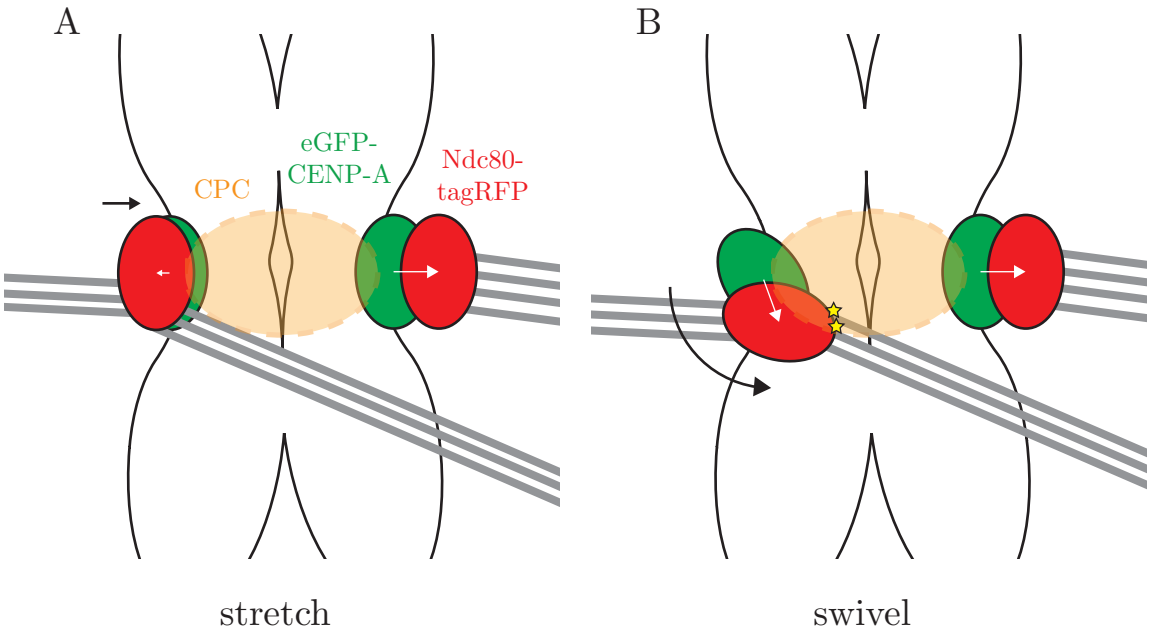

Figure 7.5 *Swivel allows easier interaction with error correction machinery.* In the case of merotelic attachment, a kinetochore may experience deformation. (A) Current model of error correction relies on a movement of the outer kinetochore (Ndc80-tagRFP; red) towards the chromosome passenger complex (CPC; gold). This brings erroneous contacts into a small portion of the CPC pool. White arrows represent measured delta distances.
(B) Proposed model of error correction dependent on swivel of outer kinetochore about the centromeric chromatin (eGFP-CENP-A; green) so that a larger proportion of erroneous contacts can reach the CPC pool for phosphorylation (yellow stars) of Aurora B's target sites. White arrows represent measured delta distances, where each the two arrows have the same magnitude.

et al., 2014), work in this thesis demonstrates how Cdk1 activity in pseudo-anaphase causes individual kinetochores to exhibit back-and-forth motion towards and away from their spindle pole. This behaviour has the same characteristic half-period as oscillations exhibited by kinetochore pairs about the spindle equator during metaphase. These oscillations are caused by regulation of microtubule dynamics. However, during normal anaphase these movements are suppressed, perhaps due to a switching off of microtubule rescue at anaphase onset. Accompanying experiments by Lola Vázquez-Novelle (see Vázquez-Novelle *et al.*, 2014) demonstrated that Aurora B remains at kinetochores in pseudo-anaphase. Their interpretation of the observed back-and-forth motion of pseudo-anaphase kinetochores is therefore that kMT attachments are destabilised by Aurora B's kinase activity. This was based on the assumption that loss of inter-kinetochore tension (sisters are separated in pseudo-anaphase) results in loss of intra-kinetochore stretch, and therefore the error correction pathway would be active. However, the result that the human kinetochore does not stretch under force now contradicts this assumption.

The hypothesis that kMT attachments were destabilised during pseudo-anaphase was contradicted by a number of observations. Firstly kinetochores exhibited temporally regulated back-and-forth motion, which would be very unlikely if kinetochores became continuously unattached from their k-fibres. Next, kinetochores had similar speed of movement both towards and away from the spindle pole during pseudo-anaphase. An unattached kinetochore would be unlikely to drift away from the spindle pole with speeds similar to that generated by depolymerising microtubules. Finally, back-and-forth motion continued in inhibition of Aurora B activity, which acts to stabilise kinetochore attachments to its k-fibres.

However, this does not represent a complete loss of CPC activity. For example, kinetochores may experience more pronounced swivel as they are pushed away from the spindle pole by their attached k-fibres. Based on my suggestion of an adjusted concentration gradient model of error correction, increased swivel would increase interaction between the outer kinetochore and Aurora B (Figure 7.5). Therefore at-

tachment between the outer kinetochore and kMTs may be destabilised. This would promote detachment of kinetochores from their k-fibres. However, as described above, this is not likely, and therefore it is unlikely that kinetochore swivel increases during pseudo-anaphase. However, this requires direct observation to confirm this. An alternative possibility may be explained using the polar ejection force (PEF), as these forces may also remain in pseudo-anaphase. During metaphase, the PEF is mediated by chromokinesins, which are plus-directed motor proteins that bind chromosome arms (Rieder *et al.*, 1986). These chromokinesins then direct chromosomes towards the spindle equator during metaphase. If there are PEFs during psuedo-anaphase, they would be working in the same direction as forces from polymerising k-fibres (away from the spindle poles), and therefore any potential swivel caused by drag forces on chromosomes would be eliminated. In this situation, only the "dog leash" model of error correction can take place, as the outer kinetochore is not in the vicinity of the inner centromere. Therefore Aurora B can mediate, but no longer destabilise, kMTs attachments. This could explain the ability for kinetochores to exhibit back-and-forth motion during pseudo-anaphase. In support of this, the inhibition of Aurora B in pseudo-anaphase resulted in longer time between directional switches in kinetochore back-and-forth motion. MCAK is phosphorylated by Aurora B during metaphase in order to promote its depolymerase activity. Inhibition of Aurora B would therefore cause reduced depolymerase activity at k-fibres, so that the frequency of rescues is decreased, which would result in longer duration between directional switches, as observed.

A novel observation in this work is that kinetochores temporally regulate microtubules in their k-fibres to generate back-and-forth motion in the absence of their sister. Therefore kinetochores do not require tension in order to initiate directional switches. This supports proposed models of an intrinsic "tension-clock" mechanism within kinetochores that determines a common rate of directional switching on each sister kinetochore (Burroughs *et al.*, 2015; Figure 7.6 A). During metaphase, the presence of tension between kinetochores acts to accelerate the P kinetochore clock, while it stabilises (slows) the AP clock. With efficient tension generation, this causes a dis-

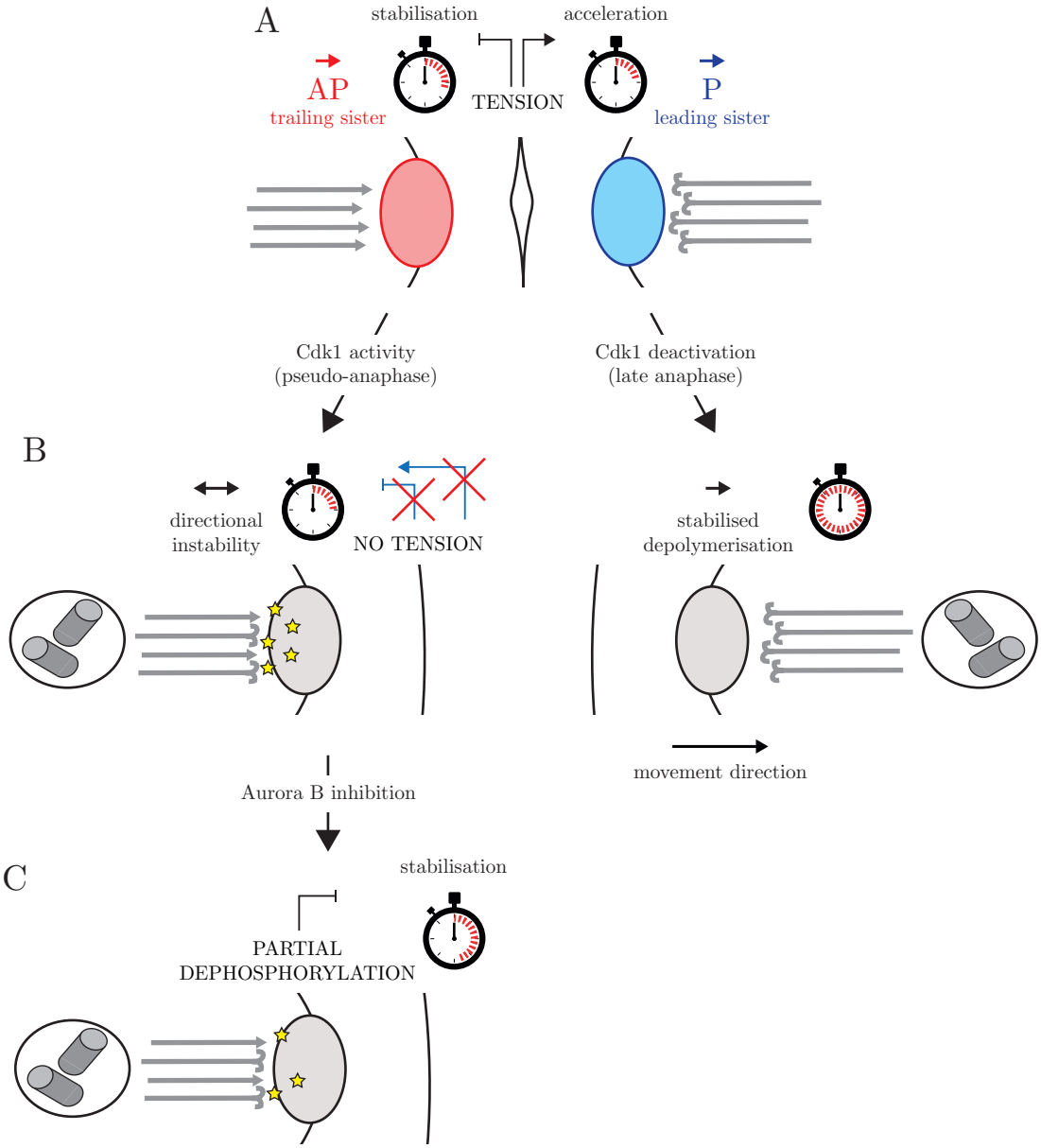

Figure 7.5 *Intrinsic kinetochore clock mechanism depends on Aurora B activity.*
(A) The recent tension-clock model of kinetochore directional instability (Burroughs *et al.* 2015) suggests that kinetochores have intrinsic timing between directional switches. Clock timing correlates with inter-kinetochore tension, so that it is slowed at the trailing sister (AP, red), and accelerated at the leading sister (P, blue). The average oscillation period remains that of a clock unaffected by tension.
(B) After sister chromatid dysjunction, Cdk1 activity results in normal clock timing with phosphorylated clock-defining kinetochore subunits (yellow stars). Due to lack of tension, clocks are unaffected and oscillate with the same average frequency.
(C) Alternatively, Cdk1 deactivation allows dephosphorylation of kinetochore subunits, including those defining clock timing, resulting in an infinitely stabilised clock.
(C) After Aurora B inhibition, the intrinsic clock is stabilised by partial decrease in phosphorylated timing-defining kinetochore subunits. One idea is its effect on MCAK's depolymerase activity.
Figure adapted from Burroughs *et al.* 2015.

tinction between the two clocks' timing, and a bias towards lead-initiated directional switches (LIDS) is established. During anaphase, Cdk1 is deactivated and multiple substrates within the kinetochore become dephosphorylated. The kinetochore's suppressed kMT dynamics can then be interpreted as a hyper-stabilisation of the clock, resulting in all kinetochores becoming P (Figure 7.6 B, right). However, when Cdk1 activity is high during pseudo-anaphase, kinetochore substrates usually dephosphorylated during anaphase remain phosphorylated, and the clock is no longer destabilised (Figure 7.6 B, left). Due to lack of tension between sister chromatids (after dysjunction) the kinetochore clocks are no longer stabilised or accelerated depending on kinetochore state, however still maintains oscillation frequency consistent with that in metaphase. During pseudo-anaphase in which Aurora B kinase activity is inhibited, oscillations are made less frequent ($\sim 2\times$ unperturbed psuedo-anaphase). The loss of Aurora B activity therefore may result in a partial dephosphorylation of the kinetochore in pseudo-anaphase, resulting in stabilisation of the kinetochore clock, and therefore longer time between directional switches (Figure 7.6 C). This suggests a testable hypothesis that directional switches may be affected by Aurora B substrates, which may be regulated by the "dog leash" error correction method described above.

7.4 Summary

Investigation of the structure of individual kinetochores in 3D during mitosis demonstrate that kinetochores form a stiff linkage between centromeric chromatin. Instead, kinetochores can swivel relative to the sister-sister axis, which has previously been wrongly interpreted as a loss of intra-kinetochore stretch, Δ. This is due to a projection of 3D Δ into one or two dimensions. Swivel may occur through a couple of mechanisms. Swivel may be the rotation of the entire kinetochore, meaning that inner and outer kinetochore proteins would rotate together. This has previously been observed in fixed cells, and is called tilt (Wan *et al.*, 2009; Magidson *et al.*, 2016). However, tilt cannot completely explain the observed decrease in Δ in lower dimensions, and therefore another mechanism for swivel must exist. Additionally to tilt, it is

possible that the outer kinetochore layer rotates about the inner kinetochore. This is called remodelling. I now propose a phosphorylation-driven mechanism to describe this novel form of rotation within kinetochores. This allows the kinetochore to form new sites for kMT attachment in region of chromatin neighbouring the centromere. In this case, CENP-C is recruited, which then recruits microtubule-binding outer kinetochore proteins. Additionally, kinetochore swivel requires an adjustment to current models of error correction mechanisms. Rotation of outer kinetochore substrates of Aurora B caused by extreme erroneous attachment moves these substrates directly into the inner centromeric pool of CPC. Meanwhile, the "dog leash" method of error correction would instead be a regulator of kMT dynamics through mitotic motors, such as MCAK, phosphorylated by Aurora B. These dynamics are regulated during mitosis by a complex array of kinases, which upon anaphase onset are deactivated to suppress intra-kinetochore clock mechanisms capable of regulating microtubule dynamics during mitosis.

Bibliography

Adams R R, Wheatleya S P and Gouldsworthy A M (2000). INCENP binds the Aurora-related kinase AIRK2 and is required to target it to chromosomes, the central spindle and cleavage furrow, *Curr. Biol.* **10**(17), 1075–1078.

Agarwal S and Varma D (2014). How the SAC gets the axe: Integrating kinetochore microtubule attachments with spindle assembly checkpoint signaling, *Bioarchitecture* **5**(1-2), 1–12.

Ainsztein A M, Kandels-Lewis S E, M M A and Earnshaw W C (1998). INCENP Centromere and Spindle Targeting: Identification of Essential Conserved Motifs and Involvement of Heterochromatin Protein HP1, *J. Cell Biol.* **143**(7), 1763–1774.

Alushin G M, Ramey V H, Pasqualato S, Ball D A, Grigorieff N, Musacchio A and Nogales E (2010). The Ndc80 kinetochore complex forms oligomeric arrays along microtubules, *Nature* **467**(7317), 805–810.

Amano M, Suzuki A, Hori T, Backer C, Okawa K, Cheeseman I M and Fukagawa T (2009). The CENP-S complex is essential for the stable assembly of outer kinetochore structure, *J. Cell Biol.* **186**(2), 173–182.

Amaro A C, Samora C P, Holtackers R, Wang E, Kingston I J, Alonso M, Lampson M, McAinsh A D and Meraldi P (2010). Molecular control of kinetochore-microtubule dynamics and chromosome oscillations, *Nat. Cell Biol.* **12**(4), 319–329.

Amor D J and Choo K H A (2002). Neocentromeres: Role in Human Disease, Evolution, and Centromere Study, *Am. J. Hum. Genet.* **71**(4), 695–714.

Andrews P D, Ovechkina Y, Morrice N and Wagenbach M (2004). Aurora B regulates MCAK at the mitotic centromere, *Dev. Cell* **6**(2), 253–268.

Aravamudhan P, Felzer-Kim I, Gurunathan K and Joglekar A P (2014). Assembling the Protein Architecture of the Budding Yeast Kinetochore-Microtubule Attachment using FRET, *Curr. Biol.* **24**(13), 1437–1446.

Armond J W, Harry E F, McAinsh A D and Burroughs N J (2015b). Inferring the Forces Controlling Metaphase Kinetochore Oscillations by Reverse Engineering System Dynamics, *PLoS Comput. Biol.* **11**(11), e1004607.

Armond J W, Vladimirou E, Erent M, McAinsh A D and Burroughs N J (2015a). Probing microtubule polymerisation state at single kinetochores during metaphase chromosome motion, *J. Cell Sci.* **128**(10), 1991–2001.

Bancroft J, Auckland P, Samora C P and McAinsh A D (2015). Chromosome congression is promoted by CENP-Q- and CENP-E-dependent pathways, *J. Cell Sci.* **128**(1), 171–184.

Barisic M, Aguiar P, Geley S and Maiato H (2014). Kinetochore motors drive congression of peripheral polar chromosomes by overcoming random arm-ejection forces., *Nat. Cell Biol.* **16**(12), 1249–1256.

Basilico F, Maffini S, Weir J R, Prumbaum D, Rojas A M, Zimniak T, De Antoni A, Jeganathan S, Voss B, van Gerwen S, Krenn V, Massimiliano L, Valencia A, Vetter I R, Herzog F, Raunser S, Pasqualato S and Musacchio A (2014). The pseudo GTPase CENP-M drives human kinetochore assembly, *eLife* **3**, e02978.

Berg J M, Tymoczko J L and Stryer L (2002). *Biochemistry, Fifth Edition*, W. H. Freeman.

Bishop J D and Schumacher J M (2002). Phosphorylation of the Carboxyl Terminus of Inner Centromere Protein (INCENP) by the Aurora B Kinase Stimulates Aurora B Kinase Activity, *J. Biol. Chem.* **277**, 27577–27580.

Blower M D, Sullivan B A and Karpen G H (2002). Conserved organization of centromeric chromatin in flies and humans, *Dev. Cell* **2**(3), 319–330.

Bollen M, Gerlich D W and Lesage B (2009). Mitotic phosphatases: from entry guards to exit guides., *Trends Cell Biol.* **19**(10), 531–541.

Brady D M and Hardwick K G (2000). Complex formation between Mad1p, Bub1p and Bub3p is crucial for spindle checkpoint function, *Curr. Biol.* **10**(11), 675–678.

Bratman S V and Chang F (2007). Stabilization of overlapping microtubules by fission yeast CLASP., *Dev. Cell* **13**(6), 812–827.

Bringmann H, Skiniotis G, Spilker A, Kandels-Lewis S, Vernos I and Surrey T (2004). A kinesin-like motor inhibits microtubule dynamic instability., *Science* **303**(5663), 1519–1522.

Bu W and Su L K (2001). Regulation of microtubule assembly by human EB1 family proteins., *Oncogene* **20**(25), 3185–3192.

Buffin E, Lefebvre C, Huang J, Gagou M E and Karess R E (2005). Recruitment of Mad2 to the kinetochore requires the Rod/Zw10 complex, *Curr. Biol.* **15**(9), 856–861.

Burroughs N J, Harry E F and McAinsh A D (2015). Super-resolution kinetochore tracking reveals the mechanisms of human sister kinetochore directional switching, *eLife* **13**(4).

Cai S, O'Connell C B, Khodjakov A and Walczak C E (2009). Chromosome congression in the absence of kinetochore fibres., *Nat. Cell Biol.* **11**(7), 832–838.

Caldas G V and DeLuca J G (2014). KNL1: bringing order to the kinetochore., *Chromosoma* **123**(3), 169–181.

Caldas G V, DeLuca K F and DeLuca J G (2013). KNL1 facilitates phosphorylation of outer kinetochore proteins by promoting Aurora B kinase activity, *J. Cell Biol.* **203**(6), 957–969.

Carmena M, Pinson X, Platani M, Salloum Z, Xu Z, Clark A, MacIsaac F, Ogawa H, Eggert U, Glover D M, Archambault V and Earnshaw W C (2012). The Chromosomal Passenger Complex Activates Polo Kinase at Centromeres, *PLoS Biol.* **10**(1), e1001250.

Carroll C W, Milks K J and Straight A F (2010). Dual recognition of CENP-A nucleosomes is required for centromere assembly, *J. Cell Biol.* **189**(7), 1143–1155.

Carroll C W, Silva M C C, Godek K M, Jansen L E T and Straight A F (2009). Centromere assembly requires the direct recognition of CENP-A nucleosomes by CENP-N, *Nat. Cell Biol.* **11**(7), 896–902.

Chan Y W, Jeyaprakash A A, Nigg E A and Santamaria A (2012). Aurora B controls kinetochore-microtubule attachments by inhibiting Ska complex-KMN network interaction., *J. Cell Biol.* **196**(5), 563–571.

Cheeseman I M (2014). The kinetochore., *Cold Spring Harb. Perspect. Biol.* **6**(7), a015826.

Cheeseman I M, Chappie J S and Wilson-Kubalek E M (2006). The conserved KMN network constitutes the core microtubule-binding site of the kinetochore, *Cell* **127**(5), 983–997.

Cheeseman I M and Desai A (2008). Molecular architecture of the kinetochore–microtubule interface, *Nat. Rev. Mol. Cell Biol.* **9**(1), 33–46.

Cheeseman L P, Harry E F, McAinsh A D, Prior I A and Royle S J (2013). Specific removal of TACC3-ch-TOG-clathrin at metaphase deregulates kinetochore fiber tension., *J. Cell Sci.* **126**(Pt 9), 2102–2113.

Chu Y, Yao P Y, Wang W, Wang D, Wang Z, Zhang L, Huang Y, Ke Y, Ding X and Yao X (2011). Aurora B kinase activation requires survivin priming phosphorylation by PLK1, *J. Mol. Cell Biol.* **3**(4), 260–267.

Churchman L S, Okten Z, Rock R S, Dawson J F and Spudich J A (2005). Single molecule high-resolution colocalization of Cy3 and Cy5 attached to macromolecules measures intramolecular distances through time., *Proc. Natl. Acad. Sci. U.S.A.* **102**(5), 1419–1423.

Ciferri C, DeLuca J G, Monzani S, Ferrari K J, Ristic D, Wyman C, Stark H, Kilmartin J V, Salmon E D and Musacchio A (2005). Architecture of the Human Ndc80-Hec1 Complex, a Critical Constituent of the Outer Kinetochore, *J. Biol. Chem.* **280**(32), 29088–29095.

Ciferri C, Pasqualato S, Screpanti E, Varetti G, Santaguida S, Dos Reis G, Maiolica A, Polka J, DeLuca J G, De Wulf P, Salek M, Rappsilber J, Moores C A, Salmon E D and Musacchio A (2008). Implications for Kinetochore-Microtubule Attachment from the Structure of an Engineered Ndc80 Complex, *Cell* **133**(3), 427–439.

Cimini D, Wan X, Hirel C B and Salmon E D (2006). Aurora Kinase Promotes Turnover of Kinetochore Microtubules to Reduce Chromosome Segregation Errors, *Curr. Biol.* **16**(17), 1711–1718.

Civelekoglu-Scholey G, He B, Shen M, Wan X, Roscioli E, Bowden B and Cimini D (2013). Dynamic bonds and polar ejection force distribution explain kinetochore oscillations in PtK1 cells., *J. Cell Biol.* **201**(4), 577–593.

Clijsters L, van Zon W, Riet B T, Voets E, Boekhout M, Ogink J, Rumpf-Kienzl C and Wolthuis R M F (2014). Inefficient degradation of cyclin B1 re-activates the spindle checkpoint right after sister chromatid disjunction., *Cell Cycle* **13**(15), 2370–2378.

Clute P and Pines J (1999). Temporal and spatial control of cyclin B1 destruction in metaphase., *Nat. Cell Biol.* **1**(2), 82–87.

Cohen R L, Espelin C W, De Wulf P, Sorger P K, Harrison S C and Simons K T (2008). Structural and Functional Dissection of Mif2p, a Conserved DNA-binding Kinetochore Protein, *Mol. Biol. Cell* **19**(10), 4480–4491.

Comings D E and Okada T A (1971). Fine structure of kinetochore in Indian muntjac, *Exp. Cell Res.* **67**(1), 97–110.

Compton D A (2000). Spindle assembly in animal cells., *Annu. Rev. Biochem.* **69**, 95–114.

Dambacher S, Deng W, Hahn M, Sadic D, Fröhlich J, Nuber A, Hoischen C, Diekmann S, Leonhardt H and Schotta G (2014). CENP-C facilitates the recruitment of M18BP1 to centromeric chromatin, *Nucleus* **3**(1), 101–110.

Daum J R, Wren J D, Daniel J J, Sivakumar S, McAvoy J N, Potapova T A and Gorbsky G J (2009). Ska3 is required for spindle checkpoint silencing and the maintenance of chromosome cohesion in mitosis., *Curr. Biol.* **19**(17), 1467–1472.

De Wulf P, McAinsh A D and Sorger P K (2003). Hierarchical assembly of the budding yeast kinetochore from multiple subcomplexes, *Genes Dev.* **17**(23), 2902–2921.

DeLuca J G, Dong Y, Hergert P, Strauss J, Hickey J M, Salmon E D and McEwen B F (2004). Hec1 and Nuf2 Are Core Components of the Kinetochore Outer Plate Essential for Organizing Microtubule Attachment Sites, *Mol. Biol. Cell* **16**(2), 519–531.

DeLuca J G, Gall W E, Ciferri C, Cimini D and Musacchio A (2006). Kinetochore Microtubule Dynamics and Attachment Stability Are Regulated by Hec1, *Cell* **127**(5), 969–982.

DeLuca K F, Lens S M A and DeLuca J G (2011). Temporal changes in Hec1 phosphorylation control kinetochore-microtubule attachment stability during mitosis, *J. Cell Sci.* **124**(4), 622–634.

Dornblut C, Quinn N, Monajambashi S, Prendergast L, van Vuuren C, Münch S, Deng W, Leonhardt H, Cardoso M C, Hoischen C, Diekmann S and Sullivan K F (2014). A CENP-S/X complex assembles at the centromere in S and G2 phases of the human cell cycle, *Open Biol.* **4**(2), 130229.

Doxsey S, Zimmerman W and Mikule K (2005). Centrosome control of the cell cycle, *Trends Cell Biol.* **15**(6), 303–311.

Draviam V M, Shapiro I, Aldridge B and Sorger P K (2006). Misorientation and reduced stretching of aligned sister kinetochores promote chromosome missegregation in EB1- or APC-depleted cells., *EMBO J.* **25**(12), 2814–2827.

Drpic D, Pereira A J, Barisic M, Maresca T J and Maiato H (2015). Polar Ejection Forces Promote the Conversion from Lateral to End-on Kinetochore-Microtubule Attachments on Mono-oriented Chromosomes., *Cell Rep.* **13**(3), 460–469.

Dumont S and Mitchison T J (2009). Force and length in the mitotic spindle., *Curr. Biol.* **19**(17), R749–61.

Dumont S, Salmon E D and Mitchison T J (2012). Deformations within moving kinetochores reveal different sites of active and passive force generation, *Science* **337**(6092), 355–358.

Dunphy W G and Kumagai A (1991). The cdc25 protein contains an intrinsic phosphatase activity., *Cell* **67**(1), 189–196.

Earnshaw W C (2015). *Discovering centromere proteins: from cold white hands to the A, B, C of CENPs.*, Vol. 16, Nature Reviews Molecular Cell Biology, Wellcome Trust Centre for Cell Biology, Institute of Cell Biology, University of Edinburgh, Michael Swann Building, Kings Buildings, Mayfield Road, Edinburgh EH9 3JR, UK.

Earnshaw W C and Rothfield N (1985). Identification of a family of human centromere proteins using autoimmune sera from patients with scleroderma, *Chromosoma* **91**(3), 313–321.

Ems-McClung S C, Hainline S G, Devare J, Zong H, Cai S, Carnes S K, Shaw S L and Walczak C E (2013). Aurora B inhibits MCAK activity through a phosphoconformational switch that reduces microtubule association., *Curr. Biol.* **23**(24), 2491–2499.

Ems-McClung S C, Hertzer K M, Zhang X, Miller M W and Walczak C E (2007). The interplay of the N- and C-terminal domains of MCAK control microtubule depolymerization activity and spindle assembly., *Mol. Biol. Cell* **18**(1), 282–294.

Eshleman H D and Morgan D O (2014). Sgo1 recruits PP2A to chromosomes to ensure sister chromatid bi-orientation during mitosis, *J. Cell Sci.* **127**(22), 4974–4983.

Eskat A, Deng W, Hofmeister A, Rudolphi S, Emmerth S, Hellwig D, Ulbricht T, Döring V, Bancroft J M, McAinsh A D, Cardoso M C, Meraldi P, Hoischen C, Leonhardt H and Diekmann S (2012). Step-wise assembly, maturation and dynamic behaviour of the human CENP-P/O/R/Q/U kinetochore sub-complex, *PLoS One* **7**(9), e44717.

Etemad B, Kuijt T E F and Kops G J P L (2015). Kinetochore-microtubule attachment is sufficient to satisfy the human spindle assembly checkpoint., *Nat. Commun.* **6**, 8987.

Fachinetti D, Han J S, McMahon M A, Ly P, Abdullah A, Wong A J and Cleveland D W (2015). DNA Sequence-Specific Binding of CENP-B Enhances the Fidelity of Human Centromere Function, *Dev. Cell* **33**(3), 314–327.

Fang J, Liu Y, Wei Y, Deng W, Yu Z, Huang L, Teng Y, Yao T, You Q, Ruan H, Chen P, Xu R M and Li G (2015). Structural transitions of centromeric chromatin regulate the cell cycle-dependent recruitment of CENP-N, *Genes Dev.* **29**(10), 1058–1073.

Folco H D, Campbell C S, May K M, Espinoza C A, Oegema K, Hardwick K G, Grewal S I S and Desai A (2015). The CENP-A N-Tail Confers Epigenetic Stability to Centromeres via the CENP-T Branch of the CCAN in Fission Yeast, *Curr. Biol.* **25**(3), 348–356.

Foley E A, Maldonado M and Kapoor T M (2011). Formation of stable attachments between kinetochores and microtubules depends on the B56-PP2A phosphatase, *Nat. Cell Biol.* **13**(10), 1265–1271.

Foltz D R, Jansen L E T, Black B E, Bailey A O, Yates J R and Cleveland D W (2006). The human CENP-A centromeric nucleosome-associated complex, *Nat. Cell Biol.* **8**(5), 458–469.

Fraschini R, Beretta A, Sironi L, Musacchio A, Lucchini G and Piatti S (2001). Bub3 interaction with Mad2, Mad3 and Cdc20 is mediated by WD40 repeats and does not require intact kinetochores, *EMBO J.* **20**(23), 6648–6659.

Fritzler M J, Kinsella T D and Garbutt E (1980). The CREST syndrome: a distinct serologic entity with anticentromere antibodies, *Am. J. Med.* **69**(4), 520–526.

Fujita R, Otake K, Arimura Y, Horikoshi N, Miya Y, Shiga T, Osakabe A, Tachiwana H, Ohzeki J i, Larionov V, Masumoto H and Kurumizaka H (2015). Stable complex formation of CENP-B with the CENP-A nucleosome, *Nucleic Acids Res.* **43**(10), 4909–4922.

Fukagawa T (2012). Formation of a centromere-specific chromatin structure, *Epigenetics* **7**(7), 672–675.

Fukagawa T, Mikami Y, Nishihashi A, Regnier V, Haraguchi T, Hiraoka Y, Sugata N, Todokoro K, Brown W and Ikemura T (2001). CENP-H, a constitutive centromere component, is required for centromere targeting of CENP-C in vertebrate cells, *EMBO J.* **20**(16), 4603–4617.

Gaitanos T N, Santamaria A, Jeyaprakash A A, Wang B, Conti E and Nigg E A (2009). Stable kinetochore–microtubule interactions depend on the Ska complex and its new component Ska3/C13Orf3, *EMBO J.* **28**(10), 1442–1452.

Gascoigne K E, Takeuchi K, Suzuki A, Hori T, Fukagawa T and Cheeseman I M (2011). Induced Ectopic Kinetochore Assembly Bypasses the Requirement for CENP-A Nucleosomes, *Cell* **145**(3), 410–422.

Gassmann R, Carvalho A, Henzing A J, Ruchaud S, Hudson D F, Honda R, Nigg E A, Gerloff D L and Earnshaw W C (2004). Borealin: a novel chromosomal passenger required for stability of the bipolar mitotic spindle, **166**(2), 179–191.

Gautier J, Solomon M J, Booher R N, Bazan J F and Kirschner M W (1991). cdc25 is a specific tyrosine phosphatase that directly activates p34cdc2., *Cell* **67**(1), 197–211.

Ghongane P, Kapanidou M, Asghar A, Elowe S and Bolanos-Garcia V M (2014). The dynamic protein Knl1 – a kinetochore rendezvous, *J. Cell Sci.* **127**(16), 3415–3423.

Goshima G, Nédélec F and Vale R D (2005). Mechanisms for focusing mitotic spindle poles by minus end-directed motor proteins., *J. Cell Biol.* **171**(2), 229–240.

Griffis E R, Stuurman N and Vale R D (2007). Spindly, a novel protein essential for silencing the spindle assembly checkpoint, recruits dynein to the kinetochore, *J. Cell Biol.* **177**(6), 1005–1015.

Grimaldi A D, Maki T, Fitton B P, Roth D, Yampolsky D, Davidson M W, Svitkina T, Straube A, Hayashi I and Kaverina I (2014). CLASPs are required for proper microtubule localization of end-binding proteins., *Dev. Cell* **30**(3), 343–352.

Gudimchuk N, Vitre B, Kim Y, Kiyatkin A, Cleveland D W, Ataullakhanov F I and Grishchuk E L (2013). Kinetochore kinesin CENP-E is a processive bi-directional tracker of dynamic microtubule tips., *Nat. Cell Biol.* **15**(9), 1079–1088.

Guimaraes G J, Dong Y, McEwen B F and DeLuca J G (2008). Kinetochore-microtubule attachment relies on the disordered N-terminal tail domain of Hec1, *Curr. Biol.* **18**(22), 1778–1784.

Guse A, Carroll C W, Moree B, Fuller C J and Straight A F (2011). In vitro centromere and kinetochore assembly on defined chromatin templates, *Nature* **477**(7364), 354–358.

Hagting A, Den Elzen N, Vodermaier H C, Waizenegger I C, Peters J M and Pines J (2002). Human securin proteolysis is controlled by the spindle checkpoint and reveals when the APC/C switches from activation by Cdc20 to Cdh1., *J. Cell Biol.* **157**(7), 1125–1137.

Hanisch A, Silljé H H W and Nigg E A (2006). Timely anaphase onset requires a novel spindle and kinetochore complex comprising Ska1 and Ska2., *EMBO J.* **25**(23), 5504–5515.

Hardwick K G, Johnston R C, Smith D L and Murray A W (2000). MAD3 Encodes a Novel Component of the Spindle Checkpoint which Interacts with Bub3p, Cdc20p, and Mad2p, *J. Cell Biol.* **148**(5), 871–882.

Hauf S, Cole R W, LaTerra S and Zimmer C (2003). The small molecule Hesperadin reveals a role for Aurora B in correcting kinetochore–microtubule attachment and in maintaining the spindle assembly checkpoint, *J. Cell Biol.* **161**(2), 281–294.

Heeger S, Leismann O, Schittenhelm R, Schraidt O, Heidmann S and Lehner C F (2005). Genetic interactions of separase regulatory subunits reveal the diverged Drosophila Cenp-C homolog, *Genes Dev.* **19**, 2041–2053.

Hellwig D, Emmerth S, Ulbricht T, Döring V, Hoischen C, Martin R, Samora C P, McAinsh A D, Carroll C W, Straight A F, Meraldi P and Diekmann S (2011). Dynamics of CENP-N kinetochore binding during the cell cycle, *J. Cell Sci.* **124**(22), 3871–3883.

Hellwig D, Hoischen C, Ulbricht T and Diekmann S (2009). Acceptor-photobleaching FRET analysis of core kinetochore and NAC proteins in living human cells, *Eur. Biophys. J.* **38**(6), 781–791.

Hellwig D, Münch S, Orthaus S, Hoischen C, Hemmerich P and Diekmann S (2008). Live-cell imaging reveals sustained centromere binding of CENP-T via CENP-A and CENP-B, *J. Biophoton.* **1**(3), 245–254.

Hemmerich P, Weidtkamp-Peters S, Hoischen C, Schmiedeberg L, Erliandri I and Diekmann S (2008). Dynamics of inner kinetochore assembly and maintenance in living cells, *J. Cell Biol.* **180**(6), 1101–1114.

Hertzer K M, Ems-McClung S C and Walczak C E (2003). Kin I kinesins: insights into the mechanism of depolymerization., *Crit. Rev. Biochem. Mol. Biol.* **38**(6), 453–469.

Hiruma Y, Sacristan C, Pachis S T, Adamopoulos A, Kuijt T, Ubbink M, von Castelmur E, Perrakis A and Kops G J P L (2015). Competition between MPS1 and microtubules at kinetochores regulates spindle checkpoint signaling, *Science* **348**(6240), 1264–1267.

Hoffman D B, Pearson C G, Yen T J, Howell B J and Salmon E D (2001). Microtubule-dependent changes in assembly of microtubule motor proteins and mitotic spindle checkpoint proteins at PtK1 kinetochores., *Mol. Biol. Cell* **12**(7), 1995–2009.

Honda R, Körner R and Nigg E A (2003). Exploring the Functional Interactions between Aurora B, INCENP, and Survivin in Mitosis, *Mol. Biol. Cell* **14**(8), 3325–3341.

Hori T, Amano M, Suzuki A, Backer C B, Welburn J P, Dong Y, McEwen B F, Shang W H, Suzuki E, Okawa K, Cheeseman I M and Fukagawa T (2008). CCAN Makes Multiple Contacts with Centromeric DNA to Provide Distinct Pathways to the Outer Kinetochore, *Cell* **135**(6), 1039–1052.

Hori T, Shang W H, Takeuchi K and Fukagawa T (2013). The CCAN recruits CENP-A to the centromere and forms the structural core for kinetochore assembly, *J. Cell Biol.* **200**(1), 45–60.

Hornung P, Maier M, Alushin G M, Lander G C, Nogales E and Westermann S (2011). Molecular architecture and connectivity of the budding yeast Mtw1 kinetochore complex., *J. Mol. Biol.* **405**(2), 548–559.

Hornung P, Troc P, Malvezzi F, Maier M, Demianova Z, Zimniak T, Litos G, Lampert F, Schleiffer A, Brunner M, Mechtler K, Herzog F, Marlovits T C and Westermann S (2014). A cooperative mechanism drives budding yeast kinetochore assembly downstream of CENP-A, *J. Cell Biol.* **206**(4), 509–524.

Howell B J, McEwen B F, Canman J C, Hoffman D B, Farrar E M, Rieder C L and Salmon E D (2001). Cytoplasmic dynein/dynactin drives kinetochore protein transport to the spindle poles and has a role in mitotic spindle checkpoint inactivation., *J. Cell Biol.* **155**(7), 1159–1172.

Hua S, Wang Z, Jiang K, Huang Y, Ward T, Zhao L, Dou Z and Yao X (2011). CENP-U Cooperates with Hec1 to Orchestrate Kinetochore-Microtubule Attachment, *J. Biol. Chem.* **286**(2), 1627–1638.

Huang H, Feng J, Famulski J, Rattner J B, Liu S T, Kao G D, Muschel R, Chan G K T and Yen T J (2007). Tripin/hSgo2 recruits MCAK to the inner centromere to correct defective kinetochore attachments, *J. Cell Biol.* **177**(3), 413–424.

Hunter A W, Caplow M, Coy D L, Hancock W O, Diez S, Wordeman L and Howard J (2003). The kinesin-related protein MCAK is a microtubule depolymerase that forms an ATP-hydrolyzing complex at microtubule ends., *Mol. Cell* **11**(2), 445–457.

Jansen L E T, Black B E, Foltz D R and Cleveland D W (2007). Propagation of centromeric chromatin requires exit from mitosis., *J. Cell Biol.* **176**(6), 795–805.

Jaqaman K, King E M, Amaro A C, Winter J R, Dorn J F, Elliott H L, Mchedlishvili N, McClelland S E, Porter I M, Posch M, Toso A, Danuser G, McAinsh A D, Meraldi P and Swedlow J R (2010). Kinetochore alignment within the metaphase plate is regulated by centromere stiffness and microtubule depolymerases, *J. Cell Biol.* **188**(5), 665–679.

Jeyaprakash A A, Klein U R, Lindner D, Ebert J, Nigg E A and Conti E (2007). Structure of a Survivin–Borealin–INCENP Core Complex Reveals How Chromosomal Passengers Travel Together, *Cell* **131**(2), 271–285.

Jeyaprakash A A, Santamaria A, Jayachandran U, Chan Y W, Benda C, Nigg E A and Conti E (2012). Structural and functional organization of the Ska complex, a key component of the kinetochore-microtubule interface., *Mol. Cell* **46**(3), 274–286.

Ji Z, Gao H and Yu H (2015). Kinetochore attachment sensed by competitive Mps1 and microtubule binding to Ndc80C, *Science* **348**(6240), 1260–1264.

Joglekar A P, Bloom K and Salmon E D (2009). In vivo protein architecture of the eukaryotic kinetochore with nanometer scale accuracy., *Curr. Biol.* **19**(8), 694–699.

Jokelainen P T (1967). The ultrastructure and spatial organization of the metaphase kinetochore in mitotic rat cells, *J. Ultrastruct. Res.* **19**(1-2), 19–44.

Kagawa N, Hori T, Hoki Y, Hosoya O, Tsutsui K, Saga Y, Sado T and Fukagawa T (2014). The CENP-O complex requirement varies among different cell types, *Chromosome Res.* **22**(3), 293–303.

Kaitna S, Mendoza M, Jantsch-Plunger V and Glotzer M (2000). Incenp and an aurora-like kinase form a complex essential for chromosome segregation and efficient completion of cytokinesis, *Curr. Biol.* **10**(19), 1172–1181.

Kamenz J and Hauf S (2014). Slow checkpoint activation kinetics as a safety device in anaphase., *Curr. Biol.* **24**(6), 646–651.

Kang J, Chaudhary J, Dong H, Kim S, Brautigam C A and Yu H (2011b). Mitotic centromeric targeting of HP1 and its binding to Sgo1 are dispensable for sister-chromatid cohesion in human cells, *Mol. Biol. Cell* **22**(8), 1181–1190.

Kang Y H, Park C H, Kim T S, Soung N K, Bang J K, Kim B Y, Park J E and Lee K S (2011a). Mammalian polo-like kinase 1-dependent regulation of the PBIP1-CENP-Q complex at kinetochores., *J. Biol. Chem.* **286**(22), 19744–19757.

Kapoor T M, Lampson M A, Hergert P, Cameron L, Cimini D, Salmon E D, McEwen B F and Khodjakov A (2006). Chromosomes can congress to the metaphase plate before biorientation., *Science* **311**(5759), 388–391.

Kato H, Jiang J, Zhou B R, Rozendaal M, Feng H, Ghirlando R, Xiao T S, Straight A F and Bai Y (2013). A Conserved Mechanism for Centromeric Nucleosome Recognition by Centromere Protein CENP-C, *Science* **340**(6136), 1110–1113.

Kawashima S A, Yamagishi Y, Honda T, Ishiguro K i and Watanabe Y (2010). Phosphorylation of H2A by Bub1 Prevents Chromosomal Instability Through Localizing Shugoshin, *Science* **327**(5962), 172–177.

Kelly A E, Ghenoiu C, Xue J Z, Zierhut C, Kimura H and Funabiki H (2010). Survivin Reads Phosphorylated Histone H3 Threonine 3 to Activate the Mitotic Kinase Aurora B, *Science* **330**(6001), 235–239.

Kelly A E, Sampath S C, Maniar T A, Woo E M and Chait B T (2007). Chromosomal enrichment and activation of the aurora B pathway are coupled to spatially regulate spindle assembly, *Dev. Cell* **12**, 31–43.

Kim Y, Heuser J E, Waterman C M and Cleveland D W (2008). CENP-E combines a slow, processive motor and a flexible coiled coil to produce an essential motile kinetochore tether., *J. Cell Biol.* **181**(3), 411–419.

Kiyomitsu T, Murakami H and Yanagida M (2011). Protein interaction domain mapping of human kinetochore protein Blinkin reveals a consensus motif for binding of spindle assembly checkpoint proteins Bub1 and . . . , *Mol. Cell. Biol.* **31**(5), 998–1011.

Klare K, Weir J R, Basilico F, Zimniak T, Massimiliano L, Ludwigs N, Herzog F and Musacchio A (2015). CENP-C is a blueprint for constitutive centromere-associated network assembly within human kinetochores, *J. Cell Biol.* **210**(1), 11–22.

Klein U R, Nigg E A and Gruneberg U (2006). Centromere Targeting of the Chromosomal Passenger Complex Requires a Ternary Subcomplex of Borealin, Survivin, and the N-Terminal Domain of INCENP, *Mol. Biol. Cell* **17**(6), 2547–2558.

Knowlton A L, Vorozhko V V, Lan W and Gorbsky G J (2009). ICIS and Aurora B coregulate the microtubule depolymerase Kif2a, *Curr. Biol.* **19**(9), 758–763.

Kops G J P L, Kim Y, Weaver B A A, Mao Y, McLeod I, Yates J R, Tagaya M and Cleveland D W (2005). ZW10 links mitotic checkpoint signaling to the structural kinetochore., *J. Cell Biol.* **169**(1), 49–60.

Krasinska L, Domingo-Sananes M R, Kapuy O, Parisis N, Harker B, Moorhead G, Rossignol M, Novák B and Fisher D (2011). Protein phosphatase 2A controls the order and dynamics of cell-cycle transitions., *Mol. Cell* **44**(3), 437–450.

Krishan A and Buck R C (1965). Ultrastructure of cell division in insect spermatogenesis, *J. Ultrastruct. Res.* **13**(5-6), 444–458.

Kwon M S, Hori T, Okada M and Fukagawa T (2007). CENP-C Is Involved in Chromosome Segregation, Mitotic Checkpoint Function, and Kinetochore Assembly, *Mol. Biol. Cell* **18**(6), 2155–2168.

Lampson M A and Cheeseman I M (2011). Sensing centromere tension: Aurora B and the regulation of kinetochore function., *Trends Cell Biol.* **21**(3), 133–140.

Lampson M A, Renduchitala K, Khodjakov A and Kapoor T M (2004). Correcting improper chromosome–spindle attachments during cell division, *Nat. Cell Biol.* **6**(3), 6–237.

Lan W, Zhang X, Kline-Smith S L and Rosasco S E (2004). Aurora B phosphorylates centromeric MCAK and regulates its localization and microtubule depolymerization activity, *Curr. Biol.* **14**(4), 273–286.

Li Y, Yu W, Liang Y and Zhu X (2007). Kinetochore dynein generates a poleward pulling force to facilitate congression and full chromosome alignment., *Cell Res.* **17**(8), 701–712.

Logsdon G A, Barrey E J, Bassett E A, DeNizio J E, Guo L Y, Panchenko T, Dawicki-McKenna J M, Heun P and Black B E (2015). Both tails and the centromere targeting domain of CENP-A are required for centromere establishment, *J. Cell Biol.* **208**(5), 521–531.

Loncarek J, Hergert P, Magidson V and Khodjakov A (2008). Control of daughter centriole formation by the pericentriolar material, *Nat. Cell Biol.* **10**(3), 322–328.

London N and Biggins S (2014). Mad1 kinetochore recruitment by Mps1-mediated phosphorylation of Bub1 signals the spindle checkpoint, *Genes Dev.* **28**, 140–152.

Lu M S and Johnston C A (2013). Molecular pathways regulating mitotic spindle orientation in animal cells., *Development* **140**(9), 1843–1856.

Maffini S, Maia A R R, Manning A L, Maliga Z, Pereira A L, Junqueira M, Shevchenko A, Hyman A, Yates J R, Galjart N, Compton D A and Maiato H (2009). Motor-independent targeting of CLASPs to kinetochores by CENP-E promotes microtubule turnover and poleward flux., *Curr. Biol.* **19**(18), 1566–1572.

Magidson V, He J, Ault J G, O'Connell C B, Yang N, Tikhonenko I, McEwen B F, Sui H and Khodjakov A (2016). Unattached kinetochores rather than intrakinetochore tension arrest mitosis in taxol-treated cells., *J. Cell Biol.* **212**(3), 307–319.

Magidson V, Paul R, Yang N, Ault J G, O'Connell C B, Tikhonenko I, McEwen B F, Mogilner A and Khodjakov A (2015). Adaptive changes in the kinetochore architecture facilitate proper spindle assembly., *Nat. Cell Biol.* **17**(9), 1134–1144.

Malik R, Lenobel R, Santamaria A, Ries A, Nigg E A and Körner R (2009). Quantitative Analysis of the Human Spindle Phosphoproteome at Distinct Mitotic Stages, *J. Proteome Res.* **8**(10), 4553–4563.

Malvezzi F, Litos G, Schleiffer A, Heuck A, Mechtler K, Clausen T and Westermann S (2013). A structural basis for kinetochore recruitment of the Ndc80 complex via two distinct centromere receptors, *EMBO J.* **32**(3), 409–423.

Maresca T J and Salmon E D (2009). Intrakinetochore stretch is associated with changes in kinetochore phosphorylation and spindle assembly checkpoint activity., *J. Cell Biol.* **184**(3), 373–381.

Martin-Lluesma S, Stucke V M and Nigg E A (2002). Role of Hec1 in spindle checkpoint signaling and kinetochore recruitment of Mad1/Mad2, *Science* **297**(5590), 2267–2270.

Masumoto H, Masukata H, Muro Y, Nozaki N and Okazaki T (1989). A human centromere antigen (CENP-B) interacts with a short specific sequence in alphoid DNA, a human centromeric satellite, *J. Cell Biol.* **109**(5), 1963–1973.

Mattiuzzo M, Vargiu G, Totta P, Fiore M, Ciferri C, Musacchio A and Degrassi F (2011). Abnormal kinetochore-generated pulling forces from expressing a N-terminally modified Hec1., *PLoS One* **6**(1), e16307.

Mayr M I, Hümmer S, Bormann J, Grüner T, Adio S, Woehlke G and Mayer T U (2007). The human kinesin Kif18A is a motile microtubule depolymerase essential for chromosome congression., *Curr. Biol.* **17**(6), 488–498.

McAinsh A D, Meraldi P, Draviam V M, Toso A and Sorger P K (2006). The human kinetochore proteins Nnf1R and Mcm21R are required for accurate chromosome segregation, *EMBO J.* **25**(17), 4033–4049.

McCleland M L, Kallio M J, Barrett-Wilt G A, Kestner C A, Shabanowitz J, Hunt D, Gorbsky G J and Stukenberg P T (2004). The Vertebrate Ndc80 Complex Contains Spc24 and Spc25 Homologs, which Are Required to Establish and Maintain Kinetochore-Microtubule Attachment, *Curr. Biol.* **14**(2), 131–137.

McClelland S E, Borusu S, Amaro A C, Winter J R, Belwal M, McAinsh A D and Meraldi P (2007). The CENP-A NAC/CAD kinetochore complex controls chromosome congression and spindle bipolarity, *EMBO J.* **26**(24), 5033–5047.

McEwen B F, Heagle A B, Cassels G O, Buttle K F and Rieder C L (1997). Kinetochore fiber maturation in PtK1 cells and its implications for the mechanisms of chromosome congression and anaphase onset., *J. Cell Biol.* **137**(7), 1567–1580.

McEwen B F, Hsieh C E, Mattheyses A L and Rieder C L (1998). A new look at kinetochore structure in vertebrate somatic cells using high-pressure freezing and freeze substitution, *Chromosoma* **107**(6-7), 366–375.

McGowan C H and Russell P (1993). Human Wee1 kinase inhibits cell division by phosphorylating p34cdc2 exclusively on Tyr15., *EMBO J.* **12**(1), 75–85.

Mchedlishvili N, Wieser S, Holtackers R, Mouysset J, Belwal M, Amaro A C and Meraldi P (2012). Kinetochores accelerate centrosome separation to ensure faithful chromosome segregation, *J. Cell Sci.* **125**(4), 906–918.

McKinley K L, Sekulic N, Guo L Y, Tsinman T, Black B E and Cheeseman I M (2015). The CENP-L-N Complex Forms a Critical Node in an Integrated Meshwork of Interactions at the Centromere-Kinetochore Interface, *Mol. Cell* **60**(6), 886–898.

Meppelink A, Kabeche L, Vromans M J M, Compton D A and Lens S M A (2015). Shugoshin-1 Balances Aurora B Kinase Activity via PP2A to Promote Chromosome Bi-orientation, *Cell Rep.* **11**(4), 508–515.

Merzlyak E M, Goedhart J, Shcherbo D, Bulina M E, Shcheglov A S, Fradkov A F, Gaintzeva A, Lukyanov K A, Lukyanov S, Gadella T W J and Chudakov D M (2007). Bright monomeric red fluorescent protein with an extended fluorescence lifetime., *Nat. Meth.* **4**(7), 555–557.

Milks K J, Moree B and Straight A F (2009). Dissection of CENP-C-directed Centromere and Kinetochore Assembly, *Mol. Biol. Cell* **20**(19), 4246–4255.

Miller S A, Johnson M L and Stukenberg P T (2008). Kinetochore Attachments Require an Interaction between Unstructured Tails on Microtubules and Ndc80Hec1, *Curr. Biol.* **18**(22), 1785–1791.

Minoshima Y, Hori T, Okada M, Kimura H, Haraguchi T, Hiraoka Y, Bao Y C, Kawashima T, Kitamura T and Fukagawa T (2005). The Constitutive Centromere Component CENP-50 Is Required for Recovery from Spindle Damage, *Mol. Cell. Biol.* **25**(23), 10315–10328.

Montenegro Gouveia S, Leslie K, Kapitein L C, Buey R M, Grigoriev I, Wagenbach M, Smal I, Meijering E, Hoogenraad C C, Wordeman L, Steinmetz M O and Akhmanova A (2010). In vitro reconstitution of the functional interplay between MCAK and EB3 at microtubule plus ends., *Curr. Biol.* **20**(19), 1717–1722.

Moree B, Meyer C B, Fuller C J and Straight A F (2011). CENP-C recruits M18BP1 to centromeres to promote CENP-A chromatin assembly, *J. Cell Biol.* **194**(6), 855–871.

Moritz M, Zheng Y and Alberts B M (1998). Recruitment of the γ-tubulin ring complex to Drosophila salt-stripped centrosome scaffolds, *J. Cell Biol.* **142**(3), 775–786.

Moroi Y, Peebles C and Fritzler M J (1980). Autoantibody to centromere (kinetochore) in scleroderma sera, *Proc. Nat. Acad. Sci. USA* **77**(3), 1627–1631.

Moyle M W, Kim T, Hattersley N, Espeut J, Cheerambathur D K, Oegema K and Desai A (2014). A Bub1-Mad1 interaction targets the Mad1-Mad2 complex to unattached kinetochores to initiate the spindle checkpoint, **204**(5), 647–657.

Mueller P R, Coleman T R and Dunphy W G (1995). Cell cycle regulation of a Xenopus Wee1-like kinase., *Mol. Biol. Cell* **6**(1), 119–134.

Muñoz-Barrera M and Monje-Casas F (2014). Increased Aurora B activity causes continuous disruption of kinetochore–microtubule attachments and spindle instability, *Proc. Nat. Acad. Sci. USA* **111**(38), E3996–E4005.

Nishihashi A, Haraguchi T, Hiraoka Y, Ikemura T, Regnier V, Dodson H, Earnshaw W C and Fukagawa T (2002). CENP-I Is Essential for Centromere Function in Vertebrate Cells, *Dev. Cell* **2**(4), 463–476.

Nishimura K, Fukagawa T, Takisawa H, Kakimoto T and Kanemaki M (2009). An auxin-based degron system for the rapid depletion of proteins in nonplant cells, *Nat. Meth.* **6**(12), 917–922.

Nishino T, Rago F, Hori T, Tomii K, Cheeseman I M and Fukagawa T (2013). CENP-T provides a structural platform for outer kinetochore assembly, *EMBO J.* **32**(3), 424–436.

Nishino T, Takeuchi K, Gascoigne K E, Suzuki A, Hori T, Oyama T, Morikawa K, Cheeseman I M and Fukagawa T (2012). CENP-T-W-S-X Forms a Unique Centromeric Chromatin Structure with a Histone-like Fold, *Cell* **148**(3), 487–501.

Nixon F M, Gutiérrez-Caballero C, Hood F E, Booth D G, Prior I A and Royle S J (2015). The mesh is a network of microtubule connectors that stabilizes individual kinetochore fibers of the mitotic spindle., *eLife* **4**.

Nousiainen M, Sillje H H W, Sauer G, Nigg E A and Körner R (2006). Phosphoproteome analysis of the human mitotic spindle, *Proc. Nat. Acad. Sci. USA* **103**(14), 5391–5396.

Nozawa R S, Nagao K, Masuda H T, Iwasaki O, Hirota T, Nozaki N, Kimura H and Obuse C (2010). Human POGZ modulates dissociation of HP1α from mitotic chromosome arms through Aurora B activation, *Nat. Cell Biol.* **12**(7), 719–727.

O'Connell C B, Khodjakov A and McEwen B F (2012). Kinetochore flexibility: creating a dynamic chromosome–spindle interface, *Curr. Opin. Cell Biol.* **24**(1), 40–47.

O'Connell C B and Wang Y L (2000). Mammalian spindle orientation and position respond to changes in cell shape in a dynein-dependent fashion., *Mol. Biol. Cell* **11**(5), 1765–1774.

Ohta S, Bukowski-Wills J C, Wood L, de Lima Alves F, Chen Z, Rappsilber J and Earnshaw W C (2010). Proteomics of isolated mitotic chromosomes identifies the kinetochore protein Ska3/Rama1., *Cold Spring Harb. Symp. Quant. Biol.* **75**, 433–438.

Ohzeki J i, Nakano M, Okada T and Masumoto H (2002). CENP-B box is required for de novo centromere chromatin assembly on human alphoid DNA, *J. Cell Biol.* **159**(5), 765–775.

Okada M, Cheeseman I M, Hori T, Okawa K, McLeod I X, Yates J R, Desai A and Fukagawa T (2006). The CENP-H–I complex is required for the efficient incorporation of newly synthesized CENP-A into centromeres, *Nat. Cell Biol.* **8**(5), 446–457.

Palmer D K, O'Day K, Trong H L, Charbonneau H and Margolis R L (1991). Purification of the centromere-specific protein CENP-A and demonstration that it is a distinctive histone., *Proc. Nat. Acad. Sci. USA* **88**(9), 3734–3738.

Park C H, Park J E, Kim T S, Kang Y H, Soung N K, Zhou M, Kim N H, Bang J K and Lee K S (2015). Mammalian Polo-like kinase 1 (Plk1) promotes proper chromosome segregation by phosphorylating and delocalizing the PBIP1 · CENP-Q complex from kinetochores., *J. Biol. Chem.* **290**(13), 8569–8581.

Park J E, Erikson R L and Lee K S (2011). Feed-forward mechanism of converting biochemical cooperativity to mitotic processes at the kinetochore plate., *Proc. Natl. Acad. Sci. U.S.A.* **108**(20), 8200–8205.

Pawley J (2006). *Handbook of Biological Confocal Microscopy*, 3 edn, Springer Science & Business Media, Boston, MA.

Peplowska K, Wallek A U and Storchova Z (2014). Sgo1 Regulates Both Condensin and Ipl1/Aurora B to Promote Chromosome Biorientation, *PLoS Genet.* **10**(6), e1004411.

Peters J M (2006). The anaphase promoting complex/cyclosome: a machine designed to destroy., *Nat. Rev. Mol. Cell Biol.* **7**(9), 644–656.

Petrovic A, Mosalaganti S, Keller J, Mattiuzzo M, Overlack K, Krenn V, De Antoni A, Wohlgemuth S, Cecatiello V, Pasqualato S, Raunser S and Musacchio A (2014). Modular Assembly of RWD Domains on the Mis12 Complex Underlies Outer Kinetochore Organization, *Mol. Cell* **53**(4), 591–605.

Petrovic A, Pasqualato S, Dube P, Krenn V, Santaguida S, Cittaro D, Monzani S, Massimiliano L, Keller J, Tarricone A, Maiolica A, Stark H and Musacchio A (2010). The MIS12 complex is a protein interaction hub for outer kinetochore assembly, *J. Cell Biol.* **190**(5), 835–852.

Prendergast L, van Vuuren C, Kaczmarczyk A, Doering V, Hellwig D, Quinn N, Hoischen C, Diekmann S and Sullivan K F (2011). Premitotic Assembly of Human CENPs -T and -W Switches Centromeric Chromatin to a Mitotic State, *PLoS Biol.* **9**(6), e1001082.

Primorac I, Weir J R, Chiroli E, Gross F, Hoffmann I, van Gerwen S, Ciliberto A, Musacchio A and Pines J (2013). Bub3 reads phosphorylated MELT repeats to promote spindle assembly checkpoint signaling, *eLife* **2**, e01030.

Przewloka M R, Venkei Z, Bolanos-Garcia V M, Debski J, Dadlez M and Glover D M (2011). CENP-C Is a Structural Platform for Kinetochore Assembly, *Curr. Biol.* **21**(5), 399–405.

Raaijmakers J A, Tanenbaum M E, Maia A F and Medema R H (2009). RAMA1 is a novel kinetochore protein involved in kinetochore-microtubule attachment., *J. Cell Sci.* **122**(Pt 14), 2436–2445.

Rago F and Cheeseman I M (2013). Review series: The functions and consequences of force at kinetochores., *J. Cell Biol.* **200**(5), 557–565.

Rago F, Gascoigne K E and Cheeseman I M (2015). Distinct Organization and Regulation of the Outer Kinetochore KMN Network Downstream of CENP-C and CENP-T, *Curr. Biol.* **25**(5), 671–677.

Rattani A, Vinod P K, Godwin J, Tachibana-Konwalski K, Wolna M, Malumbres M, Novák B and Nasmyth K (2014). Dependency of the spindle assembly checkpoint on Cdk1 renders the anaphase transition irreversible., *Curr. Biol.* **24**(6), 630–637.

Ribeiro S A, Vagnarelli P, Dong Y, Hori T, McEwen B F, Fukagawa T, Flors C and Earnshaw W C (2010). A super-resolution map of the vertebrate kinetochore, *Proc. Nat. Acad. Sci. USA* **107**(23), 10484–10489.

Rieder C L (2005). Kinetochore fiber formation in animal somatic cells: dueling mechanisms come to a draw., *Chromosoma* **114**(5), 310–318.

Rieder C L, Davison E A, Jensen L C, Cassimeris L and Salmon E D (1986). Oscillatory movements of monooriented chromosomes and their position relative to the spindle pole result from the ejection properties of the aster and half-spindle., *J. Cell Biol.* **103**(2), 581–591.

Rieder C L and Salmon E D (1994). Motile kinetochores and polar ejection forces dictate chromosome position on the vertebrate mitotic spindle., *J. Cell Biol.* **124**(3), 223–233.

Roos U P (1973). Light and electron microscopy of rat kangaroo cells in mitosis, *Chromosoma* **40**(1), 43–82.

Samejima I, Spanos C, de Lima Alves F, Hori T, Perpelescu M, Zou J, Rappsilber J, Fukagawa T and Earnshaw W C (2015a). Whole-proteome genetic analysis of dependencies in assembly of a vertebrate kinetochore, *J. Cell Biol.* **211**(6), 1141–1156.

Samejima K, Platani M, Wolny M, Ogawa H, Vargiu G, Knight P J, Peckham M and Earnshaw W C (2015b). The Inner Centromere Protein (INCENP) Coil Is a Single α-Helix (SAH) Domain That Binds Directly to Microtubules and Is Important for Chromosome Passenger Complex (CPC) Localization and Function in Mitosis, *J. Biol. Chem.* **290**(35), 21460–21472.

Samora C P, Mogessie B, Conway L, Ross J L, Straube A and McAinsh A D (2011). MAP4 and CLASP1 operate as a safety mechanism to maintain a stable spindle position in mitosis., *Nat. Cell Biol.* **13**(9), 1040–1050.

Schittenhelm R B, Heeger S, Althoff F, Walter A, Heidmann S, Mechtler K and Lehner C F (2007). Spatial organization of a ubiquitous eukaryotic kinetochore protein network in Drosophila chromosomes., *Chromosoma* **116**(4), 385–402.

Schmidt J C, Arthanari H, Boeszoermenyi A, Dashkevich N M, Wilson-Kubalek E M, Monnier N, Markus M, Oberer M, Milligan R A, Bathe M, Wagner G, Grishchuk E L and Cheeseman I M (2012). The kinetochore-bound Ska1 complex tracks depolymerizing microtubules and binds to curved protofilaments., *Dev. Cell* **23**(5), 968–980.

Schmitzberger F and Harrison S C (2012). RWD domain: a recurring module in kinetochore architecture shown by a Ctf19-Mcm21 complex structure., *EMBO Rep.* **13**(3), 216–222.

Schnackenberg B J and Khodjakov A (1998). The disassembly and reassembly of functional centrosomes in vitro, *Proc. Nat. Acad. Sci. USA* **95**(16), 9295–9300.

Schuh M, Lehner C F and Heidmann S (2007). Incorporation of Drosophila CID/CENP-A and CENP-C into centromeres during early embryonic anaphase., *Curr. Biol.* **17**(3), 237–243.

Screpanti E, De Antoni A, Alushin G M, Petrovic A, Melis T, Nogales E and Musacchio A (2011). Direct binding of Cenp-C to the Mis12 complex joins the inner and outer kinetochore, *Curr. Biol.* **21**(5), 391–398.

Shao H, Huang Y, Zhang L, Yuan K, Chu Y, Dou Z, Jin C, Garcia-Barrio M, Liu X and Yao X (2015). Spatiotemporal dynamics of Aurora B-PLK1-MCAK signaling axis orchestrates kinetochore bi-orientation and faithful chromosome segregation, *Sci. Rep.* **2**, 12204.

Shrestha R L and Draviam V M (2013). Lateral to end-on conversion of chromosome-microtubule attachment requires kinesins CENP-E and MCAK., *Curr. Biol.* **23**(16), 1514–1526.

Silió V, McAinsh A D and Millar J B (2015). KNL1-Bubs and RZZ Provide Two Separable Pathways for Checkpoint Activation at Human Kinetochores, *Dev. Cell* **35**(5), 600–613.

Skibbens R V, P S V and Salmon E D (1993). Directional instability of kinetochore motility during chromosome congression and segregation in mitotic newt lung cells: a push-pull mechanism, *J. Cell Biol.* **122**(4), 859–875.

Snyder J A and Mullins J M (1993). Analysis of spindle microtubule organization in untreated and taxol-treated PtK1 cells., *Cell Biol. Int.* **17**(12), 1075–1084.

Song K, Gronemeyer B, Lu W, Eugster E and Tomkiel J E (2002). Mutational Analysis of the Central Centromere Targeting Domain of Human Centromere Protein C, (CENP-C), *Exp. Cell Res.* **275**(1), 81–91.

Stumpff J, Du Y, English C A, Maliga Z, Wagenbach M, Asbury C L, Wordeman L and Ohi R (2011). A tethering mechanism controls the processivity and kinetochore-microtubule plus-end enrichment of the kinesin-8 Kif18A., *Mol. Cell* **43**(5), 764–775.

Stumpff J, von Dassow G, Wagenbach M, Asbury C and Wordeman L (2008). The kinesin-8 motor Kif18A suppresses kinetochore movements to control mitotic chromosome alignment., *Dev. Cell* **14**(2), 252–262.

Stumpff J, Wagenbach M, Franck A, Asbury C L and Wordeman L (2012). Kif18A and chromokinesins confine centromere movements via microtubule growth suppression and spatial control of kinetochore tension., *Dev. Cell* **22**(5), 1017–1029.

Sudakin V, Chan G K T and Yen T J (2001). Checkpoint inhibition of the APC/C in HeLa cells is mediated by a complex of BUBR1, BUB3, CDC20, and MAD2, *J. Cell Biol.* **154**(5), 925–936.

Sugata N, Munekata E and Todokoro K (1999). Characterization of a Novel Kinetochore Protein, CENP-H, *J. Biol. Chem.* **274**(39), 27343–27346.

Sullivan K F, Hechenberger M and Masri K (1994). Human CENP-A contains a histone H3 related histone fold domain that is required for targeting to the centromere., *J. Cell Biol.* **127**(3), 581–592.

Suzuki A, Badger B L, Wan X, DeLuca J G and Salmon E D (2014). The architecture of CCAN proteins creates a structural integrity to resist spindle forces and achieve proper intrakinetochore stretch, *Dev. Cell* **30**(6), 717–730.

Suzuki A, Hori T, Nishino T, Usukura J, Miyagi A, Morikawa K and Fukagawa T (2011). Spindle microtubules generate tension-dependent changes in the distribution of inner kinetochore proteins, *J. Cell Biol.* **193**(1), 125–140.

Tachiwana H, Müller S, Blümer J, Klare K, Musacchio A and Almouzni G (2015). HJURP Involvement in De Novo CenH3CENP-A and CENP-C Recruitment, *Cell Rep.* **11**(1), 22–32.

Takeuchi K, Nishino T, Mayanagi K, Horikoshi N, Osakabe A, Tachiwana H, Hori T, Kurumizaka H and Fukagawa T (2014). The centromeric nucleosome-like CENP-T-W-S-X complex induces positive supercoils into DNA, *Nucleic Acids Res.* **42**(3), 1644–1655.

Tanaka K, Chang H L, Kagami A and Watanabe Y (2009). CENP-C functions as a scaffold for effectors with essential kinetochore functions in mitosis and meiosis, *Dev. Cell* **17**(3), 334–343.

Tanenbaum M E, Macurek L, van der Vaart B and Galli M (2011). A complex of Kif18b and MCAK promotes microtubule depolymerization and is negatively regulated by Aurora kinases, *Curr. Biol.* **21**(16), 1356–1365.

Tanno Y, Kitajima T S, Honda T, Ando Y, Ishiguro K i and Watanabe Y (2010). Phosphorylation of mammalian Sgo2 by Aurora B recruits PP2A and MCAK to centromeres, *Genes Dev.* **24**(19), 2169–2179.

Tauchman E C, Boehm F J and DeLuca J G (2015). Stable kinetochore-microtubule attachment is sufficient to silence the spindle assembly checkpoint in human cells., *Nat. Commun.* **6**, 10036.

Thrower D A, Jordan M A and Wilson L (1996). Modulation of CENP-E organization at kinetochores by spindle microtubule attachment., *Cell Motil. Cytoskeleton* **35**(2), 121–133.

Tirnauer J S, Canman J C, Salmon E D and Mitchison T J (2002). EB1 targets to kinetochores with attached, polymerizing microtubules., *Mol. Biol. Cell* **13**(12), 4308–4316.

Toso A, Winter J R, Garrod A J, Amaro A C, Meraldi P and McAinsh A D (2009). Kinetochore-generated pushing forces separate centrosomes during bipolar spindle assembly, *J. Cell Biol.* **184**(3), 365–372.

Uchida K S K, Takagaki K, Kumada K, Hirayama Y, Noda T and Hirota T (2009). Kinetochore stretching inactivates the spindle assembly checkpoint, *J. Cell Biol.* **184**(3), 383–390.

Vader G, Medema R H and Lens S (2006). The chromosomal passenger complex: guiding Aurora-B through mitosis, *J. Cell Biol.* **173**(6), 833–837.

van der Horst A and Lens S (2014). Cell division: control of the chromosomal passenger complex in time and space, *Chromosoma* **123**, 25–42.

van der Vaart B, Akhmanova A and Straube A (2009). Regulation of microtubule dynamic instability., *Biochem. Soc. Trans.* **37**(Pt 5), 1007–1013.

Varma D, Wan X, Cheerambathur D, Gassmann R, Suzuki A, Lawrimore J, Desai A and Salmon E D (2013). Spindle assembly checkpoint proteins are positioned close to core microtubule attachment sites at kinetochores, *J. Cell Biol.* **202**(5), 735–746.

Vázquez-Novelle M D, Sansregret L, Dick A E, Smith C A, McAinsh A D, Gerlich D W and Petronczki M (2014). Cdk1 inactivation terminates mitotic checkpoint surveillance and stabilizes kinetochore attachments in anaphase., *Curr. Biol.* **24**(6), 638–645.

Vitre B, Gudimchuk N, Borda R, Kim Y, Heuser J E, Cleveland D W and Grishchuk E L (2014). Kinetochore-microtubule attachment throughout mitosis potentiated by the elongated stalk of the kinetochore kinesin CENP-E., *Mol. Biol. Cell* **25**(15), 2272–2281.

Vladimirou E, Mchedlishvili N, Gasic I, Armond J W, Samora C P, Meraldi P and McAinsh A D (2013). Nonautonomous movement of chromosomes in mitosis., *Dev. Cell* **27**(1), 60–71.

Vleugel M, Tromer E, Omerzu M, Groenewold V, Nijenhuis W, Snel B and Kops G J P L (2013). Arrayed BUB recruitment modules in the kinetochore scaffold KNL1 promote accurate chromosome segregation, *J. Cell Biol.* **203**(6), 943–955.

von Schubert C, Cubizolles F, Bracher J M, Sliedrecht T, Kops G J P L and Nigg E A (2015). Plk1 and Mps1 cooperatively regulate the Spindle Assembly Checkpoint in human cells, *Cell Rep.* **12**(1), 66–78.

Wan X, Cimini D, Cameron L A and Salmon E D (2012). The coupling between sister kinetochore directional instability and oscillations in centromere stretch in metaphase PtK1 cells, *Mol. Biol. Cell* **23**(6), 1035–1046.

Wan X, O'Quinn R P, Pierce H L, Joglekar A P, Gall W E, DeLuca J G, Carroll C W, Liu S T, Yen T J, McEwen B F, Stukenberg P T, Desai A and Salmon E D (2009). Protein architecture of the human kinetochore microtubule attachment site., *Cell* **137**(4), 672–684.

Wang F, Dai J, Daum J R, Niedzialkowska E, Banerjee B, Stukenberg P T, Gorbsky G J and Higgins J M G (2010). Histone H3 Thr-3 Phosphorylation by Haspin Positions Aurora B at Centromeres in Mitosis, *Science* **330**(6001), 231–235.

Wang F, Ulyanova N P, van der Waal M S and Patnaik D (2011). A positive feedback loop involving Haspin and Aurora B promotes CPC accumulation at centromeres in mitosis, *Curr. Biol.* **21**(12), 1061–1069.

Wang H, Hu X, Ding X, Dou Z, Yang Z, Shaw A W, Teng M, Cleveland D W, Goldberg M L, Niu L and Yao X (2004). Human Zwint-1 specifies localization of Zeste White 10 to kinetochores and is essential for mitotic checkpoint signaling., *J. Biol. Chem.* **279**(52), 54590–54598.

Waters J and Wittmann T (2014). *Quantitative Imaging in Cell Biology*, Methods in Cell Biology, Academic Press.

Weaver L N, Ems-McClung S C, Stout J R, LeBlanc C, Shaw S L, Gardner M K and Walczak C E (2011). Kif18A uses a microtubule binding site in the tail for plus-end localization and spindle length regulation., *Curr. Biol.* **21**(17), 1500–1506.

Wei R R, Schnell J R, Larsen N A, Sorger P K, Chou J J and Harrison S C (2006). Structure of a Central Component of the Yeast Kinetochore: The Spc24p/Spc25p Globular Domain, *Structure* **14**(6), 1003–1009.

Wei R R and Sorger P K (2005). Molecular organization of the Ndc80 complex, an essential kinetochore component, *Proc. Nat. Acad. Sci. USA* **102**(15), 5363–5367.

Welburn J P I, Grishchuk E L, Backer C B, Wilson-Kubalek E M, Yates J R and Cheeseman I M (2009). The human kinetochore Ska1 complex facilitates microtubule depolymerization-coupled motility., *Dev. Cell* **16**(3), 374–385.

Welburn J, Vleugel M, Liu D, Yates J R and Lampson M A (2010). Aurora B phosphorylates spatially distinct targets to differentially regulate the kinetochore-microtubule interface, *Mol. Cell* **38**(3), 383–392.

Wendell K L, Wilson L and Jordan M A (1993). Mitotic block in HeLa cells by vinblastine: ultrastructural changes in kinetochore-microtubule attachment and in centrosomes., *J. Cell Sci.* **104 (Pt 2)**, 261–274.

Wheatley S P, Carvalho A, Vagnarelli P and Earnshaw W C (2001). INCENP is required for proper targeting of Survivin to the centromeres and the anaphase spindle during mitosis, *Curr. Biol.* **11**(11), 886–890.

Wheatley S P, Hinchcliffe E H, Glotzer M, Hyman A A, Sluder G and Wang Y L (1997). CDK1 inactivation regulates anaphase spindle dynamics and cytokinesis in vivo., *J. Cell Biol.* **138**(2), 385–393.

Wigge P A and Kilmartin J V (2001). The Ndc80p Complex from Saccharomyces cerevisiae Contains Conserved Centromere Components and Has a Function in Chromosome Segregation, *J. Cell Biol.* **152**(2), 349–360.

Wojcik E, Basto R, Serr M, Scaërou F, Karess R and Hays T (2001). Kinetochore dynein: its dynamics and role in the transport of the Rough deal checkpoint protein., *Nat. Cell Biol.* **3**(11), 1001–1007.

Wolf F, Wandke C, Isenberg N and Geley S (2006). Dose-dependent effects of stable cyclin B1 on progression through mitosis in human cells., *EMBO J.* **25**(12), 2802–2813.

Wood L, Booth D G, Vargiu G, Ohta S, de Lima Alves F, Samejima K, Fukagawa T, Rappsilber J and Earnshaw W C (2016). Auxin/AID versus conventional knockouts: distinguishing the roles of CENP-T/W in mitotic kinetochore assembly and stability | Open Biology, *Open Biol.* **6**, 150230.

Wurzenberger C, Held M, Lampson M A, Poser I, Hyman A A and Gerlich D W (2012). Sds22 and Repo-Man stabilize chromosome segregation by counteracting Aurora B on anaphase kinetochores., *J. Cell Biol.* **198**(2), 173–183.

Wynne D J and Funabiki H (2015). Kinetochore function is controlled by a phospho-dependent coexpansion of inner and outer components., *J. Cell Biol.* **210**(6), 899–916.

Xu Z, Ogawa H, Vagnarelli P and Bergmann J H (2009). INCENP–aurora B interactions modulate kinase activity and chromosome passenger complex localization, *J. Cell Biol.* **187**(5), 637–653.

Yamagishi Y, Honda T, Tanno Y and Watanabe Y (2010). Two Histone Marks Establish the Inner Centromere and Chromosome Bi-Orientation, *Science* **330**(6001), 239–243.

Yang Z, Tulu U S, Wadsworth P and Rieder C L (2007). Kinetochore dynein is required for chromosome motion and congression independent of the spindle checkpoint., *Curr. Biol.* **17**(11), 973–980.

Yao X, Anderson K L and Cleveland D W (1997). The microtubule-dependent motor centromere-associated protein E (CENP-E) is an integral component of kinetochore corona fibers that link centromeres to spindle microtubules., *J. Cell Biol.* **139**(2), 435–447.

Zaytsev A V, Mick J E, Maslennikov E, Nikashin B, DeLuca J G and Grishchuk E L (2015). Multisite phosphorylation of the NDC80 complex gradually tunes its microtubule-binding affinity, *Mol. Biol. Cell* **26**(10), 1829–1844.

Zaytsev A V, Sundin L J R, DeLuca K F, Grishchuk E L and DeLuca J G (2014). Accurate phosphoregulation of kinetochore–microtubule affinity requires unconstrained molecular interactions, *J. Cell Biol.* **206**, 45–59.

Zhang G, Lischetti T, Hayward D G and Nilsson J (2015). Distinct domains in Bub1 localize RZZ and BubR1 to kinetochores to regulate the checkpoint, *Nat. Commun.* **6**, 7162.

Zhang G, Lischetti T and Nilsson J (2014). A minimal number of MELT repeats supports all the functions of KNL1 in chromosome segregation, *J. Cell Sci.* **127**(4), 871–884.

Zhang X, Lan W, Ems-McClung S C, Stukenberg P T and Walczak C E (2007). Aurora B Phosphorylates Multiple Sites on Mitotic Centromere-associated Kinesin to Spatially and Temporally Regulate Its Function, *Mol. Biol. Cell* **18**(9), 3264–3276.

Zong H, Carnes S K, Moe C, Walczak C E and Ems-McClung S C (2016). The far C-terminus of MCAK regulates its conformation and spindle pole focusing., *Mol. Biol. Cell* **27**(9), 1451–1464.

Appendix A

Investigating cells expressing mCherry-Mis12

Given our interest in investigating Δ in human cells, we requested access to the cell line investigated in Uchida *et al.* (2009), which investigated the distance between eGFP-CENP-A and mCherry-Mis12 in HeLa-K cells. We obtained both J-CENP-A/Mis12 and its parent cell line (J-CENP-A; expressing eGFP-CENP-A alone) from the Hirota lab (Tokyo, Japan) – these were named HeLa-J cells to distinguish from our own HeLa-K eGFP-CENP-A cell line. Upon receipt of these cell lines, we checked that they were behaving in mitosis as expected.

In order to ensure that cells were capable of progressing through mitosis in the expected time and with the expected frequency of chromosome congression or segregation errors, both J-CENP-A and J-CENP-A/Mis12 cells were imaged for eGFP-CENP-A signal over 12 hr every 3 min (Figure A.1 A). This allows measurement of average time taken to progress from nuclear envelope break down (NEBD) to metaphase plate formation and anaphase onset. J-CENP-A cells progressed from NEBD to metaphase plate formation in an average ($\pm$ standard error) 18.5 ($\pm$ 0.4) min (Figure A.1 B), and 34.7 ($\pm$ 0.8) to progress to anaphase (Figure A.1 D). However, J-CENP-A/Mis12 cells suffered a severe delay in chromosome congression timing relative to J-CENP-A (Figure A.1 B), taking 51.2 ($\pm$ 2.5) min, i.e. more than 2.5$\times$ as long, to congress its final chromosome. Furthermore, after 40 min, all chromosomes had been aligned in J-CENP-A cells, however $>$ 10% of cells contained unaligned chromosomes in J-CENP-A/Mis12 cells after 2 hr. Secondly, J-CENP-A/Mis12 cells experienced a delay in anaphase onset once the metaphase plate had been formed, taking 25.2 ($\pm$ 1.8) min (Figure A.1 C), which compares to 16.6 ($\pm$ 0.7) min in J-CENP-A cells (Figure A.1 C). How-

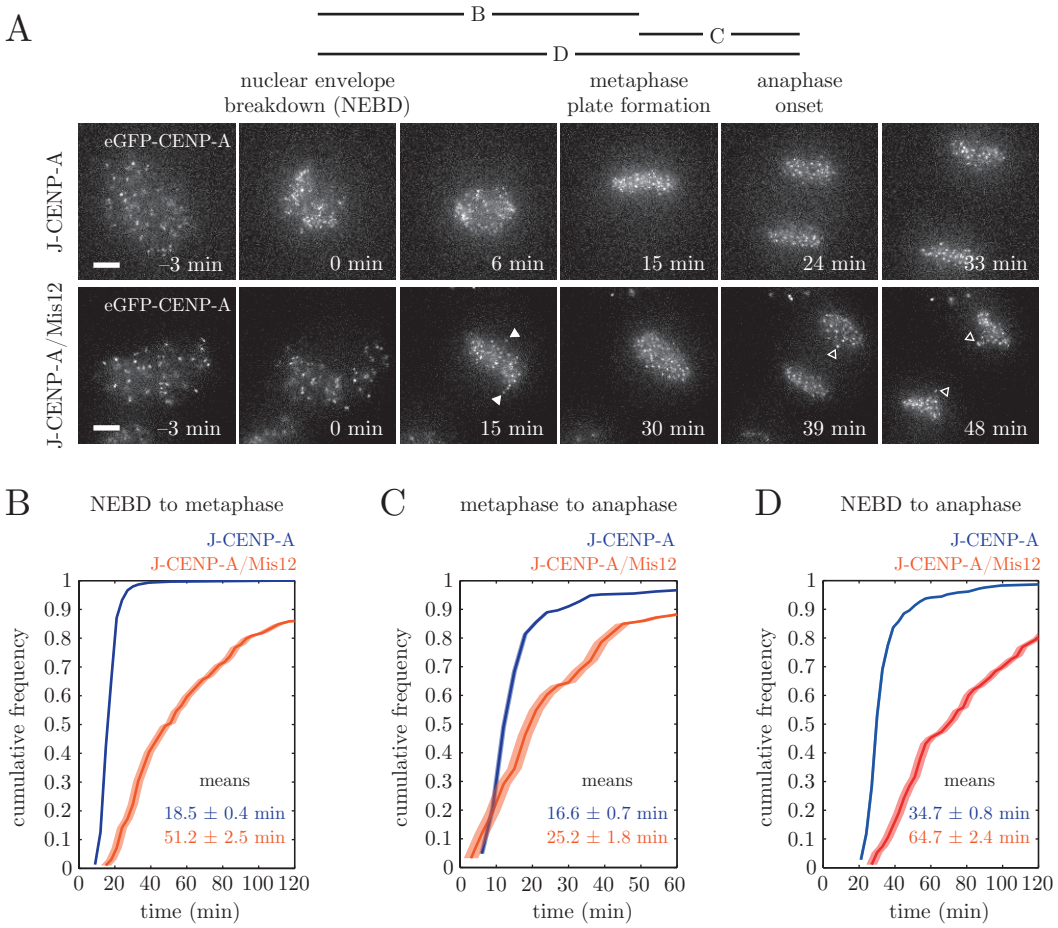

Figure A.1 *Delay in chromosome congression and anaphase onset when mCherry N-terminally tagged to Mis12.*
(A) Example images of J-CENP-A (top row) and J-CENP-A/Mis12 (bottom row) cells in mitosis, with NEBD (column 2), metaphase plate formation (column 4) and anaphase onset (column 5). Full white arrowheads denote incidences of unaligned chromosomes; hollow white arrowheads denote incidences of delayed chromosome segregation. Lines above plots denote which times are calculated for (B), (C) and (D). Scale bars = 5 μm.
(B) Cumulative frequency of time between NEBD and metaphase plate formation in J-CENP-A (blue; n = 295) and J-CENP-A/Mis12 (gold; n = 99) cells. Values given are means ± standard error.
(C) Cumulative frequency of time between metaphase plate formation and anaphase onset in J-CENP-A (blue; n = 290) and J-CENP-A/Mis12 (gold; n = 93) cells. Values given are means ± standard error.
(D) Cumulative frequency of time between NEBD and anaphase onset in J-CENP-A (blue; n = 288) and J-CENP-A/Mis12 (gold; n = 95) cells. Values given are means ± standard error.

ever it is possible that the delay in chromosome congression in J-CENP-A/Mis12 cells contributes to this effect. As a consequence of these delays, J-CENP-A/Mis12 took an extra 30 min to progress from NEBD to anaphase onset (Figure A.1 D), and only $\sim$ 80% of cells were capable of entering anaphase within 2 hr of NEBD. Given such delays, we hypothesised that kinetochores were not capable of generating the forces required to efficiently move kinetochores about the cell. In order to investigate this hypothesis, we sought to track kinetochores in live cells and measure their dynamics.

In order to investigate the congression defects in cells expressing mCherry-Mis12, both J-CENP-A and J-CENP-A/Mis12 cells were imaged for eGFP-CENP-A signal every 2 s for 5 min in order to allow tracking of kinetochores for analysis of kinetochore dynamics. This signal was measured over a 12 μm z-stack every 500 nm, allowing imaging of kinetochores across the majority of the metaphase plate. Using our established kinetochore tracking assay (Burroughs *et al.*, 2015), kinetochore signal was located using Gaussian mixture model fitting (MMF), tracked through time, and sister kinetochores assigned (Figure A.2 A,B). All kinetochores could then be represented by coordinates within a coordinate system defined by the metaphase plate: the y- and z-coordinates define the plane that is the metaphase plate, and therefore the x-coordinate defines the normal to the plate. Knowing the location of both sisters in a kinetochore pair allowed measurement of inter-kinetochore distance, d. Upon bi-orientation, the centromeric chromatin binding two kinetochores is stretched under tension, which is represented by an increase in d. Measured in both J-CENP-A (n = $73,523$) and J-CENP-A/Mis12 cells (n = $121,845$), d was slightly decreased in the cells expressing mCherry-Mis12 (Figure A.2 C). As J-CENP-A/Mis12 cells cannot generate normal levels of inter-kinetochore tension, this may represent a small perturbation to the kinetochore's ability to generate force. Additionally, kinetochores typically exhibit quasi-periodic oscillations with half-period $\sim$35-40 s in the direction of the spindle poles (e.g. Jaqaman *et al.*, 2010). This can be measured by calculating the autocorrelation of a kinetochore's change in x-coordinate, i.e. in the direction of the spindle poles. Measuring this autocorrelation for J-CENP-A cells yields quasi-periodic behaviour of

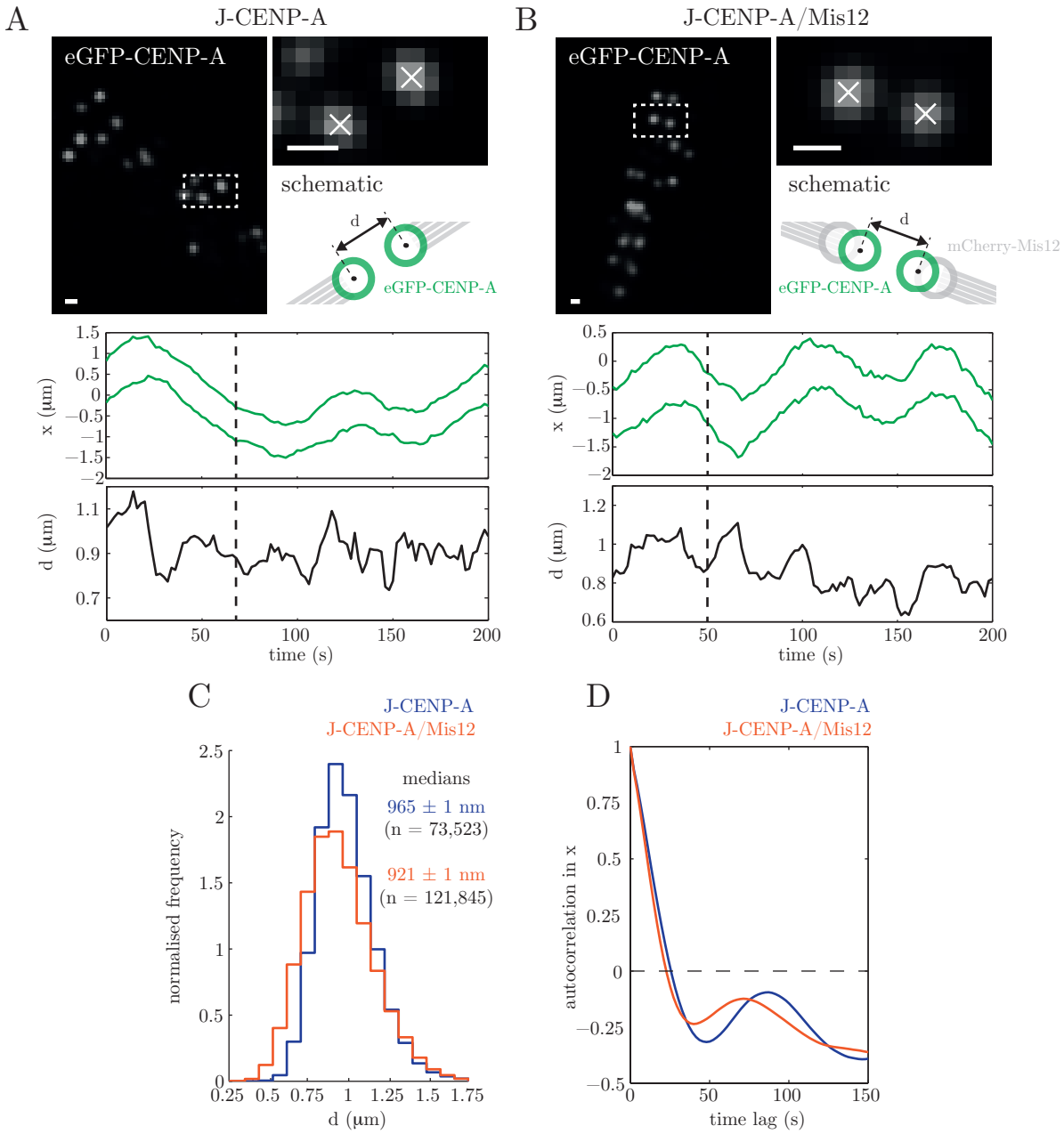

Figure A.2 *Overall dynamic kinetochore motion largely unchanged by mCherry tag to N-terminus of Mis12.*
eGFP-CENP-A signal in: (A) J-CENP-A and (B) J-CENP-A/Mis12 cells were located and tracked over time, demonstrating back-and-forth motion of the kinetochore. Dashed white boxes locate pairs of eGFP spots shown in top-right boxes; white crosses are located at the Gaussian-fitted spot centres. Schematics denote the 3D interkinetochore distance, d, measured between eGFP signals. The normal distance of each spot from the metaphase plate, x, and d are plotted over time for each kinetochore pair in top-right boxes. The dashed lines represent the time point at which these kinetochores are shown. Scale bars = 500 nm.
(C) Histograms of d for J-CENP-A (blue; n = 73,523) and J-CENP-A/Mis12 (gold; n = 121,845). Values given are median ± standard error.
(D) Autocorrelation in x for J-CENP-A (blue) and J-CENP-A/Mis12 (gold), demonstrating a small difference in periodic behaviour in x.

individual kinetochores with half-period ∼50 s (Figure A.2 D). Meanwhile kinetochores in J-CENP-A/Mis12 cells also exhibited quasi-periodic behaviour, albeit slightly less pronounced, as the first trough in the autocorrelation was deeper for J-CENP-A cells (Figure A.2 D). More importantly, the half-period of oscillation for J-CENP-A/Mis12 cells was ∼40 s. This means that kinetochores expressing mCherry-Mis12 exhibit directional switches more frequently than its parent, which could represent a decrease in binding strength of kinetochores to kinetochore-microtubules (kMTs). This would perturb a kinetochore's ability to generate force. Increased directional switch frequency could instead represent a perturbation in the intra-kinetochore 'clock' hypothesised to set this frequency (Burroughs *et al.*, 2015). In order to investigate this, we decided to investigate force generation at directional switch events in J-CENP-A/Mis12 cells.

To investigate directional switches, we fit a simplistic mathematical model of a kinetochore pair to the kinetochore coordinate data as in Armond *et al.* (2015b). Fitting was performed using a Monte Carlo Markov chain (MCMC) process, which derives probability distributions for a number of variables within the model. One such variable is the status of each sister's kinetochore-fibre (k-fibre), which reveals the individual timing of directional switches at each sister kinetochore. This means that for each directional switch it can be measured whether it was the leading (or poleward, P) or trailing (or away-from-the-pole, AP) kinetochore that initiated the switch. This allows a comparison between lead-initiated (LIDS) and trail-initiated directional switches (TIDS). However, due to an issue of identifiability within the model between a kinetochore's natural length, L, and microtubule-polymerisation/-depolymerisation speeds, $v_{\pm}$, a distribution for L first needs to be calculated. This distribution can then be enforced in the MCMC model fitting, allowing the model fitting to better explore values for $v_{\pm}$. L was measured in J-CENP-A and J-CENP-A/Mis12 cells after 16 hr incubation in 3.3 μM nocodazole (Figure A.3 A), which results in the complete loss of kMTs and therefore inter-kinetochore tension. As before, the centre of eGFP-CENP-A signal was accurately localised by Gaussian MMF and tracked, and distributions for inter-kinetochore distance, d, calculated, which would represent the inter-kinetochore

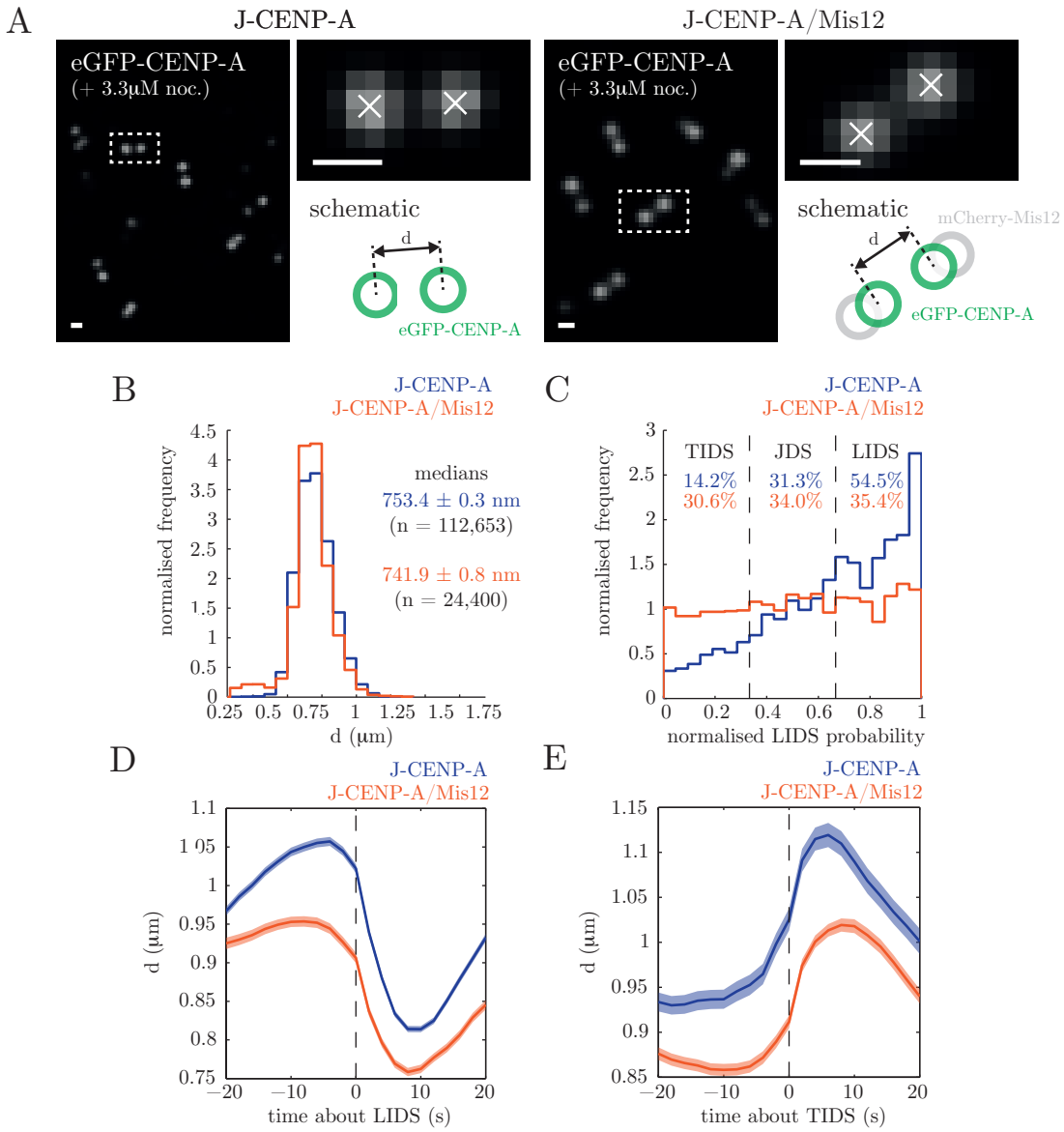

Figure A.3 *Force generation is perturbed by N-terminal tagging of Mis12.*
(A) eGFP-CENP-A signal in J-CENP-A (left) and J-CENP-A/Mis12 (right) cells treated with 3.3 μM nocodazole were located and tracked over time. Dashed white boxes locate the kinetochore pair in the top-right boxes; white crosses mark the Gaussian-fitted spot centres. Schematics demonstrate 3D interkinetochore distance, *d*, between a pair's eGFP centres. Scale bars = 500 nm.
(B) Histogram of interkinetochore distance, *d*, for nocodazole-treated J-CENP-A (blue; n = 112,653) and J-CENP-A/Mis12 (gold; n = 24,400) cells. Values given are median ± standard error.
(C) Histograms of normalised LIDS probability for J-CENP-A (blue; n = 1,761) and J-CENP-A/Mis12 (gold; n = 2,767) switch events. Vertical black dashed lines divide regions where switch events are considered LIDS, TIDS and JDS. Values given are percentage of data points within each region.
Profiles of sister separation, *d*, about: (D) LIDS and (E) TIDS for nocodazole-treated J-CENP-A (blue; $n_{LIDS} = 868$; $n_{TIDS} = 211$) and J-CENP-A/Mis12 (gold; $n_{LIDS} = 868$; $n_{TIDS} = 749$) cells.

distance under lack of tension. These distributions had mean (± standard deviation) of 753.4 (± 100.7) nm for J-CENP-A, and 741.9 (± 125.0) nm for J-CENP-A/Mis12 (Figure A.3 B) – these values were then used as priors for the MCMC in each cell line. The MCMC model fitting then yielded probabilities that each directional switch was a LIDS or TIDS.

By measuring a normalised probability that a directional switch event was a LIDS (so that the more likely a directional switch is a LIDS, the closer the normalised probability is to 1), it was possible to observe the distribution of LIDS compared to TIDS. Previous observations in HeLa-K cells expressing eGFP-CENP-A have shown that cells exhibit a bias towards LIDS (Burroughs *et al.*, 2015), which was again observed in cells also expressing spindle pole marker eGFP-Centrin1 (Armond *et al.*, 2015b). Importantly, in J-CENP-A cells, 54.5% of directional switches were lead-initiated, compared to only 14.2% that were TIDS (a ratio of 3.8:1, c.f. 3.8:1 observed in Armond *et al.*, 2015b; Figure A.3 C), which is as expected from previous measurements. However, upon incorporation of mCherry-Mis12 to kinetochores, the bias was effectively lost, so that 35.4% of directional switches were LIDS, and 30.6% TIDS (a ratio of 1.2:1; Figure A.3 C). This represents either an increase in the number of TIDS or a decrease in the number of LIDS or a combination, as the number of joint directional switches remained almost the same (31.3% in J-CENP-A compared to 34.0% in J-CENP-A/Mis12; Figure A.3 C). An increase in TIDS frequency could be due to a perturbation to tension generation in the centromeric chromatin. The tension-clock model suggested by Burroughs *et al.* (2015) suggests that tension stabilises the clock on the trail sister, while it accelerates the clock at the lead sister, therefore encouraging a LIDS. However, loss of tension may result in a smaller bias between the two clocks, and therefore more occasions for LIDS. In order to investigate tension generation before directional switches, inter-kinetochore distance, d, was measured at the time points about LIDS (Figure A.3 D) and TIDS (Figure A.3 E). This revealed an inability for a kinetochore pair in J-CENP-A/Mis12 cells to generate inter-kinetochore tension to the same amplitude or at the same rates as observed in J-CENP-A, which may explain the decrease in median

measurement of sister separation in J-CENP-Mis12 cells compared to its parent cell line. Remarkably, prior to a TIDS in J-CENP-A/Mis12 cells, the inter-kinetochore distance decreases prior to the directional switch, which means that the lead kinetochore is moving more slowly than the trailing sister. Therefore it is likely that more TIDS are observed because of an inability for kinetochores to generate sufficient tension prior to directional switches. Furthermore, it suggests that 30.6% of directional switches (i.e. those that are TIDS) in J-CENP-A/Mis12 cells are a consequence of perturbed force generation by the lead kinetochore. This explains the delay in chromosome congression in J-CENP-A/Mis12 cells relative to J-CENP-A, and explains why some kinetochore pairs are unable to generate the expected inter-kinetochore tension. However, it is unclear what the reason is for this perturbation, as it could be due to either: (a) the fusion of a fluorophore to the MIS12 complex; (b) fusion to the Mis12 subunit specifically; or (c) an over-expression of Mis12 at the kinetochore. As such, we sought to investigate which of the three scenarios could be the most likely cause.

In order to check whether the perturbation in force generation was specifically caused by fusing a fluorophore to the Mis12 constituent of the MIS12 complex, we looked to obtain a cell line that expressed another constituent of MIS12 fused to a fluorophore. Obtained from the Welburn lab, a HeLa-K cell line expressing MIS12-protein Dsn1 with GFP fused at its C-terminus was imaged for mitotic timings. Unfortunately, the Dsn1-GFP signal was not strong enough to allow imaging of GFP signal over 12 hr to allow visualisation of metaphase plate formation; this also meant that tracking of kinetochore signal was not possible. However, Dsn1-GFP cells were instead imaged in brightfield and investigated for timing of cell rounding (at the start of mitosis) and anaphase onset (Figure A.4 A); plain HeLa-K cells were used as a control. Plain HeLa-K cells exhibited average timing between cell rounding and anaphase onset of 32.0 ($\pm$ 0.9) min (Figure A.4 B), which is analagous to timing between NEBD and anaphase onset in J-CENP-A cells (Figure A.1 D). However, cells expressing Dsn1-GFP experienced a delay in mitotic timing to 50.6 min (Figure A.4 B) – while this is not as severe a delay as the cells expressing mCherry-Mis12 (64.7 min; Figure A.1 D),

this still demonstrates that incorporating a fluorescent marker to constituents within the MIS12 complex appears to cause a delay in mitosis. It does however remain possible that over-expression of MIS12 constituents could cause the observed delays. Nevertheless, these cell lines could not be faithfully used for investigation of intra-kinetochore distance measurements, and therefore another outer-kinetochore marker needed to be investigated.

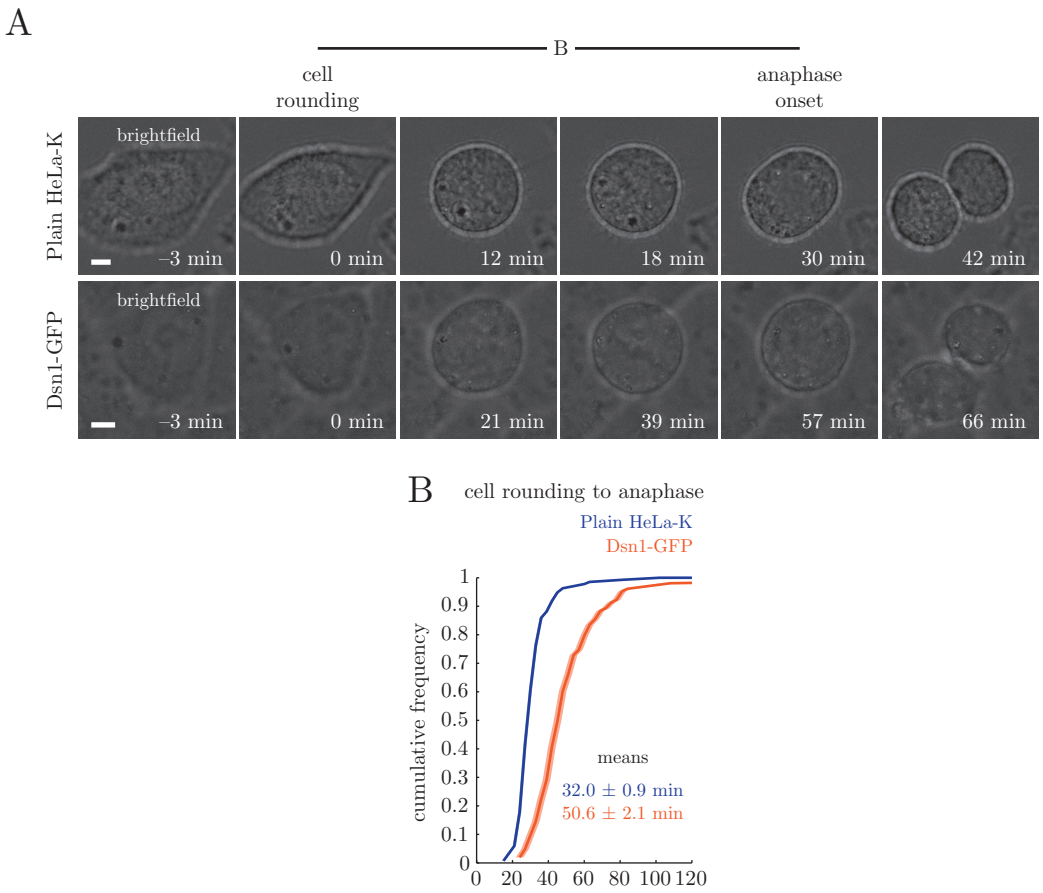

Figure A.4 *Incorporation of GFP to another MIS12 constituent results in a similar delay within mitosis.*
(A) Example images of plain HeLa-K cells (top) and Dsn1-GFP (bottom) cells in brightfield as they progress through mitosis, with cell rounding (column 2) and anaphase onset (column 5). Line above plots denotes which times are calculated for (B). Scale bars = 5 μm.
(B) Cumulative frequency of time between cell rounding and anaphase onset in plain HeLa-K (blue; n = 135) and eGFP-Dsn1 (gold; n = 102) cells. Values given are means ± standard error.

Appendix B

Inhibition of Cdk1 inactivation at anaphase onset

My supervisor was approached by Mark Petronczki (Cancer Research UK, London) with a view to collaborate on a prospective journal article that had been compiled by his post-doctoral fellow and the lead author, Lola Vázquez-Novelle. Their analyses had suggested that kinetochores moved relative to their spindle pole more in late anaphase when Cdk1 remained active – given our laboratory's expertise in kinetochore tracking, Mark sought help in tracking these movements in late anaphase to investigate this hypothesis. Andrew asked if I would like to work alongside Lola, an offer which I gladly accepted. In the final published article, I contributed to Figures 2 E and S2 F, and sections of the text pertaining to these figures.

In order to produce these results, both Lola and I prepared and imaged cells in order to allow tracking of eGFP-CENP-A and eGFP-Centrin1 signals in cells that either expressed wild-type (WT) or non-degradable (ND) CyclinB1-mCherry. Cells were imaged in metaphase and late anaphase in both cases – presence of ND CyclinB1 after anaphase onset resulted in a so-called pseudo-anaphase. I performed the tracking of eGFP signals, manually located spindle poles, and performed analyses of the kinetochore's metaphase plate position, x, and kinetochore-to-spindle pole distance, b.

These analyses allowed quantification of a kinetochore's ability to continue periodic directional switches after anaphase onset when Cdk1 activity remains high. Furthermore, though it is not stated explicitly in the text, kinetochores were capable of these directional switches independent of their sisters – this is important as many current models of force generation depend upon inter- and/or intra-kinetochore tension. For further investigation into this work, see § 5.1.

Current Biology 24, 638–645, March 17, 2014 ©2014 The Authors. Open access under CC BY-NC-ND license. http://dx.doi.org/10.1016/j.cub.2014.01.034

Report

Cdk1 Inactivation Terminates Mitotic Checkpoint Surveillance and Stabilizes Kinetochore Attachments in Anaphase

María Dolores Vázquez-Novelle,[1,*] Laurent Sansregret,[1] Amalie E. Dick,[2] Christopher A. Smith,[3] Andrew D. McAinsh,[3] Daniel W. Gerlich,[2] and Mark Petronczki[1,*]
[1]Cell Division and Aneuploidy Laboratory, Cancer Research UK London Research Institute, Clare Hall Laboratories, Blanche Lane, South Mimms, Hertfordshire EN6 3LD, UK
[2]Institute of Molecular Biotechnology of the Austrian Academy of Sciences (IMBA), Dr. Bohr-Gasse 3, 1030 Vienna, Austria
[3]Centre for Mechanochemical Cell Biology, Division of Biomedical Cell Biology, Warwick Medical School, University of Warwick, Coventry CV4 7AL, UK

Summary

Two mechanisms safeguard the bipolar attachment of chromosomes in mitosis. A correction mechanism destabilizes erroneous attachments that do not generate tension across sister kinetochores [1]. In response to unattached kinetochores, the mitotic checkpoint delays anaphase onset by inhibiting the anaphase-promoting complex/cyclosome (APC/C^{Cdc20}) [2]. Upon satisfaction of both pathways, the APC/C^{Cdc20} elicits the degradation of securin and cyclin B [3]. This liberates separase triggering sister chromatid disjunction and inactivates cyclin-dependent kinase 1 (Cdk1) causing mitotic exit. How eukaryotic cells avoid the engagement of attachment monitoring mechanisms when sister chromatids split and tension is lost at anaphase is poorly understood [4]. Here we show that Cdk1 inactivation disables mitotic checkpoint surveillance at anaphase onset in human cells. Preventing cyclin B1 proteolysis at the time of sister chromatid disjunction destabilizes kinetochore-microtubule attachments and triggers the engagement of the mitotic checkpoint. As a consequence, mitotic checkpoint proteins accumulate at anaphase kinetochores, the APC/C^{Cdc20} is inhibited, and securin reaccumulates. Conversely, acute pharmacological inhibition of Cdk1 abrogates the engagement and maintenance of the mitotic checkpoint upon microtubule depolymerization. We propose that the simultaneous destruction of securin and cyclin B elicited by the APC/C^{Cdc20} couples chromosome segregation to the dissolution of attachment monitoring mechanisms during mitotic exit.

Results and Discussion

Sister chromatids are held together until the metaphase-to-anaphase transition by a protein complex called cohesin [5]. After the destruction of securin, cleavage of cohesin by separase triggers the segregation of sister chromatids during anaphase. Cohesin cleavage also presumably abrogates the kinetochore tension that satisfies kinetochore attachment surveillance pathways. This raises the question of how eukaryotic cells avoid the potentially catastrophic action of these pathways during sister chromatid segregation at anaphase [4]. Recent work has shown that the artificial cleavage of cohesin in mitosis engages the mitotic checkpoint and destabilizes microtubule-kinetochore attachments [6, 7]. Eukaryotic cells may have solved this "anaphase problem" by entirely disabling these surveillance mechanisms at anaphase onset [8, 9]. The removal of Aurora B kinase, the tension sensor at kinetochores, from chromosomes at anaphase onset and the degradation of the checkpoint kinase Mps1 could contribute to this phenomenon [6, 8, 9]. Work in yeast cells, *Drosophila* embryos, and frog extracts has suggested that Cdk1-cyclin B, the enzyme that drives cells into mitosis, could act as an upstream regulator of the mitotic checkpoint [6, 7, 10–13]. The inactivation of Cdk1 through cyclin B proteolysis at anaphase onset could therefore disable attachment-monitoring pathways when sister chromatids split.

To investigate this hypothesis, we expressed a nondegradable (ND) version of cyclin B1 in HeLa Kyoto cells (ND cyclin B1-mCherry) (Figure 1). This mutant cyclin B1 protein (R42A and L45A) cannot be marked for proteolytic degradation by the anaphase-promoting complex/cyclosome (APC/C^{Cdc20}) ubiquitin ligase [3, 14]. Although Cdk1-cyclin B can inhibit separase [15], previous studies in *Drosophila* embryos and human cells have found that expression of a moderate level of ND cyclin B arrests cells in mitosis with separated sister chromatids [10, 16, 17]. Image quantification in our experiments revealed that both wild-type (WT) and ND cyclin B1 transgenes were expressed at levels close to the endogenous counterpart in the majority of cells (Figure S1A available online) (0.5-fold to 2-fold of endogenous cyclin B1).

WT cyclin B1 was degraded at the metaphase-to-anaphase transition, and cells underwent successful cell division before exiting mitosis (Figure 1A). In contrast, after alignment of chromosomes at the metaphase plate with normal kinetics, cells expressing ND cyclin B1 failed to degrade the transgenic protein. Cells with moderate levels of ND cyclin B1 subsequently displayed erratic chromosome movements and remained permanently arrested in mitosis (Figure 1A) (38/41 cells). The maintenance of this state, which we refer to as pseudoanaphase, was dependent on continuous Cdk1 activity (Figure S1B). The onset of pseudoanaphase in cells expressing ND cyclin B1 occurred with a timing that was comparable to anaphase onset in control cells (Figure S1C). This is in stark contrast to chromosome scattering caused by cohesion fatigue [18, 19], which takes several hours to occur in metaphase-arrested cells (Figure S1D).

Chromosome spread analysis and fluorescence in situ hybridization experiments revealed that sister chromatids were split in pseudoanaphase cells (Figures 1B and 1C). The loss of sister chromatid cohesion in pseudoanaphase cells, but not in cells lacking the cohesin protector protein Sgo1 [5], could be suppressed by addition of the proteasome inhibitor MG132 (Figures 1B, S1E, and S1F). Furthermore, chromosome scattering occurred concomitantly with the degradation of

*Correspondence: lolavazquez.novelle@cancer.org.uk (M.D.V.-N.), mark.petronczki@cancer.org.uk (M.P.)
This is an open-access article distributed under the terms of the Creative Commons Attribution-NonCommercial-No Derivative Works License, which permits non-commercial use, distribution, and reproduction in any medium, provided the original author and source are credited.

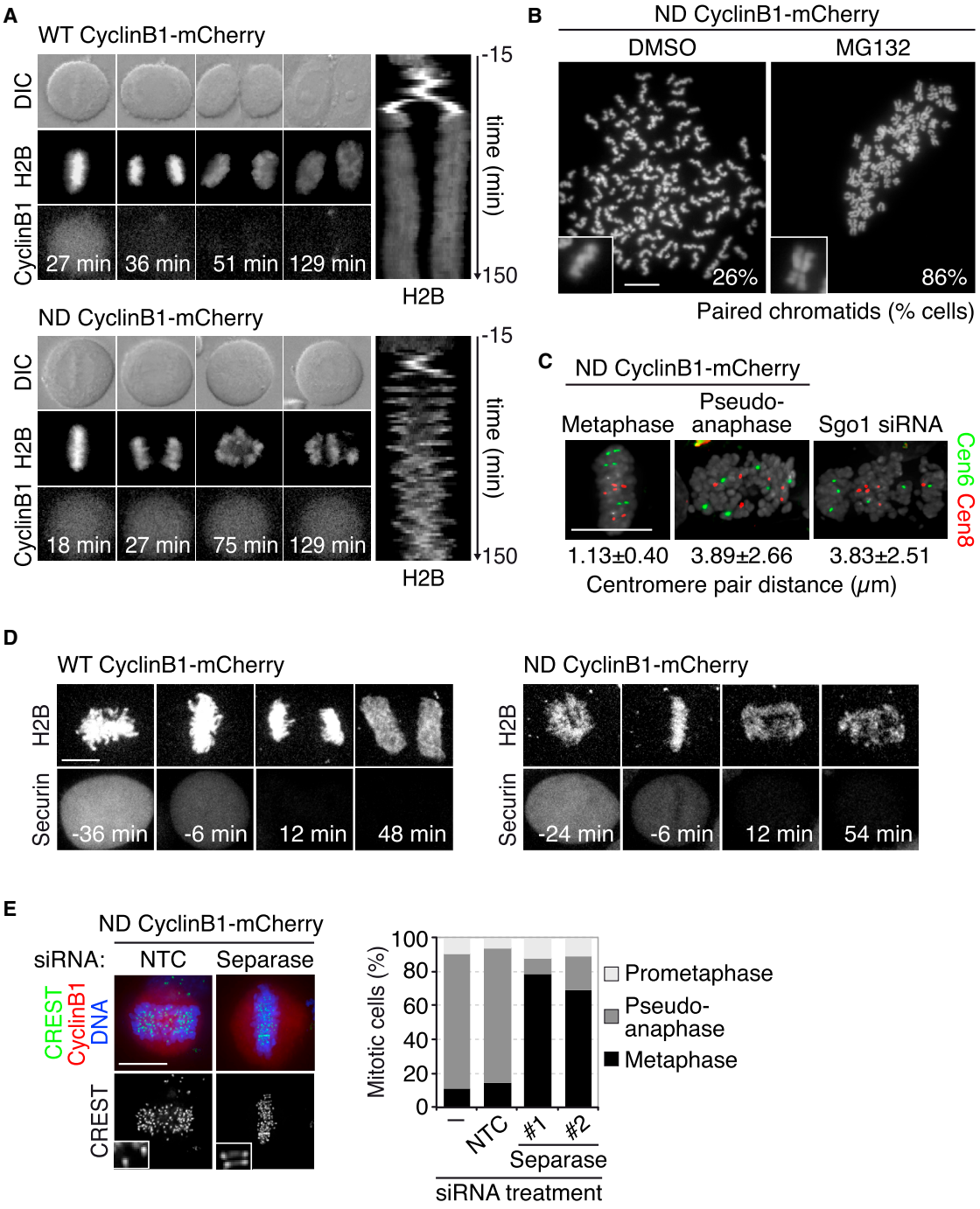

Figure 1. Expression of Moderate Levels of Nondegradable Cyclin B1 Separates APC/C^{Cdc20} Activation and Sister Chromatid Disjunction from Cdk1 Inactivation

(A) Time-lapse series and kymograph of H2B-EGFP HeLa cells expressing wild-type (WT) or nondegradable (ND) cyclin B1-mCherry. While 93% of cells expressing ND cyclin B1 arrested in mitosis, all cells expressing WT cyclin B1 exited mitosis (n > 40 cells from three independent experiments). The first time frame after nuclear envelope breakdown (NEBD) corresponds to t = 0 min. See also Figure S1.

(B) Chromosome spreads of cells expressing ND cyclin B1 that were synchronously released into mitosis and treated with DMSO (control) or the proteasome inhibitor MG132 (10 μM) for 4 hr (n > 299 spreads from 3 independent experiments). See also Figures S1E and S1F.

(C) Fluorescence in situ hybridization (FISH) analysis of the centromeres of trisomic chromosomes 6 and 8. Distance between the closest centromeres was measured on 3D pictures (n > 29 cells). Depletion of Sgo1 was used as a control for loss of sister chromatid cohesion.

(D) Analysis of securin degradation. Confocal live-cell imaging of H2B-iRFP HeLa cells expressing securin-EGFP and WT or ND cyclin B1-mCherry is shown. Time = 0 min was set to the first frame after anaphase onset. See also Figure 3A.

(E) Immunofluorescence (IF) analysis and quantification of mitotic cells expressing ND cyclin B1 and transfected with either nontargeting control (NTC) small interfering RNA (siRNA) or siRNA duplexes targeting separase (n > 152 cells from three independent experiments). See also Figure S1G.

Scale bars represent 10 μm. See also Figure S1.

securin and within a short time after removal of MG132 (Figures 1D, 3A, and S1D). Importantly, chromatid scattering in cells expressing ND cyclin B1 was abolished by depletion of separase (Figures 1E and S1G). Our observations suggest that the transition from metaphase to pseudoanaphase in cells expressing ND cyclin B1 involves APC/C-dependent proteolysis and separase-dependent disjunction of sister chromatids, a situation closely resembling normal anaphase onset. Thus, expression of moderate levels of ND cyclin B1 separates APC/C^{Cdc20} action and anaphase onset from the inactivation of Cdk1. In line with this interpretation, the tension sensor at kinetochores, Aurora B kinase [1], whose removal from chromosomes at the metaphase-to-anaphase transition depends on Cdk1 inactivation [20], remained associated with centromeres in pseudoanaphase cells (Figure S2A). Cells expressing ND cyclin B1 therefore provided a suitable model to investigate the consequences of separase-induced sister chromatid disjunction in the absence of Cdk1 inactivation.

First, we scrutinized the localization of mitotic checkpoint proteins, which in early mitosis mark unattached kinetochores or kinetochores that lack tension [1, 2]. When stable bipolar attachments are formed at metaphase, mitotic checkpoint proteins dissociate from kinetochores and subsequently become undetectable at this location in anaphase [8]. Accordingly, kinetochore localization of mitotic checkpoint proteins was undetectable (Mad1, Mad2, and Mps1) or low (Bub1 and BubR1) in ND cyclin B1-positive metaphase cells (Figures 2A and S2B–S2D). In contrast, we found that Mad1, Mad2, Bub1, BubR1, and Mps1 were all recruited to kinetochores in pseudoanaphase cells that express ND cyclin B1 (Figures 2A and S2B–S2D). Kinetochore localization of Mad2 in pseudoanaphase cells was abrogated upon treatment of cells with reversine, an inhibitor of the mitotic checkpoint kinase Mps1 [21] (Figure 2B), and upon inhibition of Aurora B kinase (Figure S2E). Imaging of cells expressing ND cyclin B1 revealed the formation of Mad2-EGFP foci on chromosomes within 10 min (12/16 cells) or 15 min (4/16 cells) of pseudoanaphase onset (Figure 2C). Mad2-EGFP remained undetectable on chromosomes in cells that underwent anaphase while degrading WT cyclin B1, despite marking unaligned chromosomes in early mitosis (Figure 2C). These results suggest that separase-dependent cohesin cleavage and sister chromatid separation cause the re-engagement of the mitotic checkpoint pathway if cyclin B1 proteolysis is prevented and Cdk1 remains active at anaphase onset.

Mad1 and Mad2 kinetochore recruitment is thought to reflect partial or complete lack of microtubule attachment [1, 2]. The chaotic chromatid movements and the localization of Mad1 and Mad2 to multiple kinetochores that is observed upon sister splitting in cells expressing ND cyclin B1 raise the possibility that kinetochore-microtubule attachments are unstable in pseudoanaphase. To test this, we analyzed the stability of kinetochore fibers using cold treatment. Exposure to low temperature allows the preservation of stable kinetochore fibers in metaphase and anaphase cells but eliminates compromised attachments, such as those in cells treated with the Polo-like kinase 1 inhibitor BI 2536 (Figure 2D). Although kinetochore fibers in cells expressing ND cyclin B1 were cold resistant at metaphase, microtubule stability was dramatically reduced in the pseudoanaphase state (Figure 2D). Furthermore, tracking experiments revealed that kinetochores in pseudoanaphase cells failed to show persistent directional movement toward the closest spindle pole and underwent directional switches (Figures 2E and S2F). In vivo analysis of kinetochore architecture in yeast found that anaphase kinetochores adopted a relaxed configuration, possibly reflecting a loss of tension [22]. Our results suggest that, if cyclin B is not degraded, sister chromatid separation at anaphase onset could cause the erroneous destabilization of microtubule attachments at tensionless kinetochores and, subsequently, the untimely recruitment of mitotic checkpoint proteins.

Next, we tested whether these responses to sister chromatid separation in pseudoanaphase cells can lead to the inhibition of the APC/C^{Cdc20}. To address this question, we analyzed the level of the APC/C^{Cdc20} substrate securin and the assembly of the mitotic checkpoint complex (MCC) over time in cells expressing either WT or ND cyclin B1 (Figure 3). The MCC is a key biochemical effector of the mitotic checkpoint and is composed of BubR1, Mad2, Bub3, and the APC/C cofactor Cdc20 [2]. In cells expressing WT cyclin B1, both securin and cyclin B1 were degraded at the metaphase-to-anaphase transition (Figure 3A). In cells expressing ND cyclin B1, securin was degraded at the time of chromosome scattering, but subsequently its protein levels rose again, albeit slowly and not reaching mitotic peak levels (Figure 3A). Coimmunoprecipitation of Cdc20 and Mad2 suggested that cells expressing ND cyclin B1 reassemble the APC/C^{Cdc20} inhibitor MCC after undergoing sister chromatid separation (Figure 3B). Importantly, inhibition of Mps1 kinase at the time of pseudoanaphase onset prevented subsequent MCC formation and securin accumulation (Figures 3C, 3D, and S3). These data suggest that although both WT and ND cyclin B1-expressing cells activate the APC/C^{Cdc20} and degrade APC/C substrates at the time of sister disjunction, maintenance of Cdk1 activity in ND cyclin B1-positive cells past the metaphase-to-anaphase transition elicits inhibition of the APC/C^{Cdc20}. Prevention of cyclin B1 proteolysis at anaphase onset appears to be sufficient to cause mitotic checkpoint engagement and APC/C^{Cdc20} inhibition in response to cohesin cleavage. The corollary of this conclusion is that the inactivation of Cdk1 just prior to anaphase onset in normal cells could be responsible for preventing untimely checkpoint engagement caused by sister chromatids splitting.

To test this hypothesis and corroborate the link between Cdk1 activity and mitotic checkpoint surveillance, we conducted acute pharmacological perturbation experiments in mitotic cells. As a proxy for mitotic checkpoint engagement, we used the rapid recruitment of Mad2-EGFP to kinetochores upon microtubule depolymerization by nocodazole (Figures 4A, 4B [upper panel], and S4A). Addition of the Cdk inhibitor flavopiridol about 2 min prior to or at the time of nocodazole application prevented the localization of Mad2-EGFP to kinetochores (Figures 4A and 4B [middle panel]). We noticed that flavopiridol treatment also slowed down the depolymerization of microtubules and dissolution of the metaphase plate after nocodazole treatment (Figure S4B). This effect, however, is unlikely to account for the absence of Mad2 recruitment, because the protein also failed to accumulate at kinetochores at time points when the spindle was largely disassembled (Figures 4B [middle panel] and S4B) and in cells with a disorganized metaphase plate (Figure 4A). Furthermore, we found that chemical inhibition of Cdk1 after microtubule depolymerization resulted in the loss of Mad2-EGFP from chromosomes within 15 min (Figure 4B, lower panel). These results suggest that Cdk1 activity is required for both mounting and maintaining a mitotic checkpoint response in human cells. The effects of chemical Cdk1 inhibition did not depend on proteolysis of other factors because addition of flavopiridol prevented or

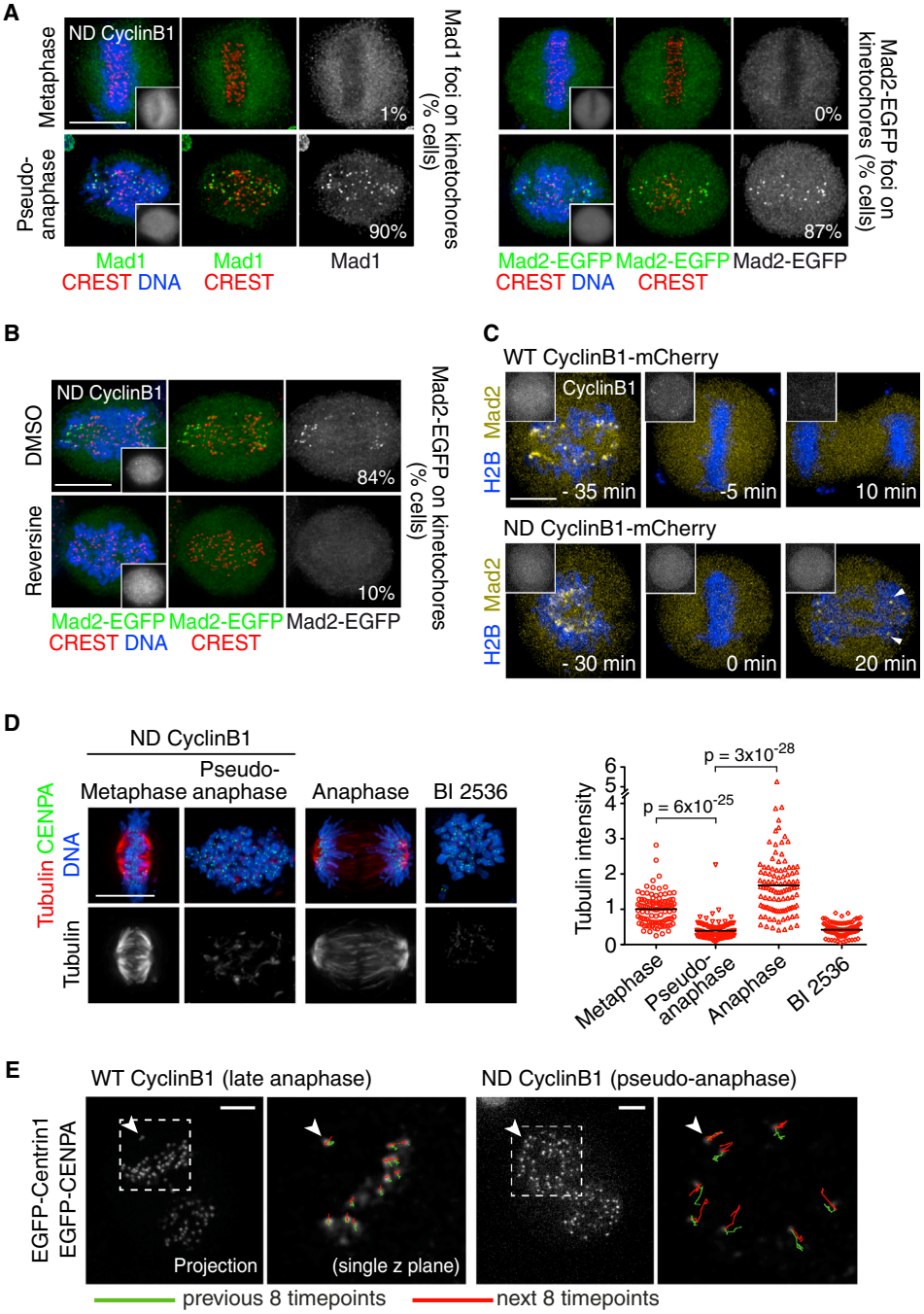

Figure 2. Preventing Cyclin B1 Proteolysis at the Time of Sister Chromatid Separation Causes Recruitment of Mitotic Checkpoint Proteins to Kinetochores and the Destabilization of Microtubule-Kinetochore Attachments

(A) Mad1 and Mad2 localization was analyzed by IF in cells expressing ND cyclin B1-mCherry (n > 149 cells from three independent experiments). See also Figures S2A–S2D for Aurora B, Bub1, BubR1, and Mps1 localization.

(B) Mad2 localization was analyzed by IF 2 hr after MG132 release in cells expressing ND cyclin B1-mCherry. DMSO or reversine (0.5 μM) was added 40 min after release from MG132 arrest (n > 149 cells from three independent experiments). See also Figure S2E for effect of Aurora B inhibition.

(C) Confocal live-cell imaging of Mad2-EGFP H2B-iRFP HeLa cells expressing WT or ND cyclin B1-mCherry. Mad2 foci on chromosomes, indicated by arrowheads, are detected 4.7 ± 3.8 min after anaphase onset (t = 0 min) (n = 16 cells from more than three independent experiments).

(D) Microtubule stability was analyzed by IF in cells using cold treatment. Integrated intensities of cold-resistant α-tubulin were measured and background corrected in EGFP-CENPA HeLa cells that were either transfected with ND cyclin B1-mCherry or treated for 2 hr with 100 nM BI 2536 (n > 101 cells from three independent experiments). Tubulin intensities per cell are normalized to the average tubulin intensity in metaphase cells in each experiment and displayed in a scatter dot plot (right). Horizontal black lines represent the mean. p values were calculated using a two-tailed t test. Scale bars represent 10 μm.

(E) Analysis of kinetochore and spindle pole (indicated by arrowheads) trajectories in late anaphase cells (WT cyclin B1) and in pseudoanaphase cells (ND cyclin B1). Images are representative of six late-anaphase and nine pseudoanaphase cells analyzed. Scale bars represent 5 μm. See also Figure S2F. See also Figure S2.

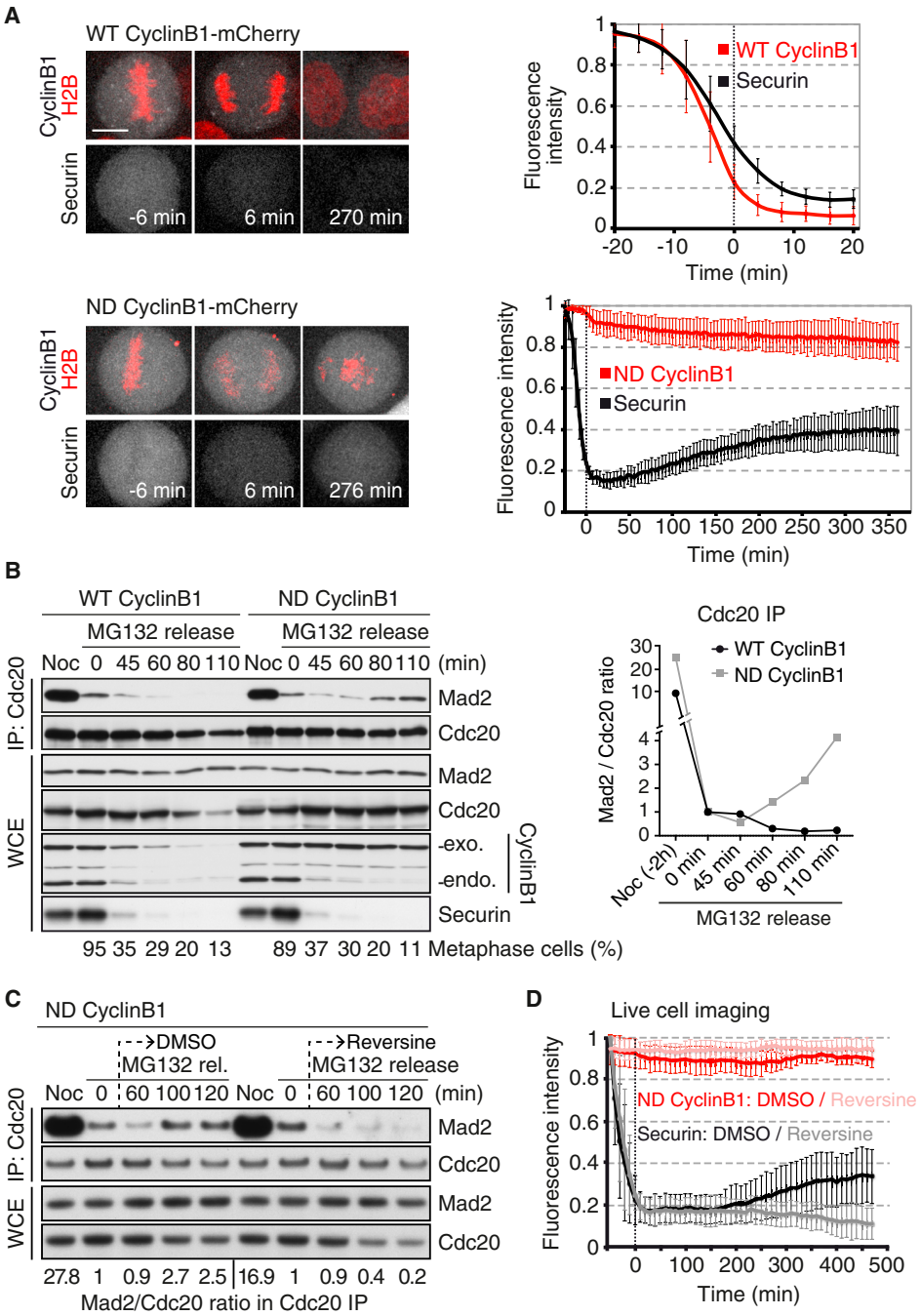

Figure 3. Reaccumulation of Securin and MCC after Sister Chromatid Disjunction in the Absence of Cyclin B1 Proteolysis

(A) Frames of confocal live-cell imaging of H2B-iRFP HeLa cells expressing securin-EGFP and WT or ND cyclin B1-mCherry are shown (left). The integrated intensities of securin-EGFP and cyclin B1-mCherry were measured, background corrected, and normalized to the maximum-intensity value obtained per cell. Measurements in different cells were aligned to t = 0 min as the first frame after anaphase onset. The graph displays the mean intensity of securin and cyclin B1 (right). Error bars represent the SD of the analysis of nine cells per condition (from three experiments). The scale bar represents 10μm.

(B) Coimmunoprecipitation analysis of mitotic checkpoint complex (MCC) formation in cells expressing WT or ND cyclin B1. Cdc20 was immunoprecipitated from extracts prepared from nocodazole-arrested (Noc) and MG132-arrested cells at t = 0 min as well as from cells released from metaphase for the indicated times. Mad2 and Cdc20 intensities were analyzed in whole-cell extracts (WCE) and the precipitated fraction (IP) by fluorescent immunoblotting. The Mad2/Cdc20 ratio in the IP fraction was determined, normalized to the ratio at 0 min, and plotted (right). Due to the degradation of Cdc20 in WT cyclin B1-expressing cells, the amount of IP fraction loaded was adjusted for comparable amounts of Cdc20. The percentage of metaphase cells was determined using time-lapse analysis (n > 102 cells).

(C) Analysis of MCC formation as in (B). Cells expressing ND cyclin B1 were treated with DMSO or 0.5 μM reversine 40 min after MG132 release.

(D) Securin-EGFP accumulation in pseudoanaphase cells depends on Mps1 kinase. One hour after release from nocodazole (30 ng/ml), cells expressing ND cyclin B1 were treated with DMSO or reversine (0.5 μM). The graph is as in (A) (n = 9 cells per condition from three independent experiments).

See also Figure S3.

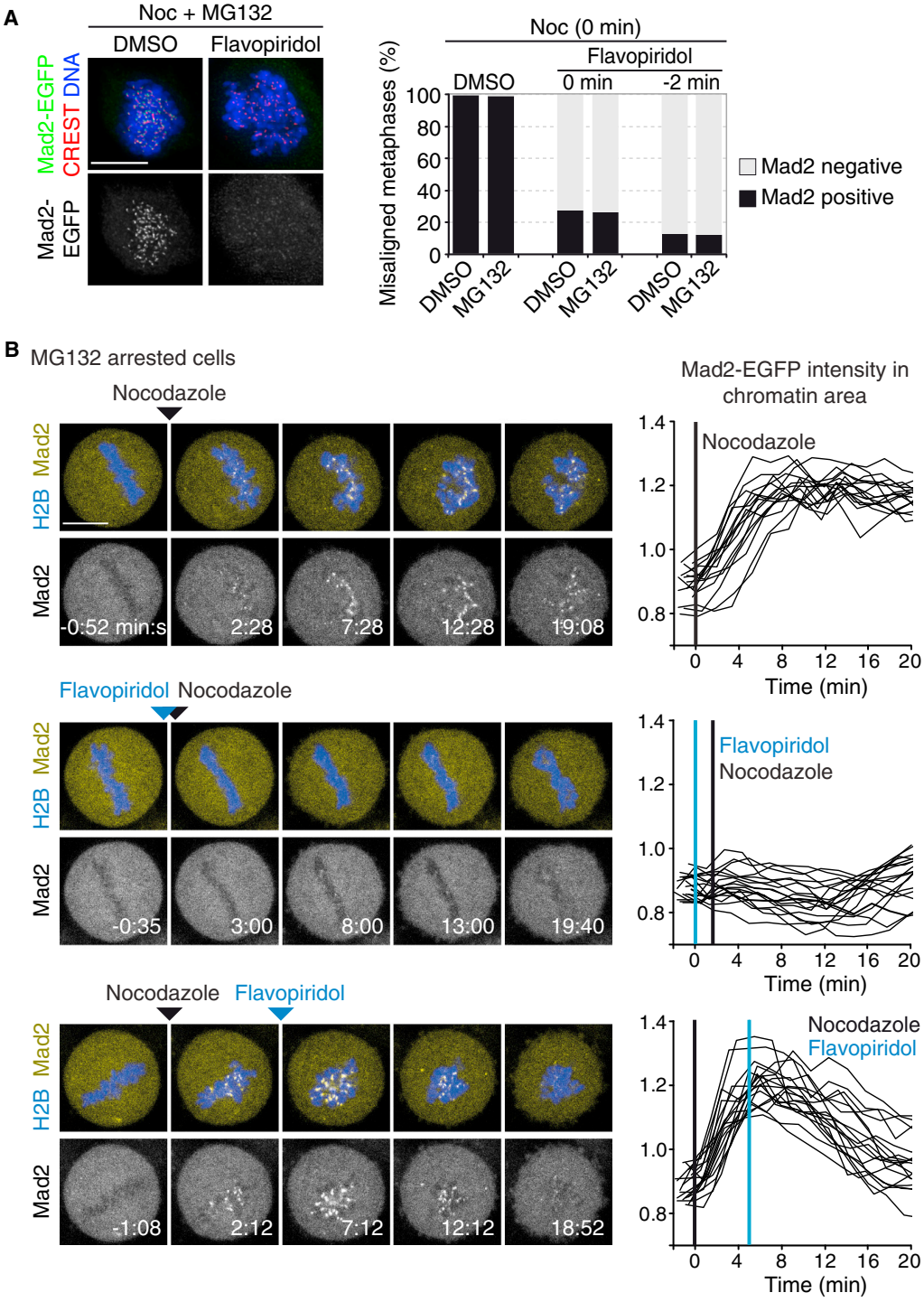

Figure 4. Cdk1 Activity Is Required for Mad2 Recruitment and Retention at Kinetochores upon Microtubule Depolymerization

(A) IF analysis of Mad2-EGFP kinetochore localization. HeLa cells were arrested in metaphase by addition of MG132 for 2 hr and subsequently released (DMSO) or kept in presence of MG132 during the experiment. DMSO or flavopiridol (15 μM) was added 2 min prior to addition of nocodazole (1 μg/ml) or at the time of nocodazole addition. Kinetochore localization of Mad2-EGFP was analyzed in cells with disrupted chromosome alignment 10 min after treatment with nocodazole (n > 300 cells from three independent experiments).

(B) Mad2-EGFP kinetochore localization in live cells. HeLa cells expressing H2B-mCherry and Mad2-EGFP were arrested in metaphase with MG132 (30–90 min) and imaged by three-dimensional confocal live-cell microscopy. Nocodazole (1 μg/ml) and flavopiridol (20 μM) were acutely added during imaging as indicated by the arrowheads and vertical lines in black and blue, respectively. Images show single confocal z sections of representative cells. Graphs show quantified kinetics of Mad2 intensity on chromatin regions over cytoplasm in individual cells (n > 15 cells from three independent experiments). Time = 0:00 min:s at the first drug addition.

Scale bars represent 10 μm. See also Figure S4 for microtubule depolymerization kinetics.

abolished the localization of Mad2-EGFP to kinetochores in the presence of MG132 (Figure 4). This indicates that the dephosphorylation of Cdk1 substrates causes the direct or indirect dissolution of mitotic checkpoint surveillance and highlights cyclin B as a key APC/C^{Cdc20} substrate for this regulation at the metaphase-to-anaphase transition.

We found that the central event of anaphase, the separase-dependent disjunction of sister chromatids, can lead to the destabilization of kinetochore attachments and the engagement of a mitotic checkpoint response with potentially deleterious consequences. Our experiments suggest that eukaryotic cells avoid this by coordinating separase activation with the termination of attachment surveillance mechanisms. This is achieved through the action of the APC/C^{Cdc20} that elicits the simultaneous destruction of securin and cyclin B. This coupling could render late metaphase cells refractory to the loss of tension caused by cohesin cleavage upon anaphase initiation and contribute to the irreversibility of mitotic exit [23]. Experiments in mouse zygotes have led to similar conclusions, suggesting conservation of this mechanism [24]. While cell-cycle surveillance mechanisms are generally considered to exist in two states, engaged or satisfied, our work highlights a third state in which a mechanism has been disabled and is no longer monitoring cellular events. The transition from the satisfied to the disabled state of the mitotic checkpoint most likely occurs very briefly before anaphase entry, as acutely detached chromosomes remain proficient in recruiting Mad2-EGFP and inhibiting APC/C^{Cdc20} throughout most of metaphase [25, 26].

Studies in *Drosophila* and yeast cells have shown that reversal of Cdk1 activity prevents engagement of the mitotic checkpoint in response to artificial sister chromatid disjunction [6, 7]. Our work suggests that cyclin B1's destruction stabilizes kinetochore attachments and terminates mitotic checkpoint surveillance after anaphase onset. Separase-induced sister chromatid separation can elicit the inhibition of APC/C^{Cdc20} if Cdk1 is not inactivated concomitantly. This raises the possibility that if the mitotic checkpoint is not disabled in anaphase, the reaccumulation of securin and cyclin B could interfere with chromatid separation and mitotic exit. However, after sister chromatid splitting in ND cyclin B1-expressing cells, securin-EGFP, as well as the endogenous APC/C^{Cdc20} substrates cyclin B1 and securin, did not reaccumulate significantly within a short timeframe (Figures 3A and 3B). The slow reaccumulation could be linked to the requirement for resynthesis and to only partial and slow inhibition of APC/C^{Cdc20} [26, 27], which may help protect mitotic exit from the adverse effects of untimely mitotic checkpoint engagement in anaphase. Nevertheless, failure to degrade cyclin B at anaphase onset in mouse zygotes causes mitotic checkpoint-dependent inhibition of APC/C^{Cdc20} substrate degradation [24], suggesting physiological importance of mitotic checkpoint dissolution by Cdk1 inactivation.

The loss of stable kinetochore attachments that we observed upon chromatid separation in the presence of Cdk1 activity in human cells could result in chromosome nondisjunction events and lead to aneuploidy. Recent work showed that the degradation of cyclin A increases the stability of kinetochore-microtubule attachments between prometaphase and metaphase [28]. Kinetochore fiber stability further increases in anaphase cells [29]. We detected destabilization of kinetochore-microtubule attachments, as judged by Mad2 recruitment to unattached kinetochores, within 10 min of sister chromatid splitting in the presence of ND cyclin B1. Thus, cyclin B proteolysis and the reversal of Cdk1-dependent phosphorylation are likely to be crucial for the generation of stable kinetochore-microtubule attachments that underlie the correct partitioning of sister chromatids in anaphase [30].

In combination with previous studies [6–8, 10–12], this work establishes Cdk1-cyclin B as a switch that sets up mitotic checkpoint surveillance as cells enter mitosis and disables surveillance during anaphase. Cdk1-dependent localization of Aurora B to centromeres [8], together with additional Cdk1-controlled effects at kinetochores, is likely to sustain the mitotic checkpoint. In the future, it will be important to identify these additional substrates whose phosphoregulation confers direct or indirect Cdk1 control over mitotic checkpoint surveillance and the stability of kinetochore-microtubule attachments.

Supplemental Information

Supplemental Information includes Supplemental Experimental Procedures and four figures and can be found with this article online at http://dx.doi.org/10.1016/j.cub.2014.01.034.

Acknowledgments

We would like to thank Julian Gannon, Silke Hauf, Tony Hyman, Peter Lenart, Andrea Musacchio, Jan-Michael Peters, Jonathon Pines, Kuan-Chung Su, and Stephen Taylor for reagents and advice. We are grateful to Peter Jordan and Daniel Zicha for help with light microscopy, Richard Mitter for bioinformatic support, and Sriramkumar Sundaramoorthy for comments on the manuscript. Research in the Gerlich laboratory has received funding from the European Community's Seventh Framework Programme FP7/2007-2013 under grant agreement numbers 241548 (MitoSys) and 258068 (Systems Microscopy), an ERC Starting Grant (agreement number 281198), the EMBO Young Investigator Programme, the Swiss National Science Foundation, the Austrian Science Fund (FWF)-funded project "SFB Chromosome Dynamics," and a Summer Research Award of the Marine Biology Laboratory Woods Hole (Laura and Arthur Colwin Endowed Summer Research Fellowship Fund). A.E.D. is a fellow of the Zurich Ph.D. Program in Molecular Life Sciences and has received funding from a Ph.D. fellowship by the Boehringer Ingelheim Fonds and from a Peter Müller fellowship. A.D.M. was supported by a Biotechnology and Biological Sciences Research Council (BBSRC) project grant (grant number BB/I021353/1). C.A.S. was supported by the Engineering and Physical Sciences Research Council (EPSRC) (grant number EP/F500378/1) via the MOAC doctoral training center. M.D.V.-N. acknowledges support by a Ramón Areces Foundation Fellowship. L.S. was supported by fellowships from the European Molecular Biology Organization (EMBO) and the Canadian Institutes of Health Research (CIHR). Work in the lab of M.P. is supported by Cancer Research UK and the EMBO Young Investigator Programme.

Received: October 16, 2013
Revised: December 24, 2013
Accepted: January 14, 2014
Published: February 27, 2014

References

1. Nezi, L., and Musacchio, A. (2009). Sister chromatid tension and the spindle assembly checkpoint. Curr. Opin. Cell Biol. *21*, 785–795.
2. Lara-Gonzalez, P., Westhorpe, F.G., and Taylor, S.S. (2012). The spindle assembly checkpoint. Curr. Biol. *22*, R966–R980.
3. Peters, J.M. (2006). The anaphase promoting complex/cyclosome: a machine designed to destroy. Nat. Rev. Mol. Cell Biol. *7*, 644–656.
4. Vázquez-Novelle, M.D., Mirchenko, L., Uhlmann, F., and Petronczki, M. (2010). The 'anaphase problem': how to disable the mitotic checkpoint when sisters split. Biochem. Soc. Trans. *38*, 1660–1666.
5. Nasmyth, K., and Haering, C.H. (2009). Cohesin: its roles and mechanisms. Annu. Rev. Genet. *43*, 525–558.
6. Mirchenko, L., and Uhlmann, F. (2010). Sli15(INCENP) dephosphorylation prevents mitotic checkpoint reengagement due to loss of tension at anaphase onset. Curr. Biol. *20*, 1396–1401.
7. Oliveira, R.A., Hamilton, R.S., Pauli, A., Davis, I., and Nasmyth, K. (2010). Cohesin cleavage and Cdk inhibition trigger formation of daughter nuclei. Nat. Cell Biol. *12*, 185–192.

8. Vázquez-Novelle, M.D., and Petronczki, M. (2010). Relocation of the chromosomal passenger complex prevents mitotic checkpoint engagement at anaphase. Curr. Biol. *20*, 1402–1407.
9. Palframan, W.J., Meehl, J.B., Jaspersen, S.L., Winey, M., and Murray, A.W. (2006). Anaphase inactivation of the spindle checkpoint. Science *313*, 680–684.
10. Parry, D.H., Hickson, G.R., and O'Farrell, P.H. (2003). Cyclin B destruction triggers changes in kinetochore behavior essential for successful anaphase. Curr. Biol. *13*, 647–653.
11. D'Angiolella, V., Mari, C., Nocera, D., Rametti, L., and Grieco, D. (2003). The spindle checkpoint requires cyclin-dependent kinase activity. Genes Dev. *17*, 2520–2525.
12. Yamaguchi, S., Decottignies, A., and Nurse, P. (2003). Function of Cdc2p-dependent Bub1p phosphorylation and Bub1p kinase activity in the mitotic and meiotic spindle checkpoint. EMBO J. *22*, 1075–1087.
13. Morin, V., Prieto, S., Melines, S., Hem, S., Rossignol, M., Lorca, T., Espeut, J., Morin, N., and Abrieu, A. (2012). CDK-dependent potentiation of MPS1 kinase activity is essential to the mitotic checkpoint. Curr. Biol. *22*, 289–295.
14. Gavet, O., and Pines, J. (2010). Progressive activation of CyclinB1-Cdk1 coordinates entry to mitosis. Dev. Cell *18*, 533–543.
15. Stemmann, O., Zou, H., Gerber, S.A., Gygi, S.P., and Kirschner, M.W. (2001). Dual inhibition of sister chromatid separation at metaphase. Cell *107*, 715–726.
16. Hagting, A., Den Elzen, N., Vodermaier, H.C., Waizenegger, I.C., Peters, J.M., and Pines, J. (2002). Human securin proteolysis is controlled by the spindle checkpoint and reveals when the APC/C switches from activation by Cdc20 to Cdh1. J. Cell Biol. *157*, 1125–1137.
17. Wolf, F., Wandke, C., Isenberg, N., and Geley, S. (2006). Dose-dependent effects of stable cyclin B1 on progression through mitosis in human cells. EMBO J. *25*, 2802–2813.
18. Daum, J.R., Potapova, T.A., Sivakumar, S., Daniel, J.J., Flynn, J.N., Rankin, S., and Gorbsky, G.J. (2011). Cohesion fatigue induces chromatid separation in cells delayed at metaphase. Curr. Biol. *21*, 1018–1024.
19. Stevens, D., Gassmann, R., Oegema, K., and Desai, A. (2011). Uncoordinated loss of chromatid cohesion is a common outcome of extended metaphase arrest. PLoS ONE *6*, e22969.
20. Hümmer, S., and Mayer, T.U. (2009). Cdk1 negatively regulates midzone localization of the mitotic kinesin Mklp2 and the chromosomal passenger complex. Curr. Biol. *19*, 607–612.
21. Santaguida, S., Tighe, A., D'Alise, A.M., Taylor, S.S., and Musacchio, A. (2010). Dissecting the role of MPS1 in chromosome biorientation and the spindle checkpoint through the small molecule inhibitor reversine. J. Cell Biol. *190*, 73–87.
22. Joglekar, A.P., Bloom, K., and Salmon, E.D. (2009). In vivo protein architecture of the eukaryotic kinetochore with nanometer scale accuracy. Curr. Biol. *19*, 694–699.
23. He, E., Kapuy, O., Oliveira, R.A., Uhlmann, F., Tyson, J.J., and Novák, B. (2011). System-level feedbacks make the anaphase switch irreversible. Proc. Natl. Acad. Sci. USA *108*, 10016–10021.
24. Rattani, A., Vinod, P.K., Godwin, J., Tachibana-Konwalski, K., Wolna, M., Malumbres, M., Novák, B., and Nasmyth, K. (2014). Dependency of the spindle assembly checkpoint on Cdk1 renders the anaphase transition irreversible. Curr. Biol. Published online February 27, 2014. http://dx.doi.org/10.1016/j.cub.2014.01.033.
25. Clute, P., and Pines, J. (1999). Temporal and spatial control of cyclin B1 destruction in metaphase. Nat. Cell Biol. *1*, 82–87.
26. Dick, A.E., and Gerlich, D.W. (2013). Kinetic framework of spindle assembly checkpoint signalling. Nat. Cell Biol. *15*, 1370–1377.
27. Collin, P., Nashchekina, O., Walker, R., and Pines, J. (2013). The spindle assembly checkpoint works like a rheostat rather than a toggle switch. Nat. Cell Biol. *15*, 1378–1385.
28. Kabeche, L., and Compton, D.A. (2013). Cyclin A regulates kinetochore microtubules to promote faithful chromosome segregation. Nature *502*, 110–113.
29. Zhai, Y., Kronebusch, P.J., and Borisy, G.G. (1995). Kinetochore microtubule dynamics and the metaphase-anaphase transition. J. Cell Biol. *131*, 721–734.
30. Higuchi, T., and Uhlmann, F. (2005). Stabilization of microtubule dynamics at anaphase onset promotes chromosome segregation. Nature *433*, 171–176.

Current Biology, Volume *24*

Supplemental Information

Cdk1 Inactivation Terminates Mitotic Checkpoint Surveillance and Stabilizes Kinetochore Attachments in Anaphase

María Dolores Vázquez-Novelle, Laurent Sansregret, Amalie E. Dick, Christopher A. Smith, Andrew D. McAinsh, Daniel W. Gerlich, and Mark Petronczki

Supplemental Figures

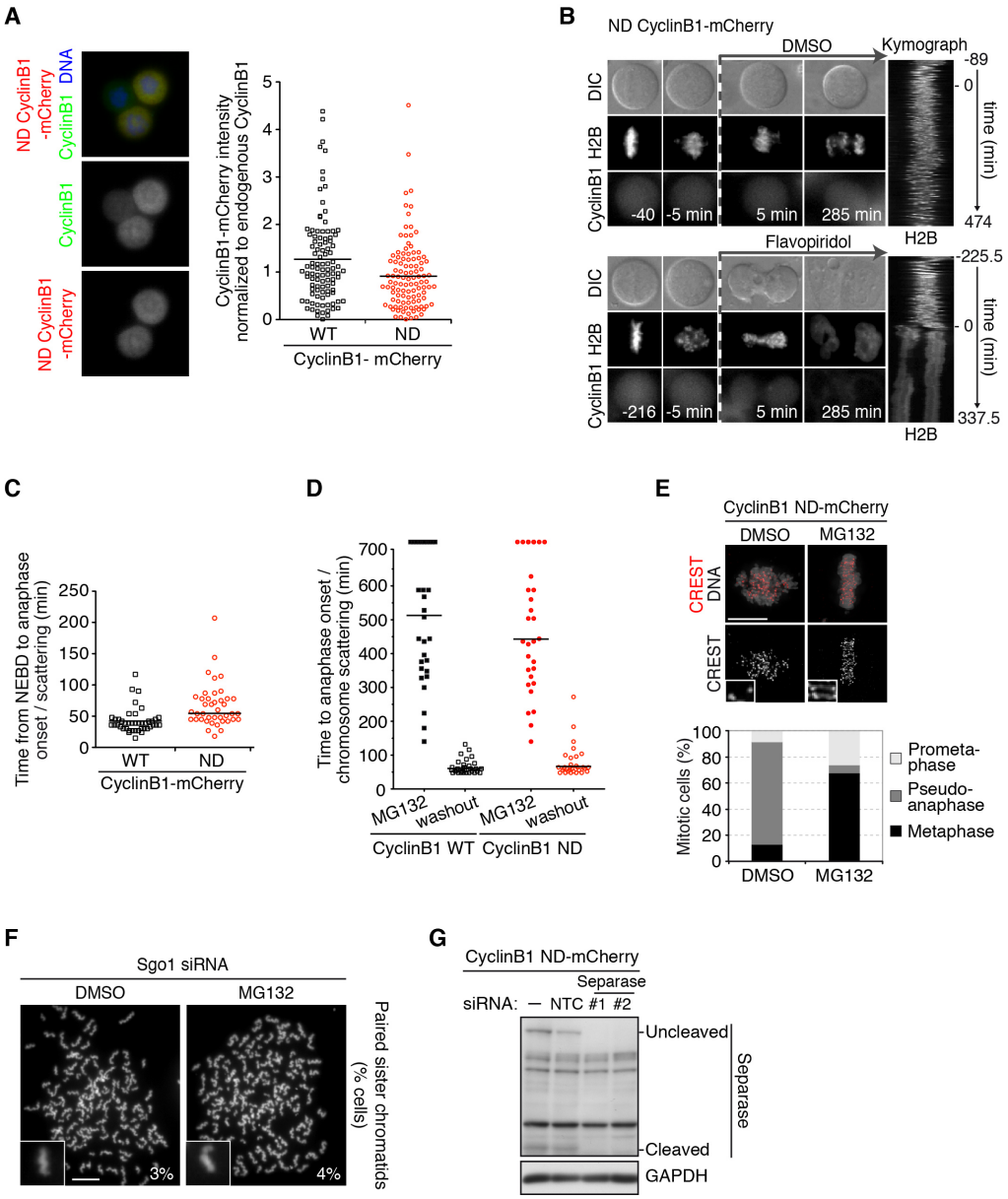

Figure S1 (Related to Figure 1). Expression of moderate levels of ND cyclin B1-mCherry causes proteolysis-dependent chromosome scattering and a Cdk activity-dependent mitotic arrest

(A) Levels of transgenic cyclin B1-mCherry (WT or ND) and endogenous cyclin B1 were measured by IF in cells arrested in prometaphase by addition of nocodazole (50 ng/ml) (n>101 cells). Cyclin B1-mCherry levels in transfected cells were normalized to the mean level of endogenous cyclin B1 in mitotic cells and are shown in a scatter plot (right). Horizontal black lines in the scatter plot represent the mean value.

(B) Time-lapse series and kymograph of cells expressing ND cyclin B1-mCherry that were treated at t = 0 min with flavopiridol or DMSO (control). 100% of cells treated with flavopiridol exited mitosis in comparison with 0% of control cells (n>5 cells).
(C) Timing of anaphase onset or chromosome scattering separation in cells expressing WT or ND cyclin B1-mCherry, respectively. The graph displays the time from NEBD to the anaphase onset or chromosome scattering (n>40 cells, in 3 independent experiments). Black lines in the dot plot mark the median.
(D) Analysis of time-lapse series of H2B-EGFP HeLa cells expressing WT or ND cyclin B1-mCherry that were arrested in metaphase (MG132 for 2 h) and subsequently (t = 0 min) released into anaphase/pseudo-anaphase, or kept in presence of MG132 (n>29). Horizontal black lines represent median in the scatter dot plot.
(E) IF analysis of centromeres in mitotic cells expressing ND cyclin B1-mCherry (n>299 cells from 3 independent experiments). Cells were synchronously released into mitosis and then treated with DMSO (control) or MG132 for 4 hours.
(F) Chromosome spread analysis of cells transfected with Sgo1 siRNA. Cells were synchronously released into mitosis and treated with DMSO (control) or MG132 for 4 hours (n>299 spreads from 3 independent experiments). Scale bars represent 10μm.
(G) Immunoblot analysis of protein extracts prepared from nocodazole-arrested cells expressing ND cyclin B1-mCherry that were transfected with NTC siRNA or siRNA duplexes targeting separase.

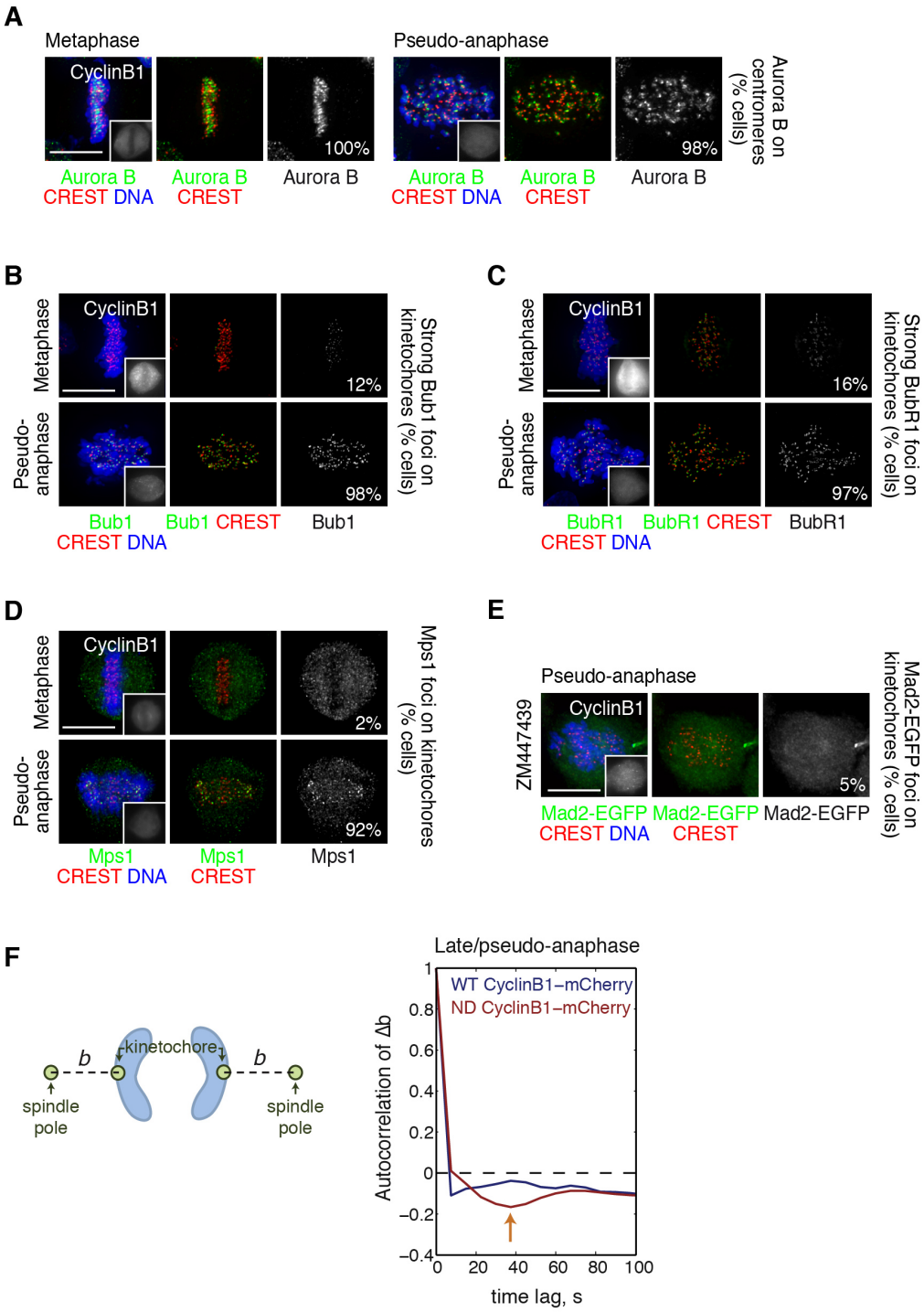

Figure S2 (Related to Figure 2). Kinetochore recruitment of mitotic checkpoint proteins and oscillatory kinetochore movements in pseudo-anaphase cells

(A) IF analysis of Aurora B, (B) Bub1, (C) BubR1 and (D) Mps1 localization in metaphase and pseudo-anaphase cells expressing ND cyclin B1-mCherry (n>149 cells from 3 independent experiments).

(E) Mad2 localization was analyzed by IF 2 h after MG132 release in cells expressing ND cyclin B1-mCherry. Aurora B kinase inhibitor ZM447439 (2 μM) [S1] was added

40 min after release from MG132 arrest (n>149 cells from 3 independent experiments). Scale bars represent 10 µm.
(F) Autocorrelation analysis [S2] of the change in distance b (see schematic) over time for late anaphase (WT cyclin B1; n=21) and pseudo-anaphase cells (ND cyclin B1; n=30). Half-period of oscillation is indicated by orange arrow. Autocorrelation analysis of the spindle pole-to-kinetochore distance over time, confirmed that there is oscillatory motion in pseudo-anaphase compared to normal late anaphase.

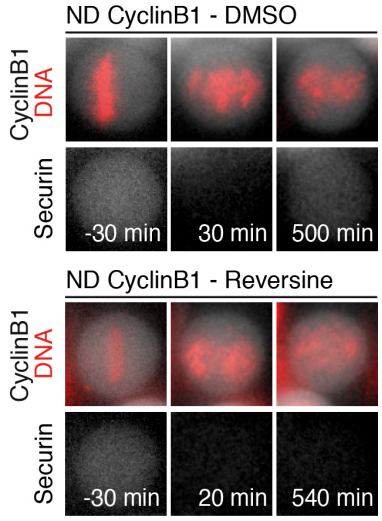

Figure S3 (Related to Figure 3). Securin-EGFP accumulation in pseudo-anaphase cells depends on Mps1 kinase activity
Frames of live-cell imaging of HeLa cells stained with Hoechst 33342 expressing securin-EGFP and ND cyclin B1-mCherry are shown. 1 h after release from nocodazole (30 ng/ml) cells expressing ND cyclin B1 were treated with DMSO or reversine (0.5 µM).

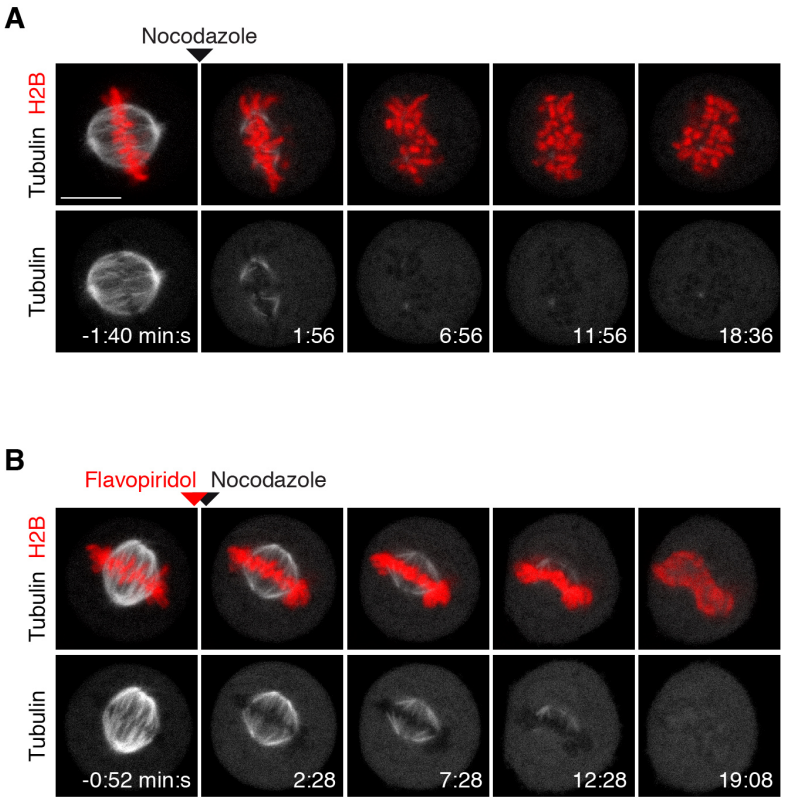

Figure S4 (Related to Figure 4). Kinetics of spindle depolymerization upon acute flavopiridol and nocodazole treatment

HeLa cells expressing H2B-mCherry and mEGFP-α-tubulin were arrested in metaphase with MG132 and imaged by 3D-confocal live-cell microscopy. Nocodazole (1 µg/ml) and flavopiridol (20 µM) were added acutely during imaging as indicated by the arrowheads. Images show single confocal z sections of representative cells. Time = 0:00 min:sec at the first drug addition.

(A) Spindle depolymerization upon nocodazole addition.

(B) Spindle depolymerization upon flavopiridol and nocodazole addition. Cells were acutely treated for 100 sec with flavopiridol prior to nocodazole addition. Scale bars, 10 µm.

Supplemental Experimental Procedures

Cell Culture, Synchronization and Drug Treatment

HeLa Kyoto, HeLa H2B-EGFP and HEK 293FT cells were grown as described in [S3]. HeLa Mad2-EGFP cells (a kind gift by Tony Hyman) [S4] were grown in medium supplemented with 500 μg/ml G418. HeLa GFP-CENPA (kindly gifted by P. Lenart [S5, 6]) were grown in medium supplemented with 0.4 μg/ml puromycin. Medium containing 200 μg/ml hygromycin B was used to grow HeLa H2B-iRFP (kind gift from K.C. Su). HeLa Mad2-EGFP H2B-iRFP cells were grown in medium supplemented with 500 μg/ml G418 and 200 μg/ml hygromycin B. HeLa Kyoto H2B-mCherry Mad2-EGFP monoclonal cells were described previously [S7] and grown in medium supplemented with 500 μg/ml G418 and 0.5μg/ml puromycin. Medium containing 300 μg/ml G418 and 0.3 μg/ml puromycin was used for growth of HeLa Kyoto EGFP-CENP-A EGFP-Centrin1 cells as previously described [S8]. For all the experiments (except Figures 4 and S4) cells were arrested for 20-22 h with 2 or 2.5 mM thymidine and subsequently synchronously released into mitosis for 8 to 17 h. For Figure 3B, 8 h after release a second thymidine arrest was performed and cells were subsequently synchronized at the metaphase-to-anaphase transition using a nocodazole-MG132 protocol according to [S3]. Drug concentrations used were 10 μM MG132 (Sigma), 15 μM flavopiridol (except in Figures 4B and S4, 20 μM flavopiridol) (Sigma), 100 nM BI 2536 [S6], 30 ng/ml nocodazole (Sigma) (Figures 3D and S3), 50 ng/ml nocodazole (Figures 3B, 3C, S1A and S1G), 1 μg/ml nocodazole (Figures 4 and S4), and 0.5 μM reversine (Sigma) [S9], and 2 μM ZM447439 (Tocris Bioscience) [S1].

siRNA Depletion, Plasmid Transfection and Lentivirus Infection.

The following siRNA duplexes were transfected at a final concentration of 20 nM using Lipofectamine RNAiMax (Invitrogen): Non targeting control (NTC, negative universal control siRNA medium GC), separase #1 (Thermo Scientific siGENOME D004104-01), separase #2 (Invitrogen Stealth HSS114543), Sgo1 (Invitrogen Stealth HSS135742). siRNA duplexes were transfected into cycling cells 24 hours prior to plasmid transfection and synchronization with thymidine (Sigma) (Figures 1E and S1G) or immediately prior to thymidine treatment (Figures 1C and S1F). Cycling cells were transfected using FuGene HD (Roche) with plasmids for expression of cyclin B1-mCherry WT (wild type) or ND (non-degradable, carrying the two D-box motif point mutations R42A and L45A) (kindly provided by J. Pines [S10]) (Figures 1, 2, 3A-C, S1 and S2) or in which the first 87 amino acids have been deleted Δ87-cyclin B1 (Figures 3D and S3), and pIRES-securin-EGFP [S11] (Addgene, 26464) (Figures 1D, 3A, 3D and S3) just prior to synchronization with thymidine. Transfection efficiency of ND cyclin B1-mCherry was determined for experiments in Figures 1B, 1C and 2D. More than 70% of mitotic cells were expressing the transgenic proteins 17 h after thymidine release and more than 50% of MG132-treated mitotic cells were transgene-positive (n>200 mitotic cells in each experiment). Viral particles were collected at 24 and 48 h after HEK 293FT cells were transfected with pLVX-IRES-Puro-cyclin B1-mCherry (WT or ND) and the two second generation packaging system plasmids psPAX2

(Addgene, 12260) and pMD2.G (Addgene, 12259) using Lipofectamine 2000 (Invitrogen). HeLa Kyoto cells were infected with lentiviral particles in presence of 8 μg/ml polybrene (Sigma) 30 minutes after released from the first thymidine block. Infection efficiency was determined after nocodazole treatment for WT cyclin B1-mCherry (>89%) and for ND cyclin B1-mCherry (>60%) (n>207 cells in each experiment) (Figure 3B and 3C).

Antibodies, dyes and FISH probes

Primary antibodies used for immunofluorescence were mouse monoclonal anti-α-tubulin (B512, Sigma, 1:500), rabbit polyclonal anti-Aurora B (ab2254, Abcam, 1:500), mouse monoclonal anti-Bub1 (clone 4H5, MBL International, 1:200), sheep anti-BubR1 (kindly provided by S. Taylor [S12], 1:1000), human CREST anti-centromere (HCT-0100, Immunovision, 1:1000), mouse monoclonal anti-cyclin B1 (GNS1, Sc-245 Santa Cruz Biotechnology, 1:400), rabbit anti-cyclin B1 (H-433, Sc-752, Santa Cruz Biotechnology, 1:500), mouse monoclonal anti-GFP (clones 7.1 and 13.1, Roche, 1:1000), mouse monoclonal anti-mCherry (632543, Living Colors, 1:1000), mouse monoclonal anti-Mps1 (clone N1, Invitrogen, 1:500), rat monoclonal anti-RFP (5F8, Chromotek, 1:400) and Alexa 488-conjugated mouse monoclonal anti-Mad1 (clone BB3-8, kindly provided by A. Musacchio [S13], 1:600). Cross-adsorbed secondary antibodies conjugated to Alexa 488, Alexa 594, Alexa 568 or Alexa 647 (Molecular Probes, Invitrogen) were used for detection. EGFP was detected in fixed cells using GFP-booster_Atto488 (Chromotek). DNA staining in fixed and living cells was performed using 1 μg/ml DAPI and 1 μM Hoechst 33342, respectively (Molecular Probes). Primary antibodies used for immunoblotting were mouse monoclonal anti-Cdc20 (clone BG1.3, kindly provided by Julian Gannon), mouse monoclonal anti-cyclin B1 (GNS1, Sc-245 Santa Cruz Biotechnology, 1:1000), mouse monoclonal anti-GAPDH (clone 6C5, ab8245, Abcam, 1:50,000), mouse monoclonal anti-Mad2 (610678, BD Transduction Laboratories, 1:500), rabbit polyclonal anti-Mad2 (A300-301A, Bethyl laboratories, 1:1000), mouse monoclonal anti-securin (DCS-280, ab3305, Abcam, 1:500) and mouse monoclonal anti-separase (XJ11-1B12, ab16170, Abcam, 1:200). Goat Hrp-conjugated secondary antibodies (GE Healthcare) were used for ECL detection and Dylight®-conjugated secondary antibodies for fluorescent immunoblotting (5257, anti-mouse IgG 800 and 5366, anti-rabbit IgG 680, Cell Signalling). Quantitative immunoblotting was analyzed on a LI-COR® Odyssey scanner. For MCC immunoprecipitation, mouse monoclonal anti-Cdc20 (p55 CDC H-7, Santa Cruz Biotechnology) was covalently coupled with Dynabeads® (Novex). For FISH (Fluorescence *in situ* hybridization), probes for the centromeres of chromosomes 6 (LPE 06G, Cytocell aquarius) and 8 (LPE 08R, Cytocell aquarius) were used.

Immunofluorescence

HeLa Kyoto and HeLa Mad2-EGFP were fixed with 4% formaldehyde at RT for 20 minutes and processed for immunofluorescence microscopy (IF) as described [S6]. The fixation solution was prepared in PBS (Figure S1A and S1E) or in PHEM buffer containing 0.2% Triton X-100 (Figures 2A, 2B and S2). Prior to fixation, 5 seconds pre-

extraction in PHEM containing 0.2% Triton X-100 was performed for Mps1 staining (Figure S2D). Cold treatment (cells were kept on ice for 20 minutes) and cold-resistant microtubule analysis were performed according to [S6] (Figure 2D).

Chromosome Spreads

Chromosome spreads of HeLa Kyoto cells were obtained by incubating mitotic cells in a hypotonic solution (DMEM:filtered deionized water at 1:2 ratio) for 6 min at room temperature (RT). Subsequently, cells were fixed with Carnoy's buffer (freshly made) for 15 min at RT and spun down, this fixation step was repeated four times. The suspension of cells in Carnoy's buffer (100 µl) is dropped on a clean slide from about 80 cm distance and let dry at RT. DAPI (1µg/ml) was added with the mounting solution (ProlongGold, Invitrogen) (Figures 1B and S1F).

Fluorescent *In Situ* Hybridization

Fluorescence *in situ* hybridization (FISH) was performed following Cytocell's instructions. Briefly, cells were grown on a coverslip and fixed with Carnoy's buffer (15 min at RT), washed with 2x SSC (saline sodium citrate), dehydrated in an ethanol series (70%, 80%, 100%) and air-dried. FISH probes (mixed with hybridization solution, provided by Cytocell aquarius) were added to a slide and the coverslip with cells was placed on top and sealed with rubber solution glue. Denaturation was performed for 2 min at 77^{o}C, and the slide was incubated overnight at 37^{o}C for hybridization in a humid and lightproof container. Subsequently, the coverslips were washed once in 0.25 x SSC for 2 min at 73^{o}C and twice in 2 x SSC with 0.05% Tween 20 for 30 sec at RT. Samples were mounted using ProlongGold (Invitrogen) with 1µg/ml DAPI (Figure 1C).

Microscopy of Fixed Samples

Images were acquired on a Zeiss Axio Imager M1 microscope using Plan Neofluor 40x/1.3 oil objective lens (Figures 2D quantification and S1A) and Plan Apochromat 63x/1.4 oil DIC objective lens (Zeiss) (Figures 1B, 1C, 1E, 2A, 2B, 2D, 4A, S1E, S1F, and S2) equipped with an ORCA-ER camera (Hamamatsu) and controlled by Volocity 5.5.1 software (Improvision). Images are displayed as maximum-intensity projections of deconvolved z planes (generated by Volocity's iterative restoration function) that were acquired in 0.1 µm sections (Figures 1C, 1E, 2A, 2B, 2D, 4A, S1E, and S2) or as a single plane (Figures 1B, S1A, S1F and mCherry images in Figures 2A, 2B and S2).

Live-Cell Imaging

Culture medium was changed to phenol-red-free CO_2-independent medium prior to start recording. Frames were acquired using an EC Plan Neofluor 40x/1.30 oil DICIII objective lens on an Axio Observer Z1 microscope (Zeiss) controlled by SimplePCI6 software equipped with a full-enclosure environmental chamber heated to 37^{o}C (Digital Pixel Imaging) and an ORCA 03GO1 camera (Hamamatsu) (Figures 1A, S1B, S3, and images for quantification in Figures 3A, 3D, S1C and S1D). Frames were recorded as three z planes (5µm apart) every 3 min (Figures 1A and S1C), every 3.5 min (Figure S1B), every 4 min (Figure 3A and Figure S1D, for image quantification) or every 10

min (Figure 3D and S3). Single z planes are displayed for DIC and cyclin B1-mCherry, whereas a maximum intensity projection is shown for H2B-GFP in Figures 1A, S1B and S3. For Figures 1D, 2C and 3A, frames were acquired as z planes (2.5 µm apart) every 6 min (Figures 1D and 3A, shown pictures) or as z planes (1 µm apart) every 5 min (Figure 2C) at 37°C using a Nikon TE2000 microscope equipped with a Plan Fluor 60x/1.4 DIC H lens (Nikon), a PerkinElmer ERS Spinning disk system, a CSU22 spinning disk scanner (Yokogawa), a IEEE 1394 Digital CCD C4742-80-12AG camera (Hamamatsu) and controlled by Volocity 6.0.1 software (Perkin Elmer). Images are displayed as maximum-intensity projections of central z planes. For Figure 2E, frames were acquired using a Nikon TiE microscope coupled with a Plan-Apochromat 100x/1.49 UV-C lens (Nikon), an UltraVIEW Vox system, CSU-X1-A3 spinning disk scanner (Yokogawa), a IEEE 1394b-2002 Digital CCD ORCA-R2 camera (Hamamatsu) and controlled by Volocity 6.1.2 software (Perkin Elmer); image stacks consisted of 25 z planes (0.5 µm apart) every 7.5 s imaged at 37°C. Tracking of EGFP-labelled CENP-A and Centrin1 was performed using the previously described Maki tracking software [S14]. Autocorrelation curves were calculated as previously described [S2]. For Figures 4B and S4, culture medium was changed to DMEM without phenol-red and riboflavin to reduce auto-fluorescence. 9 z planes (1.6 µm apart) were obtained by confocal live cell microscopy every 100 sec on a customized Zeiss LSM780 microscope using a 40x 1.4 N.A. Oil DIC Plan-Apochromat objective (Zeiss), controlled by ZEN 2011 software. The microscope was equipped with an EMBL incubation chamber (European Molecular Biology Laboratory), providing a humidified atmosphere at 37°C with 5% CO_2. Processing of images was performed using ImageJ64 1.43u and Fiji (ImageJ 1.48d) software [S15].

Image Quantification

For Figures 2D, 3A and 3D, α-tubulin, securin-EGFP and cyclin B1-mCherry integrated cellular intensities were measured and background corrected. In Figure S1A, the relative levels of cyclin B1-mCherry in each cell were calculated as follows: the mean cyclin B1 intensity of non-transfected cells (mCherry-negative) was subtracted from the mean cyclin B1 intensity of an individual transgene expressing cell (mCherry-positive). The resulting value was normalized to the mean cyclin B1 intensity of non-transfected cells (mCherry-negative) after background correction. All these measurements were performed in 16-bit single in-focus z plane images using ImageJ64 1.43u software. For Figure 4B, microscopy images were processed and analyzed using Fiji. Mad2-EGFP intensity in chromatin regions was measured in average intensity projections of the middle 6 z-sections. Chromatin regions were automatically determined in maximum intensity projections of the respective 6 z-sections using a Fiji macro: images were converted using a HiLo lookup table, then the threshold was auto-adjusted with "method=Moments white" and finally a selection at the respective area was created. To calculate Mad2-EGFP increase over cytoplasm the cytoplasmic EGFP background and image background were measured in Mad2-EGFP average intensity projections.

Immunoprecipitation

HeLa Kyoto cells infected and synchronized in mitosis as indicated before were lysed in Buffer A (50 mM Tris pH 8.0, 150 mM NaCl, 0.5% NP-40, 1 mM DTT, 1 µM okadaic acid, 1 µM MC-LR and a protease inhibitor tablet from Roche). Protein concentrations were adjusted to 4.8 mg/ml and 1.2 mg lysates were incubated with 15 µl Dynabeads® Protein A magnetic beads (Novex) coupled to Cdc20 antibodies for 1h at 4°C. After 3 washes in buffer A, proteins were eluted by incubating the beads in sample buffer for 10 minutes at 95°C. Proteins were finally resolved by SDS-PAGE and transferred to PVDF membranes.

Supplemental References

S1. Ditchfield, C., Johnson, V.L., Tighe, A., Ellston, R., Haworth, C., Johnson, T., Mortlock, A., Keen, N., and Taylor, S.S. (2003). Aurora B couples chromosome alignment with anaphase by targeting BubR1, Mad2, and Cenp-E to kinetochores. J. Cell Biol. *161*, 267-280.

S2. Vladimirou, E., McHedlishvili, N., Gasic, I., Armond, J.W., Samora, C.P., Meraldi, P., and McAinsh, A.D. (2013). Nonautonomous movement of chromosomes in mitosis. Dev. Cell *27*, 60-71.

S3. Petronczki, M., Glotzer, M., Kraut, N., and Peters, J.M. (2007). Polo-like kinase 1 triggers the initiation of cytokinesis in human cells by promoting recruitment of the RhoGEF Ect2 to the central spindle. Dev. Cell *12*, 713-725.

S4. Hutchins, J.R., Toyoda, Y., Hegemann, B., Poser, I., Heriche, J.K., Sykora, M.M., Augsburg, M., Hudecz, O., Buschhorn, B.A., Bulkescher, J., et al. (2010). Systematic analysis of human protein complexes identifies chromosome segregation proteins. Science *328*, 593-599.

S5. Kunitoku, N., Sasayama, T., Marumoto, T., Zhang, D., Honda, S., Kobayashi, O., Hatakeyama, K., Ushio, Y., Saya, H., and Hirota, T. (2003). CENP-A phosphorylation by Aurora-A in prophase is required for enrichment of Aurora-B at inner centromeres and for kinetochore function. Dev. Cell *5*, 853-864.

S6. Lenart, P., Petronczki, M., Steegmaier, M., Di Fiore, B., Lipp, J.J., Hoffmann, M., Rettig, W.J., Kraut, N., and Peters, J.M. (2007). The small-molecule inhibitor BI 2536 reveals novel insights into mitotic roles of polo-like kinase 1. Curr. Biol. *17*, 304-315.

S7. Schmitz, M.H., and Gerlich, D.W. (2009). Automated live microscopy to study mitotic gene function in fluorescent reporter cell lines. Methods Mol. Biol. *545*, 113-134.

S8. McHedlishvili, N., Wieser, S., Holtackers, R., Mouysset, J., Belwal, M., Amaro, A.C., and Meraldi, P. (2012). Kinetochores accelerate centrosome separation to ensure faithful chromosome segregation. J. Cell Sci. *125*, 906-918.

S9. Santaguida, S., and Musacchio, A. (2009). The life and miracles of kinetochores. EMBO J. *28*, 2511-2531.

S10. Gavet, O., and Pines, J. (2010). Progressive activation of CyclinB1-Cdk1 coordinates entry to mitosis. Dev. Cell *18*, 533-543.

S11. Held, M., Schmitz, M.H., Fischer, B., Walter, T., Neumann, B., Olma, M.H., Peter, M., Ellenberg, J., and Gerlich, D.W. (2010). CellCognition: time-resolved phenotype annotation in high-throughput live cell imaging. Nat. Methods *7*, 747-754.

S12. Taylor, S.S., Hussein, D., Wang, Y., Elderkin, S., and Morrow, C.J. (2001). Kinetochore localisation and phosphorylation of the mitotic checkpoint components Bub1 and BubR1 are differentially regulated by spindle events in human cells. J. Cell Sci. *114*, 4385-4395.

S13. Vink, M., Simonetta, M., Transidico, P., Ferrari, K., Mapelli, M., De Antoni, A., Massimiliano, L., Ciliberto, A., Faretta, M., Salmon, E.D., et al. (2006). In vitro FRAP identifies the minimal requirements for Mad2 kinetochore dynamics. Curr. Biol. *16*, 755-766.

S14. Jaqaman, K., King, E.M., Amaro, A.C., Winter, J.R., Dorn, J.F., Elliott, H.L., McHedlishvili, N., McClelland, S.E., Porter, I.M., Posch, M., et al. (2010). Kinetochore alignment within the metaphase plate is regulated by centromere stiffness and microtubule depolymerases. J. Cell Biol. *188*, 665-679.

S15. Schindelin, J., Arganda-Carreras, I., Frise, E., Kaynig, V., Longair, M., Pietzsch, T., Preibisch, S., Rueden, C., Saalfeld, S., Schmid, B., et al. (2012). Fiji: an open-source platform for biological-image analysis. Nat. Methods *9*, 676-682.